RMIT UNIVERSITY

Composites with Aligned Carbon Nano-reinforcements: Synergistically Improving the Damage Tolerance and Detection

A thesis submitted in fulfilment of the requirements for the degree of

Doctor of Philosophy (Aerospace Engineering)

Raj B. Ladani

Bachelor of Engineering (Hons)

School of Aerospace, Mechanical and Manufacturing Engineering

College of Science, Engineering and Health

RMIT University

June 2016

Declaration

I certify that except where due acknowledgement has been made, the work is that of the author alone; the work has not been submitted previously, in whole or in part, to qualify for any other academic award; the content of the thesis/project is the result of work which has been carried out since the official commencement date of the approved research program; any editorial work, paid or unpaid, carried out by a third party is acknowledged; and, ethics procedures and guidelines have been followed.

Raj B. Ladani

22 June 2016

Acknowledgements

I would like to sincerely thank my supervisor: Prof. Chun H. Wang of RMIT University for the wonderful level of guidance, dedication and belief in me throughout this PhD project. He has always provided tireless support and advice across all aspects of the project, and has been an invaluable source of knowledge and inspiration both professionally and personally.

I would like to extend my gratitude to the entire ARC Discovery Project (DP140100778) team who supported me throughout this PhD. Especially, Prof. Adrian Mouritz and Prof. Kamran Ghorbani of RMIT University for their support and guidance. Dr Jin Zhang of Deakin University for assistance with the FIB-SEM work. Prof. Anthony Kinloch of Imperial College London for his knowledge and guidance with the fracture modelling work. A special thank you to Dr Shuying Wu of RMIT University for forming a wonderful research collaboration with me through the ARC Discovery Project. Her expertise and guidance with nano-material synthesis and characterisation has been critical to the success and timeliness of this project. I would like to thank many of my colleagues and friends at RMIT University; Dr Khomkrit Pingkarawat, Mr Anil Ravindran, Mr Tanmay Bhat, Mr Fabio Pegorin, Mr Jarrod Hayes-Griss and Mr Geoffrey Thomas. I would also like to acknowledge the financial support provided by the ARC Discovery Grant (DP140100778) and the Australian Postgraduate Award.

I would like to sincerely thank Peter Tkatchyk and Mr Robert Ryan of the RMIT University workshop and laboratory team. The author kindly acknowledges the facilities and the technical assistance of the RMIT Microscopy and Microanalysis Facility team.

I thank my family for the wonderful support and care I have had during my PhD and over my entire academic career. Especially, my wife Payal, who I am indebted to beyond measure, for her support of my PhD and career aspirations.

Summary

Advanced fibre-reinforced polymer composites are now extensively used in aerospace industry as a result of the increasing demand for lightweighting technology to reduce fuel consumption and improve energy efficiency. Advanced fibre-reinforced polymer composites offer numerous advantages over metallic alloys, including higher specific strength and stiffness, resistance to corrosion damage and fatigue cracking. However, in the absence of through-thickness reinforcement, laminated composite materials are susceptible to interlaminar and intralaminar delamination damage due to accidental impact from bird strikes, hailstones, and tools dropped during maintenance. In addition, the low through-thickness conductivity of composites and its bonded structure presents challenges in protecting of aircraft against lightning strikes and detection of damage using traditional electrical based non-destructive techniques.

In light of these challenges, the general aim of this PhD project is to investigate the effects of carbon nano-reinforcements alignment on the fracture and electrical properties of epoxy composites. The alignment of the nano-reinforcements was investigated using two different external field based techniques, namely electric-field and magnetic-field. The carbon nano-reinforcements used for the investigations include one-dimensional carbon nanofibres (CNFs) and two-dimensional graphene nanoplatelets (GNPs). The project explores key parameters for reinforcing the epoxy composites with carbon nano-reinforcements, including their weight content, shape (one-dimensional and two-dimensional), orientation (random and aligned), and alignment techniques (electric- and magnetic-field). The PhD also investigates the influence of the alignment of CNFs on the damage detection ability of the CNF-reinforced epoxy adhesive bonded composite joints.

The PhD thesis presents a comprehensive review of published research into the fracture and electrical properties of nanocomposites and fibre-reinforced composites containing carbon nano-reinforcements. Recent advances in techniques for aligning carbon nano-reinforcements in composite materials, including mechanical force, electric-field and magnetic-field are reviewed. Based on the review, gaps and deficiencies in the use of carbon nanomaterials as matrix reinforcements are identified, and this forms the basis for the research presented in this thesis.

The first research study presented in the PhD thesis explores the fracture properties of epoxy composites reinforced with aligned CNFs. The alignment of the CNFs in the through-thickness direction is achieved using an alternating current (AC) electric-field. The study showed that the addition of just 1.0 wt% of aligned CNFs increase the fracture energy by about 1100%. A modelling technique is presented to quantify this major increase in the fracture energy with aligned CNFs. The model results were in good agreement with the experimentally measured fracture energy. The subsequent study into the use of AC electric-field aligned GNP-reinforced epoxy composites revealed similar level of improvement in the fracture energy of such composites, but at somewhat higher GNP weight fractions.

The PhD thesis presents a comparative study into the use of aligned one-dimensional (i.e. CNFs) and two-dimensional (i.e. GNPs) carbon nanomaterial reinforced epoxy composites for improving their fracture and electrical properties. A detailed fractographic analysis is used to identify the toughening mechanisms induced by the CNF and GNP reinforcements leading to the large improvements in the fracture energy of the epoxy composites. A mechanistic fracture model is presented to account for the fracture energy dissipated via each toughening mechanisms for CNF- and GNP-reinforced epoxy composites. It was discovered that CNFs are efficient at increasing the intrinsic toughness, whereas GNPs are more effective at increasing the extrinsic toughness of an epoxy composite. The electrical conductivity studies showed that alignment of the CNFs and GNPs lowers the percolation thresholds necessary to achieve direct current (DC) conductivity for the epoxy composites.

A further study investigated the use of electric-field aligned CNFs for improving the fatigue resistance of epoxy composites. The CNF-reinforced epoxy composites showed a greater resistance to fatigue cracking due to a combination of intrinsic and extrinsic toughening mechanisms induced by the CNFs. The fractographic analysis revealed that CNFs undergo a unique fatigue induced damage mechanism when subjected to cyclic loading. In addition, the PhD thesis investigates the use of CNF-reinforced epoxy as an adhesive layer to study the possibility of damage detection in bonded composite joints subjected to cyclic loading. The improved electrical conductivity of the CNF-reinforced epoxy enabled real-time *in-situ* detection of fatigue cracking using a DC potential drop technique. A simple resistivity model is used to

correlate the changes in resistance to the adhesive disbond length. During fatigue cracking, good correlation was found between the disbond length calculated from the resistivity model and the optically observed disbond length. This *in-situ* technique represents a potential alternative for detecting disbond in bonded composite structures.

In addition to the electric-field aligned CNFs, the PhD project investigates the alignment of CNFs using a magnetic-field. The CNFs were first functionalised with Fe_3O_4 nanoparticles, in order to increase their magnetic susceptibility. The improvement in the fracture energy and electrical conductivity of the epoxy composites reinforced with magnetic-field aligned Fe_3O_4@CNFs was greater than their random counterparts. However, the overall improvement in the fracture and electrical property of epoxy composites reinforced with Fe_3O_4 functionalised CNFs was lower than that reinforced with the unfunctionalised CNFs.

Finally, the delamination resistance of composite laminates containing multi-scale reinforcements, including CNFs and carbon z-pins were also investigated. The study investigated the effects of using through-thickness nano-scale (CNFs) and micro-scale (z-pin) carbon reinforcements on the delamination resistance of carbon fibre-epoxy laminates. The delamination toughness of the composite laminate reinforced concurrently with CNFs and z-pins increased (by ~400%) in comparison to the control laminate, suggesting a synergistic toughening mechanism. Under cyclic loading, the multi-scale reinforced laminates also show strong improvement in resistance against fatigue delamination growth. The new class of fibre composites with multi-scale through-thickness reinforcements offers a unique opportunity to greatly enhance the fracture toughness and fatigue resistance, and hence damage tolerance ability of advanced fibre composite materials.

Publications

- Ladani RB, Wu S, Kinloch AJ, Ghorbani K, Zhang J, Mouritz AP, Wang CH. *Improving the toughness and electrical conductivity of epoxy nanocomposites by using aligned carbon nanofibres*. Composites Science and Technology. 2015; 117:146-158.

- Ladani RB, Wu S, Kinloch AJ, Ghorbani K, Zhang J, Mouritz AP, Wang CH. *Multifunctional properties of epoxy nanocomposites reinforced by aligned nanoscale carbon*. Materials & Design. 2016; 94:554-564.

- Wu S, Ladani RB, Zhang J, Bafekrpour E, Ghorbani K, Mouritz AP, Kinloch AJ, Wang CH. *Aligning multilayer graphene flakes with an external electric field to improve multifunctional properties of epoxy nanocomposites*. Carbon. 2015; 94:607-618.

- Wu S, Ladani RB, Zhang J, Kinloch AJ, Zhao Z, Ma J, Zhang X, Mouritz AP, Ghorbani K, Wang CH. *Epoxy nanocomposites containing magnetite-carbon nanofibers aligned using a weak magnetic field*. Polymer (United Kingdom). 2015; 68:25-34.

- Ladani RB, Ravindran AR, Wu S, Pingkarawat K, Kinloch AJ, Mouritz AP, Kinloch AJ, Mouritz AP, Ritchie RO, Wang CH. *Multi-scale toughening of fibre composites using carbon nanofibres and z-pins,* Accepted for publication in Composite Science and Technology, 2016.

- Ladani RB, Wu S, Kinloch AJ, Mouritz AP, Wang CH. *The unravelling of carbon nanofibres under fatigue loading,* Small, 2016. (under review)

- Wang CH, Ladani RB, Wu S, Kinloch AJ, Zhang J, Ghorbani K, Mouritz AP. *Epoxy Nanocomposites with Aligned Carbon Nanofillers by External Electric Fields*. In Proceeding of the 26th International Conference on Composite Materials, Copenhagen, Denmark, 2015.

- Ladani RB, Wu S, Mouritz AP, Kinloch AJ, Ghorbani K, Wang CH. *Disbond Monitoring of Composite Adhesive Joints with DC Resistance Technique using Carbon Nanofibre Network*. In Proceeding of the 26th International Conference on Composite Materials, Copenhagen, Denmark, 2015.

- Ladani RB, Kinloch AJ, Wang CH. *Alignment of Carbon Nanofibers in Carbon Fiber/Epoxy Resin Adhesive Bonded Joints for Mode-I Fracture Toughness Improvement*. In Proceeding of the 22th International Conference on Processing and Fabrication of Advanced Materials, Singapore, 2013

Table of Contents

List of Figures

List of Tables

List of Abbreviations

Unit	Definition
CNT	Carbon nanotube
CNF	Carbon nanofibre
GNP	Graphene nanoplatelet
SW	Single-wall
DW	Double-wall
MW	Multi-wall
US	Ultrasonication
3RM	Three-roll-milling
HSM	High shear mixing
GF	Glass fibre
CF	Carbon fibre
VARTM	Vacuum assisted resin transfer moulding
AC	Alternate current
DC	Direct current
SEM	Scanning electron microscope
TEM	Transmission electron microscope

Nomenclature

Term	Unit	Definition
l	mm	Fibre length
d	mm	Fibre diameter
σ	MPa	Fibre strength
V		Fibre volume fraction
V_{fpo}		Fibre pull-out volume fraction
E	MPa	Young's modulus
ε		Strain
L_c	mm	Critical fibre length
l_{po}	mm	Fibre pull-out length
τ_i	MPa	Interface shear strength
η_θ		Fibre orientation efficiency factor
η_f		Fibre length efficiency factor
G	J/m^2	Strain energy release rate
G_{db}	J/m^2	Interface debonding energy
$G_{rupture}$	J/m^2	Fibre rupture energy
$G_{pull-out}$	J/m^2	Fibre pull-out energy
θ	rad	Orientation angle
μ		Snubbing friction coefficient
δ	Mm	Displacement
ω	Hz	Angular frequency
a	Mm	Crack length
t	Mm	Thickness
W	Mm	Width
A	mm^2	Cross-sectional area
k	N/mm	Stiffness
P	N	Load
σ	S/m	Conductivity
ρ	Ωmm	Resistivity
R	Ω	Resistance

Subscripts

Term	Definition
f	Fibre
m	Matrix
c	Critical
u	Ultimate
th	Threshold
eq	Equivalent
ur	Unravelling
min	Minimum
max	Maximum

Chapter 1

Introduction & Motivation

1.1 Background

Advanced fibre-reinforced polymer composites are now extensively used in aerospace sporting goods, wind turbines, offshore oil and gas production equipment, maritime, and civil infrastructures [1]. Increasingly lightweight composites are being applied in automotive vehicles and high-performance rail. The carbon-fibre composite materials market is still dominated primarily by the aerospace industry, comprising of 69% of the total composite shipment value for the fiscal year ending 2015 [2]. For instance, the latest generation of commercial aircrafts such as the Airbus 350 and Boeing 787 are comprised of more than 50% weight of composite materials. This increased use of composite materials in the latest generation commercial aircrafts can be attributed to many advantages of fibre-reinforced composites, such as higher specific strength, stiffness, resistance to corrosion damage and fatigue cracking than aluminium and other alloys commonly found in old generations of aircraft [1]. The primary driving force behind this rapid rise in the use of composite materials in commercial aircrafts has been the need for lightweighting technology to reduce fuel consumption and to improve energy efficiency.

However, from the data in Figure 1-1, the slower-than-anticipated take-up of composite materials in commercial aircrafts in comparison to military aircrafts has been attributed to their high cost of certification and relatively low resistance to mechanical impact damage from hailstones, bird strikes, tool drops, and runway debris [3], due to their low through-thickness strength and fracture toughness [4]. In choosing advanced composite materials for airframe applications, it is essential to ensure that there are no compromises in the level of safety provided by traditional metallic alloys. A significant disadvantage of laminated composite materials is their low through-thickness

mechanical because of the lack of reinforcement in that direction. For instance, the through-thickness strength of laminated composites is often less than 10% of the in-plane properties leading to poor impact damage resistance [3].

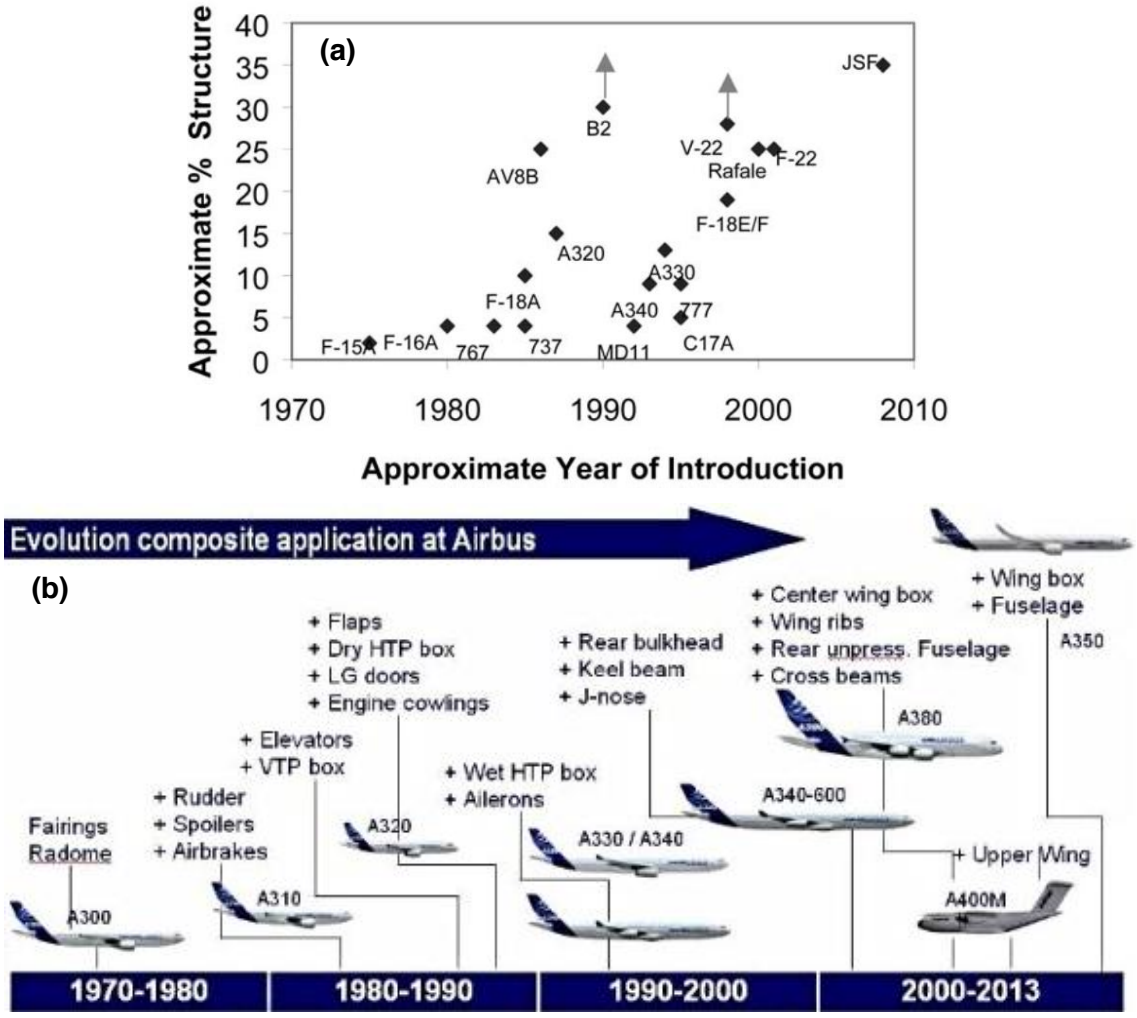

Figure 1-1 : Growth of use of advanced composite in (a) commercial and military airframe structures [3]; and (b) Airbus aircrafts [5]

Thus, in the absence of through-thickness reinforcements, composite laminates are designed conservatively so that they can sustain the ultimate design loads in the presence of delamination damage induced by accidental impact. Impact damage can result from bird strikes, hailstones, and tools dropped during maintenance. The resulting delamination damage tends to occur throughout the entire thickness of composite laminates leading to degradation in their in-plane mechanical properties under compression and bending, as shown in Figure 1-2. This damage is extremely difficult to detect, as it is largely hidden below the surface. Delamination damage can also occur

due to high interlaminar loads, edge stresses, manufacturing defects and environmental degradation of the composite [6]. Because much of the delamination damage occurs beneath the surface, existing non-destructive techniques such as visual inspection and ultrasonics are not effective for wide-area damage inspections and for regions that are hard to access. For instance, in 2012, Boeing discovered that a manufacturing flaw was causing delaminations in the longerons of the tail cone section of its carbon fibre 787 airframes. Prompting Boeing and its airline customers to inspect all in-service 787 aircrafts immediately and the delamination damage was confirmed on 3 of the 50 in-service aircrafts [7]. However, this delamination had remained undetected on the 3 particular aircrafts during regular in-service inspections and ramp damage check performed by maintenance personnel.

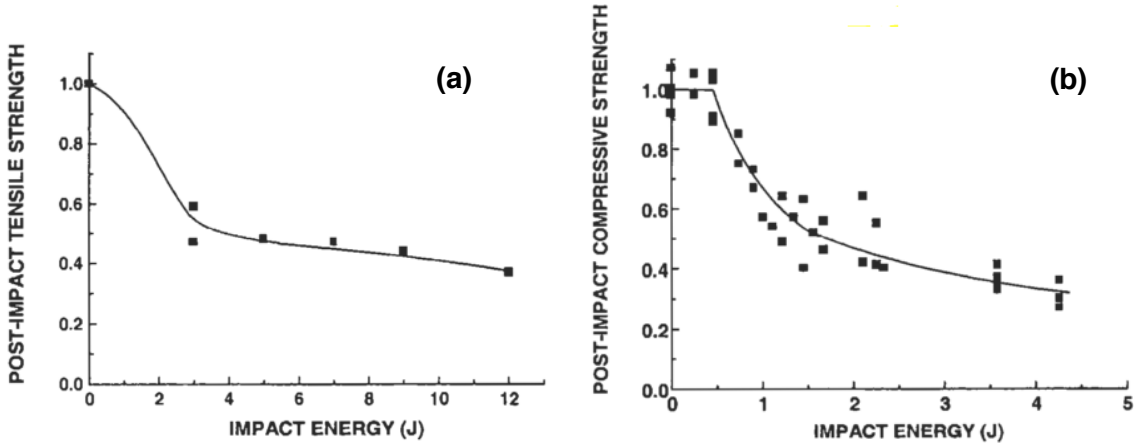

Figure 1-2 : Effect of impact energy on the residual (a) tensile and (b) compressive strength of carbon fibre-epoxy laminate normalised by the strength of pristine laminate [4].

Therefore, to ensure continuing safety of the airframe, the Federal Aviation Administration's damage tolerant design regulations specify that delamination damage within aircraft composites above a critical size must be immediately repaired or the entire damaged structure replaced for continued service [8]. In addition, there are stringent aviation safety regulations on monitoring and management of the size of the delamination damage [9].

A further problem with advanced composites is the lack of through-thickness electrical conductivity in comparison to the in-plane conductivity of the laminates. The low through-thickness conductivity of composites is due to the dielectric nature of the

polymer matrix. Thus, the traditional electrical non-destructive detection techniques such as eddy current and potential drop cannot be used for detecting delamination damage. Furthermore, the low through-thickness conductivity of composites and its bonded structure presents challenges in protecting of aircraft against lightning strikes and electromagnetic interference. Composite airframe lightning strike protection currently consists of metallic wire mesh, embedded metallic wire, metallic picture frames, diverter strips, metallic foil liners, and bonded aluminium foil, which act as a sacrificial layer designed to ablate during a lightning strike [10]. Although this provides necessary lightning protection in selected areas, it can partially offset the weight saving benefits of using advanced composite materials. If the chosen lightning protection for the composite airframe is inadequate, a lightning strike event can lead to structural damage as shown in Figure 1-3. Moreover, the repair of damage sustained from lightning strikes adds to the maintenance cost of composite airframes [11].

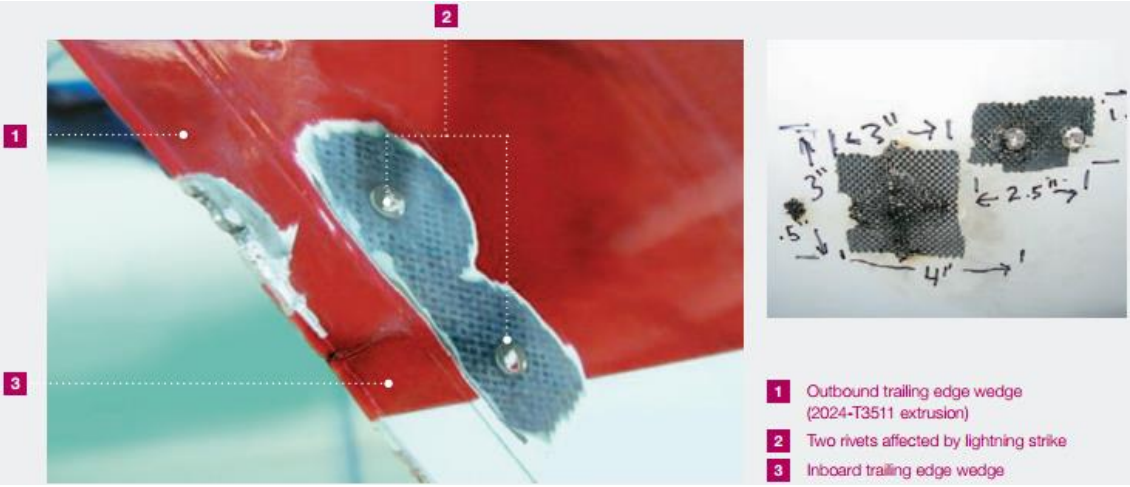

Figure 1-3 : Lightning damage to the outbound and inboard trailing edge wedge of the Boeing 787 airframe [10].

Matrix cracking is the most pronounced damage initiation mode leading to the delamination in composites. Matrix cracks initiate at inter- or intralaminar regions experiencing stresses perpendicular to the fibre direction. Thus, delamination damage in composites depends to a large extent on the fracture toughness of the matrix. Thermoset epoxies are widely used as matrices for manufacturing fibre reinforced composites and as adhesives for joining composite components. Polymerization of epoxies results in a highly-crosslinked microstructure, providing many desirable properties for structural engineering applications such as high modulus and failure strength, excellent adhesion,

good performance at elevated temperatures and resistance to chemical and environmental degradation. However, due to this highly crosslinked structure, thermoset epoxies often have low ductility and toughness leading to poor resistance to crack initiation and growth of damage. Thus, particulate reinforced matrices are commonly used to improve delamination resistance of composites. Traditional techniques to improve the damage tolerance of epoxy polymers are to form a polymeric alloy [12] via the addition of thermoplastics [13, 14], rubber toughenners [15-17] or silica particles [18, 19]. Although these methods provide significant improvements to the toughness, the electrical conductivity remains unchanged because such additives are dielectric. Micro-sized carbon pins, commonly referred to as z-pins, have been investigated to reinforce composites in the thickness direction [20, 21]. But they are effective only for resisting large-scale delamination [20].

1.2 Motivation

In recent years, studies on conductive carbon nano-reinforcements, such as CNTs [22-24], CNFs [25, 26], and GNPs [27-30], have indicated promising reinforcement efficiency as well as the ability to enhance electric properties of epoxy and their fibre reinforced composites. Carbon nano-reinforcements are the preferred choice of fillers for simultaneously improving the multifunctional properties of composite materials owing to their high aspect ratios, large specific surface area and superior mechanical as well as thermal and electrical properties. For instance, Figure 1-4a shows the effect of particle diameter on their specific surface area for various spherical and fibrous particles [31]. This figure indicates that a very small volume content of nanofillers provides a huge surface area which would lead to lower percolation thresholds for improving the thermal and electrical properties of the polymer composites. Moreover, the high aspect ratio of these nano-reinforcements provides effective mechanical reinforcement to the polymer composites. As shown in Figure 1-4b, the aspect ratio of a nano-reinforcement (fibre or platelet) has a pronounced effect on the composite modulus [32]. Several studies have shown that carbon nano-reinforcements can form conductive networks in polymeric materials at extremely low weight fractions [33, 34].

These conductive networks show great promise for *in-situ* health monitoring of delamination and disbond damage in composite laminates [35-38]

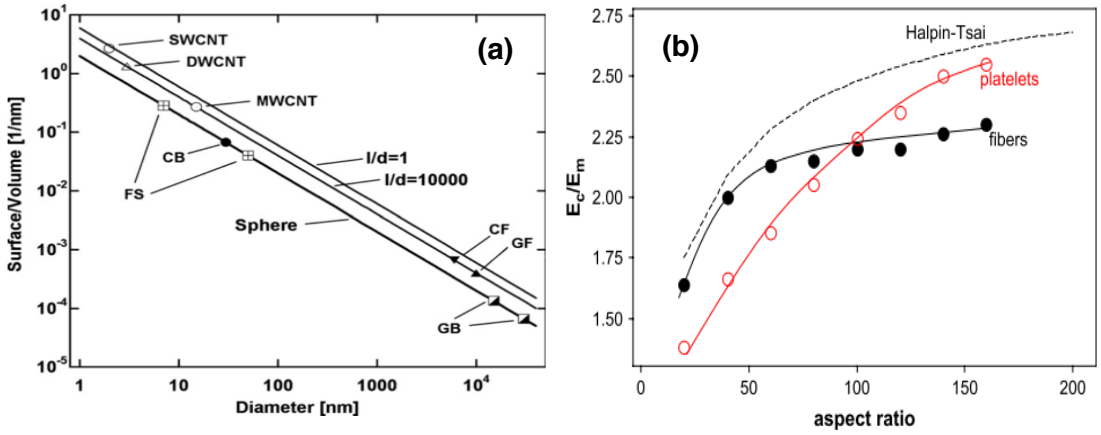

Figure 1-4 : (a) A comparison of the ratio of surface area and volume for various spherical and fibrous particles as a function of the particle diameter [31]. (b) The effect of particle aspect ratio on the composite modulus normalised by the matrix modulus value and its comparison to the Halpin-Tsai model [32].

However, a recent review article on various strategies for enhancing the properties of laminated fibre composites with carbon nano-reinforcements has indicated that the improvement in delamination resistance of the carbon nano-reinforced multi-scale composites has been much lower than expected [39]. Moreover, these improvements are significantly lower in comparison to the enhancements achieved by carbon z-pin reinforced composite laminates. For example, just 0.5 vol% carbon z-pin reinforcement aligned in the through-thickness of composite laminate can increase its mode I steady state delamination fracture energy by up to 280 %, which increases further to 1500% at a content of 2 vol% [40]. This finding suggests that aligning the carbon nano-reinforcements in the through-thickness direction of the multi-scale composite laminate is necessary for achieving a substantial improvement to their fracture energy. Indeed, numerical analyses have confirmed that in comparison to randomly oriented CNTs, a 3.0 vol% CNTs aligned in epoxy normal to the crack growth plane can enhance its toughness by up to 400% [41]. This was experimentally demonstrated by Veedu et al. [42], who used chemical vapour deposition (CVD) technique to deposit 2.0 wt% of aligned CNT forest onto SiC woven fibre preforms. The resultant multi-scale fibre-epoxy composite containing aligned CNT reinforcement showed the mode I and II fracture energy enhancement of about 280% and 54%

respectively. However, the high temperature required for achieving direct CVD growth of aligned CNTs onto carbon or glass fibre preforms is well in excess of 750 °C which weakens the structural fibres. For instance, the coating of IM7 carbon fibres with CNT via direct CVD growth at 800 °C resulted in their tensile strength being reduced by about 70% [43]. Thus, the in-plane properties of the resulting multi-scale composites could be significantly lower. Unfortunately, there is a dearth of suitable processes to align carbon nano-reinforcements along the through-thickness direction of fibre reinforced composites.

In the past decade, the use of electric- and magnetic-fields to align nanoparticles in liquid resins, prior to curing, has been reported [44-50]. Under the application of an electric- or magnetic-field, the nano-reinforcements may align to form a chain-like network in the direction of the external field [51, 52]. The nano-reinforcement can be oriented in any desired direction by manipulating and orienting the external field direction. Since thermosetting resins, such as epoxy resins, may typically possess a relatively low viscosity prior to cure, the application of an electric- and/or magnetic-field will be able to transform the randomly-oriented carbon-based nano-reinforcements to give a highly aligned structure. This mechanism of the self-aligning of conductive carbon nano-reinforcements in polymers offers a new opportunity to create multi-scale composite structures. The alignment of carbon nano-reinforcements such as CNTs [53], CNFs [52] and GNPs [49] using an electric-field has indeed been reported to improve the electrical conductivity of polymers through the formation of a chained network at a low content of the nano-reinforcements. In spite of these studies, the effects of electric-field induced alignment of the nano-reinforcements on the fracture property of its composites have not been explored. By aligning the nano-reinforcements in the direction perpendicular to the crack propagation path, a greater fraction of the nano-reinforcement could be expected to participate in fracture toughening mechanisms leading to greater improvement in the fracture resistance of epoxy nanocomposites or multi-scale fibre composites.

While an electric-field can be used to align carbon nano-reinforcements in glass fibre-reinforced composite, in a carbon fibre composite, the alignment is much difficult to realise. The main reason is that the local contact of conductive carbon fibres causes local short-circuiting which weakens the electric-field inside the composite, leading to

weaker forces for the nano-reinforcements to rotate. However, it is well known that the magnetic flux generated in a magnetic-field can penetrate through conductive materials such as carbon fibres. Therefore, magnetic-field induced alignment technique offers a promising alternative for aligning carbon nano-reinforcements in the through-thickness direction of carbon fibre composites which has yet to be explored. However, due to the low magnetic susceptibility of carbon nano-reinforcements at room temperature, an extremely strong magnetic-field (e.g. of several Teslas) is usually required for their alignment which is impractical for manufacturing of composites [54]. Very recently, a new method has been reported to functionalise carbon nano-reinforcements with magnetic nanoparticles, especially iron-based nanoparticles, so as to facilitate the alignment of carbon nano-reinforcements in a polymer matrix without needing to employ high magnetic-fields [55]. For instance, magnetite (Fe_3O_4) decorated CNTs have been recently developed and these hybrid nano-reinforcements were successfully aligned in an epoxy using a relatively weak magnetic-field of just 0.3 T [55]. Thus, these mechanisms of external field induced self-aligning of conductive carbon nano-reinforcements in polymers offers a new opportunity to create multi-scale composite structures with far superior multifunctional properties.

1.3 Research Aims and Objectives

The overall research objective of this PhD project is to advance a new enabling science for aligning nano-scale carbon reinforcements to improve the fracture and electrical properties of epoxy nanocomposites and epoxy matrices in fibre composite materials. Two types of carbon nano-reinforcements are investigated: carbon nanofibres and graphene nanoplatelets. Two different external field based alignment techniques are investigated, namely electric-field and magnetic-field to align both types of carbon nano-reinforcements in epoxy composites, particularly in the through-thickness direction. In achieving this aim the research work will address the following fundamental scientific problems:

(i) What are the effects of aligning carbon nano-reinforcements via external electric- and/or magnetic-field on the fracture and electrical properties of epoxy composites?

(ii) Which mechanistic models can be applied in the analysis of the fracture and electrical properties of one-dimensional (CNF) and two-dimensional (GNP) carbon nano-reinforced epoxy composite?

(iii) What are the benefits of aligning carbon nano-reinforcements in a composite to detect damage via electrical potential drop techniques?

This proposal presents several new scientific concepts and research methodologies to bring about the aforementioned research investigations. The discovery and successful development of these new principles and novel processes will break new ground in the creation of a new class of damage tolerant fibre-reinforced composites, as well as the concurrent development of a new contactless damage detection method taking advantage of highly aligned and chained carbon nano-reinforcements.

1.4 Thesis Outline

The next chapter presents a comprehensive and critical review of published research into carbon nano-reinforced polymer composites. The literature review focuses on the effect of fibre orientation on mechanical properties of the fibre composite which provide the foundation for this research work. Various strategies used for enhancing the fracture resistance of carbon nano-reinforced matrix in nanocomposite and multi-scale fibre reinforced composites are reviewed, highlighting the key research gaps that need to be addressed. Later, the new emerging techniques for orienting carbon nano-reinforcements along the through-thickness direction of composites are presented. It is then followed by a review of its potential application in improving the damage tolerance and detection in carbon nano-reinforced composite materials.

Each research chapter in this PhD thesis presents an abstract, introduction, description of the experimental methodology, results and discussion, and conclusion section. In addition, details of the journal and conference papers arising from the PhD research work are listed. This thesis contains published work and some of which has been co-authored. Only primary contribution by the author alone towards any co-authored published work performed as part of research collaboration has been included

in this thesis. The complete co-authored publication has been attached in the appendix where permitted by the copyright laws.

A research investigation into the use of aligned CNFs to improve the fracture resistance of epoxy composites is presented in Chapter 3. The effect of CNF orientation and concentration on the fracture energy of epoxy composites is experimentally determined. An AC electric-field is used to align CNFs in the direction perpendicular to the crack propagation path. The alignment of the CNFs in the epoxy is studied via TEM. The fracture toughening mechanisms of the CNF-epoxy composites are investigated via fractographic analysis. A mechanistic model is presented to calculate the fracture energy contribution from each toughening mechanisms identified from the fractographic analysis. A similar investigation into the use of aligned GNPs to improve the fracture resistance of epoxy composites is presented in Chapter 4. Some notable differences in the fracture behaviour and toughening mechanisms of GNP-epoxy composites were identified from the fractographic analysis. The findings from the study presented in Chapter 3 and Chapter 4 led to a direct comparative investigation into the electrical and fracture properties of CNF- and GNP-epoxy composites, which are presented in Chapter 5. Additional modelling studies of the electrical property and the fracture mechanisms of GNP-epoxy composites and its comparison to CNF-epoxy composites are presented in Chapter 5.

Chapter 6 presents an investigation into the fatigue resistance CNF-reinforced epoxy composites when subjected to mode I cyclic loading. The effects of CNF orientation and concentration on the critical and threshold strain energy release are determined experimentally. The toughening mechanisms responsible for the improvement to the fatigue crack growth resistance of the CNF-reinforced epoxy composites are identified from the fractographic analysis. The fractographic studies led to the discovery of a unique fatigue induced failure mechanisms in CNFs when subjected to cyclic loading. The results from additional *in-situ* cyclic tests on individual CNFs with fatigue damage are presented in Chapter 6. A mechanistic model is presented to evaluate the bridging traction behaviour for the CNF undergoing the unique fatigue induced failure mechanism. Chapter 7 presents an experimental investigation into the use of CNF networks to detect fatigue induced disbond and delamination damage in composites. The effects of CNF concentration and orientation

on the electrical resistance change arising from the fatigue cracking of the epoxy composites are determined experimentally. A simple resistivity model is used to investigate the ability of embedded CNF networks to detect and monitor fatigue induced disbond in epoxy composite. The electrical resistance measurements are used in the resistivity model to characterise the change in disbond length due to fatigue cycling.

Chapter 8 presents an investigation into the use of low strength magnetic-field to align Fe_3O_4 functionalised CNFs in epoxy composites. The CNFs are first functionalised with Fe_3O_4 nanoparticles using a co-precipitation method developed by a research collaborator. The effects of alignment of the Fe_3O_4 functionalised CNFs on the electrical conductivity and fracture property of epoxy composites are experimentally determined.

Chapter 9 presents an experimental investigation into the delamination resistance of composite laminates containing multi-scale reinforcements. The study investigated the effects of using through-thickness nano-scale (CNFs) and micro-scale (z-pins) carbon reinforcements on the delamination resistance of carbon fibre-epoxy laminates under quasi-static and cyclic loading. The effect of CNF reinforcements on the z-pin pull-out behaviour is determined experimentally. A mechanistic model is presented to study the effects of CNF reinforcements on the interface property of z-pins and its bridging traction behaviour. The final chapter summarises the main conclusions obtained from the research performed in this PhD project and highlights the future research areas essential for further investigation into the carbon nano-reinforced composites.

Chapter 2

Literature Review

The addition of carbon nano-reinforcement is now a popular strategy utilised in the synthesis of composite materials in pursuit of superior multi-functional properties. This research effort has led to the publication of over 20,000 journal articles[1] including 613 review articles on carbon nano-reinforcement during the period beginning with the advent of carbon nanotube up until the year 2012. Several of these review articles have reported a comprehensive overview of research in the context of carbon nano-reinforced composites focusing on improvement to their mechanical [56, 57], electrical [57, 58] and thermal properties [59]; synthesis and processing of carbon nano-reinforcements [60-62]; fabrication of carbon nanocomposites [63]; fundamental aspects of nano-reinforcements [31, 32]; application for sensing [64], battery [65] and biomedical technology [65, 66]; and more recently on their application in multi-scale fibre reinforced composites [39, 67]. Therefore, the same will not be repeated in this chapter but instead, this wealth of knowledge is utilised to present a brief overview of the complete set of mechanisms at work in composites that would help in addressing the aim to simultaneously improve their damage tolerance and detection capacity.

The first two part of this review focuses on classical mechanisms of fibre reinforced composites and the effect of fibre orientation on mechanical properties of the discontinuous-fibre composite which provide the foundation for this research work. In the third part of this chapter, the various strategies used for enhancing the fracture resistance of carbon nano-reinforced matrix in nanocomposites and multi-scale fibre

[1] Scopus search <carbon nano*> or <graphene> and <*composite> www.scopus.com

reinforced composites are reviewed which highlights the key research gaps that need to be addressed. Later in the final two sections, the new emerging techniques for improving the orientation efficiency of the carbon nano-reinforcements are presented which is then followed by a review of its current application in improving the electrical property and damage detectability of carbon nano-reinforced composites.

2.1 Strength of Fibre Reinforced Composite

Prediction of mechanical properties of fibre reinforced composites is a complex but a crucial problem. Even in the case of continuous-fibre composites with stress applied in the fibre direction, failure may occur in the fibres, in the matrix phase, or at an interface. In continuous-fibre composites with a varying ply orientation, failure may take place in a tensile or shear mode, even when subjected to tensile stress. Furthermore, the nature of failure could be brittle or ductile, and is highly dependent on the difference between the strength and toughness of the composite. The prediction of strength and toughness of a short-fibre composite system is even more complex. The following section outlines a review of the existing theory for predicting strength and toughness of fibre composites and highlights the most important parameters that could be optimised for further improvement.

2.1.1 Continuous-Fibre Composites

The problem of strength prediction is best illustrated in Figure 2-1, wherein we see that unlike for stiffness, the strength of short-fibre composite system, even at high aspect ratios, is much lower than that for continuous-fibre composites. Moreover, a considerable reduction in strength occurs due solely to fibre orientation. In comparison to the continuous aligned-fibre system, the strength of a short-fibre composite with randomly oriented fibres has dropped by 400%. Therefore, in short-fibre composites, the degradation phenomena due to fibre orientation should be well understood for successful prediction of the strength and toughness.

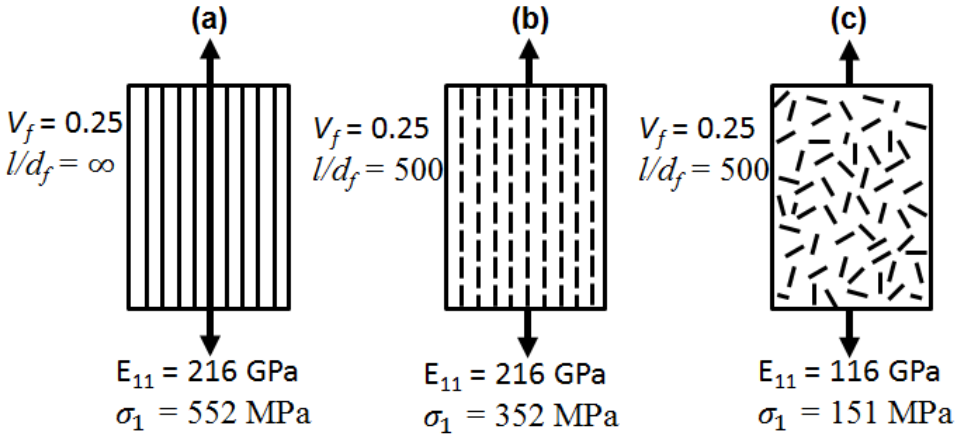

Figure 2-1 : The effect of fibre aspect ratio and orientation on the stiffness and strength of glass fibre-epoxy composites reinforced with (a) continuous-fibre, (b) aligned short-fibre, and (c) random short-fibre [68].

It is appropriate at this point to introduce the widely accepted theory for estimating the upper bound for strength of an aligned continuous-fibre system; namely, the rule-of-mixture expression [69],

$$\sigma_u = \sigma_f V_f + E_m \varepsilon_m (1 - V_f) \tag{2-1}$$

The strength of the left most system in Figure 2-1 can be reasonably predicted with the above relationship (2-1). It is against this upper bound that aligned short-fibre composite system performance is generally compared. If the fibres have a random orientation distribution, which can occur due to short-fibre composite processing variations, the penalty for this must be accounted for, as was first pointed out by Cox [70].

2.1.2 Short-fibre Composites

Historically, the prediction of the strength of short-fibre composite systems with a random fibre distribution began with the landmark paper by Cox [70], which served as the basis for later development of what is now called the "shear lag" theory. Cottrell introduced the concept of a critical fibre length, l_{cr} above which the fibre's ultimate strength will be fully realised [68]. The critical fibre principal was further extended by Kelly and Tyson [71], which can be utilised to attain up to 95% of continuous-fibre composite strength in short-fibre systems if perfect uniaxial fibre alignment can be achieved. This theory gives a good approximation of short-fibre composite strength [69,

72, 73] by postulating that if the fibres are discontinuous, then the fibre may carry stress only by shear transfer process at the interface. This led to the concept of a critical fibre length, L_c given by Kelly-Tyson [71],

$$L_c = \frac{\sigma_f d_f}{2\tau_i} \tag{2-2}$$

Other researchers [74, 75] have later proposed a modified expression for the rule of mixture by utilising the critical fibre length (i.e. shear lag) theory and the fibre orientation efficiency factor originally proposed by Cox as follows:

$$\sigma_{uc} = \eta_\theta \eta_f \sigma_f V_f + E_m \varepsilon_m (1 - V_f) \tag{2-3}$$

where the fibre orientation efficiency factor and the fibre length factors are given as follows:

$$\eta_\theta \begin{cases} = \frac{1}{3} \text{ for a 2D spatial fibre orientation distribution} \\ = \frac{1}{6} \text{ for a 3D spatial fibre orientation distribution} \end{cases}$$

$$\eta_f \begin{cases} = 1 - \frac{L_c}{2l} & (l > L_c) \\ = \frac{l}{2L_c} & (l < L_c) \end{cases}$$

The above expression suggests that in addition to the strength reduction due to fibre discontinuity, there is an additional penalty of 600% if the fibres are randomly oriented in a three-dimensional volume of matrix. Therefore, any attempts to improve the existing fibre-reinforced composite should consider the influence of fibre orientation on the mechanical properties of the composites.

2.1.3 Nano-carbon Reinforced Composites

In recent years, the advent of nano-scale carbon reinforcements such as carbon nanotube (CNT), carbon nanofibre (CNF) and graphene nanoplatelet (GNP) have shown tremendous potential for improving the mechanical, thermal and electrical properties of polymer composites. Carbon nano-reinforcements are the preferred choice of fillers for improving the multifunctional properties of composite materials owing to their high aspect ratios, immense specific surface area and superior mechanical as well

as thermal and electrical properties. For instance, Figure 1-4a shows the effect of particle diameter on the specific surface area for various spherical and fibrous particles [31]. This figure shows that a very small volume content of nanofillers provides a huge surface area which would lead to lower percolation thresholds for improving the thermal and electrical properties of the polymer composites. Moreover, the high aspect ratio of these nanofillers leads to an improved filler efficiency factor in Eq. (2-3), thereby providing effective mechanical reinforcement of the polymer composites. As shown in Figure 1-4b, the aspect ratio of a nanofiller (fibre or platelet) has a pronounced effect on the composite modulus [32]. According to the shear lag theory discussed earlier, for effective reinforcement of the composite, the nano-reinforcements ought to have high aspect ratio for efficient transfer of stress from matrix to the nano-reinforcements [76].

Despite the carbon nano-reinforcements possessing all the necessary attributes for providing effective mechanical reinforcement for polymer composites, the improvement to the stiffness and strength of nanocomposite has been much lower than originally predicted. Ajayan et al. [77] had first suggested that the alignment of the nano-reinforcements in the loading direction is essential to realistically transfer their remarkable properties to a polymer matrix. Indeed, numerical analyses have confirmed that 1.0 vol% aligned CNTs should increase the stiffness of an epoxy by about 300% [26] in the alignment direction. However, the mechanical properties of CNT composites have been much lower than predicted due to several obstacles, such as low CNT loading, poor interfacial bonding, short CNT length and lack of preferential alignment. The experimental work by Cheng et al. [78, 79] has successfully demonstrated that composites with aligned CNTs can have significantly improved stiffness and strength in comparison to their random counterparts. They reported that the stiffness and strength of the aligned CNT composite were higher by about 800% and 400% respectively, in comparison to the composite containing randomly-oriented CNTs [80]. Thus confirming the macro-mechanics principles (i.e. Eq. 2-3) developed for short-fibre composites are applicable for optimising the mechanical performance of the nano-reinforced composites. More recently, Wang et al. [81] have reported a novel (see Figure 2-2a-b) approach for processing high volume fraction aligned CNT-polymer composites. As can be seen in Figure 2-2c-d**,** the resultant aligned CNT-polymer composites possessed far superior specific strength in comparison to the existing high-

strength carbon fibre-reinforced polymer composites. Therefore, the effects of the orientation of carbon nano-reinforcements in the epoxy composites should be carefully consider for any future study aimed at improving their mechanical properties.

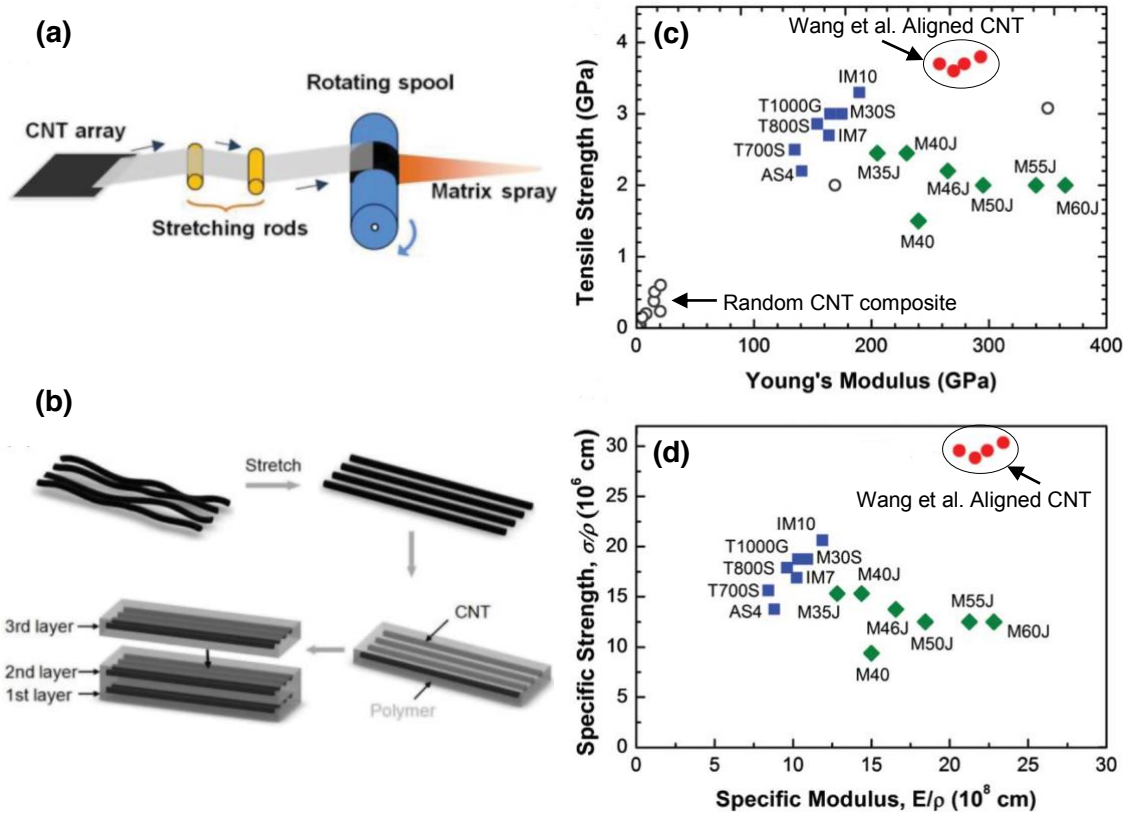

Figure 2-2 : (a-b) Schematic illustration of the experimental setup for the stretch-winding process to fabricate high volume fraction aligned CNT polymer matrix composites [81]. (c-d) Comparison of the tensile strength and stiffness of various high performance carbon fibre-epoxy composites to the stretch-wound aligned CNT-epoxy composite studied by Wang et al. [81].

2.2 Toughness Problem in Fibre Composites

The fracture toughness of fibre composites is probably one of the most complex and the least understood of all the mechanical responses. For most composites, including short-fibre composites, it is believed that as the strength increases, the toughness decreases [82]. Although this is generally the case for continuous-fibre reinforced brittle matrix composites, it is not always true for short-fibre reinforced polymer composites and particulate filled systems. The fracture toughness of a short-fibre composite is dependent on many factors including, strength of the reinforcing fibres and matrix;

aspect ratio, length distribution, volume fraction, uniformity and orientation of the fibres; the integrity of the fibre-matrix interface and the interfacial bond strength [82]. In this chapter, theories of fracture toughness of composites concerning micro-failure mechanisms which make up the total work of fracture are discussed with a particular emphasis on how the fracture toughness of composites is affected by the fibre orientation and length distribution.

2.2.1 Origins of Fracture Resistance in Fibre Composites

As a crack moves through a matrix containing fibre reinforcement, the following micro-failure mechanisms may be expected to operate: (i) matrix fracture, (ii) fibre-matrix interface debonding, (iii) post-debonding fibre pull-out, (iv) fibre fracture, (v) stress redistribution, etc. By considering the sequence of microscopic fracture events that lead to the propagation of a macroscopic crack under monotonically increasing loads, we can characterise the origins of fracture toughness in composites.

Fibre-matrix Interface Debonding

In a composite which features fibres with much greater fracture strain than that of matrix (i.e $\varepsilon_f \gg \varepsilon_m$), the fibre and matrix deform differentially when subjected to a monotonically increasing load. This strain differential at the fibre-matrix interface causes the build-up of interfacial shear stresses; which eventually leads to the interfacial debonding once the shear stresses exceed the total static interfacial shear strength. The interface strength is specific to each fibre-matrix system. It is dependent on the nature of bonding mechanisms which in turn is influenced by the chemical properties of the fibre as well as on the molecular conformation of the matrix [82]. The primary interface bonding mechanisms as highlighted by Hull [83] includes, van der Waals attraction, hydrogen bonding, adsorption and wetting, interdiffusion, electrostatic attraction, chemical bonding and mechanical bonding. Therefore, the fracture energy released during interfacial debonding is dependent on the fracture toughness of the interface and the fibre geometry as follows [83]:

$$\Delta G_{db} = \frac{V_f l_{po} G_i}{d_f} \tag{2-4}$$

Post-debonding Frictional Pull-out

After interfacial debonding, the fibre and matrix move relative to each other as the crack continue to propagate. According to the shear lag theory which was originally proposed by Cottrell-Kelly [69], the energy dissipated during the pull-out of the fibre from the matrix is equal to the work done by the friction shear stress times the differential displacement between fibre and matrix. By assuming the friction shear stress to be constant over a fibre pull-out distance, the frictional pull-out energy is given by [82],

$$\Delta G_{\mathrm{pull-out}} = \frac{2V_{\mathrm{fpo}}\tau_{\mathrm{i}}l_{\mathrm{po}}^2}{d_{\mathrm{f}}} \tag{2-5}$$

The fibre pull-out length is difficult to determine with accuracy from images of the fracture surfaces, particularly for samples with a relatively high fibre volume fraction. Also, relatively long fibres are expected to rupture at the crack plane, since their embedded lengths on either side of the crack plane are long enough for the stress in the fibre to build up sufficiently to break them. Two outcomes are possible depending on the length of the embedded fibre: (i) the fibre pull-out when its length is equal to or shorter than the critical length given by the classical Kelly-Tyson [2,51] formula given by Eq. (2-2), or (ii) the fibre ruptures when its length is longer than the critical length.

For the first possible outcome, when the length of the embedded fibre is less than the critical fibre length, we substitute $l_{po} = l / 2$ in Eq. (2-5),

$$\Delta G_{pull-out} = \frac{V_{fpo}\,\tau_i l^2}{2d_f} \qquad \text{for } l < L_c \tag{2-6}$$

However, if the fibre length is greater than the critical length given by Eq. (2-2), then the longest possible pull-out length of the fibre is equal to half the critical fibre length as given by the Kelly-Tyson formula [71]:

$$l_{po} = \frac{\sigma_f d_f}{4\tau_i} \tag{2-7}$$

Therefore, when the length of the embedded fibre is equal to the critical fibre length, by substituting Eq. (2-7) into Eq. (2-6) we get the estimate of the pull-out energy in terms of the inherent properties of the composite as follows:

$$\Delta G_{pull-out} = \frac{V_{fpo}\sigma_f^2 d_f}{8\tau_i} \qquad \text{for } l = L_c \tag{2-8}$$

The energy dissipation via fibre pull-out is the most dominant toughening mechanism in fibre composites and it promotes fibre bridging zones behind the crack tip. On the contrary, if the composite contains fibres with lengths greater than the critical fibre length, then a large fraction of fibres will rupture; and the fraction of fibres which can be pulled out is reduced by L_c/l (on the basis of normal probability) with l_{po} ranging from 0 to $L_c/2$. Hence, the pull-out fracture energy is then given by,

$$\Delta G_{pull-out} = \frac{V_{fpo}\,\tau_i L_c^2}{2d_f}\left(\frac{L_c}{l}\right) \qquad \text{for } l < L_c \tag{2-9}$$

From the above expression, it can be seen that the fracture energy contribution from fibre pull-out increases as the critical fibre length (i.e. $L_c = \sigma_f d_f/2\tau_i$) is increased. This implies that the fracture energy from fibre pull-out increases when τ_i is made smaller. Wagner et al [84] gave a graphical representation of the effect of interface strength on the fracture energy contribution from fibre pull-out, as can be seen in Figure 2-3.

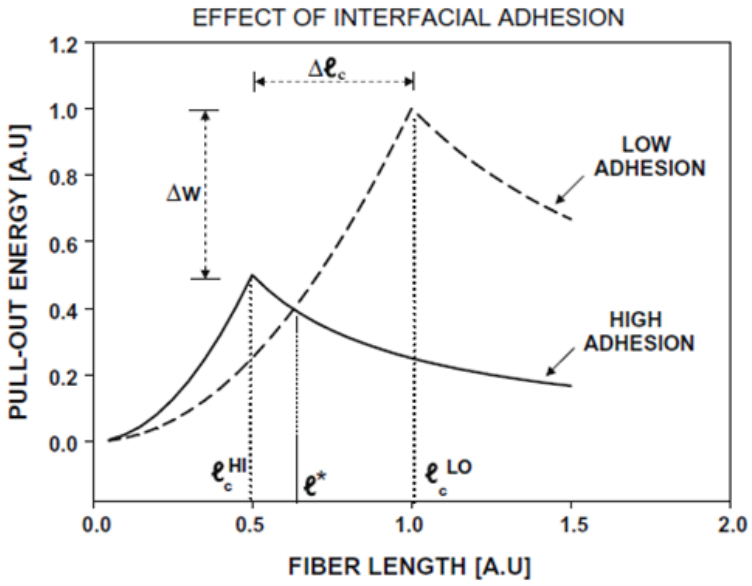

Figure 2-3 : Effect of reinforcement length on the pull-out energy when the level of adhesion is doubled [84].

Fibre Rupture Energy

The probabilistic approach outlined above overestimates the energy dissipation due to fibre pull-out for the case when the embedded fibre length is much greater than the critical fibre length. In fact, the actual energy dissipation during fibre rupture is much smaller [85] and is given by,

$$\Delta G_{\text{rupture}} = \frac{V_{\text{fpo}} \sigma_{\text{f}} \, l_{\text{f}} \, \varepsilon_{\max}}{2} = \frac{V_{\text{fpo}} \sigma_{\text{f}}^2 \, l_{\text{f}}}{2 \, E_{\text{f}}} \tag{2-10}$$

If the fracture energy dissipation mechanisms described above co-exist, then by adding the fracture energy contribution of the matrix, the total fracture energy of the composite can be estimated by Eq. (2-11). If any of the above mechanism is absent, the corresponding toughness term must be excluded from the fracture energy estimate.

$$G_{Ic} = G_{CU} + \frac{V_f \sigma_f^2 d_f}{8\tau_f} + \frac{V_f \sigma_f^2 \, l_f}{2 \, E_f} + \frac{V_f l_{po} G_i}{d_f} \tag{2-11}$$

2.2.2 Effects of Fibre Orientation on Toughness of Short-fibre Composites

The above micro-mechanical fracture theories do not account for the penalty due to the fibre orientation. As was highlighted earlier in section 2.1, there is a severe knockdown in the strength of composites with randomly-oriented fibres; and a similar penalty must be imposed on the fracture toughness estimates for a random fibre orientation distribution. Wetherhold and Jain [86, 87] first developed a probabilistic theoretical micro-mechanical interpretation of the work of fracture in short-fibre reinforced composites which accounts for the influence of the reinforcing fibre orientation. Fu and Lauke [88] have extended this work to incorporate the influence of the reinforcing fibre length distribution. The key findings from their model are presented here to highlight the major influence of fibre orientation on the fracture toughness of composites.

The fracture energy from fibre pull-out mechanism is largely dependent on the critical fibre length which is a function of fibre strength (see Eq. 2-2). Let's first examine the effects of fibre misalignment angle on the single fibre fracture strength. When a fibre is pulled out of the matrix at an angle with respect to the loading direction, the fracture stress of the fibre is reduced. This is due to the additional flexural

stress resulting from the fibre curvature close to the crack face known as “snubbing” friction effect [89].

Later work by Khatibzadeh and Piggott [90] experimentally investigated the effect of a fibre orientation on the fracture strength of individual fibre via single fibre pull-out tests. Figure 2-4 shows the effect of fibre orientation angle on the fracture strength of various fibre types. This figure shows that the fibre breaking stress decreases quite steeply with increasing angle. The reduction in fracture strength of misaligned fibres would lead to a much smaller critical pull-out length which would result in a steep decline in the fracture energy dissipation from fibre pull-out mechanism according to Eq. (2-9).

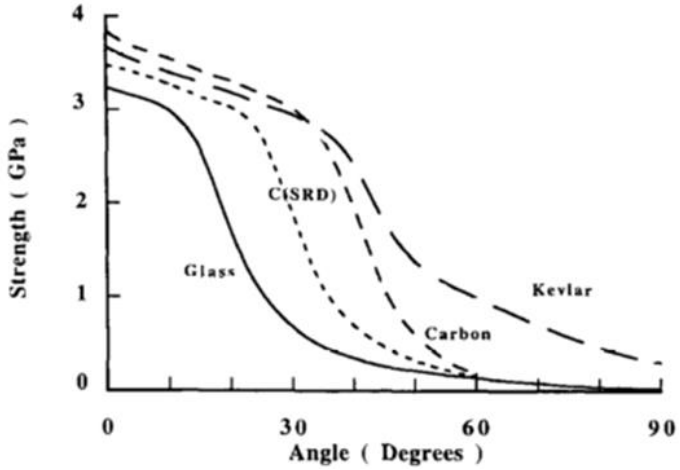

Figure 2-4 : Fibre strength as a function of the pull-out angle [90].

The result in Figure 2-4 led to the concept of 50% angle, which is defined as the angle at which there is about 50% reduction in the fracture strength of the fibre. Fu and Lauke [88] used this concept to evaluate the fibre pull-out energy by establishing a new definition for the critical fibre length of misaligned fibres given by the following expression:

$$L_{c\theta} = \frac{\sigma_{fu\theta} \cdot d_f}{2\tau_i e^{\mu\theta}} \tag{2-12}$$

Fu and Lauke [88] introduced two probability density functions, one for modeling the effect of the fibre-length and the other for fibre-orientation distributions. In addition, the fibre pull-out energy was derived by also considering the snubbing-friction effect

and the inclined fibre-strength effect given by Eq. (2-13). Their final expression derived for evaluating the fibre pull-out energy of short fibre composites is given by,

$$G_{pull-out} = \frac{8V_f a_0}{d_f L}\left[\int_{\theta=0}^{\theta_{max}}\int_{L=L_{min}}^{L_{c\theta}}\int_{l=0}^{L/2}\left(\frac{l^2}{2}+\frac{a_1 l^3}{6a_0}+\frac{a_2 l^4}{12a_0}\right) \times f(L)g(\theta)\cos(\theta)\, e^{(\mu\theta)} d/dL\, d\theta + \int_{\theta=0}^{\theta_{max}}\int_{L=L_{c\theta}}^{L_{max}}\int_{l=0}^{L_{c\theta}/2}\left(\frac{l^2}{2}+\frac{a_1 l^3}{6a_0}+\frac{a_2 l^4}{12a_0}\right) \times f(L)g(\theta)\cos(\theta)\, e^{(\mu\theta)} d/dL\, d\theta\right] \quad (2-13)$$

In the above expression, *f(L)* and *g(θ)* are the fibre-length and fibre-orientation distribution; while the interfacial friction shear stress was assumed to be of the following form,

$$\tau_i(\delta) = a_0 + a_1\delta + a_2\delta^2 \quad (2\text{-}14)$$

where δ is the fibre displacement during pull-out.

In summary, the derivation of Eq. (2-13) has the following logical order for evaluating the pull-out energy. For a given fibre orientation angle, first, the modified fibre critical length is evaluated. Second, the fibre pull-out energy is integrated over a fibre-length distribution. Finally, the composite fibre pull-out energy is estimated by applying a spatial fibre-orientation distribution.

Fu and Lauke [88] demonstrated the influence of each parameter in Eq. (2-13) on the fibre pull-out energy by fixing the remainder of the parameter. Let's first examine the advantage of having fibre with a random orientation distribution in a composite. Figure 2-5 shows the influence of the snubbing friction coefficient on the fibre pull-out energy as a function of the mean fibre length when the fibre loading angle is equal to 33 degrees. The shape of the curves (a-e) in Figure 2-5 which is given by Eq. (2-13) is similar to that shown earlier in Figure 2-3 wherein the peak fibre pull-out energy corresponds to the critical fibre length.

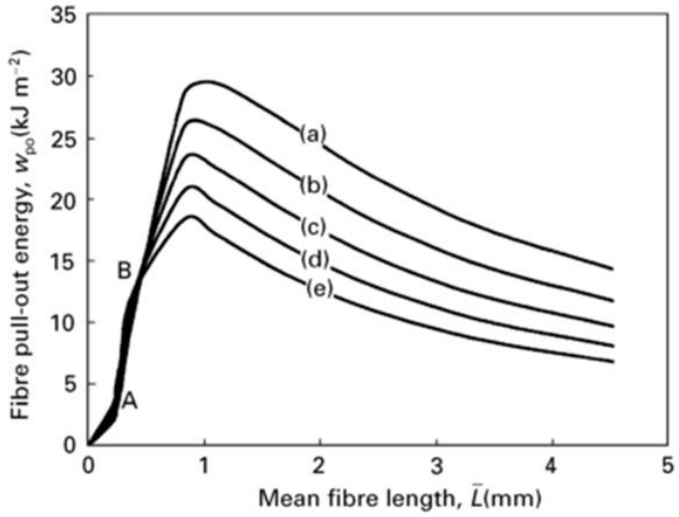

Figure 2-5 : Fibre pull-out energy as a function of mean fibre length for various snubbing friction coefficients : (a) μ= 0, (b) μ = 0.25, (c) μ = 0.5, (d) μ = 0.785 and (e) μ = 1 [88].

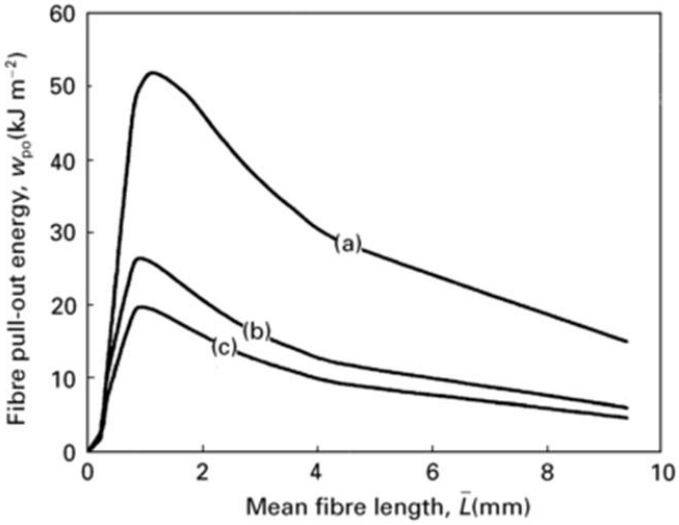

Figure 2-6 : Fibre pull-out energy as a function of mean fibre length for various snubbing friction coefficients : (a) $\theta = 0$, (b) $\theta = 33^o$ and (c) $\theta = 45^o$ [88].

In Figure 2-5 the fibre pull-out energy increases with the snubbing friction coefficient. This is due to the increase in the pull-out load as a result of the increased snubbing-friction effect. It is believed that the greater the fibre misalignment angle, the higher the snubbing-friction effect. Therefore, somewhat higher fibre pull-out energy is realised with fibre misalignment angle. But as the mean fibre length increases to a certain value, the fibre pull-out energy is very similar for all values of snubbing friction coefficient as can be seen from the crossover points A and B in Figure 2-5. However, if the fibre length is equal to or greater than the critical fibre length, the highest pull-out energy

corresponds to the lowest snubbing friction coefficient (i.e. curve-a) which is for the aligned fibre case. Thus, fibre misalignment angle provides little beneficial improvement to the fibre pull-out energy. In comparison, the advantage of having a perfect fibre alignment in a composite can be seen from the Figure 2-6, wherein the maximum fibre pull-out energy corresponds to the fibres aligned in the loading direction (i.e curve-a). However, if the fibres are aligned at an angle of 33 degrees (i.e. curve-b) to the loading direction, then the fibre pull-out energy is reduced to about half; a seemingly large penalty for a small misalignment. This significant penalty is not only due to the lower probability of the crack encountering the fibres, but is also due to the increase in interfacial shear stress and the corresponding reduction in the critical fibre pull-out length when the fibre is oriented at an angle to the loading direction.

2.2.3 Problem of Delamination Resistance and Detection in Continuous-fibre Composites

In this section, a review of the traditional techniques and recent development towards improving the delamination resistance of fibre composite laminates is presented. The problem of fracture resistance in composite laminates with continuous multi-directional fibre reinforcement is even more complicated and there is no simple unified theory which can be applied to predict their fracture toughness. In the absence of through-thickness reinforcement, continuous fibre reinforced composite are susceptible to delamination cracking due to the inherent low strength and fracture toughness of the polymer matrix and fibre-matrix interface. Delamination damage can result from high interlaminar loads, impact or environmental degradation of the composite. The growth of delamination is a major concern for designing composite structures. It is the most prevalent life-limiting damage mode which has become one of the major obstacles to the application of advanced composite materials in primary structural applications. Although delamination may not lead to catastrophic failure of a component, it can have a significant influence on residual strength and fatigue life of the structure.

Delamination damage can grow under relatively low cyclic interlaminar stresses caused by the fatigue loading of the composite. A major safety concern is that when subjected to cyclic loading, the delamination can grow almost undetected due to fatigue

until they are long enough to cause catastrophic failure of the composite structure. For instance, experimental [91, 92] and numerical [93-95] studies have shown that impact-induced delamination damage can significantly reduce the tensile and compressive properties of composites. The Federal Aviation Administration's damage tolerant design regulations specify that delamination damage within aircraft composites above a critical size must be immediately repaired or the entire damaged structure replaced for continued service [8]. Besides, there are stringent aviation safety regulations on management of critical size of the delamination damage [9]. The critical size depends on several parameters including the properties of the structural material, loading, geometry of the structure; and most importantly the technique utilised for detection and monitoring the damage site. Detection of damage in a composite structure is currently limited to ultrasonic, radiography and acoustic emission techniques which can only be performed during scheduled maintenance intervals [96]. The visual inspections performed during daily service of an aircraft structure cannot detect delamination cracks due to their hidden nature. Moreover, the traditional electrical based non-destructive detection techniques such as potential drop and eddy current cannot be used due to the lack of through-thickness conductivity in composites owing to the dielectric property of the polymer matrix. Thus, the problem of delamination resistance and detection in continuous-fibre reinforced composites is dominated by the fracture toughness and electrical conductivity of the matrix phase. Therefore, to address the issue of delamination resistance and detection in fibre composites, it is advantageous to simultaneously improve the fracture toughness and electrical conductivity of the polymer matrix.

2.3 Fracture Resistance of Epoxy Composites with Carbon Nano-reinforcements

Matrix cracking is the most pronounced damage initiation mode leading to the delamination in composites. Matrix cracks initiate at inter- or intralaminar regions experiencing stresses perpendicular to the fibre direction. As the load is monotonically increased or cycled, matrix cracks in adjacent plies connect by growing short cracks along the matrix rich interface regions. The subsequent growth and coalescence of

interfacial cracks lead to the development of delamination. Delamination damage in composites depends to a large extent on the fracture toughness of the matrix. Thus, particulate reinforced matrices are commonly used to improve delamination resistance of composites. Thermoset epoxies are widely used as matrices for manufacturing fibre reinforced composites and as adhesives for joining composite components. Polymerization of epoxies results in a highly-crosslinked microstructure, providing many desirable properties for structural engineering applications such as high modulus and failure strength, excellent adhesion, good performance at elevated temperatures and resistance to chemical and environmental degradation. However, due to this highly crosslinked structure, thermoset epoxies often have low ductility and toughness leading to poor resistance to crack initiation and growth of damage. Therefore, despite offering many desirable properties, thermosetting polymers typically exhibit a low electrical conductivity and fracture toughness.

Traditional techniques to improve the damage tolerance of epoxy polymers are to form a polymeric alloy [12] via the addition of thermoplastics [13, 14], rubber tougheners [15-17, 97] or silica particles [18, 19]. The addition of thermoplastics and rubber tougheners can yield a significant increase of up to 500% in the fracture energy of the epoxy [98, 99]. However, the inclusion of soft phase such as thermoplastics and rubber tougheners can also cause a reduction in the stiffness of the epoxy [98, 100]. In comparison, rigid inclusions such as silica particles can simultaneously improve the stiffness and toughness [101]. The large improvement in the toughness of particulate filled epoxy is due to several toughening mechanisms [12, 19, 99, 101] involving, (1) shear band formation near the particles; (2) cavitation, (3) stretching, (4) debonding and (5) fracture of soft rubber particles; crack (6) bridging, (7) pinning, (8) deflection and (9) crazing by hard particles; and (10) epoxy void growth around debonded particles. The level of improvement depends on the type of filler, particle size and shape, volume fraction, particle-matrix interface and the test environment [101]. Although these methods provide significant improvements to the toughness, the electrical conductivity remains unchanged because such additives are dielectric. More recently, studies on conductive carbon nano-reinforcements, such as carbon nanotubes (CNTs) [7–9], carbon nanofibres (CNFs) [10–12] and graphene nanosheets (GNPs) [13,14], have shown significant promise to increase the toughness of epoxy polymers, as well as the ability to improve their electric conductivity [24].

In the following sections, first, the effects of carbon nano-reinforcements on the fracture toughness and toughening mechanism of epoxy-based nanocomposites are discussed. It is followed by a review of the improvement to the delamination resistance of fibre reinforced composites containing carbon nano-reinforcements.

2.3.1 Carbon Nano-reinforcement of the Epoxy Matrix

Fracture Properties

At present various types of carbon nano-reinforcements such as single, double or multi-walled CNTs, CNFs and GNPs have been investigated for their abilities to enhance the fracture resistance of epoxy composites. They have been primarily studied in the framework of a bulk matrix containing carbon nano-reinforcements which are referred to as "epoxy nanocomposite". In this section, a brief review of the effect of different types of carbon nano-reinforcement on the fracture resistance and the corresponding toughening mechanisms in epoxy nanocomposites are presented. Many studies have reported moderate to substantial improvement in the fracture resistance of the epoxy nanocomposite containing one- or two-dimensional carbon nano-reinforcements and these results are listed in Table 2-1. The reference to the results in Table 2-1 will be based on the weight fraction of the carbon nano-reinforcements which are divided into three categories namely, low for 0.1-0.25 wt%, intermediate for 0.3 to 0.75 wt% and high for 0.8-5.0 wt%.

As can be seen in Table 2-1**,** few studies have investigated the fracture toughness of epoxy nanocomposites reinforced with SWCNTs. The toughness of epoxy nanocomposites containing low content (i.e. 0.1-0.3 wt%) of SWCNTs show meagre improvement. For instance, Gojny et al. [102] found that at 0.3 wt%, the toughness of epoxy reinforced with SWCNTs was almost half of that observed for DWCNTs or MWCNTs. However, the tensile stiffness and strength of SWCNT-epoxy nanocomposite were similar or better than the other types of CNTs.

Table 2-1**:** The fracture property of carbon nano-reinforced epoxy composites (SW, single wall; DW, double wall; CNF, carbon nanofibres; GNP, graphene nanoplatelets; US, ultrasonication; 3RM, three-roll-milling).

Source	**Nanofiller**	**Content** (wt%)	**Dispersion**	**Property**	**Improvement** (%)
Rafiee et al. [103]	SWCNT	0.1	US	K_{Ic}	13
Gojny et al. [102]	SWCNT	0.1	3RM	K_{Ic}	23
Gojny et al. [102]	SWCNT	0.3	3RM	K_{Ic}	12
Sun et al. [104]	SWCNT	1.0	US	K_{Ic}	18
Gojny et al. [105]	DWCNT	0.1	3RM	K_{Ic}	18
Gojny et al. [102]	DWCNT	0.3	3RM	K_{Ic}	41
Rafiee et al. [103]	CNT	0.1	US	K_{Ic}	18
Gojny et al. [102]	CNT	0.3	3RM	K_{Ic}	31
Hsieh et al. [106]	CNT	0.1	US	G_{Ic}	22
Hsieh et al. [106]	CNT	0.3	US	G_{Ic}	41
Thostenson et al. [107]	CNT	0.25	3RM	K_{Ic}	75
Sumfleth et al. [108]	CNT	0.3	3RM	K_{Ic}	7
Hsieh et al. [106]	CNT	0.5	US	G_{Ic}	68
Sumfleth et al. [108]	CNT	0.5	3RM	K_{Ic}	17
Chatterjee et al.	CNT	0.5	3RM	K_{Ic}	80
Thostenson et al. [107]	CNT	0.5	3RM	K_{Ic}	65
Thostenson et al. [107]	CNT	1.0	3RM	K_{Ic}	65
Tang et al. [109]	CNT	1.0	3RM	G_{Ic}	130
Yu et al. [110]	CNT	1.0	US	K_{Ic}	34
Yu et al. [110]	CNT	3.0	US	K_{Ic}	66
Zhang et al. [111]	CNF	0.22	3RM	G_{Ic}	18
Zhang et al. [111]	CNF	0.45	3RM	G_{Ic}	35
Palmeri et al. [112]	CNF	0.68	US	G_{Ic}	113
Zhang et al. [111]	CNF	0.9	3RM	G_{Ic}	41
Zhang et al. [111]	CNF	1.35	3RM	G_{Ic}	37
Rafiee et al. [103]	GNP	0.1	US	K_{Ic}	54
Chatterjee et al. [113]	GNP	0.1	3RM	K_{Ic}	53
Bortz et al. [114]	GNP	0.1	3RM	K_{Ic}	26
Bortz et al. [114]	GNP	0.25	3RM	K_{Ic}	50
Ma et al. [115]	GNP	0.25	US	G_{Ic}	75
Ma et al. [115]	GNP	0.5	US	G_{Ic}	115
Bortz et al. [114]	GNP	0.5	3RM	K_{Ic}	60
Chatterjee et al. [113]	GNP	0.5	3RM	K_{Ic}	63
Chatterjee et al. [113]	GNP	1.0	3RM	K_{Ic}	70

Table 2-1: Continued on next page

Bortz et al. [114]	GNP	1.0	3RM	K_{Ic}	60
Chatterjee et al. [113]	GNP	2.0	3RM	K_{Ic}	80
Zaman et al. [116]	GNP	2.5	US	G_{Ic}	100
Zaman et al. [116]	GNP	4.0	US	G_{Ic}	210
Zaman et al. [116]	GNP	6.0	US	G_{Ic}	200

This can be explained by considering the influence of CNT aspect ratio and surface area on its reinforcing efficiency. As can be seen in Figure 1-4a, SWCNTs typically possess the highest aspect ratio and surface area amongst the family of one-dimensional carbon nano-reinforcement. Although this is highly advantageous for improving the stiffness and strength of the epoxy nanocomposites, it is detrimental for enhancing their toughness. According to Eq. (2-3), higher aspect ratio reinforcements are more efficient at improving the stiffness and strength. But according to the theory of fracture mechanics discussed in Section 2.2.1, if the length of reinforcement exceeds the critical length, then they will rupture instead of pull-out. The process of fibre pull-out dissipates much greater amounts of energy in comparison to their rupture and this effect can be seen from Figure 2-3. Moreover, at a higher weight fraction i.e. 1.0, the agglomeration of the SWCNTs from Van der Waals attraction due to their high surface area leads to no further improvement as was later observed by Sun et al. [104]. The problem of property degradation due to CNT agglomeration is commonly found in epoxy nanocomposites.

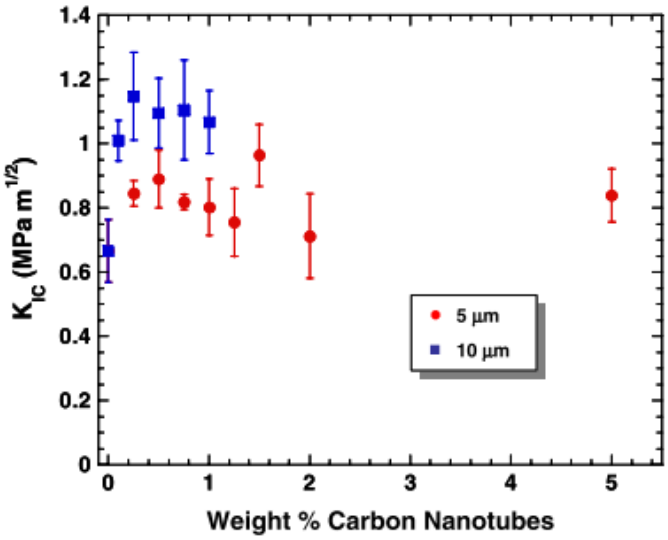

Figure 2-7 : Effect of the three-roll-mill calendering shear rate on the fracture toughness of the CNT-epoxy nanocomposite as a function of CNT content. 5 µm and 10 µm correspond to the gap size leading to the high and low shear rates, respectively [107].

As can be seen from Figure 2-7, as the CNT weight fraction is gradually increases, there is a sharp rise in the fracture toughness corresponding to an intermediate level of CNT concentration. However, at higher CNT weight fractions, there is no further improvement in the fracture toughness of the CNT-epoxy nanocomposite but instead, there occurs a reduction due to the agglomeration of CNTs. Moreover, if the severity of the dispersion process is increased to achieve a homogeneous dispersion of CNTs, there occurs about 50% reduction in the peak fracture toughness improvement corresponding to the intermediate CNT weight fraction (see Figure 2-7). This is due to the unavoidable damage to the CNTs from the excessive shear rates or prolonged exposure to the shear forces [117]. The preservation of the length of the nano-reinforcement during dispersion process is crucial for improving the fracture toughness of the epoxy nanocomposites as was demonstrated by Thostenson et al. [107]. This is because when the length of the reinforcement is smaller than the critical fibre length, the pull-out energy which is given by Eq. (2-6) increases as the square of the reinforcement length. Therefore, any reduction in the length of the carbon nano-reinforcements caused by their damage during dispersion process would lead to a significant reduction in the energy dissipation via the pull-out mechanism. Thostenson et al. [107] have shown that if the CNTs are subjected to excessive shear rates during the three-roll-mill calendering process, the improvement in the fracture toughness of the resulting CNT-epoxy nanocomposite is reduced by about 50%, as can be seen in Figure 2-7. A similar effect would also be expected for CNT-epoxy nanocomposites prepared by the ultrasonication process. Many of the epoxy nanocomposite properties can be significantly affected by the process used to disperse the nano-reinforcements. The effect of the selected dispersion process on the electrical and mechanical properties of epoxy nanocomposites has been extensively studied by Ma et al. [63]. As can be seen in Table 2-2, five primary dispersion methods are typically employed for preparing polymer nanocomposites, namely ultrasonication, calendering, ball milling, shear mixing and extrusion. The suitability of each of this dispersion process is specific to the type of polymer nanocomposite and the viscosity of the mixture. As can be seen from Table 2-1, ultrasonication and three-roll-mill calendering are the most common of all dispersion processes employed for preparing epoxy nanocomposites. The comparative study of all these dispersion processes by Ma et al. [63] has demonstrated that the calendering process has the least detrimental effect on CNTs and the mechanical,

electrical and thermal properties of the resulting nanocomposites. This is also apparent from Table 2-1 wherein for specific weight fraction of a carbon nano-reinforcement, a somewhat larger improvement to the fracture toughness can be observed for the epoxy nanocomposites prepared with the three-roll-mill calendering process. Moreover, ultrasonication has been reported to cause microstructural changes as well as surface defects in CNTs [118].

As can be seen from Table 2-1, very few studies have reported the use of CNFs to improve the fracture toughness of epoxy nanocomposite. This is surprising because CNFs have been shown to be equally effective at improving the fracture toughness of epoxy nanocomposites. For example, Palmeri et al. [22] demonstrated that the addition of just 0.68 wt% CNFs improved the fracture toughness of an epoxy by about 112%. While the highest improvement in the fracture toughness of 1 wt% CNT-epoxy nanocomposite was reported to be about 130%. CNFs may be an excellent alternative to CNTs due to their wide availability and lower cost [59]. Instead, some recent studies have attempted to improve the fracture toughness of epoxy composites by reinforcing them with the two-dimensional GNPs. Epoxy nanocomposites reinforced with low GNP weight fractions (0.1 and 0.25 wt%) have shown promising reinforcing capability with fracture toughness improvement of up to 55%. From Table 2-1 it can be seen that for a low weight fraction GNP reinforcement, the level of improvement to the fracture toughness of epoxy nanocomposites is twice of what has been achieved with any type of CNT or CNF reinforcements. Indeed, the comparative study of the reinforcing effects of different type of CNTs and GNPs by Rafiee et al. [103] have also shown that better level of improvement to the fracture toughness of epoxy nanocomposite can be achieved with low fractions of GNP. Whereas, Zaman et al. [116] have shown that the fracture toughness of epoxy nanocomposites could be enhanced by up to 200% by using a high (4 and 6 wt%) weight fraction of surface functionalised GNP reinforcements. Although, the improvements listed in Table 2-1 for carbon nano-reinforcements are impressive; they are significantly lower than the 900 % increase in fracture toughness reported for nano-silica [119] and rubber particle modified epoxy polymers [99]. But the use of carbon nano-reinforcements can simultaneously improve the electric conductivity and mechanical properties, unlike nano-silica and rubber particles.

Table 2-2 : Comparison of various techniques for dispersing nano-reinforcement in polymer matrix [63]

Technique	**Factor**			
	Damage to CNTs	**Suitable polymer matrix**	**Governing factors**	**Availability**
Ultrasonication	Yes	Soluble polymer, low viscous polymer or oligomer, monomer	Power and mode of sonicator, sonication time	Commonly used in lab, easy operation and cleaning after use
Calendering	No. CNTs may be aligned in matrix	Liquid polymer or oligomer, monomer	Rotation speed, distance between adjacent rolls	Operation training is necessary, hard to clean after use
Ball milling	Yes	Powder (polymer or monomer)	Milling time, rotation speed, size of balls, balls/CNT ratio	Easy operation, need to clean after use
Shear mixing	No	Soluble polymer, low viscous polymer or oligomer, monomer	Size and shape of the propeller, mixing speed and time	Commonly used in lab, easy operation and cleaning after use
Extrusion	No	Thermoplastics	Temperature, configuration and rotation speed of the screw	Large-scale production, operation training is necessary, hard to clean use

Toughening Mechanisms

Many of the studies listed in Table 2-1 have reported the improvement in the fracture toughness of carbon nano-reinforced epoxy nanocomposites due to several toughening mechanisms [12, 19, 99, 101] involving, (1) debonding of the nano-reinforcement/matrix interface; (2) inelastic matrix deformation and void growth around debonded nano-reinforcement; (3) crack pinning and deflection; (4) crack tip blunting; (5) nano-reinforcement pull-out and subsequent crack bridging; and (6) nano-reinforcement rupture. A typical featureless and smooth fracture surface is reported for the unmodified epoxy which is indicative of a very brittle fracture [106, 116]. In contrast, the carbon nano-reinforced epoxy nanocomposites show a distinct whitening of the polymer along the crack initiation lines on the fracture surface. Examination of these regions using the SEM reveals a pattern of tear marks, which provides evidence of plastic deformation of the epoxy polymer along the line of crack initiation [116]. The size of the stress-whitened region is reported to increase with the weight fraction of the nano-reinforcement [116]. The increase in the severity of the tear marks and the roughness with increasing nano-reinforcement content is indicative of the crack pinning and deflection process promoted by the nano-reinforcements [107, 116]. During crack deflection around the nano-reinforcements, the tilting and twisting of the crack front lead to the local crack propagation under mixed mode conditions which require higher driving force. This process promotes higher fracture toughness of the epoxy nanocomposite [103]. Rafiee et al. [103] have observed that nano-reinforcement with higher aspect ratio or two-dimensional (i.e. GNPs) geometry are more effective at promoting the crack deflection process.

In addition, a greater contribution to fracture energy dissipation is almost always observed to be due to a significant number of nano-reinforcements being pulled-out from the epoxy. Moreover, the CNF-epoxy nanocomposites have shown evidence of uncoiling of the CNFs due to their unique helical graphene structure [120-122]. The uncoiling has also been previously observed using TEM, revealing a nanoribbon of graphene uncoiling from the CNFs [120]. This phenomenon is reported to dissipate additional amounts of energy in CNF-epoxy nanocomposites [112] and is believed to promote crack bridging at much higher crack opening displacement via uncoiling CNFs

as shown schematically in Figure 2-8. However, the nano-reinforcement pull-out mechanism is typically the most dominant toughening mechanism responsible for increasing the fracture energy [104-107, 109]. The increase in the fracture energy during pull-out is due to the work of friction by the interfacial shear stress between the nano-reinforcements and the epoxy polymer. During this pull-out process, the nano-reinforcements also form a bridging zone behind the crack tip as shown in Figure 2-9 [123]. In order to pull-out and bridge the crack, the nano-reinforcements must first debond from the epoxy. The strain energy absorbed in overcoming the adhesion of the nano-reinforcement/epoxy interface during the debonding process would also increase the fracture energy but to a lesser extent. If the interfacial bond strength exceeds the strength of the nano-reinforcements, then they would rupture prematurely before pull-out occurs. However, the rupture of the nano-reinforcements would result in smaller improvements in the values of the fracture energy, since the strain energy consumed during fibre rupture is reported to be significantly lower than that pertinent to pull-out [41, 85].

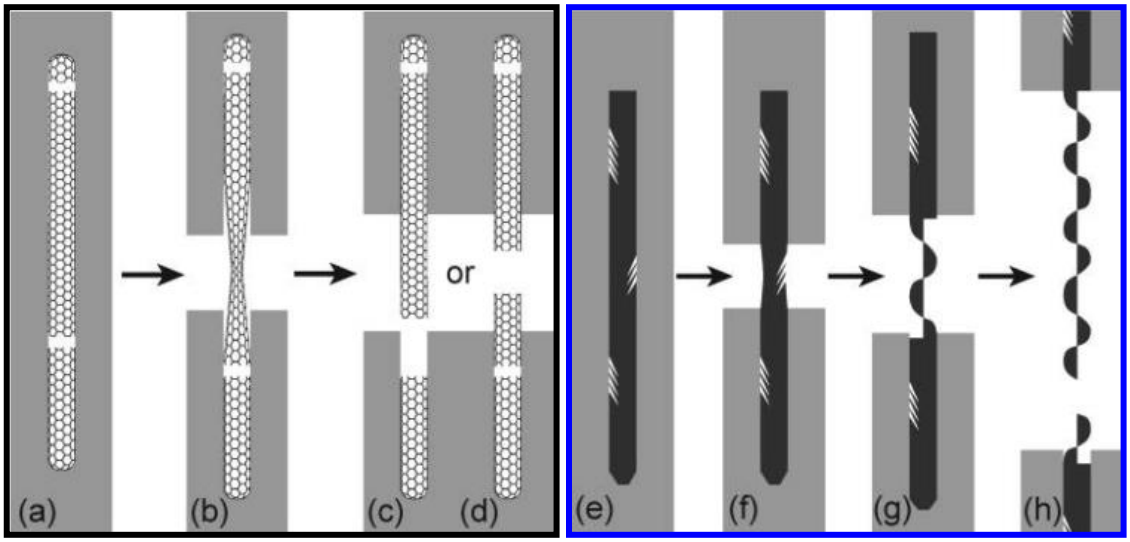

Figure 2-8 : Schematic illustration of the crack bridging process in nanocomposite containing (a-d) CNTs and (e-h) CNFs. (a-b) Pull-out and (c-d) rupture of CNT during crack bridging. (e-f) Pull-out and (g-h) unravelling of CNF during crack bridging [112].

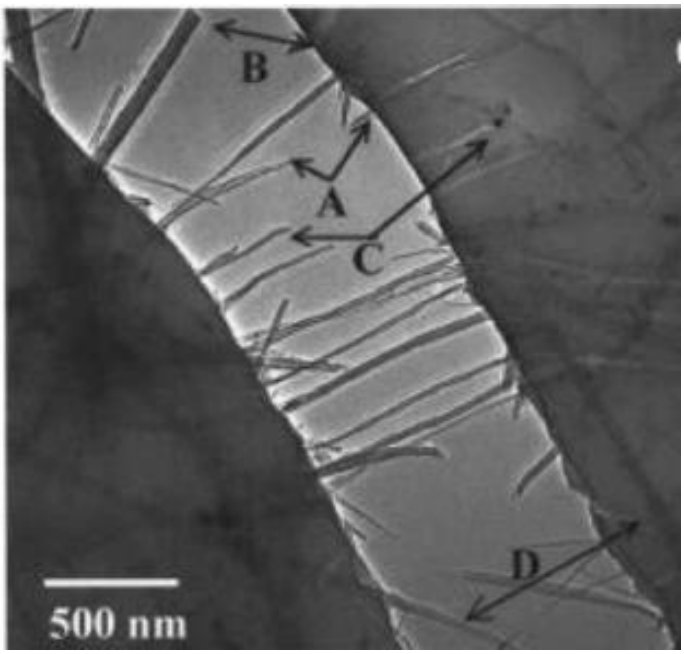

Figure 2-9 : Crack bridging process in CNT nanocomposite [123]

Furthermore, a significant number of relatively large voids are observed around the nano-reinforcements which are indicative of the plastic void growth of epoxy polymer in the process zone, which leads to an additional increase in the fracture energy, compared to the unmodified epoxy [106, 112, 116]. This arises because, in the process zone ahead of the crack tip, where a triaxial stress-field exists, the nano-reinforcements debond from the epoxy as the local stresses increase at the crack tip. The debonded nano-reinforcements act as voids in the epoxy which allows the polymer to deform plastically, and so the voids increase in size. For rubber- and nanosilica-toughened epoxies, this plastic void growth mechanism has been shown to significantly increase the fracture toughness of the material [119, 124].

A majority of studies listed in Table 2-1 have reported that the level of improvement depends on the type of nano-reinforcement and its dispersion quality; nano-reinforcement size and shape, volume fraction and particle-matrix interface. However, except for the study by Hsieh et al. [106], none of these studies have quantified the contribution of each of the aforementioned toughening mechanisms towards improving the fracture toughness of the epoxy nanocomposites. As can be seen in Figure 2-10, Hsieh et al. [106] used an analytical model similar to that given by Eq. (2-11) to quantify the contribution from each of the toughening mechanisms identified from the SEM observations of the fracture surface of MWCNT reinforced epoxy

nanocomposites. Moreover, at present, there is no study reporting a similar analytical modelling approach that could be utilised to quantify the various toughening mechanisms proposed for GNP-epoxy nanocomposites. As can be seen from the breakdown of the energy dissipation from each toughening mechanisms calculated by Hsieh et al. [106] which are listed in Table 2-3, CNT pull-out and CNT-matrix debonding were the two most dominant toughening mechanisms responsible for improvement in the fracture energy of CNT-epoxy nanocomposites. For energy dissipated via CNT pull-out, they also observed that although the embedded CNT length was 120 μm, the actual CNT pull-out length was less than about 10% of this value. They attributed the smaller pull-out length to be due to the random orientation of the CNTs in the epoxy matrix which led to their rupture rather than pull-out. This observation confirms the fracture mechanism theory discussed earlier for random and aligned short-fibre composites in Section 2.2.2. According to the theoretical models, carbon nano-reinforcements with some misalignment angle with respect to the loading direction can be expected to experience greater snubbing friction which will reduce the critical fibre length and its pull-out length given by Eqs. (2-12) and (2-7), respectively. Thus, the improvement in the fracture toughness of epoxy nanocomposites containing randomly oriented nano-reinforcements is lower than what could be achieved if the nano-reinforcements were to be aligned in the loading direction. Moreover, Hsieh et al. [106] found that only about 60% of the total CNTs that can be expected to pull-out on the fracture surface were observed to have been intersected by the crack path due to their random orientation. The probability of the crack intersecting the carbon nano-reinforcements is much lower when they are randomly oriented in the matrix which further reduces the expected improvement in the fracture toughness as was demonstrated in Figure 2-6 in the Section 2.2.2.

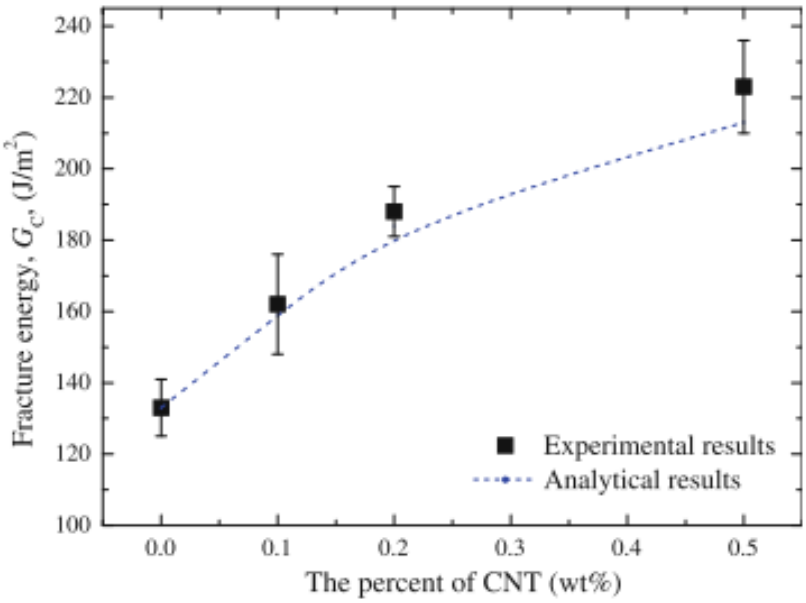

Figure 2-10 : Experimental results of the fracture energy of CNT-epoxy nanocomposite as a function of CNT content and its comparison to the theoretical predictions [106].

Table 2-3 : Theoretically calculated fracture energy contribution from various toughening mechanisms and its comparison to the experimental results [106].

MWCNT (wt%)	V_{fpo} (%)	$V_{fv} - V_{fp}$ (%)	V_{fdb} (%)	$\Delta G_{pull\text{-}out}$ (J/m^2)	ΔG_v (J/m^2)	ΔG_{db} (J/m^2)	G_c (J/m^2) predicted	G_c (J/m^2) measured
0	0	0	0	-	-	-	-	133
0.1	0.063	0.005	0.063	10.0	0.07	15.7	159	162
0.2	0.125	0.009	0.125	20.0	0.15	31.2	184	188
0.5	0.194	0.024	0.194	31.0	0.37	48.6	213	223

Therefore, in addition to the nano-reinforcement size and shape; dispersion quality; volume fraction and particle-matrix interface; the alignment of the nano-reinforcements in the loading direction is critical for enhancing the fracture toughness of epoxy nanocomposites. Indeed, numerical analyses have confirmed that in comparison to randomly oriented CNTs, a 3.0 vol% CNTs aligned in epoxy normal to the crack growth plane can enhance its toughness by up to 400% [41]. Unfortunately, there is a dearth of suitable processes to align carbon nano-reinforcements along the through-thickness direction of composites. However, recently the use of electric- and magnetic-fields [39] to align nanoparticles in liquid resins, prior to curing, has been reported [44-50]. The electro-mechanisms of the alignment process of carbon nano-

reinforcements leading to their rotation and chaining in a dielectric medium in the presence of an external field will be reviewed in a later section.

2.3.2 Multi-scale Composites with Carbon Nano-reinforcements

One major issue impeding the wide adoption of fibre-reinforced composites is their low through-thickness strength and toughness, and the difficulty to cost-effectively inspect and repair damage sustained during service. The Achilles heel of composites is their susceptibility to microscale damage, such as matrix cracking, interfacial debonding, fibre breakage and delamination. The initiation of damage has significant implications on the structural integrity and durability of composite structures (12). Even relatively low levels of damage, referred to as Barely Visible Impact Damage (BVID), can cause reductions of up to 60% in the residual compressive strength. Because much of the impact damage occurs beneath the surface, existing non-destructive techniques such as visual inspection and ultrasonics are not effective for wide-area damage inspections and for regions that are hard to access. Traditional techniques to improve through-thickness properties include polymer "alloying" of brittle thermoset matrix with thermoplastic [125-128], rubber toughener [99, 129] or silica particles [99, 129] in the matrix or at interply region. Micro-sized carbon pins, commonly referred to as z-pins, have been investigated to reinforce composites in the thickness direction [20, 21]. It is widely recognised that z-pins are effective only for resisting large-scale delamination. In recent years, studies on conductive carbon nano-reinforcement, such as CNTs [22, 23], CNFs [25, 26], and GNPs [27-30], have indicated promising reinforcement efficiency as well as the ability to enhance electric properties of the fibre reinforced epoxy composites. As can be seen from Table 2-4, numerous studies have investigated the use of CNTs and CNFs to enhance the interlaminar fracture energy of fibre reinforced epoxy composites. However, at present, there is no reported study on the use of GNPs to improve the interlaminar fracture properties of fibre-epoxy composites despite the remarkable improvement in the fracture and fatigue resistance of GNP-epoxy nanocomposite demonstrated by earlier investigations [114, 116].

Table 2-4 : Interlaminar fracture energy of multi-scale composites containing carbon nano-reinforcements (CF, carbon fibre; GF, glass fibre; SiC, silicon carbide, US, ultrasonication; 3RM, three-roll-milling; HSM, high shear mixing; VACNT, vertically aligned carbon nanotube forrest).

Source	**Composite Processing**	**Dispersion Process**	**Multi-scale Composite**	**Nanofiller** (wt%)	**Improvement** G_I (%)	G_{II} (%)
Wichmann et al. [130]	VARTM-Matrix	3RM	GF + DWCNT	0.3	-10	-
Karapappas et al. [131]	Wetlayup-Matrix	BM	CF + CNT	0.1	-10	-
				0.5	40	-
				1.0	60	-
Tugrul et al. [132]	VARTM-Matrix	3RM	GF + CNT	0.1	-22	12
Warrier et al. [133]	Prepreg-Matrix	HSM	GF + CNT	0.5	-35	-
Godara et al. [134]	Prepreg-Matrix	HSM	CF + DWCNT	0.5	55	-
			CF + CNT	0.5	83	-
Zhu et al. [135]	Prepreg-Matrix	US	GF + CNT	0.25	4	-19
			GF + CNT	0.5	-2	5
			GF + CNT	1.0	9	14
Zhu et al. [135]	Prepreg-Interlayer	US	GF + CNT	0.25	95	109
			GF + CNT	0.5	66	86
			GF + CNF	0.5	57	41
Sadeghian et al. [136]	VARTM-Matrix	US	GF + CNF	1.0	100	-
Kostopoulous et al. [137]	Wetlayup-Matrix	HSM	GF + CNF	1.25	133	-
Li et al. [138]	Prepreg-Interlayer	PS	CF + CNF	12.7	26	-
Yokozekiu et al. [139]	Prepreg-Matrix	BM	CF + CNF	5.0	98	30
Yokozekiu et al. [140]	Prepreg-Matrix+ Interlayer	BM + PS	CF + CNF	5 + 5	121	92
		BM + Film	CF + CNF	5 + 5	87	32
Khan et al. [141]	VARTM-Interlayer	3RM	CF + CNF	10	104	-
Veedu et al. [42]	Wetlayup-Interlayer	CVD	SiC + VACNT	2.0	350	54
Garcia et al. [142]	Prepreg-Interlayer	CVD	CF + VACNT	1.0	250	300

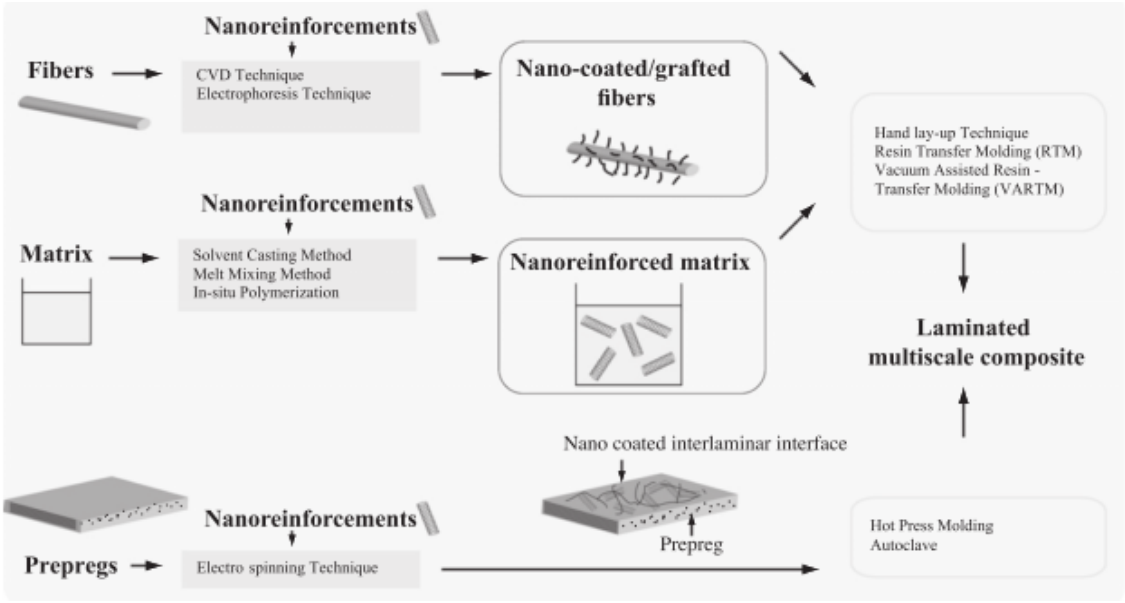

Figure 2-11 : Diagram of fabrication techniques for nano-reinforced multi-scale composites [39].

As shown schematically in Figure 2-11, various approaches have been utilized by researchers attempting to incorporate the carbon nano-reinforcements in the fibre-epoxy composites which were recently reviewed by Lubineau and Rahman [39]. The selection of technique for adding nano-reinforcements in a laminate depends on the final fabrication method to be employed for manufacturing the composite, namely wet layup or prepreg. In the wet layup process, the nano-reinforcements are pre-dispersed in the epoxy resin using methods similar to that used for preparing epoxy nanocomposites which were discussed earlier in section 2.3.1. The nano-reinforcement/epoxy mixture is then applied as the matrix phase to the dry fibre preform using either hand layup or vacuum assisted resin transfer molding (VARTM) technique. Hand layup is by far the simplest method for adding nano-reinforcements to the matrix phase of fibre-epoxy composites. Whereas, VARTM technique is now widely accepted for manufacturing high quality fibre-epoxy laminates in large volume production. But there are additional complications in using this method for fabricating multi-scale composites with nano-reinforcements. The VARTM process relies on low viscosity resin for effective infiltration of the fibre preform. However, the viscosity of the epoxy resin increases dramatically with the addition of even low weight fraction of the nano-reinforcements [136]. This leads to the problem of nano-reinforcements filtration during the resin transfer molding process which results in inhomogeneous reinforcement of the laminate

[136]. To overcome this problem, nano-reinforcements are applied as an interlayer in the form of a veil or tissue which is placed in the interply regions prior to resin infiltration during the VARTM process [141]. Although interply reinforcement technique provides toughening to the interlaminar regions, it is ineffective at preventing intralaminar damage suffered from impact events or fatigue loading. As an alternative approach, researchers have pre-coated the reinforcement fibre preforms with CNTs [143-145], CNFs [146, 147] and GNPs [27] using electrophoretic deposition (EPD) technique. The nano-reinforcement coated fibre preforms can be then used for VARTM process without the issue of localized toughening from filtration effects. Whereas, in a prepreg fibre-epoxy system, the carbon nano-reinforcements are added as either an interlayer veil [148]; or via powder sprinkle [138]; or they are grafted on to the fibres during the processing of the first stage cured fibre-epoxy pregregs [133, 134].

As can be seen in Table 2-4, a wide range of improvements to the mode I and II interlaminar fracture energy have been reported for CNT and CNF-reinforced multi-scale composites. From these results, it appears that for specific weight content of the nano-reinforcements, the level of improvement achieved by the addition of CNFs are similar to that reported for the more expensive CNT reinforced multi-scale composites. For instance, Sadeghian et al. [136] were among the first research group to demonstrate up to 100% improvement in the fracture energy of CNF-reinforced multi-scale composite manufactured using the VARTM technique. Similarly, Zhu et al. [135] showed that similar level of toughening could be achieved by adding 0.5 wt% of either CNF or CNT reinforcements as an interlayer in the multi-scale composites manufactured using prepreg system. Moreover, researchers have been able to add much higher weight fraction of CNFs in the form of an interlayer into multi-scale composites which led to a somewhat greater improvement to their interlaminar fracture energies. Similar to the epoxy nanocomposites, the improvement to the fracture energy of carbon nano-reinforced multi-scale composites is due to several toughening mechanisms including, (1) debonding of nano-reinforcement/matrix interface [133, 134]; (2) inelastic matrix deformation and void growth around debonded nano-reinforcement [26]; (3) crack pinning and deflection [134, 141]; (4) enhanced fibre/matrix interface [141]; (5) nano-reinforcement pull-out and subsequent crack bridging [130, 140]; and (6) nano-reinforcement rupture [26].

However, the improvement in delamination resistance of the carbon nano-reinforced multi-scale composites has been much lower than that reported for carbon z-pins reinforced composite laminates. For example, just 1 wt% carbon z-pin reinforcement aligned in the through-thickness of composite laminate can increase its mode I delamination fracture energy by up to 280 %, which increases further to 1500% at a content of 4 wt% [40]. This finding suggests that aligning the carbon nano-reinforcements in the through-thickness direction of the multi-scale composite laminate is necessary for achieving a substantial improvement to their fracture energy. This was demonstrated by Veedu et al. [42], who used CVD technique to deposit 2.0 wt% of aligned CNT forest directly onto SiC woven fibre preforms, as shown in Figure 2-12. Indeed, the resultant multi-scale fibre-epoxy composite containing aligned CNT reinforcements showed the mode I and II fracture energy enhancement of about 280% and 54% respectively. However, the high temperature required for achieving direct CVD growth of aligned CNTs onto carbon or glass fibre preforms is well in excess of 750 °C which weakens the structural fibres. For instance, the coating of IM7 carbon fibres with CNTs via direct CVD growth at 800 °C resulted in their tensile strength being reduced by about 40% when the CVD was performed under inert gas (Argon) environment and up to 70% under vacuum environment, respectively [43]. Thus, the in-plane properties of the resulting multi-scale composites could be significantly lower.

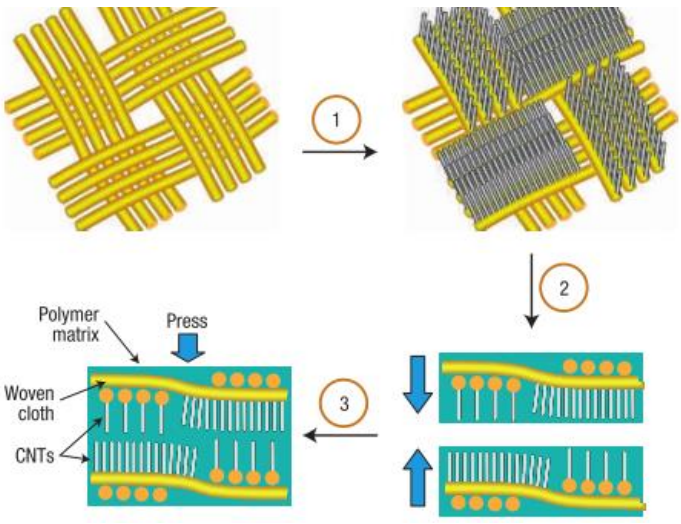

Figure 2-12 : Schematic illustration of the fabrication process for manufacturing aligned CNT-reinforced multi-scale composites [42].

In order to overcome this problem, Garcia et al. [142] have demonstrated a novel technique for transferring aligned CNT forest onto prepreg fibre-epoxy system without any additional processing or tooling requirements. Their multi-scale composite containing just 1 wt% of aligned CNT reinforcements in the interlaminar regions led to about 250% and 300% increase in the mode I and II fracture energy respectively. The primary toughening mechanisms in the presence of aligned CNT interlayer were plastic deformation and crack bridging, as shown in Figure 2-13. In particular, a greater contribution from CNT crack bridging process zone was observed and later quantified to be responsible for such large toughening effects [85]. Moreover, all of the aligned CNTs participated in the pull-out process which promoted the crack bridging process zone leading to significant toughening of the interlaminar regions. However, the authors pointed out that this interleaving technique has the drawback of decreasing the in-plane laminate properties. But their study did not characterize the in-plane properties of the aligned CNTs reinforced laminates. Although this technique has been by far the most successful at improving the fracture resistance of multi-scale composites, the amount of aligned CNT forest necessary for the industrial level high volume manufacturing of such composites is currently unavailable.

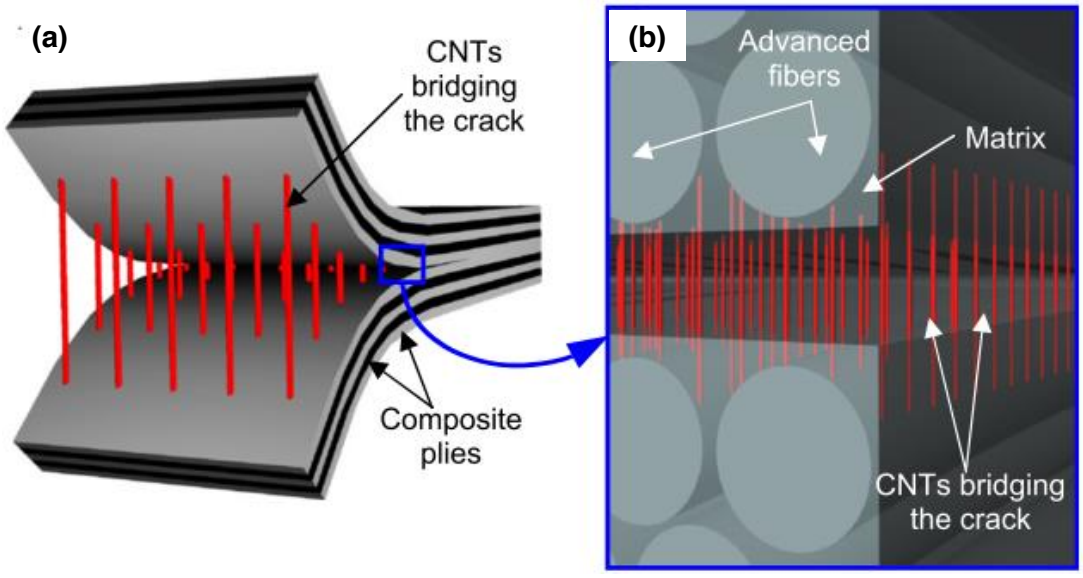

Figure 2-13 : Schematic illustration of the (a) crack bridging process in aligned CNT reinforced multi-scale composites, and (b) high magnification diagram of the crack bridging by aligned CNTs [142].

While interleaving technique provides effective toughening to the interlaminar regions, it cannot prevent intralaminar damage suffered from impact events or cyclic fatigue loading. Therefore, it is necessary to align the carbon nano-reinforcements in the through-thickness direction throughout the matrix phase to achieve effective toughening of the interlaminar and intralaminar regions. Unfortunately, there is a dearth of suitable processes to align carbon nano-reinforcements along the through-thickness direction of fibre reinforced composites. However, recently the use of electric- and magnetic-fields to align nanoparticles in liquid resins, prior to curing, has been reported [44-50]. The various alignment techniques and the electro-mechanical response of the carbon nano-reinforcement leading to their rotation and alignment are discussed in the following section.

2.4 Alignment of Carbon Nano-reinforcements in Composites

One major factor limiting the property improvements achieved to date in epoxy composites has been the fact that the carbon nano-reinforcements are typically randomly-oriented, which arises naturally from the dispersion process using ultrasonication and/or mechanical mixing. Unsurprisingly, the improvements achieved in many important properties of the epoxy nanocomposites containing randomly-oriented carbon nano-reinforcements are significantly lower than what would be expected had the nanofillers been aligned in the desired direction. Different approaches have been reported for orienting carbon nano-reinforcements, mainly based on mechanical stretching [149], or aligning with an electric [44, 51, 150] or magnetic-field [151, 152].

2.4.1 Mechanical Alignment Techniques

The alignment of the carbon nano-reinforcements using mechanical approach includes various techniques, namely shear flow field, mechanical stretching, infiltration, and electrospinning. Vigolo et al. [153] used the shear flow technique to process long ribbons of PVA/CNT composite fibres containing well-oriented CNT reinforcements.

In order to achieve the alignment of the CNTs, they injected the dispersed CNT/surfactant solution through a syringe needle into a PVA solution. In comparison to the CNT dispersion, the high viscosity of the PVA solution induced shear stresses at the flow boundary which led to the shear flow induced alignment of the CNTs. Other researchers [154, 155] have undertaken a systematic study of the effect of shear flow rate on the degree of CNT alignment. Haggenmuller et al. [156] used melt processing to prepare aligned CNT/PMMA composite films. The resulting composite films showed higher conductivity and mechanical properties in the CNT alignment direction. Thostenson and Chou [157] prepared CNT/PS composite films by extruding the composite melt through a die followed by drawing the film prior to cooling which resulted in the in-plane alignment of CNTs, as shown in Figure 2-14a-b. The alignment of the CNTs in PS film enhanced its strength and modulus by 137% and 49%, respectively. Although the alignment of CNTs through mechanical stretching is one of the simplest technique for processing aligned CNT/polymer composites, it is limited in its application to thin films with thickness less than 2 mm [158]. Alternatively, electrospinning has been widely used for assembling nonwoven fibres and membranes made of polymers containing carbon nano-reinforcements [159, 160]. As shown in Figure 2-14c-d, Chen et al. [159] fabricated polyimide fibres containing aligned CNTs using electrospinning. Electrospinning has also been used for fabricating polymer nanocomposite membranes with aligned CNTs. Sen et al. [160] were the first to demonstrate that electrospinning can be used to prepare aligned SWCNT-polyurethane membranes leading to a significant enhancement in their mechanical properties.

Although the techniques discussed above can be effectively used to fabricate polymer fibres, films and membranes containing aligned nano-reinforcements, they cannot be used for through-thickness alignment of carbon nano-reinforcement within the matrix phase of the fibre composites. However, recently the use of electric- and magnetic-fields to align nanoparticles in liquid resins, prior to curing, has been reported [44, 45, 49, 50, 52, 161-165]. Under the application of an electric- or magnetic-field, the nano-reinforcements may align to form a chain-like network in the direction of the external field [51, 52]. The nano-reinforcements can be oriented in any desired direction by manipulating and orienting the external field direction. Since thermosetting resins, such as epoxy resins, may typically possess a relatively low viscosity prior to cure, the application of an electric- and/or magnetic-field will be able to transform the

randomly-oriented carbon-based nano-reinforcements to give a highly aligned structure. This mechanism of the self-aligning of conductive carbon nano-reinforcements in polymers offers a new opportunity to create multi-scale composite structures.

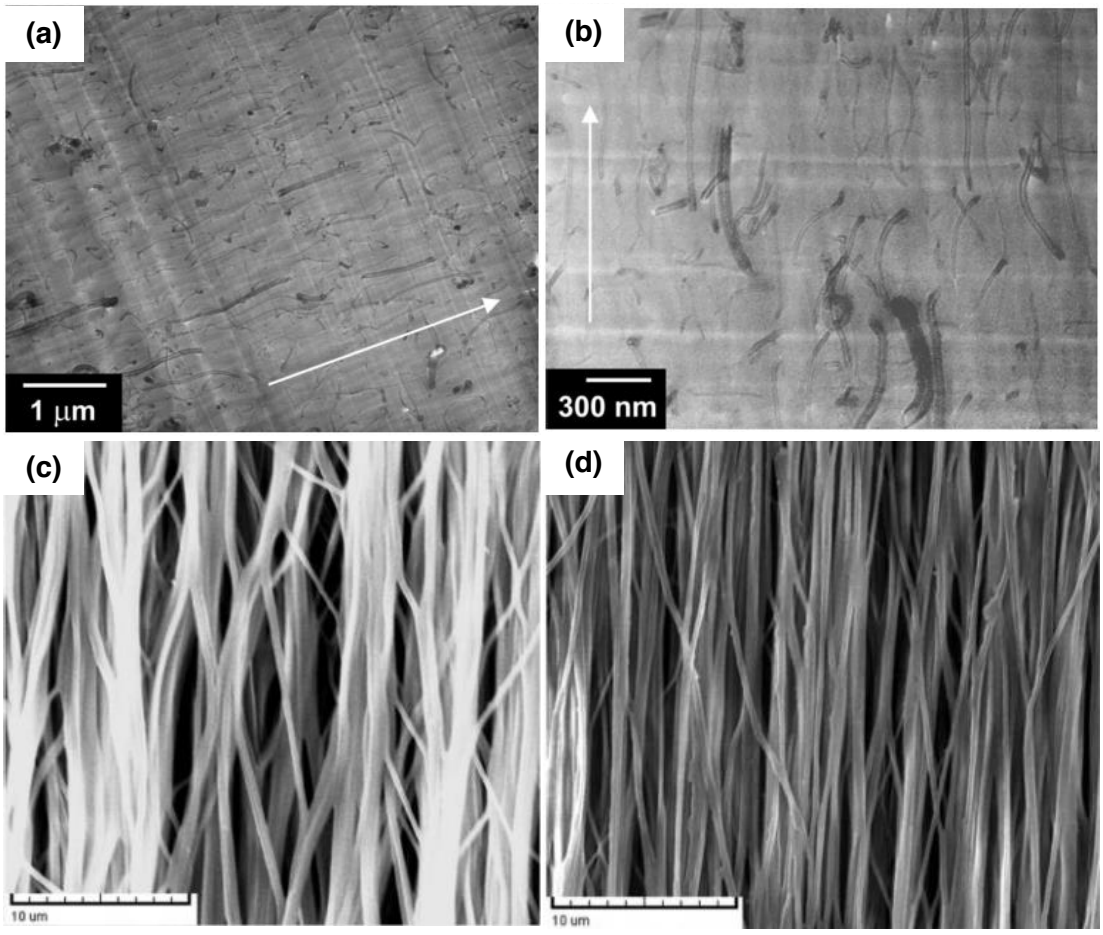

Figure 2-14 : (a-b) TEM micrographs showing the alignment of CNTs in composite films fabricated via extrusion process [157]. (c-d) SEM micrographs of the aligned nanofibres membranes fabricated using the electrospinning process [159].

2.4.2 Electric-field Induced Alignment

The use of an external electric-field is a simple and more effective approach used to align carbon nano-reinforcements in a polymer matrix. In 1996, Fishbine [166] first proposed that CNTs could be aligned in a dielectric medium using external electric-field. In the same year, Yamamoto et al. [167] became the first group to demonstrate the use of direct current (DC) electric-field to align CNTs dispersed in isopropyl alcohol. In a later study [168], the same group demonstrated that high frequency (i.e. 10

MHz) alternating current (AC) electric-field to be more effective than DC electric-field for aligning CNTs. Electric-field has also been used to align CNFs [52] and CNTs [53] in epoxy resins prior to their curing. As shown in Figure 2-15 and Figure 2-16, under the application of an electric-field between a pair of parallel plate electrodes, the nano-reinforcements may align within a polymer resin to form a chain-like network in the direction of the electric-field [51, 52]. The alignment of the nano-reinforcement has been attributed to the *dielectrophoresis* process, which is widely used for electrophoretic deposition of particles [169].

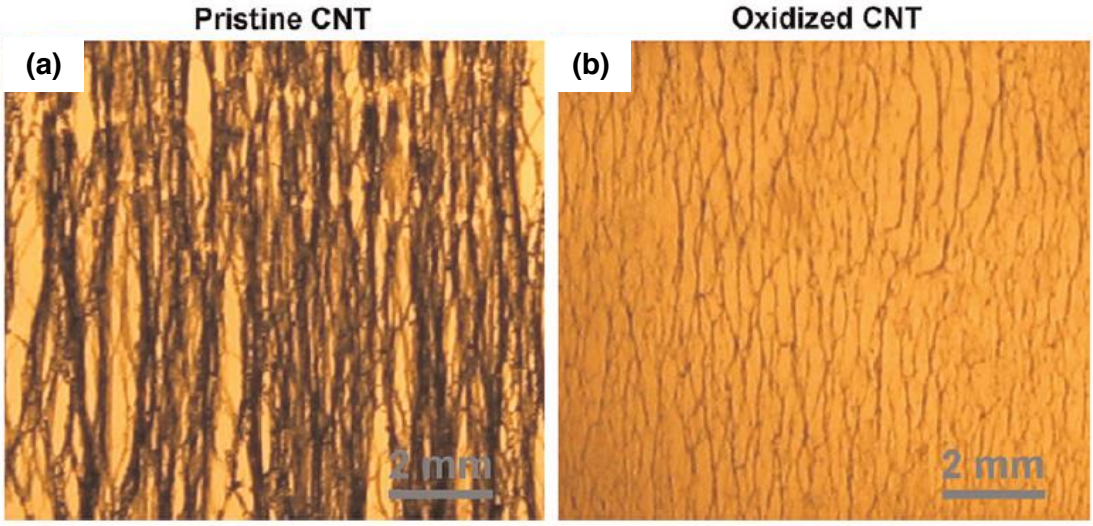

Figure 2-15 : (a-b) Optical micrographs of the CNT alignment process under the application of an AC electric-field [51].

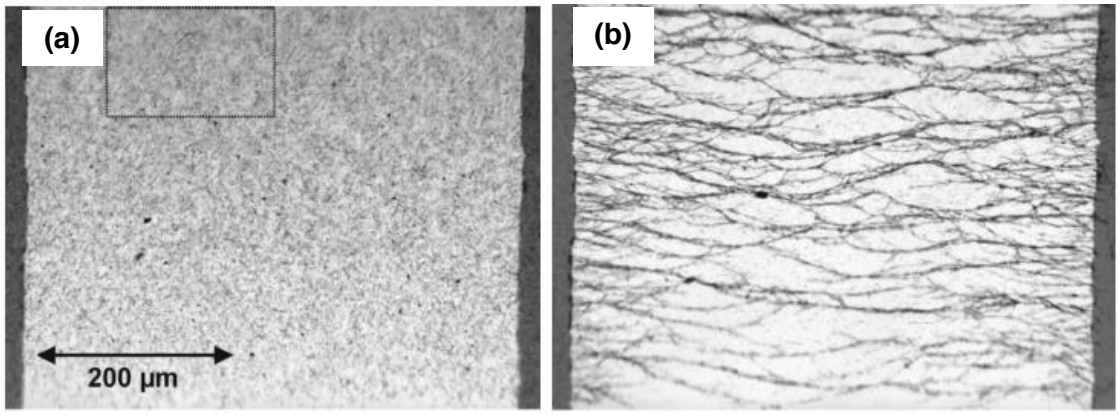

Figure 2-16 : (a-b) Optical micrographs of the CNF alignment using an AC electric-field of strength 400 V/cm at 1 kHz; (a) before application of electric-field; and (b) 30 minutes after the application of electric-field [52].

In the dielectrophoresis process, a particle immersed in a dielectric medium undergoes polarization when subjected to an externally applied electric-field. This arises from the difference in the dielectric properties and the electrical conductivities between the particle and the medium. For one-dimensional particles, such as CNFs and CNTs, due to their shape anisotropy the longitudinal polarizability is at least an order of magnitude greater than the transverse polarizability [170, 171]. Therefore, when subjected to an electric-field, the difference in polarizability of the nano-reinforcements results in an induced dipole and its interaction with the electric-field gradient generates a torque resulting in rotation of the long axis of nano-reinforcements, so causing them to align along the external-field direction [172]. Subsequently, a coulomb attraction force is generated between oppositely charged ends of aligned CNTs. This attraction force causes the aligned CNTs to migrate and connect their ends to form a chained network which stretches across the electrodes to provide a conductive pathway, as shown in Figure 2-15 and Figure 2-16 [173]. It is believed that upon curing of the polymer, the aligned nano-reinforcements network will remain in place in the resulting polymer nanocomposites. The chained network of aligned carbon nano-reinforcements should lead to a significantly lower electrical and thermal percolation threshold while simultaneously improving the conductivity of the polymer composite.

It is encouraging to know that the alignment of carbon nano-reinforcements such as CNTs [51, 53, 174-176], CNFs [52] and GNPs [49, 177] using an electric-field has indeed been reported to improve the electrical conductivity of polymers through the formation of a percolating network at extremely low content of the nano-reinforcements. In spite of these studies, the effects of electric-field-induced alignment of the nano-reinforcement on the fracture property of its composites have not been explored. By aligning the nano-reinforcements in the direction perpendicular to the crack propagation path, a greater fraction of the nano-reinforcements could be expected to participate in fracture toughening mechanisms discussed in section 2.3.1. This would lead to more significant improvement in the fracture toughness of epoxy composites with aligned carbon nano-reinforcements. More importantly, the electric-field technique could also be used to *in-situ* align carbon nano-reinforcements in the through-thickness direction of the matrix of fibre composites. This would lead to a greater reinforcement of the interlaminar as well as intralaminar regions of fibre composites. The chaining of the nano-reinforcements between the fibre plies would further enhance the through-

thickness conductivity of the fibre-epoxy composites. This was first demonstrated by Domingues et al. [178] who used an AC electric-field to align just 0.1 wt% CNTs in the through-thickness direction of a glass fibre reinforced composite laminate fabricated using resin infusion process. The conductivity of the fibre composites fabricated with the application of the electric-field was enhanced by an order of magnitude in comparison to the laminate prepared in its absence. However, no apparent improvement to the mode I interlaminar fracture toughness of the fibre composites occurred by the addition of such low content (i.e. 0.1 wt%) of CNTs. Moreover, they did not confirm whether the CNTs were indeed aligned in the through-thickness direction of the laminates.

Although an electric-field can be used to align carbon nano-reinforcements in glass fibre-reinforced composites, in a carbon fibre composite, the alignment is much more difficult to realise. The main reason is that the local contact of conductive carbon fibres causes local short-circuiting which weakens the electric-field inside the composite, leading to weaker forces for the nano-reinforcements to rotate. Electric-field cannot penetrate through conductive material due to the accumulation of surface charge which lead to the cancelling of the field flux via a well know effect referred to as the "Faradays" effect. Therefore, in a carbon fibre composite, an external electric-field may not be able to penetrate beyond the outermost plies leading to no possible alignment effect in the interlaminar and intralaminar matrix regions. However, it is well known that the magnetic flux generated in a magnetic-field can penetrate through conductive materials such as carbon fibres. Therefore, magnetic-field induced alignment techniques offer promising alternative for aligning carbon nano-reinforcements in the through-thickness direction of carbon fibre composites.

2.4.3 Magnetic-field Induced Alignment

Kimura et al. were the first to use a very high strength constant magnetic-field of 10 T to fabricate CNT-polyester matrix composites [179]. The resulting composites with aligned CNTs possessed anisotropic electrical and mechanical properties. Experimental studies [180, 181] and theoretical predictions [182] have indicated that CNTs are paramagnetic in the direction of their long axes, and thus they are susceptible to high strength magnetic-fields. Their magnetic susceptibility decreases with the increase in

temperature, suggesting strong dependency on the temperature. As shown in Figure 2-17, Takahashi et al. [183] demonstrated the use of medium strength magnetic-field of 2.4 T to align CNFs in polycarbonate matrix subjected to a temperature of 300 ^{o}C. Although the magnetic susceptibility of the CNFs or CNTs decreases with temperature, the lowering of the viscosity of the polymer at high temperature enables the magnetic torque to overcome the viscous drag effect which leads to their alignment under low magnetic-fields. Other researchers [54, 184, 185] have studied the fabrication and properties of CNT-epoxy composites prepared with the application of high strength magnetic-field of 25 T and observed a favourable increment in their thermal and electrical conductivity. However, due to their low magnetic susceptibility at room temperature, an extremely strong magnetic-field (e.g. of several Teslas) is usually required to align carbon nano-reinforcements which is impractical for manufacturing of composites [54, 165, 186, 187]. For instance, Camponeschi and co-workers [54] employed a magnetic-field of up to 25 T to orientate and align CNTs in an epoxy resin and found that the properties of the resulting nanocomposites were superior to those prepared in the absence of a magnetic-field. Mahfuz et al. [186] reported a similar attempt of using magnetic-fields of up to 28 T to align CNFs in a two-phase toughened epoxy resin system. They were able to achieve 21% and 3% increase in the compressive strength and modulus compared to randomly-oriented CNFs. The necessity to employ such high magnetic-fields limits the practical application of this method. Besides, the use of high strength magnetic-field can have adverse effect on the mechanical properties of CNT-epoxy composites. For instance, Camponeschi et al.[54] found a significant reduction in the Young's modulus of the CNT-epoxy nanocomposites fabricated under the application of very high magnetic-field strength of 25 T in comparison to the ones prepared under 15 T. They attributed this to (a) the reduction in average polymer chain length and (b) also polymer chain alignment and conformation induced by a high strength external magnetic-field.

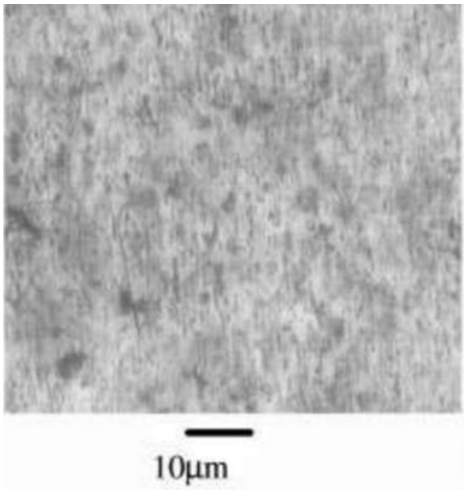

Figure 2-17 : CNF alignment using magnetic-field [183]

In recent years, various methods have been reported to functionalise carbon nano-reinforcements with magnetic nanoparticles, especially iron-based nanoparticles, so as to facilitate the alignment of carbon nano-reinforcements in a polymer matrix without needing to employ high magnetic-fields [55, 188, 189]. For instance, magnetite (Fe_3O_4) decorated CNTs [190] and GNPs [152] have been recently developed and these hybrid nano-reinforcements were successfully aligned in an epoxy using a relatively weak magnetic-field of just 0.3 T [152, 190]. The alignment of the Fe_3O_4 decorated carbon nano-reinforcements may be ascribed to the anisotropic nature of the dipolar interactions of the iron oxide nanoparticles close to the ends of the nano-reinforcements [191, 192]. Without an externally applied magnetic-field, the magnetic moments of the iron oxide nanoparticles are randomly oriented leading to vanishing net magnetization. However, upon the application of a sufficiently large magnetic-field, the magnetic moments of the nanoparticles align along the external field direction, and the resultant dipolar interactions orient the Fe_3O_4 decorated nano-reinforcements. Attraction of the north and south poles of the magnetic carbon nano-reinforcements resulted in the formation of the chain-like structure.

Moreover, CNTs and GNPs based magnetic hybrids have also been prepared by using a wet-chemical co-precipitation method. The resulting composites contained GNP-hybrid in an epoxy aligned under a relatively low magnetic-field to achieve high thermal conductivity [152] and excellent gas barrier properties [189]. However, at present, there is no reported study on the investigation of the effect of magnetic-field

alignment of the carbon nano-reinforcements on the fracture properties of epoxy composites. Especially, the decoration of carbon nano-reinforcements with Fe_3O_4 nanoparticles will affect the nano-reinforcement/epoxy interface bonding state which would, in turn, change its reinforcing efficacy. Moreover, the aforementioned magnetic-field induced alignment techniques hold the promise for achieving the alignment of carbon nano-reinforcements in the through-thickness direction of carbon fibre composites. The fabrication and properties of such multi-scale carbon fibre composite prepared with magnetic-field are yet to be explored.

2.5 Damage Detection using Carbon Nano-reinforcements

Impact-induced delamination damage can grow under relatively low cyclic interlaminar stresses caused by the fatigue loading of the composite. Delamination damage can significantly reduce the tensile and compressive properties of composites which is a major safety concern [91, 92]. Moreover, if subjected to cyclic loading, the delamination can grow almost undetected due to fatigue until they are long enough to cause catastrophic failure of the composite structure. Therefore, there are stringent aviation safety regulations on management of critical size of the delamination damage [9]. The critical size depends on several parameters including the properties of the structural material, loading, geometry of the structure; and most importantly the technique utilized for detection and monitoring the damage site. Due to the low electrical conductivity of fibre reinforced composites, many non-destructive damage inspection methods, such as eddy current and electrical resistance, which are commonly used for metallic structures, are rendered ineffective [96]. Similarly, detection of damage in adhesive bonded composite joints is currently limited to ultrasonic, radiography and acoustic emission techniques during scheduled maintenance intervals. Potential drop and eddy current technique cannot be used in the absence of through-thickness conductivity in bonded joint due to the dielectric property of the epoxy adhesives. Furthermore, the visual inspections performed during daily service of an aircraft structure cannot detect delamination and disbond damage due to their hidden nature.

2.5.1 Detection in Nano-reinforced Fibre Composites

Numerous studies have shown that carbon nano-reinforcements can form conductive networks in polymeric materials at extremely low weight fractions [33, 34]. The coupling between the mechanical and electrical response of CNTs was first investigated by Baughman et al. [193]. Fiedler et al. [194] later reviewed the prospects of using CNTs for sensing damage in composites using electrical methods. Several other studies have since investigated the use of CNT [38, 195-198], CNF [199, 200] and GNP [201, 202] networks embedded in polymer composites for strain sensing applications. These conductive networks could also be utilised for *in-situ* health monitoring of delamination and disbond damage in composite laminates [35, 64, 203-206] and their bonded [36, 207] joints. For instance, Gao et al. [206, 208] have utilized CNT networks embedded in the matrix phase of glass fibre-epoxy composites to study the onset and evolution of damage under monotonically increasing loads, as shown in Figure 2-18. In a separate study, their group investigated the electrical resistance response of CNT networks in glass fibre-epoxy composites subjected to cyclic fatigue loading [209]. They demonstrated that the CNT networks can be used to accurately detect the onset and progression of fatigue damage in fibre composites. Similarly, Monti et al. [204] have successfully employed CNFs to detect the onset and evolution of damage due to monotonic as well as impact loading of the glass fibre-epoxy composites. As can be seen in Figure 2-19, their results demonstrated that the fibre composites containing low weight fraction (i.e. 0.5 wt%) of CNFs show greater electrical resistance response to impact damage when compared to the composites with higher (i.e. 1.0 wt%) content of CNFs. This suggests that in carbon nano-reinforced composites it is advantageous to achieve electrical percolations at low nano-reinforcement contents in order to improve their sensitivity to electrical response due to damage. The electric- and magnetic-field induced aligning and chaining of carbon nano-reinforcements in composites can indeed lead to ultra-low electrical percolation thresholds in comparison to the randomly oriented nano-reinforcements [51-53, 185]. Moreover, the anisotropic electrical properties of aligned carbon nano-reinforced composites could further enhance their electrical responsiveness to damage.

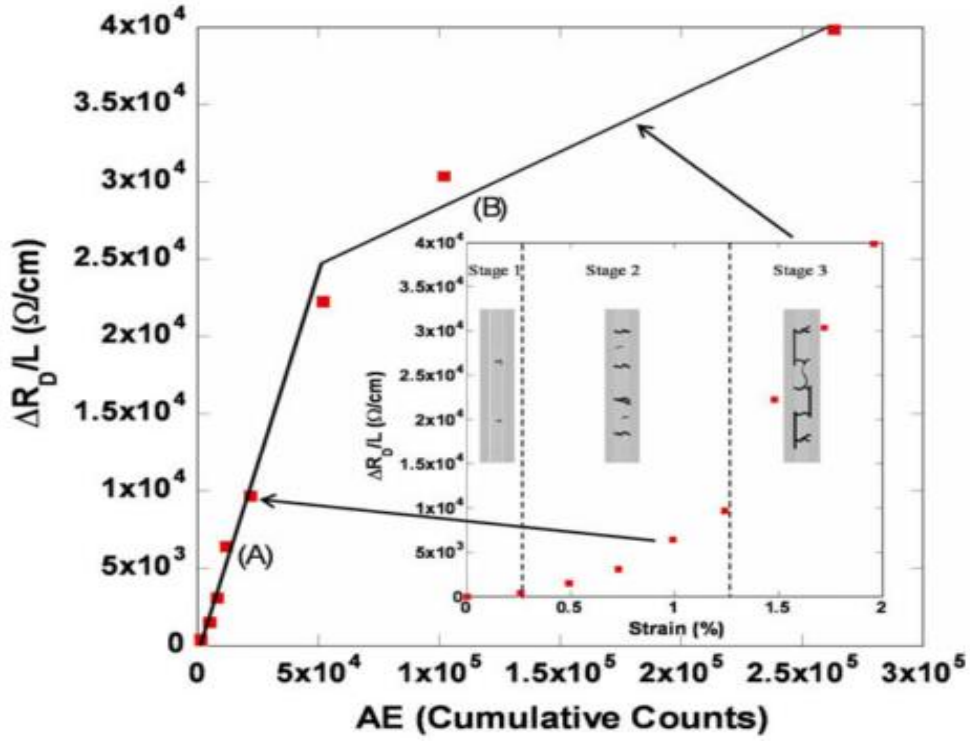

Figure 2-18 : The comparison of the acoustic event (AE) and the change in resistance during composite damage. Inset: Resistance change behaviour for various stage of the damage evolution in CNT-reinforced multi-scale composites [206].

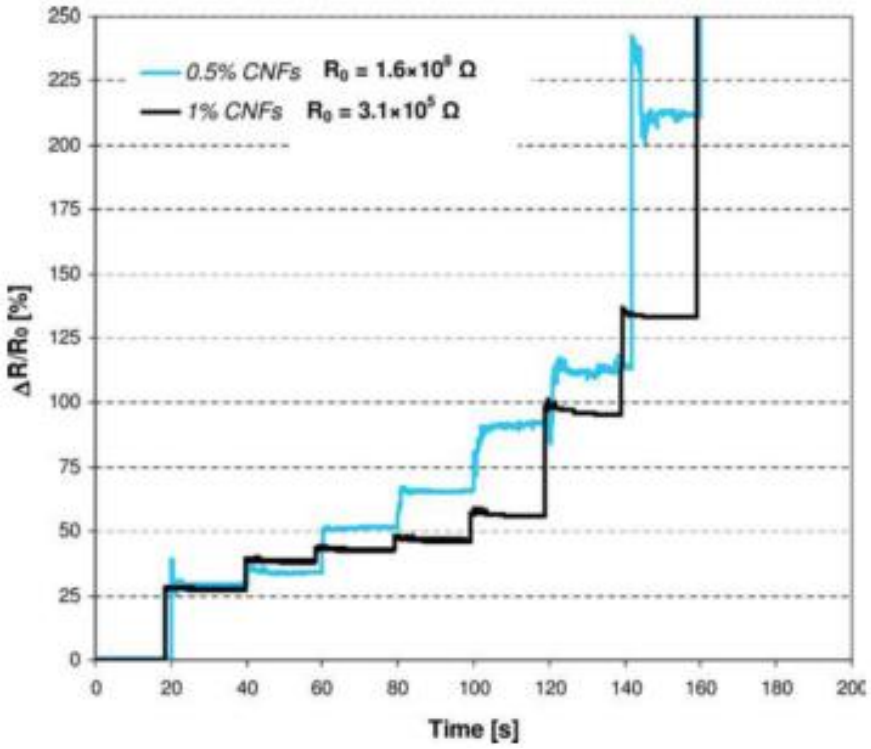

Figure 2-19 : Electrical resistance change in CNF-reinforced multi-scale composites as a results of cyclic impact induced damage [204].

2.5.2 Diagnosis of Damage in Nano-reinforced Composite Joints

In comparison, only two studies have investigated the use of carbon nano-reinforced epoxy adhesives for detecting disbond damage in adhesively bonded composite joints [36, 207]. These studies were primarily focused on investigating the electrical response of CNT networks to shear stresses in a lap shear joint configuration. For example, Lim et al. [36] reported the use of CNT networks to monitor the initiation of damage in CNT reinforced epoxy adhesive bonded lap joints subjected to quasi-static and cyclic tensile loading. They demonstrated that *in-situ* resistance measurements can be used to identify the joint failure mechanisms, but did not establish whether this technique could be used to determine the size of disbond damage. Whereas, Mactabi et al. [207] studied the use of CNT networks to monitor the fatigue life of adhesive bonded lap joints subjected to tensile cyclic loading. As can be seen in Figure 2-20, they found that there was no change in resistance until the joint had reached almost 85% of its fatigue life cycles which was then followed by a sharp rise corresponding to the failure of the joint. However, they did not establish whether this technique could be used to monitor the size or propagation of damage.

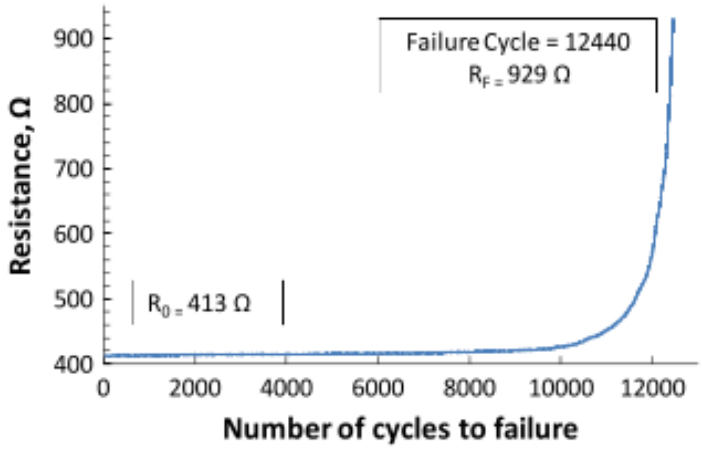

Figure 2-20 : *In-situ* electrical resistance measurement during tensile fatigue loading of lap shear joints bonded with CNT-reinforced epoxy adhesive [207].

For composite aircraft structures, it is necessary to be able to identify the size and its growth for the continued service of the aircraft. The Federal Aviation Administration's damage tolerant design regulations specify that delamination damage within aircraft composites above a critical size must be immediately repaired or the

entire damaged structure replaced for continued service [8]. In addition, there are stringent aviation safety regulations on management of critical size of the disbond damage [9]. The critical size depends on the technique used for detection and monitoring the damage site. An earlier study by Zhang et al. [210] demonstrated the use of CNT networks in epoxy nanocomposites to monitor and predict the underlying crack growth damage during mode I fatigue tests performed on compact tension specimens. The study successfully demonstrated that changes in resistance induced by crack growth in epoxy nanocomposites can be used to determine the size of the underlying damage as shown in Figure 2-21. The potential application of this technique to monitor and detect fatigue crack growth in adhesive bonded composite joints has never been studied.

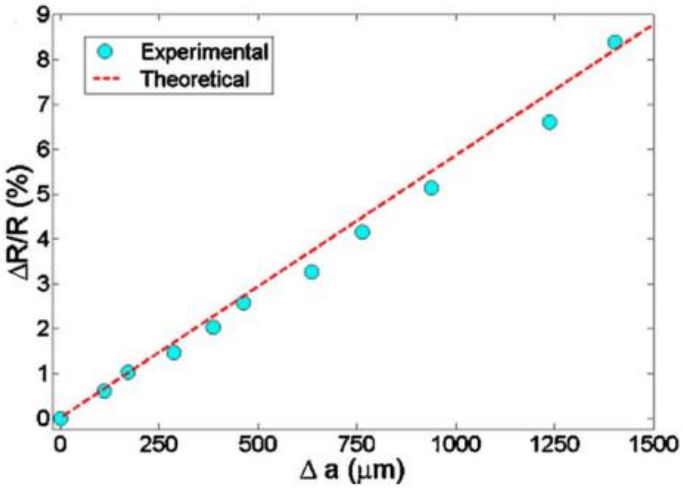

Figure 2-21 : Electrical resistance change measured as a function of fatigue crack growth in a compact tension specimen for a CNT-epoxy composite subjected to cyclic loading [210].

2.6 Summary and Outstanding Research Issues

Research into polymer nanocomposites has recently advanced to a level where several important properties, such as strength and stiffness, can be predicted using various modelling approaches [211-215]. This has enabled an effective 'materials design' approach for this new class of materials, which reduces the cost and accelerates the introduction of novel and improved nanocomposite materials. Similarly, carbon nano-

reinforced epoxy composites have shown good improvement to the fracture resistance and electrical property.

While the fracture property improvements listed in Table 2-1 for various carbon nano-reinforcements are impressive, they are significantly lower than the 900 % increase in fracture toughness reported for nano-silica [119] and rubber particle modified epoxy polymers [99]. But the use of carbon based nano-reinforcements can simultaneously improve the electric conductivity and mechanical properties, unlike nano-silica and rubber particles. One major factor limiting the property improvements achieved to date in epoxy composites has been the fact that the carbon nano-reinforcements are typically randomly-oriented, which arises naturally from the dispersion process using ultrasonication and/or mechanical mixing. Therefore, in addition to the nano-reinforcement size and shape; dispersion quality; volume fraction and particle-matrix interface; the alignment of the nano-reinforcements in the loading direction is critical for enhancing the fracture toughness of epoxy nanocomposites as demonstrated by numerical models. Similarly, experimental studies suggest that aligning the carbon nano-reinforcements in the through-thickness direction of the multi-scale composite laminate is necessary for achieving a significant improvement to their fracture energy [42, 142]. The alignment of carbon nano-reinforcements using an electric-field has indeed been reported to improve the electrical conductivity of polymers through the formation of a chained network at low content of the nano-reinforcements. The effects of electric-field-induced alignment of the nano-reinforcements on the fracture property of its composites have yet to be explored. Besides, only limited research has been reported on the comprehensive modelling of the fracture properties of nanocomposites [106], and this study was focused on one-dimensional nano-reinforcements such as CNTs. Thus, there is a lack of suitable models that can be utilized to analyse the fracture properties of nanocomposites with two-dimensional nano-reinforcements such as GNPs.

Electric-field can be used to align carbon nano-reinforcements in glass fibre-reinforced composite, but it will be ineffective for carbon fibre composite. Alternatively, very high strength magnetic-field has been shown to align carbon nano-reinforcements in epoxy composites. However, high strength magnetic-fields can also cause breakdown of the polymer chains which can be detrimental to the mechanical

properties of their nanocomposites. On the other hand, the carbon nano-reinforcements need to be functionalised with magnetic nanoparticles, in order for them to be aligned using weak magnetic-field. The alignment of Fe_3O_4 decorated nano-reinforcement holds the promise for achieving the preferential (i.e through-thickness) interlaminar reinforcements in carbon fibre composites. However, the effects of magnetic-field induced alignment of Fe_3O_4 functionalised carbon nano-reinforcements on the fracture properties of epoxy composites have not been studied.

Several studies have shown that carbon nano-reinforcements can form conductive networks in polymeric materials at extremely low weight fractions [33, 34]. These conductive networks have been utilised for *in-situ* health monitoring of delamination and disbond damage in composite laminates [35, 36]. However, the short communication by Zhang et al. [210] is the only study reported on utilizing CNT networks to predict the crack growth damage in epoxy nanocomposite subjected to fatigue loading. In addition, very little research has been reported on the use of carbon nano-reinforcements to detect disbond damage in bonded composite joints. This PhD project will extend the technique proposed by Zhang et al. [210] to detect disbond damage in composite joints bonded with aligned carbon nano-reinforced epoxy.

Chapter 3

Improving the Fracture Toughness of Epoxy Composites using Aligned Carbon Nanofibres

Abstract

There is an increasing demand for high performance composites with enhanced mechanical and electrical properties. Carbon nanofibres offer a promising solution but their effectiveness has been limited by difficulty in achieving directional alignment. This chapter investigates the use of an alternating current (AC) electric-field to align carbon nanofibres in an epoxy. During the cure process of an epoxy resin, carbon nanofibres (CNFs) are observed to rotate and align with the applied electric-field, forming a chain-like structure. The fracture energies of the resultant epoxy nanocomposites containing different concentrations of CNFs (up to 1.6 wt%) are measured using double cantilever beam specimens. The results show that the addition of 1.6 wt% of aligned CNFs increases the fracture energy, G_{Ic}, by about 1600% from 134 to 2345 J/m^2. A modelling technique is presented to quantify this major increase in the fracture energy with aligned CNFs. The results of this research open up new opportunities to create multi-scale composites with greatly enhanced multifunctional properties.

The research presented in this chapter has been published in the following journal and conference papers:

- Ladani RB, Wu S, Kinloch AJ, Ghorbani K, Zhang J, Mouritz AP, Wang CH. *Improving the toughness and electrical conductivity of epoxy nanocomposites by using aligned carbon nanofibres*. Composites Science and Technology. 2015; 117:146-158.
  The open access journal article from Composite Science and Technology is attached in Appendix A.I.

- Wang CH, Ladani RB, Wu S, Kinloch AJ, Zhang J, Ghorbani K, Mouritz AP. *Epoxy Nanocomposites with Aligned Carbon Nanofillers by External Electric Fields*. In Proceeding of the 26th International Conference on Composite Materials, Copenhagen, Denmark, 2015.

- Ladani RB, Kinloch AJ, Wang CH. *Alignment of Carbon Nanofibers in Carbon Fiber/Epoxy Resin Adhesive Bonded Joints for Mode-I Fracture Toughness Improvement*. In Proceeding of the 22th International Conference on Processing and Fabrication of Advanced Materials, Singapore, 2013

3.1 Introduction

One major factor limiting the property improvements achieved to date in epoxy nanocomposites has been the fact that the carbon nano-reinforcements are typically randomly-oriented, which arises naturally from the dispersion process using ultrasonication and/or mechanical mixing [63]. Theoretical modelling and computational simulations suggest that aligning nano-scale structures (e.g. CNTs and CNFs) in a certain direction should lead to substantial advantages compared with randomly-oriented nano-reinforcements. Indeed, numerical analyses have confirmed that 1.0 vol% aligned CNTs should increase the stiffness of an epoxy by about 300% [216] in the alignment direction. Similarly, the alignment of 3.0 vol% CNTs in epoxy normal to the crack growth plane is predicted to enhance the toughness by up to 400% [41]. Unfortunately, there is a dearth of suitable processes to align carbon nano-reinforcements along the through-thickness direction of composites. However, recently the use of electric- and magnetic-fields to align nanoparticles in liquid resins, prior to curing, has been reported [44-46, 161, 216]. Under the application of an electric-field between a pair of parallel plate electrodes, the nano-reinforcements may align to form a chain-like network in the direction of the electric-field [52]. This mechanism of the self-aligning of conductive carbon nano-reinforcements in polymers offers a new opportunity to create multi-scale structures. Since thermosetting resins, such as epoxy resins, may typically possess a relatively low viscosity prior to cure, the application of an electric- and/or magnetic-field will be able to transform the randomly-oriented carbon-based nano-reinforcements to give a highly aligned structure. Upon curing, the aligned nano-reinforcements will remain in place in the resulting epoxy nanocomposite. The alignment of CNFs [52] and CNTs [150] using an electric-field has indeed been reported to improve the electrical conductivity of polymers through the formation of a percolating network at extremely low weight fractions of the added CNFs or CNTs. Khan et al. [150] has reported an additional 30% increase in the fracture toughness of CNT modified epoxy nanocomposites due to the alignment of the CNTs normal to the crack growth plane using a direct current (DC) electric-field. Although randomly aligned CNFs have also been reported [112] to improve the fracture toughness of nanocomposites, the effect of their alignment on the fracture energy has never been studied.

Considering that CNFs may be an excellent alternative to CNTs due to their wide availability and lower cost [59], this chapter focuses on dual improvements in the electrical conductivity and fracture toughness of an epoxy nanocomposite containing aligned CNFs. The alignment is accomplished by applying an external AC electric-field whilst the resin is liquid prior to crosslinking. Upon curing the epoxy resin, the resultant epoxy nanocomposite contains aligned CNFs. The effects of alignment of the CNFs on the fracture toughness of the epoxy nanocomposite are measured and theoretical modelling studies are undertaken to quantify the increase in the fracture toughness due to the alignment of the CNFs. The results are then compared to the values pertinent to the unmodified epoxy and the epoxy nanocomposites containing randomly-oriented CNFs.

3.2 Materials and Experimental Methodology

Materials

The epoxy resin used was a liquid blend of bisphenol A and bisphenol F ('105' from West System) and the hardener ('206' from West System) was a blend of aliphatic amines and aliphatic amine adducts based on diethylenetriamine and triethylenetetramine. Commercially-available vapour-grown carbon nanofibres, Pyrograf® - III PR-24-HHT and supplied by Applied Sciences Inc., USA, were employed as the nano-reinforcement. The CNFs had a diameter of about 70 to 200 nm and a length of 50 to 200 μm [34]. Carbon fibre composite substrates were manufactured using 12 plies of unidirectional T700 carbon-fibre/epoxy-prepreg (VTM 264 supplied by Applied Composites Group). The substrates, with dimensions of 300 mm x 250 mm x 2.5 mm, were cured and consolidated in an autoclave at 120^{o} C for 1 h, in accordance with the manufacturer's recommended cure process. The substrate surfaces were abraded using 320 grit aluminium oxide abrasive paper, cleaned under running tap water for about 2 minutes, degreased with acetone, and finally cleaned with distilled water to remove any surface impurities. The substrates were then used as the electrodes between which the liquid epoxy resin mixed with the CNFs, prepared according the procedure described below, acted as an adhesive layer.

Dispersion and in-situ alignment of the CNFs in the liquid epoxy resin

A three-roll mill (Dermamill 100) was used to disperse the CNFs in the liquid epoxy resin. Firstly, 1.0 wt% of the CNFs were hand mixed with dispersion-aiding additives based upon solvent-free acrylate copolymers, namely Disperbyk-191 and -192 (supplied by BYK ®). The dispersive surfactants that were added to the CNFs were equal to the weight of the CNFs, resulting in a mixture of CNFs:191:192 weight ratio of 1:1:1. The CNF-surfactant mixture was then added to the epoxy resin, with no curing agent yet added, and hand mixed for 5 minutes. This mixture was then passed four times through the three-roll mill at 150 rpm with varying gap sizes. In order to achieve a homogeneous dispersion of CNFs, with each subsequent pass the mill gap size was gradually reduced until the smallest gap setting of 20 μm had been reached. The 1.0 wt% CNF/epoxy mixture was then diluted by adding epoxy resin, to achieve the desired weight fraction of CNFs (0.1%, 0.4%, and 0.7%) in the epoxy resin. A batch of 1.6 wt% CNFs was mixed and dispersed separately following the above procedure, due to its relatively higher weight fraction in the epoxy resin.

To observe the AC electric-field induced alignment of the CNFs, a 0.1 wt% CNF/epoxy resin mixture was placed on a glass slide between two parallel carbon electrodes with a 1.5 mm separation distance. VTM264 carbon fibre-epoxy prepreg strips were used as electrodes. An AC signal generator (Tektronix CFG250) in combination with a wideband amplifier (Krohnhite 7602M) was used to apply 70 V AC at 10 kHz to generate the AC electric-field of 30 V/mm strength. The *in-situ* alignment of the CNFs in the liquid epoxy resin was observed using a Leica optical microscope. Time-lapsed images of the CNFs were acquired using a Leica DC 300 digital camera to observe the alignment of the CNFs in the epoxy resin. The distribution of the orientation angles of the CNFs was ascertained using the Leica image processing software.

Joint manufacturing and testing

The surface-treated carbon-fibre composite substrates (150 x 250 x 2.5 mm) were placed between glass fibre frames which were used as a dam to prevent the epoxy mixture from flowing out of the joint. Spacers, 2 mm in thickness made of glass slides,

were placed at both ends of the joint to control the thickness of the epoxy layer between the substrates. Teflon-coated tape about 30 mm long and 11 μm thick was placed at an approximately equal distance between the two substrates, at one end of the joint, to act as a crack starter. The amine-based curing agent was added to the dispersed CNF/epoxy resin mixture and hand-mixed for approximately 5 minutes. This CNF-modified epoxy resin mixture was then poured between the substrates. Such bonded joints were prepared using the epoxy nanocomposite as the adhesive layer for six different concentrations of CNFs (i.e. 0.0, 0.1, 0.4, 0.7, 1.0 and 1.6 wt%). Studies were undertaken for two different orientations of the CNFs (i.e. randomly-oriented and aligned). In order to achieve a highly aligned network of CNFs in the through-thickness direction of the epoxy nanocomposite layer, an AC electric-field of 30 V/mm at 10 kHz was applied between the carbon-fibre composite substrates during the initial one hour period of the curing cycle of the epoxy resin. The epoxy resin was then cured at room temperature (i.e. 25^0C) for 48 h in total to form the epoxy nanocomposite. After this time period, the CNF-epoxy nanocomposite is referred to as 'n Random' or 'n Aligned', where 'n' refers to the amount of CNF by percentage weight of the total epoxy resin followed by the orientation. The joints were then cut into 20 mm wide double-cantilever beam (DCB) adhesively-bonded specimens. Figure 3-1 shows a schematic of the DCB specimen.

A sharp crack tip was achieved by carefully wedging the crack opening from the tip of the Teflon film. A minimum of five DCB specimens were tested in a 10 kN Instron machine at a crosshead speed of 1 mm/min in accordance with ISO 25217 [217]. The load versus displacement curves were recorded continuously, and a travelling optical microscope was used to observe the crack length in the epoxy nanocomposite layer. The mode I fracture energy, G_{Ic}, was calculated based on 'corrected beam theory' [217]. The crack was always found to propagate cohesively through the epoxy nanocomposite layer itself.

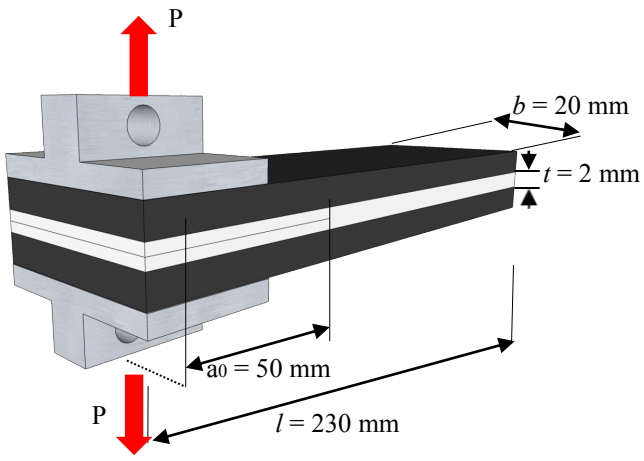

Figure 3-1 : Schematic diagram of the double cantilever beam (DCB) specimen for fracture toughness testing.

3.3 Results and Discussion

3.3.1 Dispersion and In-situ Alignment Studies

The as-supplied CNFs were in the form of agglomerates, as shown in Figure 3-2a. The use of the three-roll milling method was efficient at breaking up the agglomerates and dispersing the CNFs, as may be seen from Figure 3-2b. The diameter of the as supplied CNFs was measured from five different SEM micrographs (see Figure 3-2a) with a total CNF population equal to 510. As shown in Figure 3-2c, the diameter distribution of the CNFs has a range from 60 nm to 200 nm with a lognormal peak of about 95 nm. The post-dispersion length of CNFs in the epoxy resin was measured using the Leica image processing software. Figure 3-2d shows the length distribution of the CNFs after three-roll milling. The three-roll mill dispersion resulted in sizes of the CNFs ranging from 2 to 50 μm, with the majority of the CNFs having lengths of 16 to 24μm. Dispersion using ultrasonication or three-roll milling would inevitably reduce the length of CNFs, however three-roll milling has been reported to be less damaging [63]. Retaining a relatively long length for the CNFs during their dispersion in the epoxy is considered to be important for obtaining an effective toughening of the epoxy nanocomposite, since the theoretical improvement in the fracture energy of the epoxy, from a fibre pull-out mechanism, will be proportional to the square of half the embedded length of the CNFs [84].

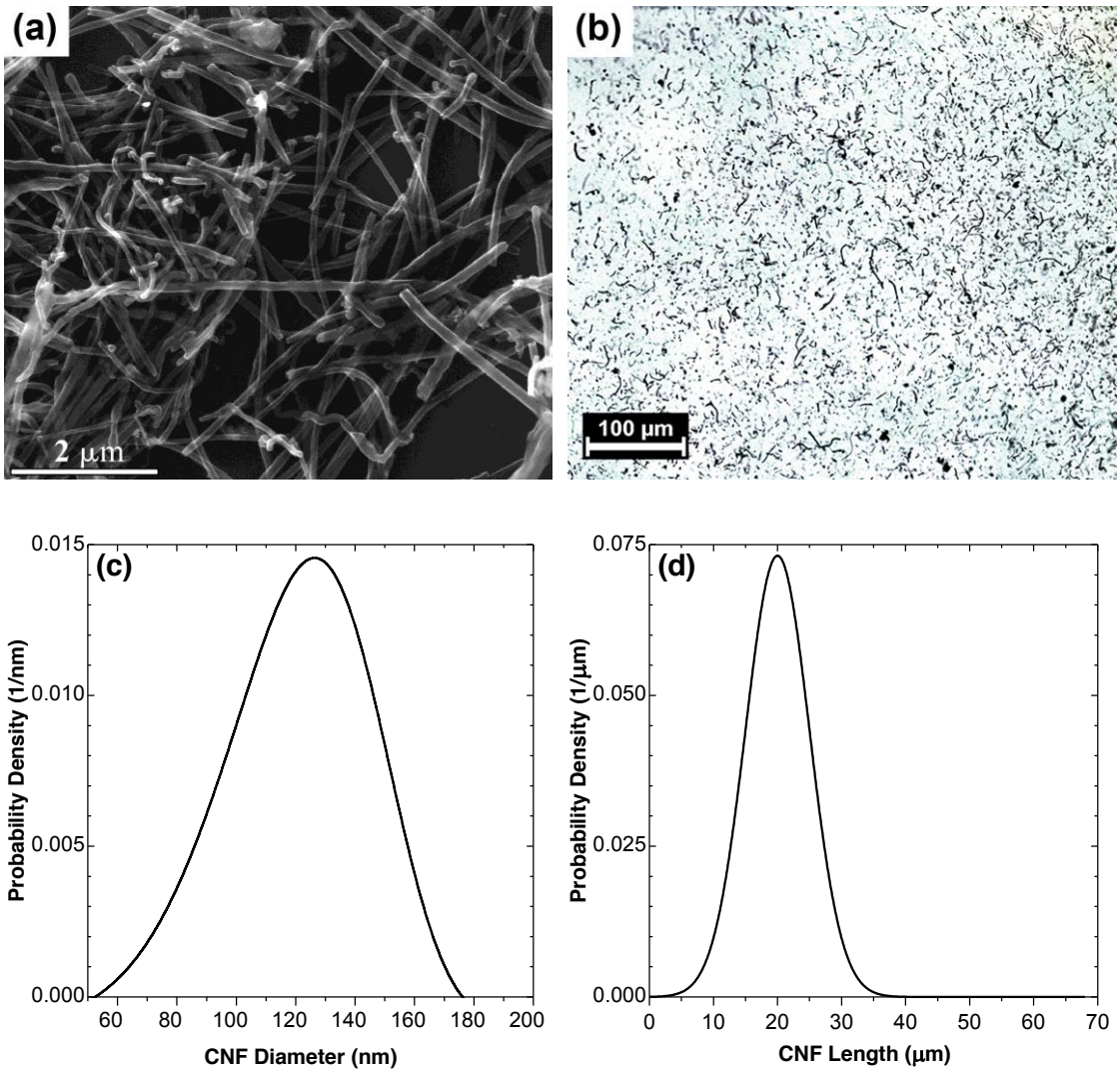

Figure 3-2 : (a) SEM micrograph of the as supplied CNF and (b) optical micrograph of the epoxy resin/0.1 wt% CNF mixtures after three-roll mill dispersing; (c) diameter probability density function of the as supplied CNFs measured from SEM micrograph and (d) length probability density function of the CNFs after the three roll-milling dispersion process from image (b).

The response of the CNFs in the liquid epoxy resin to the AC electric-field was verified through *in-situ* optical microscopy. An AC electric-field with an amplitude of 30 V/mm at 10 kHz was applied to 0.1 wt% of CNFs dispersed in the epoxy resin (i.e. containing no curing agent). Observations using the optical microscope were made to measure the time to achieve alignment. Figure 3-3a shows an optical micrograph for t=0 minutes (i.e. before the application of the AC electric-field) and, therefore, the CNFs are randomly-oriented. Upon application of the AC electric-field the CNFs rotated to align in the direction parallel to the electric-field, as shown in Figure 3-3b. For a 30 V/mm electric-field strength, the time needed to complete the alignment

process was found to be about 5 minutes; beyond which no further improvement in the degree of alignment was observed. Figure 3-3c shows a comparison of the angle distribution between the randomly-oriented CNFs (i.e. no electric-field was applied) and the CNFs where the AC electric-field was applied for 5 minutes. The use of the AC electric-field has resulted in about 80% of the population of CNFs being aligned within $\pm 10^{o}$ of the applied electric-field direction.

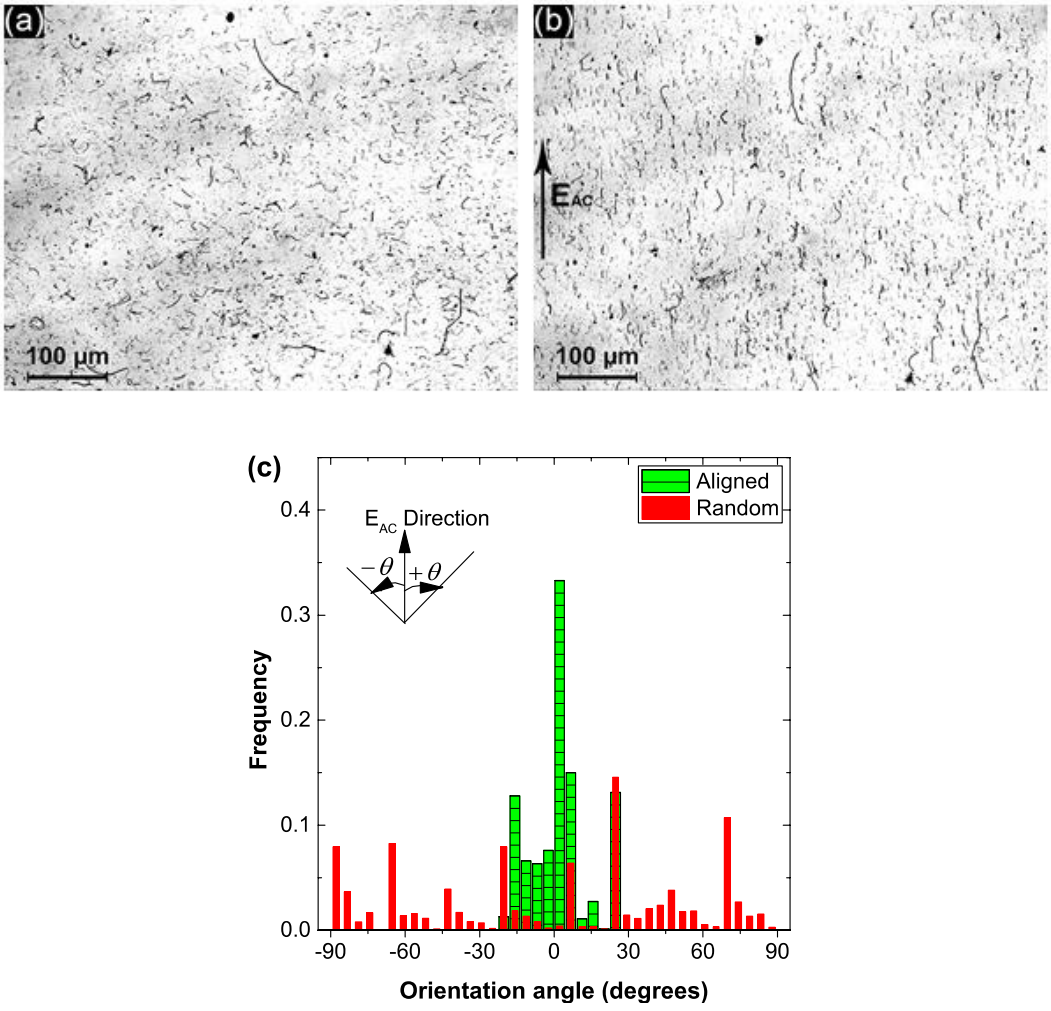

Figure 3-3 : *In-situ* alignment of 0.1 wt% CNFs in the epoxy resin using the AC electric-field (a) t = 0 minutes (i.e. randomly-oriented CNFs) and (b) t = 5 minutes (i.e. aligned CNFs), the direction of the applied AC electric-field is indicated by the arrow; (c) comparison of the angle distribution of the randomly-oriented CNFs (from Fig 3a) and the CNFs aligned after being subjected to the AC electric-field for 5 minutes (from Fig 3b).

As shown in Figure 3-4, the orientation of the CNFs was further verified using transmission electron microscopy to view 90 nm thick slices (obtained through ultramicrotomy) of the epoxy nanocomposite. The alignment of the CNFs can be

attributed to the *dielectrophoresis* process, which is widely used for electrophoretic deposition of particles [169]. In the dielectrophoresis process, a particle immersed in a dielectric medium undergoes polarization when subjected to an externally applied electric-field. This arises from the difference in the dielectric properties and the electrical conductivities between the particle and the medium. For one-dimensional particles, such as CNFs and CNTs, due to their shape anisotropy the longitudinal polarizability is at least an order of magnitude greater than the transverse polarizability [170, 171]. Therefore, when subjected to an electric-field, the difference in polarizability of the CNFs results in an induced dipole and its interaction with the electric-field gradient generates a torque resulting in rotation of the long axis of CNFs, so causing them to align along the external-field direction [172].

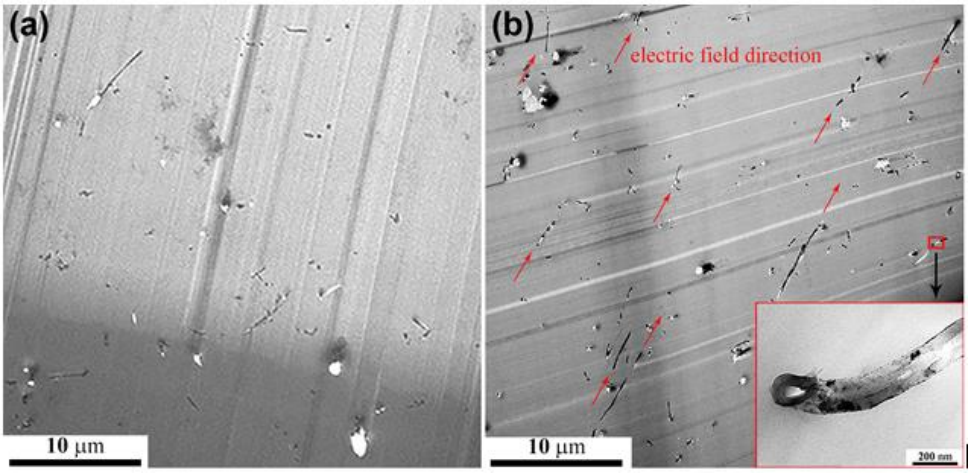

Figure 3-4 : TEM images of the epoxy nanocomposites. (a) 0.7 wt% of CNFs and randomly-oriented. (b) 0.7 wt% of CNFs and aligned via the application of the AC electric-field for 5 minutes. (The arrows indicate the direction of the applied AC electric-field.) Inset shown in (d) gives a detailed view of CNF.

3.3.2 Fracture Energy Studies

As shown in Figure 3-5**,** the applied load versus crack opening displacement curves for the DCB tests with the adhesive layer comprising of unmodified epoxy or epoxy nanocomposites containing randomly-oriented or aligned CNFs all revealed that the type of crack growth was unstable, i.e. stick-slip, in nature, with the distinct "saw-tooth" shaped load versus displacement curves typical of such failure. The maximum peak loads of these curves corresponded to the onset of crack growth, while the lower values of load corresponded to the arrest of the fast propagating crack. For the DCB

specimens with a higher weight content of CNFs in the epoxy nanocomposite layer, the length of the unstable crack growth was much greater, due to the higher maximum loads for crack propagation that were attained. Therefore, the load versus displacement curves for these samples had fewer peaks. The values of G_{Ic} for the onset of crack propagation were calculated using the maximum loads that were measured [217]. The locus of failure was along the centre of the unmodified (i.e. neat) epoxy polymer or epoxy nanocomposite layer in all cases.

The results of the fracture toughness tests of the DCB tests with the adhesive layer comprising of unmodified epoxy or epoxy nanocomposites containing randomly-oriented or aligned CNFs are shown in Figure 3-6. The average mode I fracture energy, G_{Ic}, of the unmodified epoxy layer for the DCB joint was found to be 134 J/m^2, as would be expected for a relatively brittle epoxy. An increase in the value of the fracture energy was observed for all the epoxy nanocomposites. For the nanocomposites, the fracture energy increases almost linearly with the content of CNFs. In addition, a somewhat greater improvement in the fracture energy was consistently measured for samples containing aligned CNFs, with their orientation of course normal to the direction of crack growth. The '1.6 aligned' specimen showed the highest improvement, with a sixteen fold increase in the fracture energy compared to the unmodified epoxy.

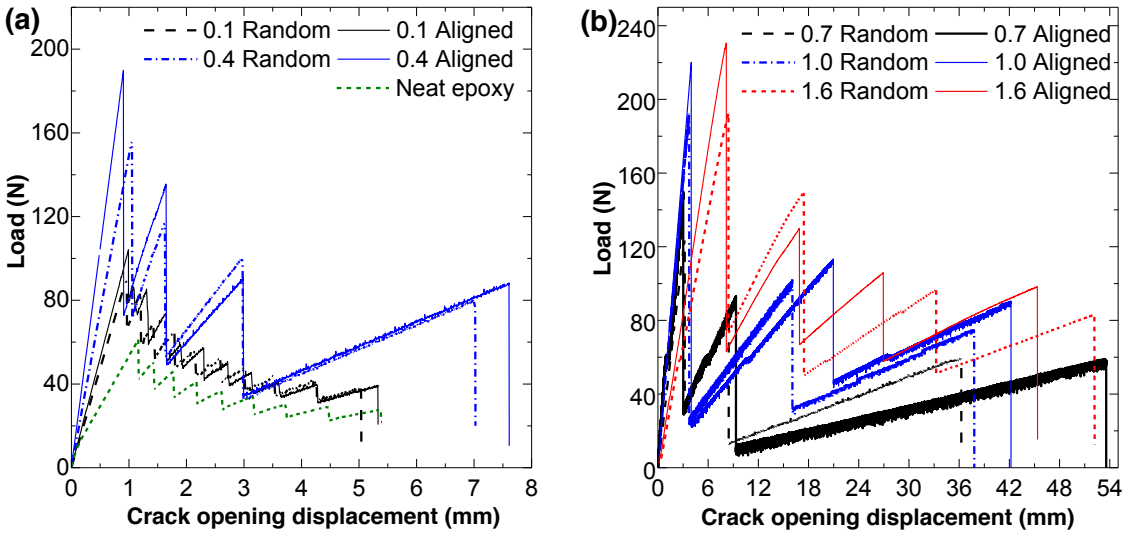

Figure 3-5 : Load versus displacement curves for the epoxy nanocomposites containing different concentrations of CNFs and for both randomly-oriented or aligned CNFs in the epoxy nanocomposite layer.

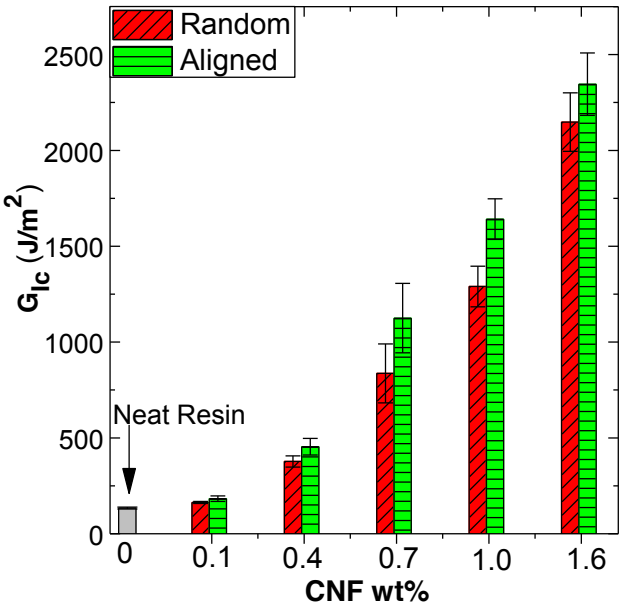

Figure 3-6 : Values of the fracture energy, G_{IC}, for the epoxy nanocomposites containing different concentrations of CNFs and for both randomly-oriented or aligned CNFs in the epoxy nanocomposite layer.

Further, compared to the nanocomposites containing randomly-oriented CNFs, the alignment of the CNFs resulted in a consistent rise of about an additional 25% increase in the fracture energy for the concentrations investigated at, and below, 1.0 wt%. However, a further increase in the content of the CNFs to 1.6 wt% showed a relatively small difference between the fracture energies of the aligned and randomly-oriented CNF nanocomposites which was not statistically significant. Similar observations have been reported for CNT/epoxy nanocomposites at relatively high concentrations of CNTs, and were suggested to be due to the lack of free space available for the rotation and alignment of the CNTs in the epoxy when a relatively high concentration of nano-reinforcement was present [150].The toughening mechanisms responsible for these observed improvements in the measured toughness are discussed in the following section.

3.3.3 Toughening Mechanisms

Post-failure examination of the fracture surfaces of the DCB samples gave an insight into the toughening mechanisms responsible for the improvements in the fracture energy of the epoxy nanocomposites. A typical featureless and smooth fracture surface was observed for the unmodified epoxy which was indicative of a very brittle fracture.

Figure 3-7 shows a photograph of the fracture surface for a nanocomposite sample where the regions of crack initiation and arrest are visible as curved lines across the width of the sample. In the epoxy layer of the DCB test, crack growth occurred under predominantly plane-strain conditions but with limited plane-stress conditions at the specimen edges of the specimen, which caused the curved profile of the crack front. There is a distinct whitening of the polymer along these crack initiation/arrest lines. Examination of these regions using the SEM revealed a pattern of tear marks, which provides evidence of plastic deformation in the epoxy polymer along the line of crack initiation, which would have occurred immediately before the onset of the rapid growth of the crack. Further away from the stress-whitened regions, where the crack had propagated rapidly, there was very little evidence of ductile, plastic deformation, and the glassy fracture surface was representative of a very brittle fracture having occurred. Figure 3-8 shows SEM micrographs of the stress-whitened region which correspond to the location of the onset of crack growth (i.e. the crack initiation location, see the inset in Figure 3-8) in the epoxy nanocomposites containing different contents of aligned CNFs. Patterns of tear marks were observed in most of these images, revealing the plastic deformation of the epoxy that had occurred in the stress-whitened regions, either just ahead of the crack tip or due to some extent of slow crack growth occurring prior rapid crack growth taking place. The size and roughness of the stress-whitened region both increased with CNF content. The increase in the severity of the tear marks and the roughness with increasing CNF content is indicative of the increased plastic deformation of the epoxy in the process zone ahead of the crack tip due to the presence of the CNFs.

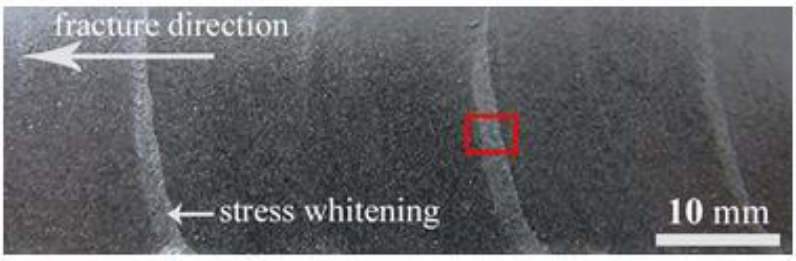

Figure 3-7 : Photograph of the crack fronts on the fracture surface of an epoxy nanocomposite with 1.0 wt% aligned CNFs.

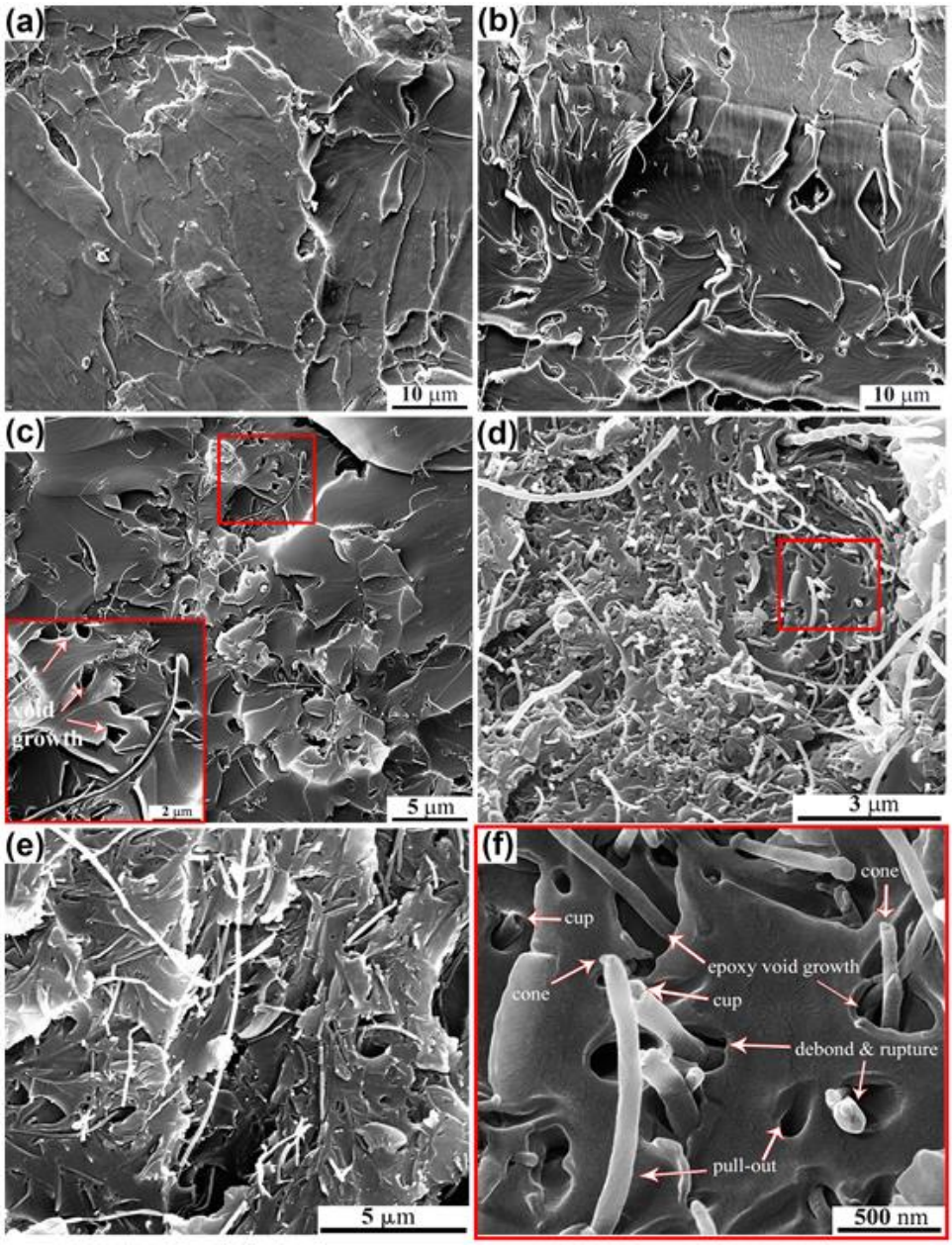

Figure 3-8 : SEM images of the crack initiation region of the fracture surfaces for the epoxy nanocomposites containing aligned CNFs of concentration; (a) 0.1 wt%; (b) 0.4 wt%; (c) 0.7 wt%; (d) 1.0 wt%; (e) 1.6 wt% and (f) is of the inset of (d) at a higher magnification for the1.0 wt% nanocomposite.

As shown in Figure 3-8, a significant number of CNFs were pulled out of the epoxy, leaving behind a void on the opposite crack surface. The areal density of the pulled-out regions of the CNFs increased with the increasing content of aligned CNFs. Moreover, some of the CNFs showed evidence of having experienced uncoiling and a cup-cone type of failure. This uncoiling phenomenon is unique to CNFs due to their stacked graphene cup morphology [112], which has been previously observed using

TEM, revealing an uncoiled nanoribbon of graphene sheet [120]. The uncoiling and cup-cone type failure of CNFs was observed for both aligned and randomly-oriented CNF-epoxy nanocomposites. However, the fibre pull-out mechanism is typically the most dominant mechanism in increasing the fracture energy [82]. The increase in the fracture energy during pull-out is due to the work of friction by the interfacial shear stress between the CNFs and the epoxy polymer. During this pull-out process the CNFs also formed a bridging zone behind the crack tip. This is evident from SEM observations of the crack bridging by CNFs, as shown in Figure 3-9. The average length of the CNFs bridging the crack at its maximum opening displacement was about 8 μm. The bridging density of the CNFs decreased with decreasing content of CNFs, with almost no bridging being observed for the 0.1 wt% CNF-epoxy nanocomposite samples. In order to pull-out and bridge the crack, the CNF must firstly debond from the epoxy. The strain energy absorbed in overcoming the adhesion of the epoxy/CNF interface during the debonding process would also increase the fracture energy, but to a lesser extent. If the interfacial bond strength exceeds the strength of the nanofibres, the CNFs would rupture prematurely before pull-out occurred. However, the rupture of the CNFs would result in smaller improvements in the values of the fracture energy, since the strain energy consumed during fibre rupture is reported to be significantly lower than that pertinent to pull-out [85].

Further, a significant number of relatively large voids are present around the CNFs (see Figure 3-8c-f) and are indicative of plastic void growth of the epoxy polymer in the process zone, which leads to an additional increase in the fracture energy, compared to the unmodified epoxy. This arises because in the process zone ahead of the crack tip, where a triaxial stress-field exists, the CNFs debond from the epoxy as the local stresses increase at the crack tip. The debonded CNFs act as voids in the epoxy which allows the polymer to deform plastically, and so the voids increase in size. For rubber- and nanosilica-toughened epoxies, this plastic void growth mechanism has been shown to significantly increase the fracture toughness of the material [99, 119]. Therefore, the aggregate increase in the fracture energy of the epoxy due to the addition of the CNFs is considered to be a combination of the energy dissipated by (a) interfacial debonding of the CNFs from the epoxy, (b) the frictional energy associated with the CNFs now pulling-out from the epoxy, (c) void growth of the epoxy which

initiates from the hole created by the debonded CNFs, and (d) the CNFs bridging and finally rupturing across the crack faces, behind the advancing crack tip.

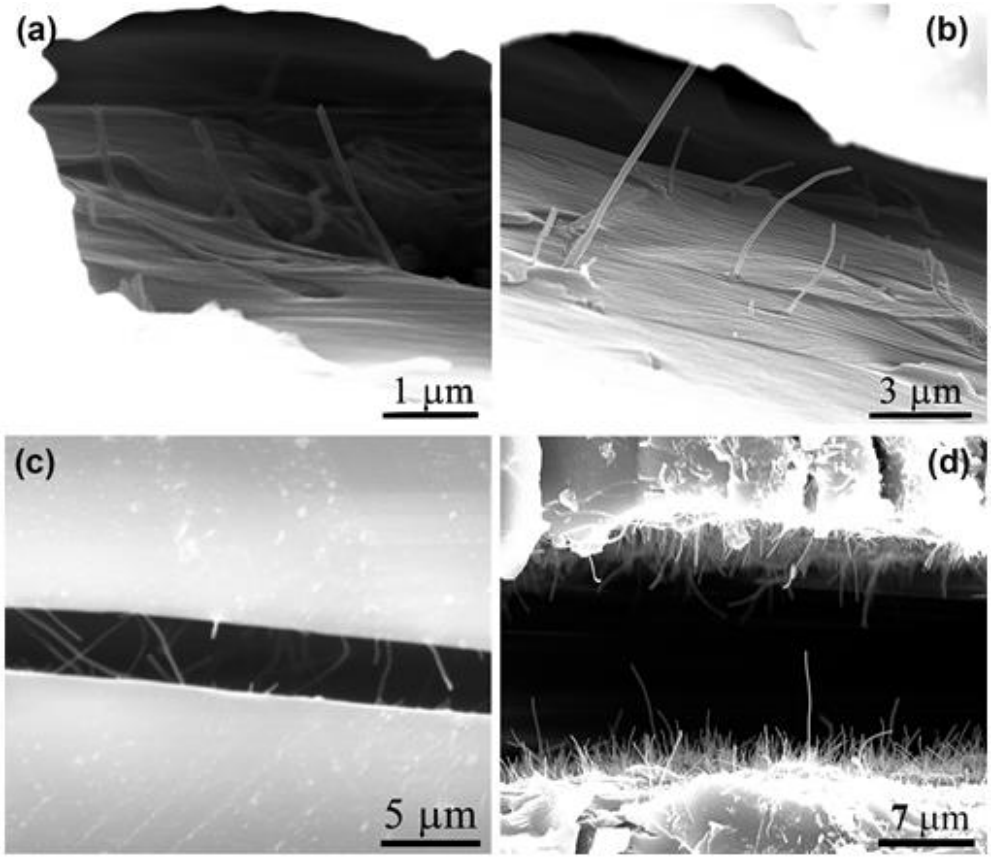

Figure 3-9 : SEM images of CNFs bridging the crack in epoxy nanocomposites. (a) '0.4 random'; (b) '0.4 aligned'; (c) '0.7 random'; and (d) '1.0 aligned'.

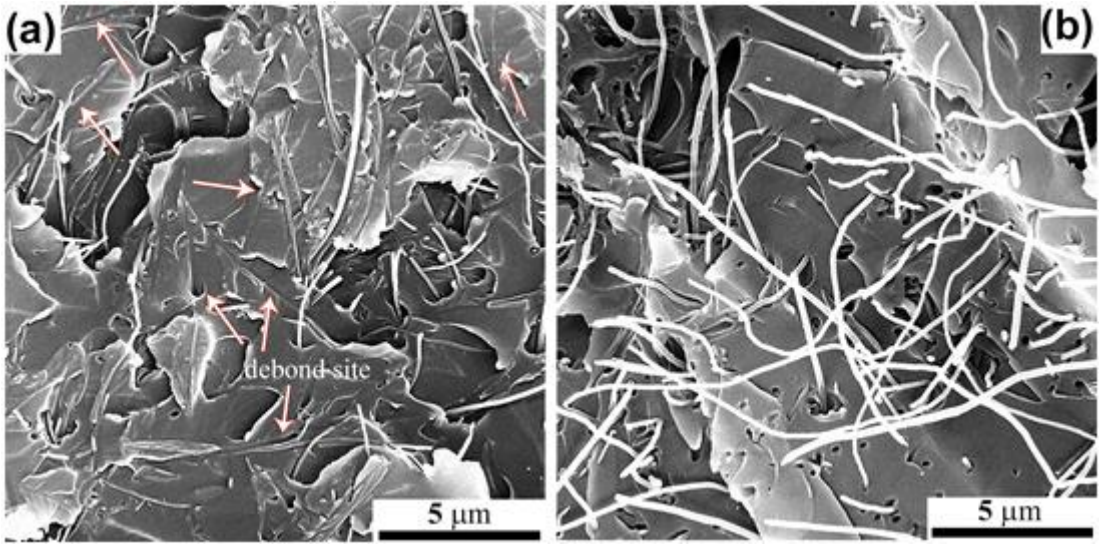

Figure 3-10 : Comparison of the pull-out of CNFs in the epoxy nanocomposites for (a) '1.0 random' and (b) '1.0 aligned' samples.

Considering the alignment of the CNFs perpendicular to the crack path in the nanocomposites, such alignment of the CNFs would lead to a higher fraction of CNFs participating in the above toughening mechanisms. For a random orientation of CNFs in the epoxy, the probability of the crack front encountering the CNFs depends on their orientation angle. For short fibre composites with a random fibre orientation, this probability is given by cosθ (refer to Figure 3-3c for the orientation axes), and for an orientation angle above 60^{o} the probability is less than 50% [41, 218]. This would lead to a lower fraction of CNFs involved in the pull-out, bridging and rupturing mechanisms for the epoxy nanocomposites containing the randomly-oriented CNFs. This is clearly evident for the randomly-oriented materials, as is shown in Figure 3-10a**,** where a greater number of CNFs which were oriented parallel to the crack path have undergone debonding but without participating in the pull-out or void growth toughening mechanisms. While for the aligned epoxy nanocomposites, as shown in Figure 3-10b**,** almost all the CNFs have now undergone debonding and pull-out, and hence lead to the void growth mechanism being operative. In addition, if aligned normal to the direction of crack growth, the CNFs are far more likely to bridge the crack faces and undergo tensile rupture as the crack tip advances, as may be seen from comparing Figure 3-9c and Figure 3-9d.

3.3.4 Theoretical Modelling of the Fracture Energy

As discussed in the previous section, the primary toughening mechanisms in the epoxy nanocomposites based on the fractographic evidence were debonding and pull-out of the CNFs, plastic void growth of the epoxy initiated by the voids formed by the CNFs debonding and the CNFs bridging and finally rupturing across the crack faces behind the advancing crack tip. Assuming the application of continuum mechanics is valid at the nanoscale and the interfacial stress being constant [106, 219], the energy dissipated by fibre pull-out based on the conventional expression from Hull [83] is given by:

$$\Delta G_{\mathrm{pull-out}} = \frac{N_{\mathrm{po}} \pi d_{\mathrm{f}} \tau_{\mathrm{i}} l_{\mathrm{po}}^{2}}{2} \tag{3-2}$$

where l_{po} is the nanofibre pull-out length, d_f is the diameter of the CNF, τ_{i} is the interfacial shear strength and N_{po} is the total number of nanofibres per unit area of crack

surface. N_{po} is related to the volume fraction, V_{fpo}, of CNFs which are pulled-out from the epoxy:

$$N_{\mathrm{po}} = \frac{\text{nanofibre volume}}{\text{volume per nanofibre}} = \frac{l_{\mathrm{f}} V_{\mathrm{fpo}}}{l_{\mathrm{f}} A_{\mathrm{f}}} = \frac{V_{\mathrm{fpo}}}{A_{\mathrm{f}}} \tag{3-3}$$

where A_f is the nanofibre cross-sectional area and l_f is the nanofibre length. For a given weight fraction of CNFs in the epoxy, not all of the CNFs are involved in the pull-out process. Therefore, the volume fraction of CNFs pulled-out from the epoxy V_{fpo} has been determined by counting from the SEM micrographs the number of CNFs on the fracture surface. A total of sixteen SEM micrographs were used per sample type to determine the CNF pull-out volume fraction. Previous studies have successfully demonstrated the use of a similar approach to analytically calculate the strength [220] and toughness [106] of CNT containing polymer composites. (Note: the CNF pull-out count from the fracture surfaces also includes the voids left behind by the CNFs pulled-out onto the opposite crack face). Substituting Eq. (3-3) into (3-2) gives:

$$\Delta G_{\mathrm{pull-out}} = \frac{2 V_{\mathrm{fpo}} \tau_{\mathrm{i}} l_{\mathrm{po}}^2}{d_{\mathrm{f}}} \tag{3-4}$$

The CNF pull-out length is difficult to determine with accuracy from SEM images of the fracture surfaces, particularly for samples with a relatively high volume fraction of CNFs. Also, relatively long CNFs are expected to rupture at the crack plane, since their embedded lengths on either side of the crack plane are long enough for the stress in the CNF to build up sufficiently to break them. Two outcomes are possible depending on the length of the embedded CNFs: (a) the CNFs pull-out when the length is shorter than the critical length given by the classical Kelly-Tyson [71] formula i.e. $L_c = \sigma_f d_f / 2\tau_i$, or (b) the CNFs rupture when their length is longer than the critical length. The longest possible pull-out length of the CNFs is equal to half the critical length of the CNFs embedded in the nanocomposites as given by the Kelly-Tyson formula:

$$l_{\mathrm{po}} = \frac{\sigma_{\mathrm{f}} d_{\mathrm{f}}}{4 \tau_{\mathrm{i}}} \tag{3-5}$$

where σ_f is the nanofibre strength. Substituting Eq. (3-5) into (3-4) gives the estimate of the pull-out energy in terms of the inherent properties of the nanocomposite as follows:

$$\Delta G_{\text{pull-out}} = \frac{V_{\text{fpo}} \sigma_{\text{f}}^2 d_{\text{f}}}{8\tau_{\text{i}}} \tag{3-6}$$

A wide range of values for the interfacial shear strength between CNFs and epoxies have been reported in the literature [221, 222]. However, the maximum possible interface strength between the epoxy and CNFs is limited by the shear strength of the epoxy polymer. From Table 3-1 the shear strength of the epoxy polymer may be taken to be half that of the tensile yield strength using Tresca yield criterion, giving a value of 25 MPa. This value is used to estimate the contribution to the fracture energy from pull-out of the CNFs.

The contribution to the fracture energy due to CNF bridging is from the energy required to pull-out the bridging CNFs from the epoxy, and is therefore accounted by $\Delta G_{\text{pull-out}}$ [85]. Whereas, the energy contribution due to the elastic deformation of the CNFs prior to rupturing, whether in the plastic zone ahead of the crack tip or in its wake, is given by [41]:

$$\Delta G_{\text{rupture}} = \frac{V_{\text{fpo}} \sigma_{\text{f}} \, l_{\text{f}} \, \varepsilon_{\text{max}}}{2} = \frac{V_{\text{fpo}} \sigma_{\text{f}}^2 \, l_{\text{f}}}{2 \, E_{\text{f}}} \tag{3-7}$$

where E_{f} and ε_{max} are the Young's modulus and the tensile failure strain of the CNFs, respectively.

The CNFs undergo debonding prior to the pull-out process. The interfacial debonding of the CNFs is an essential process because it allows them to pull-out and initiates the occurrence of plastic void growth of the epoxy around the hole so created. The interfacial debonding energy, ΔG_{db}, is given by [83, 106]:

$$\Delta G_{\text{db}} = \frac{V_{\text{f}} l_{\text{po}} G_{\text{i}}}{d_{\text{f}}} \tag{3-8}$$

where G_{i} is the interfacial fracture energy between the CNFs and the epoxy. Ozkan et. al. [222] measured the interfacial fracture energy between CNFs and an epoxy polymeric matrix to be 3.3 J/m^2, and this value was used in the present study.

In addition to the CNF pull-out mechanism, the plastic void growth of the epoxy matrix promoted by debonding of CNFs from the epoxy matrix would further

increase the fracture energy. In previous studies [119, 124], the plastic void growth mechanism was quantitatively shown to significantly improve the fracture toughness of a nanosilica modified epoxy polymer. Huang and Kinloch [223] have shown that the fracture energy, ΔG_v, contribution from the plastic void growth mechanism can be calculated as follows:

$$\Delta G_{\mathrm{v}} = \left(1 + \frac{\mu_{\mathrm{m}}}{\sqrt{3}}\right)^2 (V_{\mathrm{void}} - V_{\mathrm{fpo}}) \sigma_{\mathrm{y}} r_{\mathrm{yu}} K_{\mathrm{vm}}^2 \tag{3-9}$$

where V_{void} is the volume fraction of the voids and μ_m is a material constant allowing for the pressure dependency of the yield stress. The parameter K_{vm} is the maximum stress concentration for the von Mises stresses around a debonded CNF, which lies between 2.11 and 2.12 [106]. The parameters σ_y and r_{yu} are respectively the tensile yield stress and the plastic zone size at fracture of the unmodified epoxy. The plastic zone size is given by:

$$r_{\mathrm{yu}} = \frac{1}{6\pi} \frac{E_{\mathrm{m}} G_{\mathrm{CU}}}{(1-\nu^2)\sigma_{\mathrm{y}}^2} \tag{3-10}$$

where G_{cu} is the fracture energy, E_m is the tensile modulus and v is the Poisson's ratio of the unmodified epoxy polymer. Each void is assumed to be a truncated cone with the smaller diameter equal to the diameter of the CNFs and the larger void diameter is determined from the SEM micrographs which have a varying distribution depending on the size of the CNFs. In the present study the void diameter was estimated from SEM micrographs to be approximately seven times the diameter of the CNFs around which the voids are formed. Therefore, the fracture energy, G_{Ic}, of the CNF toughened epoxy can be expressed as:

$$G_{\mathrm{Ic}} = G_{\mathrm{CU}} + \Delta G_{\mathrm{rupture}} + \Delta G_{\mathrm{pull-out}} + \Delta G_{\mathrm{db}} + \Delta G_{\mathrm{v}} \tag{3-11}$$

The above model is used to estimate the fracture energy improvement by considering an average CNF diameter equal to 135 nm as supplied by the manufacturer [53]. However, the energy contributions due to CNF pull-out, debonding and epoxy void growth depend strongly on the diameter of the nanofibres. The probability distribution of the CNF diameter is shown in Figure 3-2c**.** The 135 nm diameter value provided by the manufacturer corresponds to the median of this distribution. By accounting for the

distribution of the CNF diameter, the total fracture energy can be expressed in terms of the diameter probability function, $\rho(d_f)$:

$$G_{Ic} = G_{CU} + \Delta G_{rupture} + \int_{d_{min}}^{d_{max}} (\Delta G_{pull-out} + \Delta G_{db} + \Delta G_v)\, \rho(d_f)\, \mathrm{d}d_f \qquad (3\text{-}12)$$

$\Delta G_{rupture}$ is not dependent on the CNF diameter as can be seen from Eq 7. The fracture energy modelling results are calculated from the experimentally determined values of V_{fpo} for the random and aligned nanocomposite, apart from the '1.6 aligned' nanocomposite. However, for the nanocomposite with 1.6 wt% CNFs, it is difficult to determine the total number of CNFs pulled out on the crack surface due to their relatively high concentration. Therefore, the fracture energy is also modelled from the total volume fraction, V_f of the CNFs in the epoxy nanocomposites for comparison with the results obtained from the experimentally determined V_{fpo}. By assuming that all the CNFs in a unit volume of epoxy are intersected by the advancing crack, the V_f is estimated from the CNF weight fraction by considering the graphitic CNF wall density to be 1400 kg/m^3 [224]. The values of all the input parameters used to calculate the fracture energy of the epoxy polymers containing the CNFs are given in Table 3-1 and Table 3-2.

Table 3-1 : List of values for the various parameters used in the analytical modelling study.

Parameter	**Symbol**	**Unit**	**Value**	**Source**
CNF diameter	d_f	nm	135	[224]
CNF average length after dispersion	l_f	μm	20	This study
CNF strength	σ_f	GPa	8.7	[224]
Young's modulus of the CNF	E_f	GPa	320	[225]
Density of the CNF	ρ_f	kg/m^3	1400	[224]
Density of unmodified epoxy	ρ_m	kg/m^3	1011	[226]
CNF/epoxy interface fracture energy	G_i	J/m^2	3.3	[222]
Tensile yield strength of unmodified epoxy	σ_y	MPa	50.5	[226]
Young's modulus of unmodified epoxy	E_m	GPa	3.17	[226]
Pressure dependent yield stress constant	μ_m	-	0.2	[223]
Maximum von Mises stress concentration	K_{vm}	-	2.11	[106]

Table 3-2 : Measured values of the volume fraction, V_{fpo}, of CNFs which are pulled-out from the epoxy and the volume fraction, V_{void}, of the voids formed around the debonded CNFs.

CNFs (wt%)	V_f (%)	V_{fpo} (%)		V_{void} (%)	
		Aligned	Random	Aligned	Random
0.1	0.08	0.02	0.01	0.32	0.23
0.4	0.33	0.23	0.18	3.99	3.34
0.7	0.58	0.53	0.43	9.39	8.12
1.0	0.82	0.78	0.63	13.76	11.91
1.6	1.31	-	-	-	-

3.3.5 Results of theoretical models

Figure 3-11 shows the results from the theoretical modelling studies compared to the experimentally measured values of G_{Ic}. The figure shows two curves calculated using the model assuming that the CNFs have the mean diameter (Eq. 3-11) or the diameter varies according to the probability density function (Eq. 3-12). The toughness values are slightly higher when it is assumed that all the CNFs have the same (mean) diameter. Good agreement can be seen between the experimental results and the predicted fracture energies which supports the primary toughening mechanisms which have been proposed for the epoxy polymers modified using randomly-oriented or aligned CNFs. The CNF pull-out and the epoxy void growth were the two most dominant toughening mechanisms, accounting for the majority of the fracture energy enhancement for all the epoxy nanocomposites. Table 3-3 shows a comparison of the highest fracture toughness improvements that have been reported in the literature for CNT and CNF modified epoxies against the nanocomposites studied here. It is noteworthy that the toughness improvements achieved in the present study are many times higher than those reported previously. These variations in the enhancement of the fracture energy may be mainly explained by the differences in the length of the CNFs, and its effect on the fracture energy due to pull-out of the CNFs as given by Eq. (3-4). For example, if the CNF length is reduced to 6 μm, as was the case in the study by Palmeri et al. [112], the fracture energy due to pull-out will be greatly reduced. In order to obtain a better estimate for such an effect, and for the purpose of comparison between the two studies, it has been assumed that the volume fraction of CNFs that are pulled-out is only

dependent on the content of CNFs and is independent of the length. On this basis, for the 0.7 wt% of random CNF nanocomposite studied by Palmeri et al. [112], assuming that all the modelling parameters (besides the value of the nanofibre length, $l_{f,}$) are similar in value to those used in the present work, the expected improvement in the value of the fracture energy, as given by Eq. (3-11) with a CNF length equal to 6 μm, would be about 116 %. This is very similar to the measured improvement reported in their study, see Table 3-3.

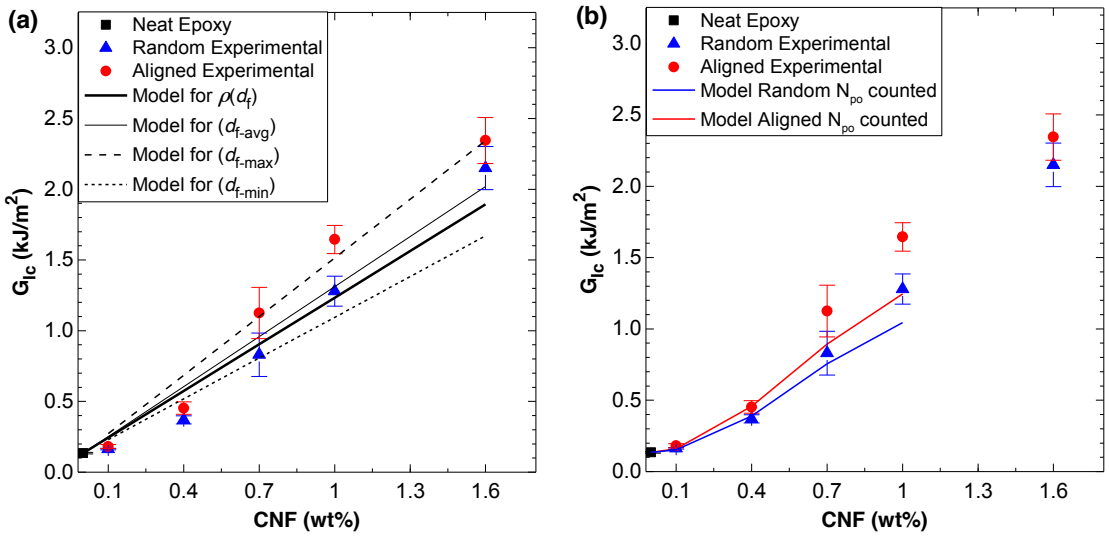

Figure 3-11 : Comparison of the experimental and theoretically calculated fracture energies as a function of the concentration of CNFs. (a) Model calculations based on total volume fraction (V_{fpo} = V_f) using minimum, mean, maximum, and probabilistic distribution of the CNF diameter; and (b) model calculations based on the experimentally measured V_{fpo} for random- and aligned-CNF nanocomposites.

The improvements in the fracture energy of epoxy polymer containing CNFs reported in some other studies can be similarly estimated and the data are given in Table 3-4. Using Eq. (3-11) or (3-12) and the relevant data in Table 3-1 and Table 3-4, the proposed model gives a reasonable estimate for the measured values of G_{Ic} reported previously in the literature, as may be seen from Table 3-3. It is also clear that the improvement in the fracture energy of the epoxy due to the addition of the CNFs or CNTs is strongly dependent on the dimensions of the nano-reinforcement, especially the fibre length. Thus, the use of longer CNFs, as in the present study, would indeed be expected to lead a better enhancement in the fracture energy of the epoxy nanocomposites.

Table 3-3 : Fracture toughness, G_{Ic}, values of epoxy polymers toughened with 1-D carbon nano-reinforcements.

Source	**Nano-reinforcement**	**Content** (wt%)	**Improvement** (%)	**Model Prediction** (%)
The present study	CNFs-Random	1.6	1500	1410
	CNFs-Random	1.0	850	880
	CNFs-Random	0.7	500	610
	CNFs-Random	0.4	180	350
Tang et al. [109]	MWCNTs	1.0	130	-
Palmeri et al. [112]	CNFs	0.68	113	95
Liu et al. [227]	CNFs	0.4	80	140
Hsieh et al. [223]	CNTs	0.5	70	60

Table 3-4 : Parameters used to calculate the fracture energy improvement in Table 3-3 using the theoretical model from Section 3.5 for the different studies from the literature.

Source	**Nano-reinforcement**	τ_i (MPa)	l_f (μm)	d_f (nm)
Palmeri et al. [112]	CNFs	36	6	135
Liu et al. [227]	CNFs	36	20	135
Hsieh et al. [223]	CNTs	47	120	120

3.4 Conclusions

The fracture energy of a thermoset epoxy polymer modified by the addition of carbon nanofibres (CNFs) has been investigated. The CNFs were dispersed in a liquid epoxy resin using a surfactant and then processed employing a three-roll mill to give a good degree of dispersion with the majority of the CNFs having lengths of between 16 to 24 μm. An AC electric-field has been found to be very effective in creating aligned CNFs, with a chain-like structure, in the epoxy resin with the majority of the CNFs lying within ± 10^0 of the applied electric-field. After alignment of the CNFs, the epoxy resin

was cured to give an epoxy polymer nanocomposite. The alignment of 0.4 wt% of CNFs in the epoxy nanocomposite resulted in an increase in the average fracture energy, G_{Ic}, from 134 J/m^2 to 453 J/m^2, compared to the unmodified epoxy polymer. The highest increase in toughness was for the epoxy nanocomposites which contained 1.6 wt% of aligned CNFs. The fracture energy of this nanocomposite was increased by about 1600% from 134 to 2345 J/m^2 and its electrical conductivity was seven orders of magnitude higher than that of the unmodified epoxy polymer. There were significant benefits of using the aligned CNFs in the epoxy nanocomposites compared to using only randomly-oriented CNFs. For example, at a content of 1.0 wt% of CNFs, the aligned CNFs in the epoxy nanocomposites resulted in a 27% increase in the fracture energy measured in the optimum directions, compared to the nanocomposites containing the randomly-oriented CNFs. The main toughening mechanisms which led to the increase in the fracture energy for the nanocomposites were identified to be (a) interfacial debonding of the CNFs from the epoxy, (b) the energy associated with the CNFs now pulling-out from the epoxy, (c) void growth of the epoxy which initiates from the hole created by the debonded CNFs, and (d) the CNFs bridging and finally rupturing across the crack faces, behind the advancing crack tip. Considering the alignment of the CNFs perpendicular to the crack path in the nanocomposites, such alignment of the CNFs led to a higher fraction of CNFs participating in the above toughening mechanisms, and thus accounted for the relatively higher values of G_{Ic} measured for these nanocomposites, compared to those containing randomly-oriented CNFs.

Chapter 4

Improving the Fracture Toughness of Epoxy Composites using Aligned Graphene Nanoplatelets

Abstract

In this chapter, the effects of the alignment of graphene nanoplatelets (GNPs) using an alternating current (AC) electric-field on the fracture toughness of GNP-reinforced epoxy composites are investigated. Compared to neat resin, the electric-field induced alignment and the formation of chain-like microstructure produced nearly nine fold increase in the fracture energy (G_{IC}) of the nanocomposites. A further enhancement in the fracture energy of about 30% was observed for the epoxy nanocomposites reinforced with aligned GNPs. Examination of the fracture surfaces reveals several toughening mechanisms attributing to the dramatic increase in fracture toughness, including crack pinning, rupture, debonding and pull-out of GNPs, crack bridging by GNPs, microcracks formation, and crack deflection.

The research presented in this chapter has been published in the following journal and conference papers:

- Wu S, Ladani RB, Zhang J, Bafekrpour E, Ghorbani K, Mouritz AP, Kinloch AJ, Wang CH. *Aligning multilayer graphene flakes with an external electric field to improve multifunctional properties of epoxy nanocomposites*. Carbon. 2015; 94:607-618.
  The open access journal article from Carbon is attached in Appendix A.II.

- Wang CH, Ladani RB, Wu S, Kinloch AJ, Zhang J, Ghorbani K, Mouritz AP. *Epoxy Nanocomposites with Aligned Carbon Nanofillers by External Electric Fields*. In Proceeding of the 26th International Conference on Composite Materials, Copenhagen, Denmark, 2015.

4.1 Introduction

Graphene shows great promise as a nano-reinforcement in polymer composites due to its unique structure, exceptional mechanical properties, and excellent thermal and electric conductivities [228, 229]. Due to the high aspect ratio of graphene nanosheets, substantial property improvements can be achieved even at small loadings [116, 230, 231]. From Table 2-1 is can be seen that for a low weight fraction GNP reinforcement, the level of improvement to the fracture toughness of epoxy nanocomposites is twice of what has been achieved with any type of CNT or CNF reinforcements. Rafiee and co-workers [103] compared the mechanical properties of epoxy nanocomposites with 0.1 wt% of graphene, sing-wall carbon nanotubes, and multi-walled carbon nanotubes. It was demonstrated that graphene significantly out-performed other carbon nano-reinforcements with 53% increase in mode I fracture toughness [103]. By varying the content of the graphene nano-reinforcement, they also found that enhancement of fracture toughness peaked at 0.125 wt% with a 115% increase [230].

The results in Chapter 3 shows that there are additional benefits of using aligned CNFs to improve the fracture toughness and electrical conductivity of epoxy composites. Although, several studies have reported the use of electric-field to align carbon nanotube [51], carbon nanofibres [52], and carbon black [232] to improve the electric conductivity and mechanical properties of their composites. Very limited research has been done on investigating the alignment of graphene nanoplatelets in polymer and its effects on the electric and fracture properties. For instance, Kim *et al*. [48, 177] developed epoxy composites with graphite aligning in the electric-field direction and demonstrated that aligned graphite composites showed anisotropic mechanical properties but thermal expansion response is essentially isotropic. Chen *et al*. [47, 49, 50] prepared polyester resin composites with graphite nanosheets orienting along the applied AC electric-field and found that anisotropic electric properties were achieved. In spite of these studies, the effects of electric-field-induced alignment of the graphene on the fracture properties of its composites remain an important open question in polymer composites.

In this chapter, an AC electric-field was applied across the liquid epoxy mixtures with graphene nanoplatelets (GNPs) during curing, producing a

nanocomposite with aligned GNPs, aiming to improve their fracture toughness. The electric-field-induced orientation and assembly were examined by using electron microscopy and in-situ optical microscopy. The properties of epoxy nanocomposites with both randomly oriented and aligned GNPs were investigated. To study the toughening effects, the GNP-epoxy composites were applied as the adhesive layer sandwiched between carbon fibre composite adherends, which also serve as the electrodes, in the form of bonded joints. GNPs were aligned in the epoxy adhesive layer along the electric-field direction normal to the bond surface. Fractographs were collected, based on which toughening mechanisms were proposed.

4.2 Materials and Experimental Methodology

Materials

The graphene nanoplatelets (GNPs) used in this study were obtained from XG Science, having an average thickness of approximately 6 to 8 nanometres and an average particle diameter of 25 μm. The C:O ratio was determined to be 93:7 by using X-ray photoelectron spectroscopy (XPS) performed on a Thermo K-alpha XPS instrument. The epoxy resin used is a liquid blend of bisphenol A and bisphenol F ('105' from West System) and slow hardener ('206' from West system; a blend of aliphatic amines and aliphatic amine adducts based on diethylene triamine and triethylenetetramine). The composite adherends were manufactured from T700 carbon fibre/epoxy prepreg (VTM 264) supplied by Applied Composites Group. 12 plies of this unidirectional prepreg with dimension of 300 mm × 250 mm × 2.65 mm were used to fabricate the adherends by curing in an autoclave at 120 ^{o}C for 1h as recommended by the manufacturer.

DCB joint manufacturing and testing

DCB joints were fabricated to study the fracture energy of epoxy nanocomposites containing 0.5, 1.0, 1.5 and 2.0 wt% of random and aligned GNPs in accordance to the procedure described in Chapter 3. The details of the fabrication process and DCB testing procedure are outlined in section 3.2. However, the dispersion of the GNPs in

the epoxy resin was achieved by combining sonication and calendaring. An appropriate amount of GNPs were first mixed with epoxy resin using a Hielscher UP200S ultrasonic homogenizer (0.5 cycles and 50% amplitude) for 30 min, which can break up the graphene agglomerates. The mixture was further processed by passing through a three-roll mill (Dermamill 100) 10 times at 150 rpm with roller gap distances of 20 μm. After the dispersion process, a stoichiometric amount of curing agent was added to the mixture of epoxy/GNPs and stirred using a mechanical stirrer at 200 rpm for 5 min. The mixture was then degassed in a chamber for ~10 min. Finally, this mixture was used as an adhesive layer to bond carbon fibre-epoxy composite laminate to form DCB specimen for fracture toughness testing. Leica optical microscope were used to observe the response of GNPs to the AC electric-field using a setup similar to that described earlier in section 3.2.

4.3 Results and Discussion

4.3.1 Electric-field Directed Orientation and Assembly of GNPs

In this work, in-situ optical microscopy was employed to investigate the response of GNPs to an AC electric-field with amplitude of 25 V/mm at 10kHz. Optical micrographs of the specimen were taken every 30s with some images shown in Figure 4-1. Within 2 minutes of the application of the electric-field, the GNPs were observed to rotate and align along the direction of the external field. Well-defined chain-like structure was observed upon applying the electric-field for 10 min which turned into thick bundles with further application of electric-field. Similar observations have been reported by other researchers who studied CNTs [44, 150, 161] or carbon black [232] systems. When subjected to an electric-field, an inclusion in a dielectric liquid is polarized and gains dipole moment due to the different dielectric properties and electrical conductivity between the inclusions and liquid [48]. The polarization moment is generally not aligned with the electric-field for materials showing crystalline or shape anisotropy and thus a torque is induced acting on the inclusions. Two-dimensional graphene nanoplatelets (GNPs) have shape anisotropy and the polarization parallel to the platelet is much higher than that perpendicular to it.

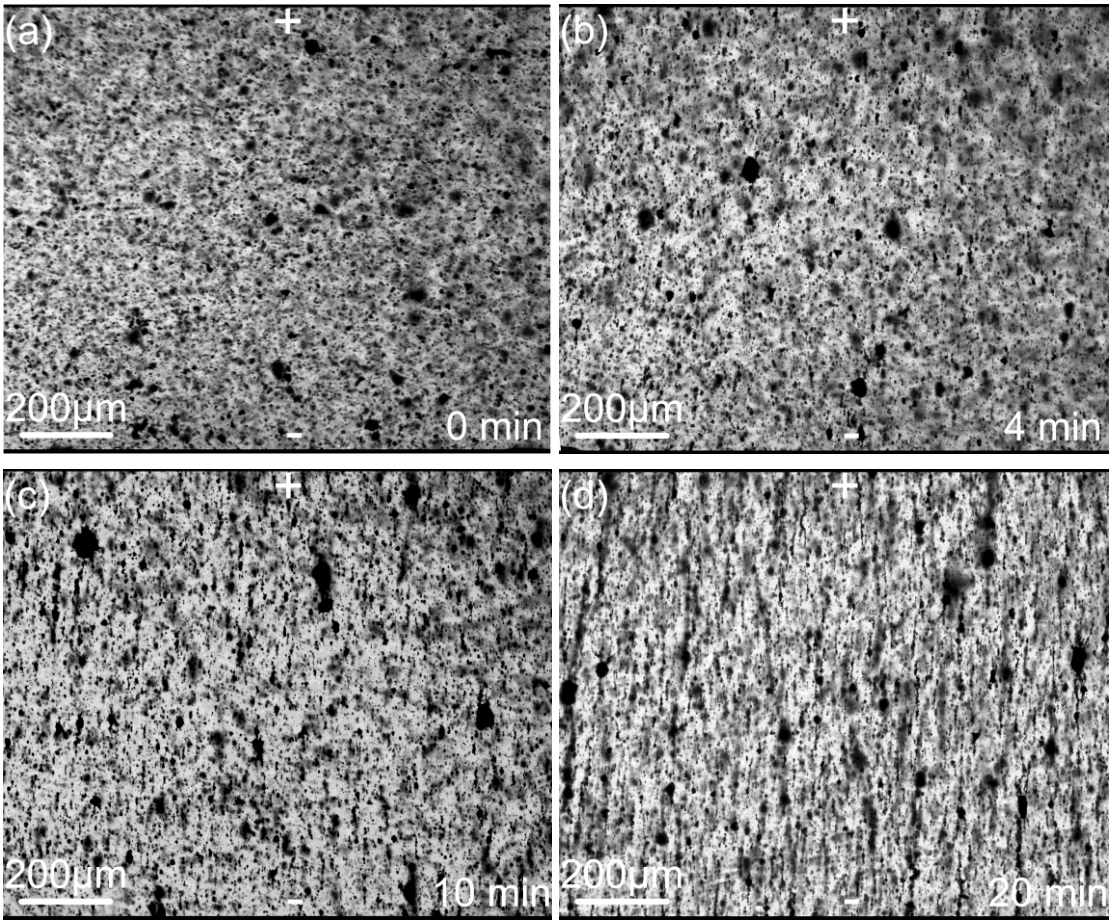

Figure 4-1 : Optical micrographs of GNPs in the liquid epoxy resin (at a content of 0.2 wt%) during the application of the AC electric-field (25 V/mm): (a) Randomly-oriented GNPs before the field was applied; (b), (c), and (d) after the field was applied for 4 minutes, 10 minutes and 20 minutes, respectively.

The overall torque acting on an inclusion is the superposition of the torques induced by fields parallel and perpendicular to its axes. The electric-field-induced force is the driving force for the orientation of the GNPs against the viscous drag of the epoxy resin along the electric-field. Dipole-dipole attraction is another important phenomenon when exposed to an external electric-field. Once the polarized inclusions are oriented along the field direction, they interact with each other as dipoles. Due to the opposite charges at their edges, they gradually move closer and connect head-to-head, forming chain-like structures [233]. Other fillers such as carbon nanotube [51], carbon nanofibres [52], and carbon black [232] carbon nanocones [234], graphite nanosheets [47, 49, 50] *etc*. are found to form a network and create chain-like structure from one electrode to the other.

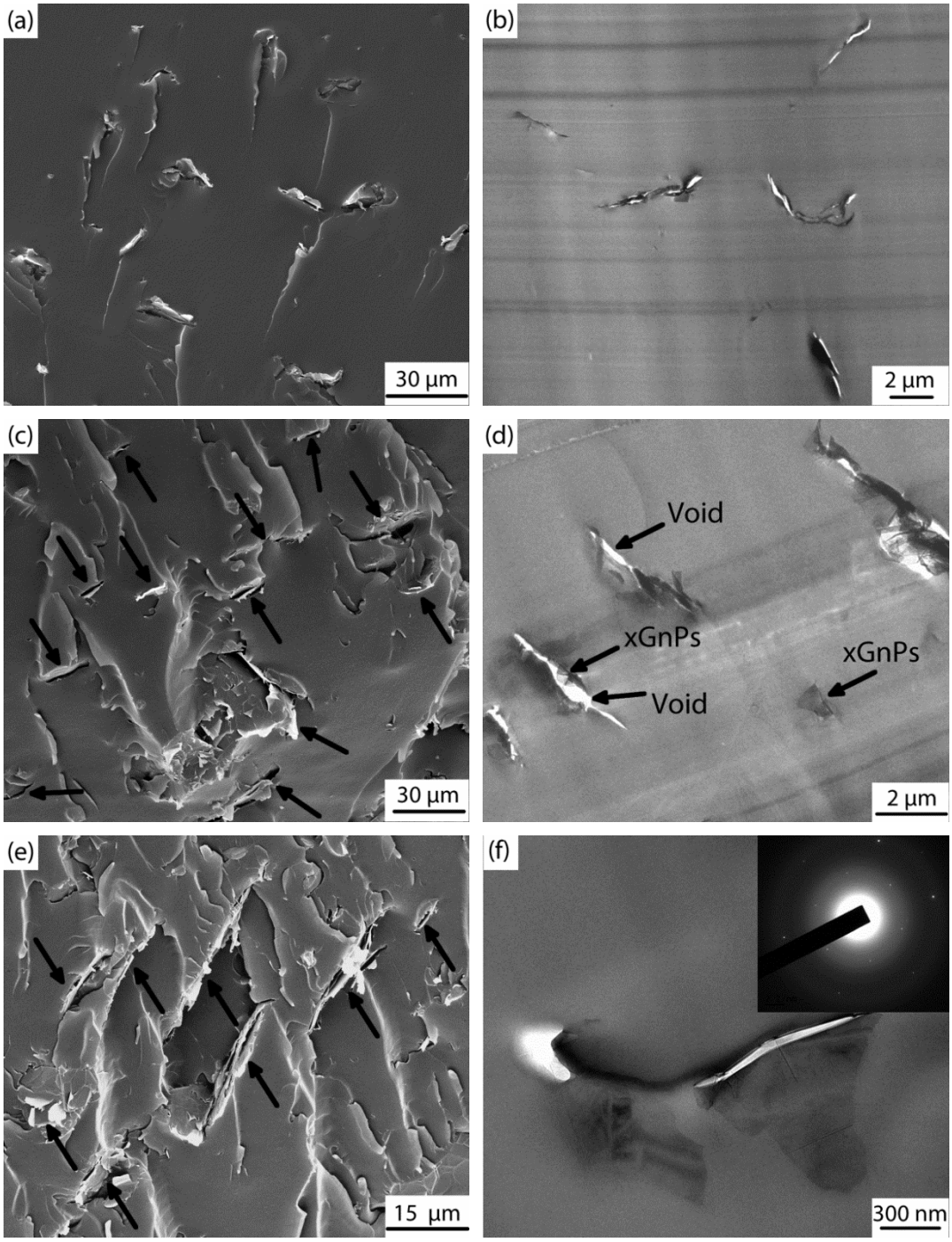

Figure 4-2 : SEM (a) and TEM (b) images of epoxy nanocomposites with randomly orientated GNPs; SEM (c) & (e) and TEM (d) & (f) images of epoxy nanocomposites with orientated GNPs taken at different magnification. The insert in (f) is SAED pattern of the graphene nanoplatelets in (f).

Figure 4-2a and b show the SEM and TEM images of 1 wt% GNP-epoxy nanocomposites prepared in the absence of an electric-field. No alignment features was revealed and GNPs was randomly oriented in epoxy matrix. However, in the case of the

GNP-epoxy nanocomposites prepared under an electric-field, it is clearly observed that the GNPs have oriented along the direction of the electric-field (see Figure 4-2c, d and e). As illustrated in Figure 4-2c and e, graphene nanoplatelets are oriented parallel to the electric-field**.** For TEM investigation, voids, separately dispersed graphene nanoplatelets, and multi-layered graphene nanoplatelets are observed, as indicated by arrows in Figure 4-2d. The diamond knife used in ultramicrotoming for TEM specimen preparation usually induced high stress. The multi-layered GNPs normally would delaminate or slip by each other under such high stress, resulting in voids which were also reported by other researchers [115, 235]. SAED (selected area electron diffraction) was employed to distinguish GNPs from amorphous epoxy matrix and Figure 4-2f gives an example. Well-defined spot pattern was obtained from the region next to the void indicating the presence of crystalline GNPs. By contrast, a diffuse diffraction ring pattern (not shown here) typical of a disordered structure was obtained from the region far away from the void. It should be noted that only a small number of GNPs can be seen within an image due to the high magnification both for SEM and TEM investigation.

4.3.2 Fracture toughness

The effects of electric-field-induced alignment of graphene nanoplatelets on the toughening in epoxy were investigated using mode I double cantilever beam specimens in the form of epoxy bonded joints. All DCB specimens showed cohesive failure within the adhesive layer. Figure 4-3 gives the representative load-displacement curves of GNP-epoxy nanocomposites with 0.5 and 2.0 wt% GNPs contents. The GNP-epoxy nanocomposites with 0.5 and 1.0 wt% GNPs exhibited a stick-slip crack growth behaviour, which was similar to the fracture behaviour of the unmodified epoxy. This was evident from the “saw-tooth” shaped load-displacement curves obtained for the samples containing 0.5 and 1.0 wt% GNPs (see Figure 4-3a). The sudden load drops correspond to the unstable crack growth of size ~ 10-30 mm. In comparison, the GNP-epoxy nanocomposites containing 1.5 and 2.0 wt% GNPs exhibited a more stable fracture behaviour with much smaller crack growth of ~ 3-5 mm.

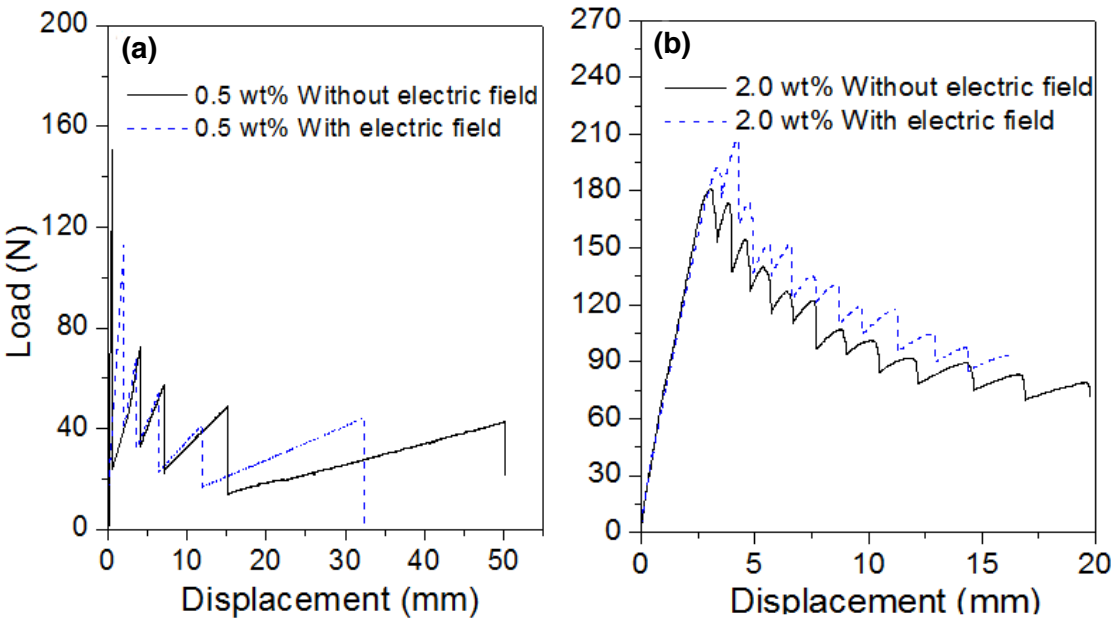

Figure 4-3 : Load versus displacement curves for the randomly-oriented or aligned GNP-epoxy nanocomposites containing (a) 0.5 wt% and (b) 2.0 wt% GNPs.

Figure 4-4 shows the strain energy release rate (G_{IC}) of epoxy nanocomposites with different GNPs contents, prepared without and with application of the electric-field. It can be seen that the fracture toughness significantly increased with the addition of GNPs. The neat epoxy showed G_{IC} at ~ 134 J/m^2, which increased to ~380 J/m^2 with the addition of 0.5 wt% of GNPs. Adding 1 wt% of GNPs brought about nearly 5-fold increase (~800 J/m^2) in the fracture toughness, which further increased to ~ 1050 J/m^2 when the concentration of GNPs was increased to 2.0 wt%. The application of an electric-field further improved the fracture toughness. The epoxy nanocomposites with 0.5, 1.0, 1.5 wt% of GNPs prepared under electric-field showed ~ 40% improvement compared with those prepared without applying an electric-field whereas only ~ 6% improvement was observed at higher concentration (2.0 wt%). The decline in fracture toughness improvement efficiency may be ascribed to the reduced degree of orientation and the deteriorating agglomeration at higher GNPs concentrations.

For comparison, maximum G_{IC} and K_{IC} (critical-stress-intensity factor) values of several GNP-epoxy nanocomposites in the literature were summarized in Table 4-1. Due to the large variations of the G_{IC} values, the increment of fracture toughness compared to the neat epoxy is given here.

Table 4-1 : Summary of the toughness and the toughening mechanisms in several epoxy/graphene nanocomposites as reported in the literature.

Filler		**Fracture test**[a]	**Maximum G_{Ic} increment**[b]	**Maximum K_{Ic}**[c] **increment**[b]	**Ref.**
GNPs	Randomly-oriented	DCB	684 % (2 wt%)		The present work.
	Aligned		891 % (1.5 wt%)		
Jeffamine/Araldite-F modified graphene		CT	597% (0.5 wt%)		[236]
Graphene foam		SENB		70% (0.1 wt%)	[237]
4,4'-diaminophenylsulfone modified graphene		CT	196% (1 wt%)	116% (1 wt%)	[115]
Thermally reduced GO		CT		52% (0.2 wt%)	[235]
Poly(butadiene acrylonitrile) modified graphene oxide (GO)		CT	140% (0.04 wt%)		[238]
Thermally expanded GO		CT	115% (0.125 wt%)		[230]
Graphite nanoplatelets		SENB		50% (1.0 wt%)	[239, 240]
Thermally reduced GO				40% (0.5 wt%)	
GO		SENB	111% (1 wt%)		[114]
4,4'-methylene diphenyl disocyanate modified graphene		CT	200% (4 wt%)		[116]
GO		SENB		75% (0.1 wt%)	[241]

[a)]Fracture tests: DCB (double cantilever beam) test; CT (compact tension); SENB (single-edge notch bending).

[b)]The value in brackets states the content of the graphene-based nano-reinforcement.

[c)]K_{Ic} is the critical value of the stress-intensity factor for fracture.

The best reported enhancement in G_{IC} is 597 % with 0.5 wt% of graphene platelets chemically modified by a surfactant followed with further modification by diglycidyl ether of bisphenol A [236]. The corresponding performance of GNP-epoxy nanocomposites presented here was among the best especially those prepared under electric-field with aligned GNPs.

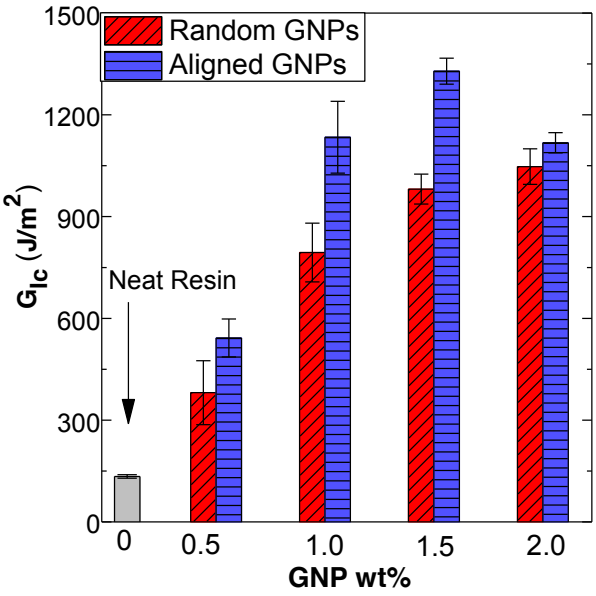

Figure 4-4 : The mode I fracture energy of the neat epoxy and its GNPs nanocomposites prepared without and with applying an electric-field.

4.3.3 Fractography

Examination of the fracture surfaces of the DCB samples gave an insight into the toughening mechanisms responsible for the improvements in the fracture energy of the epoxy nanocomposites. A typical featureless and smooth fracture surface was observed for the unmodified epoxy which was indicative of a very brittle fracture. Figure 4-5a shows a photograph of the fracture surface for a nanocomposite sample where the regions of crack initiation and arrest are visible as curved lines across the width of the sample. There is a distinct whitening of the polymer along these crack initiation/arrest lines. Figure 4-5b shows SEM image of these regions revealing a pattern of tear marks, which provides evidence of plastic deformation of the epoxy polymer along the line of crack initiation. The severity of the tear marks increased with the GNPs content in the epoxy. In comparison, the patterns of tear marks was less sever in the regions where rapid crack propagation had occurred.

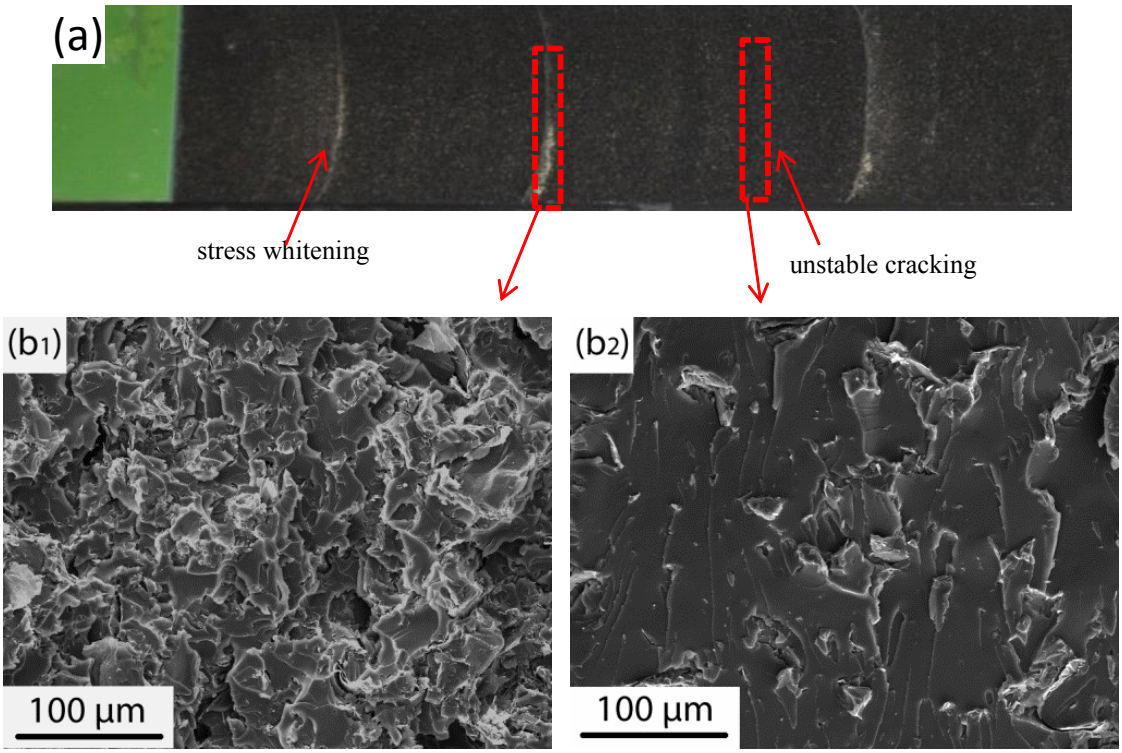

Figure 4-5 : (a) Fracture surface of DCB specimen bonded with aligned GNP-epoxy composites (1.0 wt%); SEM image of (b_1) the stress-whitened and (b_2) crack propagation area.

The fracture and toughening processes induced by the presence of the GNPs are shown in Figure 4-6 and Figure 4-7. Discrete microcracks (typically of the size of the GNPs, i.e. 10–25 µm long) were created immediately ahead of the main crack within the nanocomposites (see Figure 4-6b). The microcracks initiated at the epoxy/GNPs interfaces due to the stress concentrations created by the mismatch in the Young's modulus and Poisson's ratio of the graphene and the epoxy polymer. In addition, as evidenced in Figure 4-7, microcracks also developed due to delamination between the nanosheets within the GNPs and interfacial debonding of the GNPs from the epoxy polymer matrix. This indicates the relatively weak bonding between the graphene sheets and at the epoxy-graphene interface that occurs when GNPs are used without any functionalisation. The formation of microcracks ahead of the main crack is an intrinsic toughening mechanism which increases the fracture resistance of low toughness materials [12], and this would account, in part, for the higher toughness of the epoxy nanocomposites.

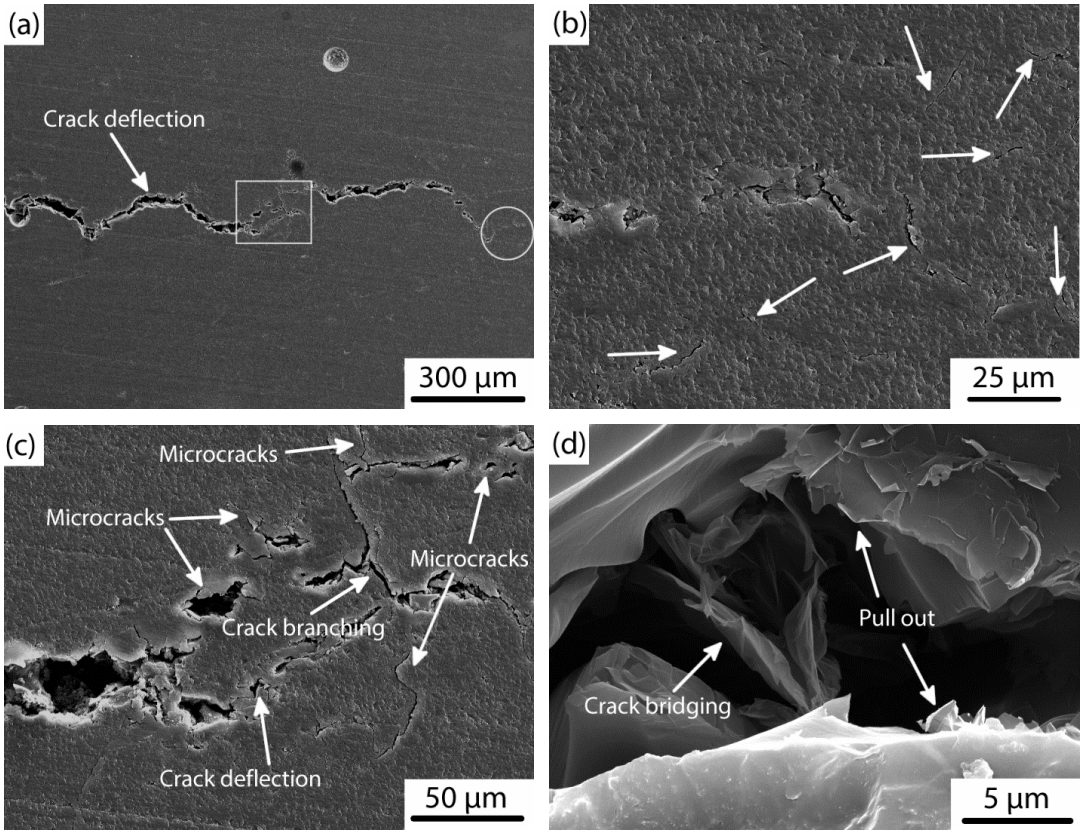

Figure 4-6 : SEM images of crack tip region of a DCB specimen with 2.0 wt% GNPs oriented in the epoxy adhesive layer, showing evidence of: (a) crack deflection; (b) microcracks at the crack tip; (c) microcracks induced crack deflection and branching; (d) crack bridging and graphene pull out. (b) and (c) are magnified SEM images taken from the circular and rectangular region in (a), respectively.

Figure 4-6c shows that the discrete microcracks coalesced into a multi-branched network of longer cracks which then connected with the main crack front. This is also an effective intrinsic toughening process which contributes to the increase in the fracture toughness of the nanocomposites. In addition, there was a progressive increase in the fracture surface roughness with the increase in content of GNPs. This was due to the increased degree of crack bifurcation and branching which would also increase the toughness of the epoxy nanocomposites. Furthermore, the orientation of the GNPs at some inclined angle to the crack growth direction will obviously increase the probability of the main crack encountering them and thus induce more crack deflection and branching. Hence, the presence of a relatively high level of inclined GNPs, approximately transverse to the crack growth direction, will provide an enhanced toughening effect in the epoxy nanocomposites. Indeed, examination of the crack tip at high magnification (Figure 4-6d) revealed fracture and pull-out of GNPs, and crack

bridging by the pulled-out GNPs. The transversely-aligned GNPs tended to initially bridge the crack over a crack-opening distance of up to ~20 μm, which is equivalent to the size of the nanoplatelets. As the crack propagated along the DCB specimen, the GNPs fractured and pulled-out from the epoxy polymer matrix. These very effective extrinsic toughening mechanisms, which are not significant in the epoxy nanocomposites containing randomly-oriented GNPs, account for the more effective toughening.

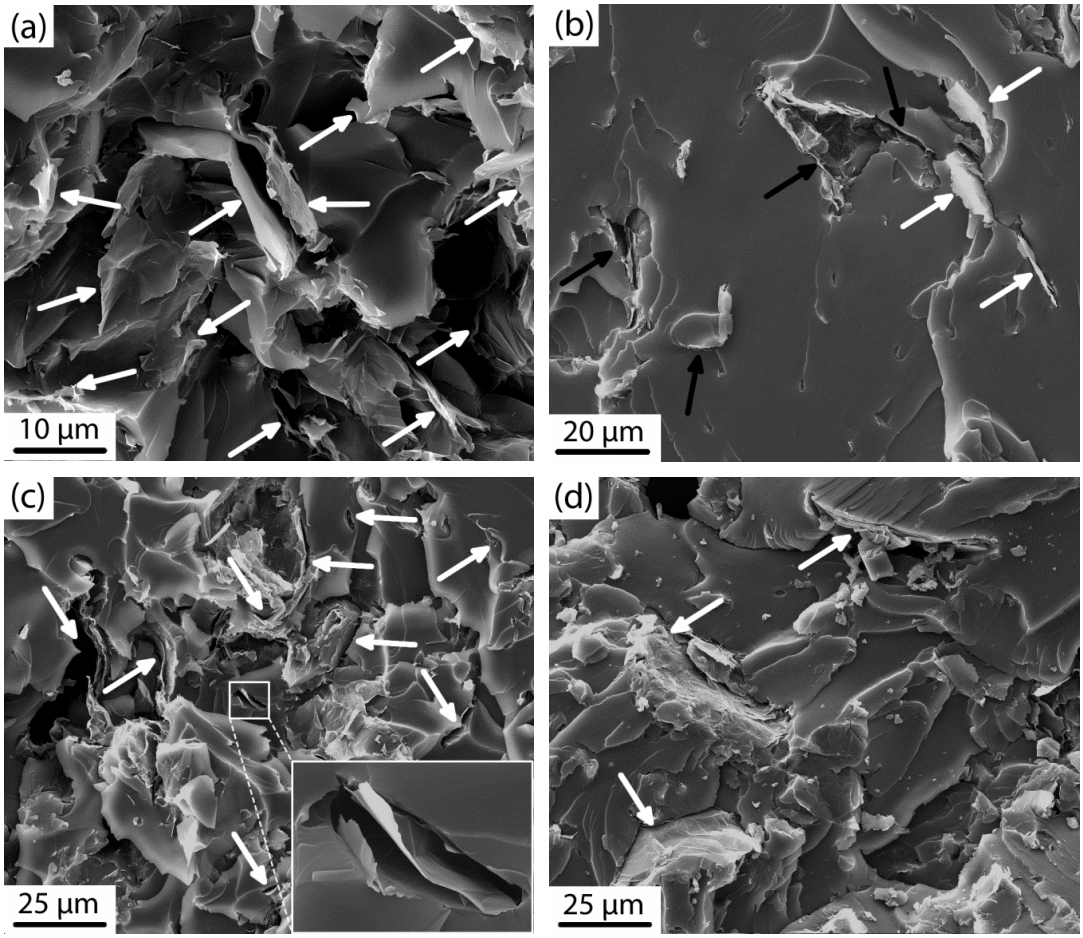

Figure 4-7 : SEM images taken at higher magnifications from fracture surface of DCB specimens with 1.0 wt% GNPs oriented in the epoxy adhesive layer, revealing evidence of: (a) graphene debonding/pull out; (b) debonding/pull out (white arrows) and rupture of graphene (black arrows); (c) microcracks; (d) crack deflection. Note that the insert in (c) is a magnified SEM image from the rectangular area in (c).

4.4 Conclusion

The application of an AC electric-field has been shown to align GNPs, and to drive the GNPs to form a chain-like network nanostructure, in an epoxy polymer along the electric-field direction. Aligning the GNPs transverse to the crack growth direction has dramatically improved the fracture toughness (of up to nearly 900%). These properties are far superior to those achieved by randomly-oriented GNPs. Both intrinsic and extrinsic toughening mechanisms have been identified as the major factors responsible for the remarkable increase in fracture toughness. Specifically, the main intrinsic toughening mechanisms for the epoxy nanocomposites containing transversely-aligned GNPs include micro-cracking and debonding of the GNPs, pinning and deflection of the main crack. The extrinsic toughening mechanisms include pull-out of and bridging by the GNPs. The orientation of the aligned GNPs transverse to the crack direction increases the probability of interactions occurring between the advancing crack tip and the GNPs. This greatly enhances the effectiveness of the extrinsic toughening mechanisms and leads to a significant increase in the fracture toughness compared to randomly-oriented GNPs. The differences in the properties between the epoxy nanocomposites containing randomly-oriented GNPs and aligned GNPs become less marked when the content of the GNPs increases to above about 1.5 wt%. This may be ascribed to the increased agglomeration and reduced degree of alignment of the GNPs at contents above about 1.5 wt%. The present chapter has clearly demonstrated that an AC electric-field can be applied to control the orientation and alignment of GNPs in an epoxy resin and therefore enables the fabrication of high-performance GNP-epoxy nanocomposites.

Chapter 5

Modelling and Comparison of the Fracture Toughness and Electrical Conductivity of Carbon Nanofibre and Graphene Nanoplatelet Reinforced Epoxy Composites

Abstract

This chapter compares improvements to the fracture energy and electrical conductivity of epoxy nanocomposite materials reinforced by one-dimensional CNFs or two-dimensional GNPs. A mechanistic model is presented to quantify the contributions from the different toughening mechanisms responsible for the improvements seen in their toughness. The effects of the shape, orientation and concentration (i.e. 0.5, 1.0, 1.5 and 2.0 wt%) of nanoscale carbon reinforcements on the property improvements are presented. The model results show that one-dimensional CNFs are more effective at increasing the intrinsic toughness of epoxy via void growth, whereas two-dimensional GNPs are more effective than CNFs at improving the extrinsic toughness via crack bridging and pull-out.

The research presented in this chapter has been published in the following journal and conference papers:

- Ladani RB, Wu S, Kinloch AJ, Ghorbani K, Zhang J, Mouritz AP, Wang CH. *Multifunctional properties of epoxy nanocomposites reinforced by aligned nanoscale carbon*. Materials & Design. 2016;94:554-564.

- Wang CH, Ladani RB, Wu S, Kinloch AJ, Zhang J, Ghorbani K, Mouritz AP. *Epoxy Nanocomposites with Aligned Carbon Nanofillers by External Electric Fields*. In Proceeding of the 26th International Conference on Composite Materials, Copenhagen, Denmark, 2015.

5.1 Introduction

Research into polymer nanocomposites has recently advanced to a level where several important properties, such as strength and stiffness, can be predicted using various modelling approaches [242, 243]. This enables an effective 'materials design' approach to be adopted for this new class of materials, which reduces the cost and accelerates the introduction of novel and improved nanocomposite materials. However, only limited research has been reported on the comprehensive modelling of the fracture properties of nanocomposites [106, 219], and these studies have focused on one-dimensional nano-reinforcements such as CNTs and CNFs. Thus, in spite of recent efforts, there is a lack of suitable fracture models that enable the optimum design of nanocomposites with two-dimensional nano-reinforcements for high crack resistance.

In this chapter, the effects of shape, orientation and concentration of the nano-reinforcements on the electrical conductivity and fracture toughness of epoxy nanocomposites are investigated. Additional epoxy nanocomposite samples containing 0.5, 1.5, and 2.0 wt% of random and aligned CNFs were fabricated and tested using the methodology presented earlier in section 3.2. This enabled a direct comparison of the fracture toughness and electrical conductivity of the CNF- and GNP-epoxy nanocomposites studied in the earlier chapters. A mechanistic fracture model is presented to quantify the improvements in fracture toughness of polymer nanocomposites reinforced by two-dimensional GNPs. The numerical accuracy of the model is compared against experimental toughness values. The model results are then used to identify the primary toughening mechanisms for the GNP-epoxy nanocomposites and it is compared against the CNF-epoxy nanocomposites.

5.2 Materials and Experimental Methodology

To study the electrical conductivity of the epoxy nanocomposites, the nano-reinforcement /epoxy mixtures were placed in a silicon rubber mould. The mould was then placed between two aluminium plates which were used to apply an AC electric-field of strength 30 V/mm in the thickness direction during the initial one hour period (resin gelation time) of the curing cycle of the epoxy resin. The epoxy was cured at

room temperature for 48 hours and then machined into rectangular test specimens of size 25 × 20 × 2 mm for electrical conductivity measurements following the ASTM D257 standard. The DC conductivity measurements were performed using a high resistance meter (Agilent 4339B) at room temperature. Similarly, the AC conductivity measurements were also performed at room temperature using an impedance analyser (HP4192A). Additional DCB joints were fabricated to study the fracture energy of epoxy nanocomposites containing 0.5, 1.0, 1.5 and 2.0 wt% of random and aligned CNFs in accordance to the procedure described in Chapter 3. The details of the fabrication process and DCB testing procedure are outlined in section 3.2.

5.3 Results and Discussion

5.3.1 Electrical Conductivity

Figure 5-1 shows the electrical conductivity of the CNF- and GNP-epoxy nanocomposites as a function of the frequency, using logarithmetic scales. For the nanocomposites containing aligned nano-reinforcements, measurements were made parallel to the alignment direction (i.e. through-thickness direction of the DCB joint). For the randomly-oriented GNP-epoxy nanocomposites with loadings of 0.5 wt% and 1.0 wt% (Figure 5-1b) there is an increase in the capacitive component with increasing frequency, which is similar to that measured for the unmodified epoxy. However, for the 0.5 wt% aligned GNP-epoxy nanocomposite, there is a frequency-independent conductivity response at frequencies below about 100 Hz, and at higher frequencies the response is similar to that of the unmodified epoxy. A similar trend also occurs for the 0.5 wt% randomly-orientated CNF-epoxy nanocomposite with a transition in frequency dependency at about 10 kHz (see Figure 5-1a).

The frequency-dependent results of the electrical conductivity can be correlated using the universal dielectric relationship originally reported by Jonsher [244, 245] for a wide range of dielectric materials,

$$\sigma(\omega) = \sigma_{dc} + A\epsilon_0\omega \tag{5-1}$$

where σ_{dc} is the DC conductivity, ϵ_0 is the dielectric permittivity of the free space ($\epsilon_0 = 8.845 \times 10^{-12}\ F/m$), ω is the angular frequency, and A is a constant. This conductivity relationship is applicable for frequencies below 1-10 GHz [244].

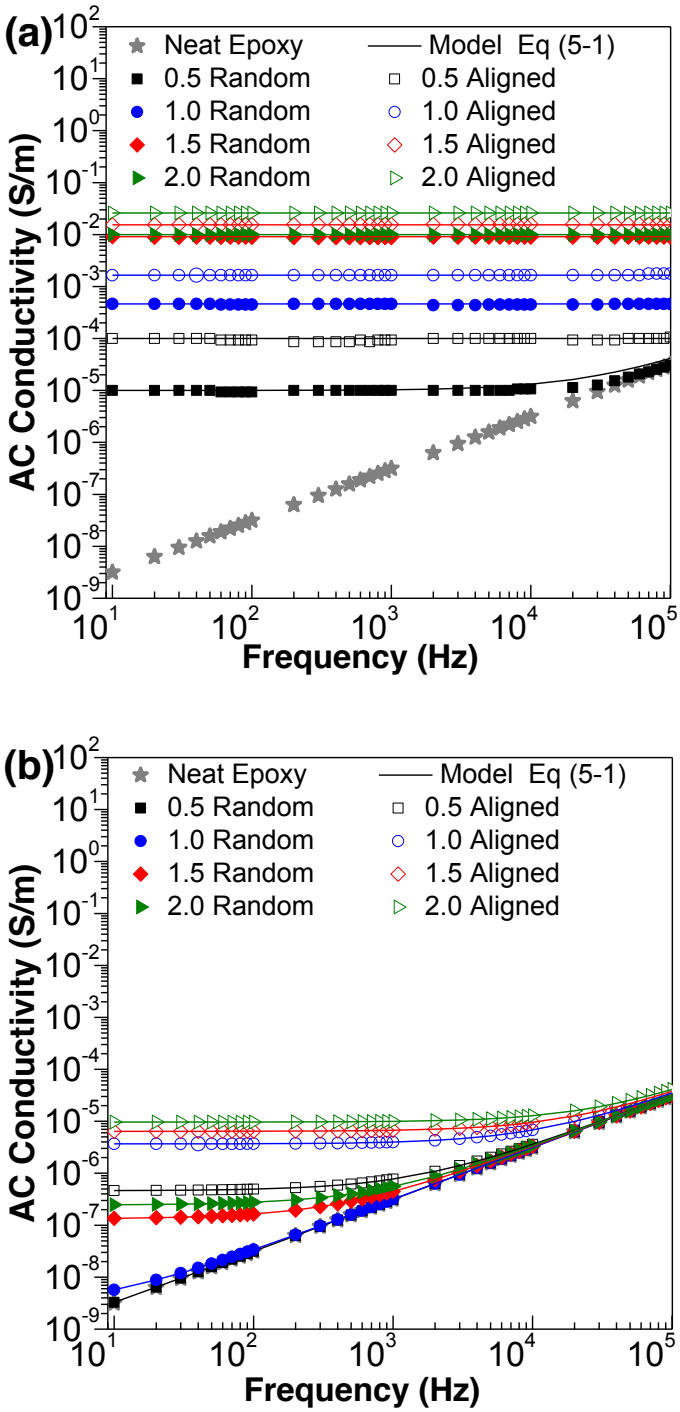

Figure 5-1 : Electrical conductivity of the epoxy nanocomposites as a function of frequency. AC conductivity of the (a) CNF-epoxy polymer nanocomposites and (b) GNP-epoxy polymer nanocomposites; all the solid lines indicate the best fit using Equation (5-1).

For a nanocomposite containing a conductive filler (e.g. CNFs, GNPs), the conductivity is governed by percolation paths at low frequency and the dielectric matrix at high frequency. By curve-fitting the AC conductivity results of the unmodified epoxy, the value of the parameter *A* has been found to be 5.65. It is interesting to note that the same value of *A* can be used to model the frequency-dependent conductivity of all the concentrations of CNFs and GNPs used in the epoxy nanocomposites in the present investigation. The appearance of a DC plateau for the 0.5 wt% aligned GNP-epoxy nanocomposite and the 0.5 wt% random CNF-epoxy nanocomposite indicates a transition from the insulating regime dominated by the epoxy to a conducting regime, which reflects the formation of some percolating nano-reinforcement networks. At higher concentrations of nano-reinforcements in the epoxy, the AC conductivity is dominated by the DC conductivity and becomes frequency-independent for both the CNF- and GNP-epoxy nanocomposites, irrespective of their orientation in the epoxy.

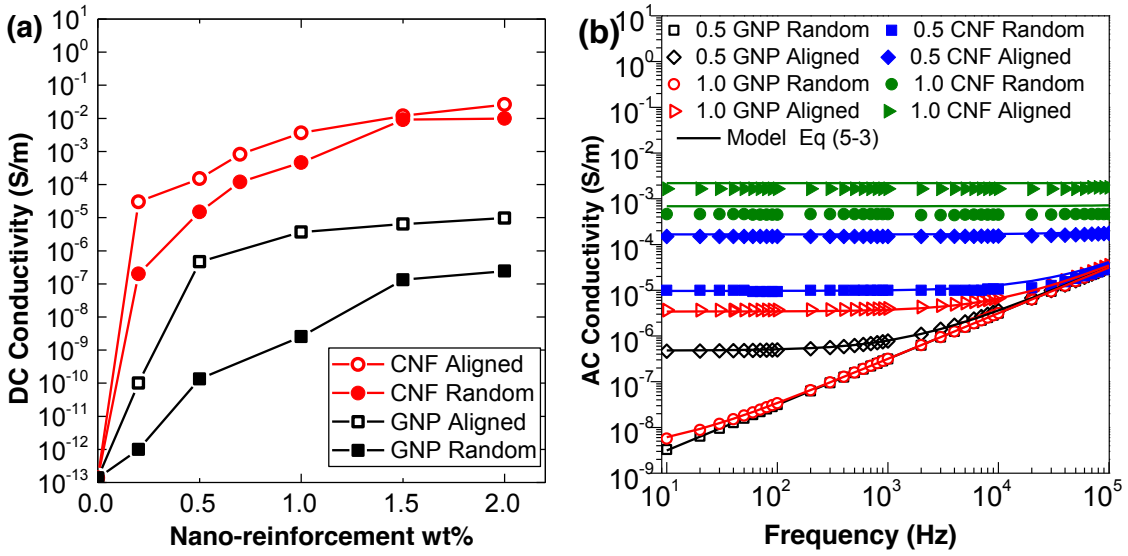

Figure 5-2 : (a) Effect of concentration and alignment of CNFs and GNPs on the DC electrical conductivities of the epoxy nanocomposites; (b) comparison of the AC electrical conductivity results with the model given by Eq. (5-3) which is represented by the solid lines for corresponding concentrations of nano-reinforcement.

The effects of nano-reinforcement content and orientation on the DC electrical conductivity of the epoxy nanocomposites is shown in Figure 5-2. The electrical conductivity of the randomly-oriented and aligned nanocomposites increase with the nano-reinforcement concentration up to ~1.5wt%, above which there is little or no

further increase. The electrical conductivity does not increase further due to the difficulty in achieving a homogeneous dispersion at relatively high concentrations of nano-reinforcement using the calendaring process, but instead there occurs a significant agglomeration and clustering of the nano-reinforcement. Furthermore, at relatively high concentrations, the very close packing of the nano-reinforcements limits the free space needed for them to rotate and align when subjected to the applied AC electric-field. The conductivity of the nanocomposites with aligned nano-reinforcements is significantly higher than that for the nanocomposites with randomly-oriented nano-reinforcements. However, the improvements in the conductivity of the CNF-epoxy nanocomposites are much more pronounced than for the GNP-epoxy nanocomposites. The conductivity of fully graphitized CNFs used in this study is reported to be about 2×10^6 S/cm [246], whereas the conductivity of the multi-layered GNPs is about 100 S/cm (perpendicular to surface) to 10^7 S/cm (parallel to surface) [247]. The anisotropic electrical conductivity of the GNPs would result in increased contact resistance between multi-layered GNP particles within a percolating network. This would lead to a lower conductivity improvement of the GNP-epoxy nanocomposites. Indeed, multi-layered graphite polymer composites have been reported to possess higher percolation thresholds with lower conductivity improvements [248] in comparison to their expanded graphite counterparts [249].

The influence of the type of nano-reinforcement, and its orientation in the epoxy, on the percolation threshold, V_{fc}, can be determined from the scaling-law equation [33].

$$\sigma_{dc} = B(V_f - V_{fc})^n \tag{5-2}$$

where V_f is the volume fraction of the nano-reinforcement and B and n are material constants. Table 5-1 lists the values of the percolation threshold and the associated material constants which are determined by curve fitting to Eq. (5-2) the experimentally measured DC conductivity data as a function of $(V_f - V_{fc})$ expressed as a weight fraction but otherwise according to the scaling-law equation. (It should be noted that the percolation threshold values and the corresponding constants are determined by searching for the highest R-value to establish the best curve fits.) The percolation thresholds for the nanocomposites with the randomly-oriented CNFs and GNPs are

found to be 0.43 wt% and 0.95 wt%, respectively. The alignment of the CNFs and GNPs lowers the percolation thresholds to 0.25 wt% and 0.4 wt% respectively. Also, from Figure 5-1, the percolation thresholds can be confirmed by the appearance of the DC plateau at the nano-reinforcement content which represents the percolation threshold. Thus, these results clearly demonstrate that the epoxy nanocomposites with aligned nano-reinforcements require a significantly lower content of nano-reinforcement in order to achieve a conductive network, with the CNFs being more effective than the GNPs.

The percolation threshold and the corresponding material constants from Table 5-1 can be used to design epoxy nanocomposite materials with the desired electrical properties using the scaling law equation and the frequency-dependent conductivity response of the epoxy with the following expression if $V_f \geq V_{fc}$

$$\sigma(\omega, V_f) = B(V_f - V_{fc})^n + A\epsilon_0\omega \tag{5-3}$$

where the dielectric response parameter (i.e. A) can be obtained by curve-fitting the conductivity results of the unmodified epoxy polymer. As can be seen from Figure 5-2b, the model predictions are in good agreement with the experimental measurements.

Table 5-1 : The value of the scaling law parameter determined by curve fitting the experimental conductivity results of the epoxy nanocomposites

Nano-reinforcement	V_{fc} **(wt%)**	***n***	***B***
CNF Aligned	0.25	2.65	6.6×10^{-3}
CNF Random	0.43	2.22	3.5×10^{-3}
GNP Aligned	0.4	1.10	6.0×10^{-6}
GNP Random	0.95	1.54	3.0×10^{-7}

Note: The value of parameter A = 5.65

5.3.2 Fracture energy comparison

Figure 5-3 shows typical applied load versus crack opening displacement curves for the epoxy nanocomposites measured from the DCB test specimen. The unmodified epoxy

and all the CNF-epoxy nanocomposites (randomly-orientated or aligned) exhibited large and abrupt load drops with increasing displacement which is characteristic of unstable "stick-slip" type crack growth. The peak loads of the curves corresponded to the onset of crack growth, while the minimum loads corresponded to crack arrest. The GNP-epoxy nanocomposites with randomly-oriented or aligned GNPs at concentrations of 0.5 and 1.0 wt% also experienced unstable crack growth similar to that observed for the CNF-epoxy nanocomposites. However, at higher GNPs concentrations of 1.5 and 2.0 wt%, the fracture process was observed to transition to a more stable form of crack growth with smaller load drops. This suggests that different toughening mechanisms may operate in the CNF- or GNP-epoxy nanocomposites. The fracture energy values, G_{Ic}, for the onset of crack propagation were calculated using the maximum loads that were measured in accordance to ISO 25217 [217]. (The first peak of the load versus displacement curve was ignored to ensure that only subsequent values of the maximum loads, which were associated with crack initiation from relatively sharp ('natural') cracks were used to calculate G_{Ic} [217]). For all of the DCB tests bonded using the epoxy polymer nanocomposite and the unmodified epoxy, the locus of failure was along the centre of the polymer layer.

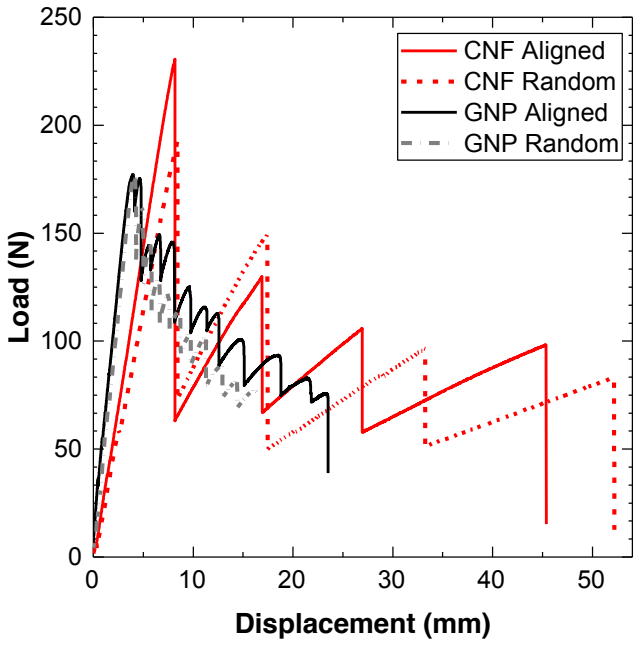

Figure 5-3 : Typical load versus displacement curves for the epoxy nanocomposites containing 1.5 wt% of CNFs or GNPs (randomly-orientated and aligned).

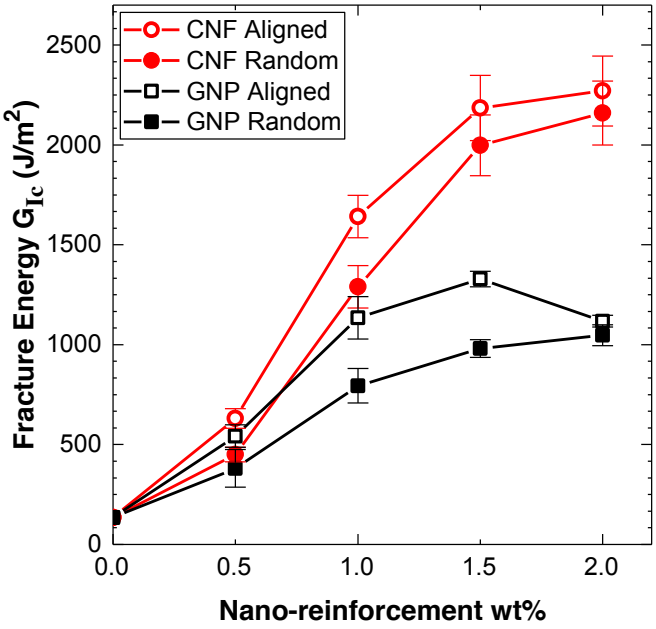

Figure 5-4 : Effects of the nano-reinforcement concentration, shape and orientation on the fracture energy of the epoxy nanocomposites.

Figure 5-4 shows the effect of the weight fraction and orientation of the CNF and GNP nanoparticles on the fracture energy, G_{Ic}. The fracture energy increases almost linearly up to a nano-reinforcement concentration of 1.5 wt%, although no further improvements occurs at the highest concentration of 2.0 wt% due to agglomeration and restricted capacity to rotate the nano-reinforcement in the case of the aligned particles. Alignment of the CNFs and GNPs resulted in an additional toughening effect, with the fracture energies being respectively 25% and 40% higher for the nano-reinforcement concentrations under 1.5 wt%. The toughening mechanisms responsible for the improvements in the measured toughness are discussed in the following section.

5.3.3 Fractographic Comparison

Fractographic analyses of the DCB specimens provided a significant insight into the toughening mechanisms responsible for the improvements in the fracture energy of the epoxy nanocomposites. As shown in Figure 5-4a, the unmodified epoxy exhibited a smooth and featureless crack surface indicative of brittle fracture. In comparison, the fracture surfaces of the DCB samples containing CNF-epoxy nanocomposites (at all concentrations) and the GNP-epoxy nanocomposites (with contents of 0.5 and 1.0 wt%) exhibited a stick-slip crack propagation with distinct stress-whitening of the epoxy in

the regions of crack initiation and arrest, as shown in a representative fracture surface in Figure 5-4b_1. The stress-whitening arises from plastic deformation associated with the crack initiation process. The lengths of these stress-whitening bands increased with increasing concentration of the nano-reinforcements and hence correlate with the observed increases in the values of their fracture energy. For GNPs-epoxy nanocomposites with a nano-reinforcement concentration of 1.5 and 2.0 wt%, the crack propagation mode was observed to transition from stick-slip to stable growth, with distinct stress-whitening extending along the entire fracture surface as shown in Figure 5-4b_2.

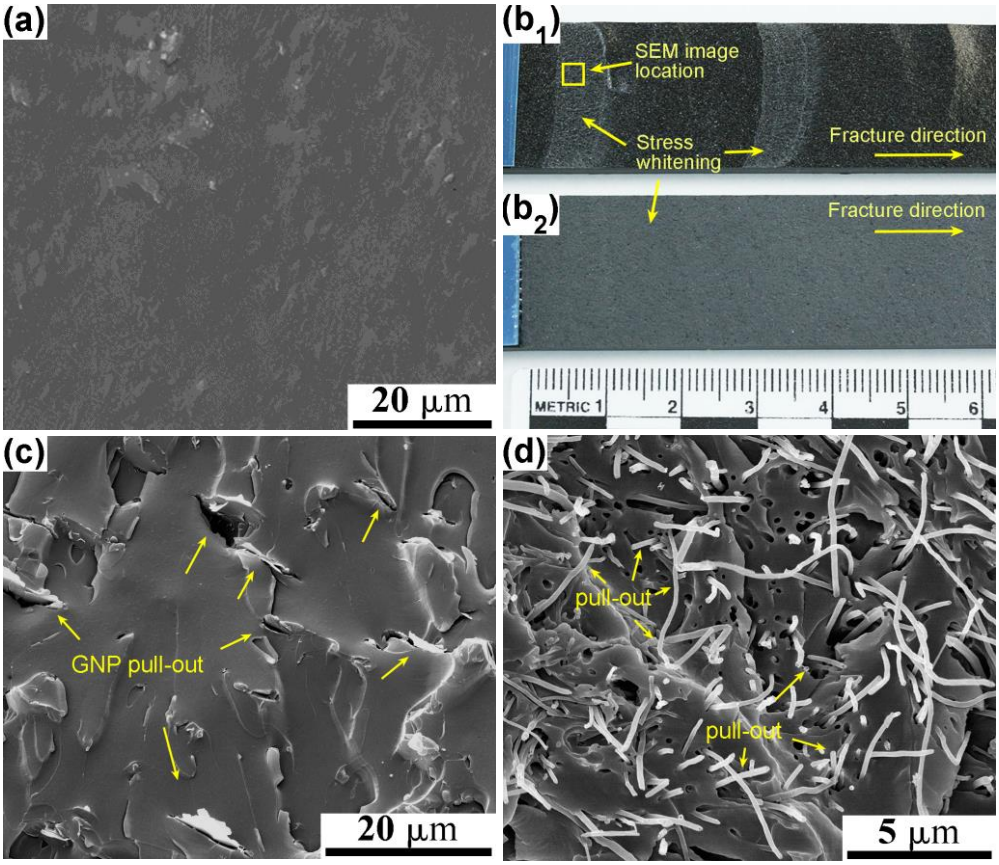

Figure 5-5 : (a) SEM image of the fracture surface of unmodified epoxy polymer; photograph of the fracture surface of epoxy nanocomposites with (b_1) 1.5 wt % aligned CNFs and (b_2) 1.5 wt% aligned GNPs; SEM images of the fracture surface of epoxy nanocomposites containing; (c) 1.5 wt% aligned GNPs; and (d) 1.5 wt% aligned CNFs.

The fracture energy of the epoxy nanocomposites is increased by both intrinsic toughening processes ahead of the crack tip together with extrinsic toughening behind the crack front. In Figure 5-6, a significant number of relatively large voids are visible around both the CNF and GNP nano-reinforcements in the process zone immediately

ahead of the crack. These voids are indicative of high-strain plastic flow of the epoxy in the process zone. The epoxy void growth mechanism occurs when the triaxial stress-field ahead of the crack tip is sufficiently high to cause debonding of the nano-reinforcements from the epoxy.

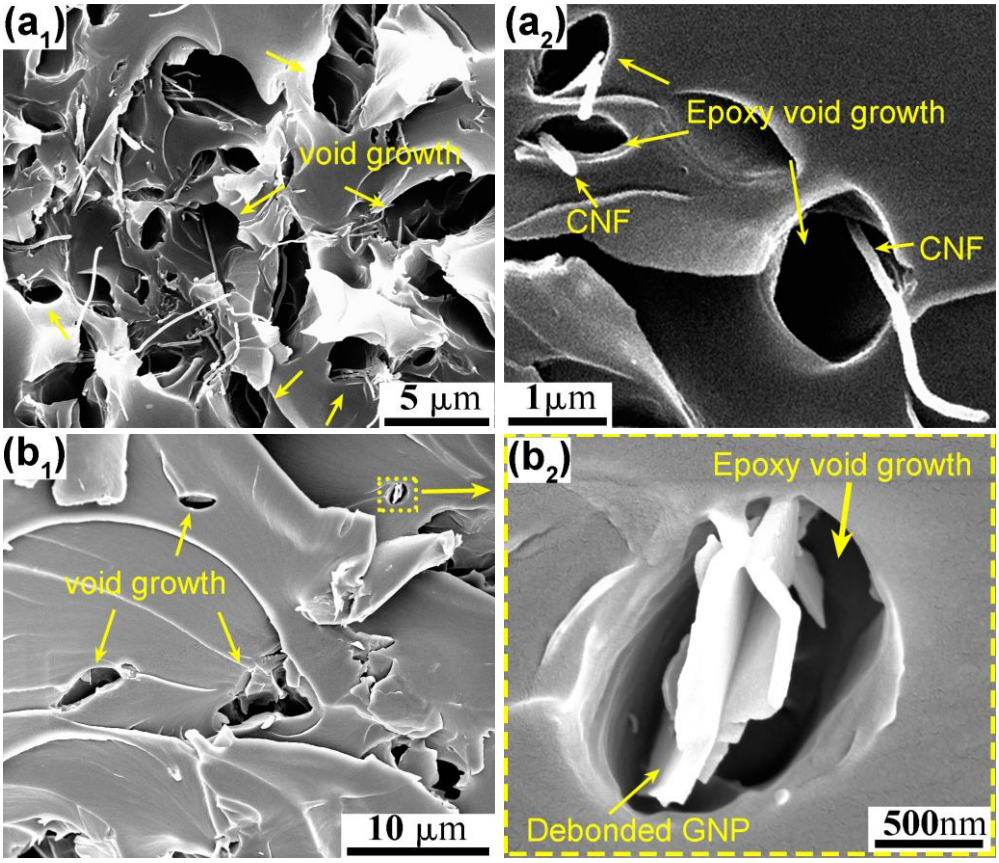

Figure 5-6 : Representative SEM images of the fracture surfaces of the region immediately ahead of the crack front of the epoxy polymer nanocomposites containing, (a_1) and (a_2) 1.5 wt% of CNFs which are randomly-oriented; (b_1) 1.5 wt% GNPs which are randomly-oriented and (b_2) is inset of b_1 at higher magnification.

A large amount of plastic strain energy is absorbed via debonding, initiation and growth of the voids, and this contributes to the increased fracture energy of the epoxy nanocomposites. The volume content of voids increased with the nano-reinforcement content, and this would account in part for the increased fracture energy of the nanocomposites with increasing CNF or GNP content. Indeed, for rubber- and nanosilica-toughened epoxies, this plastic void growth mechanism significantly increases the fracture toughness [99, 119]. Void growth occurred in the nanocomposites with randomly-orientated or aligned nano-reinforcements. However, as may be seen from Figure 5-6, the voids around the CNFs were significantly larger than around the

GNPs, and this would account for the higher fracture energy of the CNF-epoxy nanocomposites.

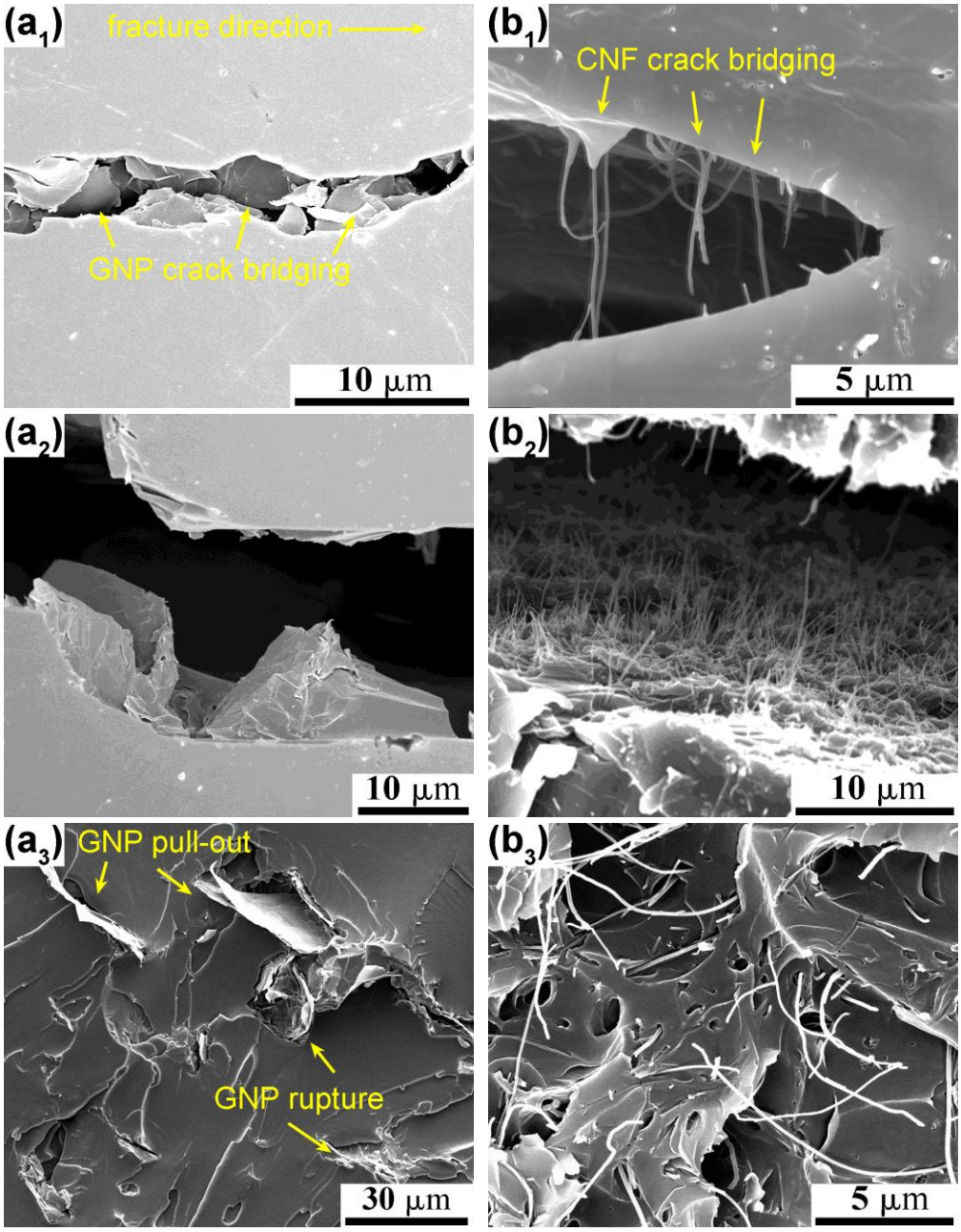

Figure 5-7 : SEM images of the nano-reinforcement bridging the crack in epoxy nanocomposites containing; 1.0 wt% aligned GNPs (a_1) at the crack tip and (a_2) further down the crack wake; 1.0 wt% aligned CNFs (b_1) at the crack tip and (b_2) further down the crack wake. SEM image of the fracture surfaces of the 1.0 wt% of aligned nano-reinforcements in epoxy nanocomposite containing (a_3) GNP and (b_3) CNF nano-reinforcements.

The epoxy nanocomposites also exhibited extrinsic toughening processes in the forms of bridging and pull-out of the nano-reinforcements, as shown in Figure 5-7. The

formation of the crack bridging zone was observed to begin with the pull-out of the nano-reinforcements from the epoxy, as shown in Figure 5-7a_1 and b_1. As the crack front passes across the nano-reinforcements, they start to debond and pull-out from the side with the shorter embedded lengths on either side of the crack plane (see Figure 5-7a_2 and b_2), and this toughening process shields the crack tip from the applied stress. The length of the nano-reinforcement bridging zone was longer for the GNP-epoxy nanocomposites compared to the CNF-epoxy nanocomposites, as shown in Figure 5-7a_1 and b_1. The frictional energy induced by the pull-out of nano-reinforcements from an epoxy is known to be a dominant toughening mechanism. The relatively long nano-reinforcements rupture close to the crack plane since their embedded lengths is sufficiently long that they will break rather than pull-out (see Figure 5-7a_3 and b_3). The absorbed strain energy associated with this tensile rupture of the nano-reinforcements contributes to the increases observed in the fracture energy.

The improvements to the fracture energy of the epoxy nanocomposites therefore result from the (a) frictional energy dissipated by pull-out of the nano-reinforcements, (b) rupture of the nano-reinforcements, (c) interfacial debonding of the nano-reinforcements, and (d) plastic void growth which initiates from the microvoids created by the debonded nano-reinforcements. While these toughening mechanisms were common to both the randomly-oriented and aligned nano-reinforcements, the contribution of each toughening mechanisms depends on the nano-reinforcement orientation. Alignment of the nano-reinforcements perpendicular to the crack path leads to a higher fraction of the nano-reinforcement participating in the toughening mechanisms. For randomly-oriented nano-reinforcements, the probability of the crack front encountering the nano-reinforcements depends on their orientation, and for an oblique angle above 60^0 to the crack plane this probability is less than 50% [41, 218]. This would lead to fewer nano-reinforcements being pulled-out and contributing to the bridging and rupturing mechanisms.

5.3.4 GNP Epoxy Composite Fracture Energy Modelling

The primary toughening mechanisms operative in the nanocomposites were identified as (a) plastic void growth initiated by the debonded nano-reinforcements in the process zone ahead of the crack, (b) debonding and pull-out of the nano-reinforcements, and (c)

bridging and rupture of the nano-reinforcements behind the crack tip. Assuming the application of continuum mechanics is valid at the nanoscale and the interfacial stress between the nano-reinforcement and epoxy is constant, then the energy dissipated by the pull-out of two-dimensional platelets such as GNPs can be calculated using the conventional expression for particle pull-out [82]:

$$\Delta G_{pull-out} = N\ 2(t + W)\ \tau_G\ l_{po}^2 \tag{5-4}$$

where t, W, l_{po} are the thickness, width and pull-out length of the GNPs respectively and τ_G is the interfacial shear strength. N is the total number of GNPs per unit area of crack surface, which is related to their volume fraction, V_f, using:

$$N = \frac{GNP\ volume}{volume\ per\ GNP} = \frac{l\ V_f}{l\ A_{GNP}} = \frac{V_f}{A_{GNP}} = \frac{V_f}{t\ W} \tag{5-5}$$

A_{GNP} and l are the cross-sectional area and total length of the GNPs in the epoxy, respectively. Substituting Eq. (5-5) into (5-4) gives:

$$\Delta G_{pull-out} = \frac{2V_f\ (t+W)\ \tau_G\ l_{po}^2}{t\ W} \tag{5-6}$$

The GNP pull-out length is difficult to determine with any high degree of accuracy from the SEM micrographs of the fracture surfaces. However, the pull-out length can be estimated in a similar way to the determination of the critical fibre length given by the classical Kelly-Tyson approach [71] where:

$$l_c = \frac{\sigma\ t\ W}{(t+W)\ \tau_G}. \tag{5-7}$$

However, GNPs with lengths exceeding the critical length given by Eq. (5-7) are expected to fracture across the crack plane, since their embedded lengths on either side of the crack plane are sufficiently long for the stress in the GNP to build-up to cause their rupture. Therefore, the longest pull-out length without breaking is equal to half the critical length of the GNPs embedded in the epoxy:

$$l_{po} = \frac{t\ W\ \sigma}{2\ (t+W)\ \tau_G} \tag{5-8}$$

where σ is the tensile strength of the GNP. Considering the GNP properties as supplied by the manufacturer and with the experimentally measured interface strength between GNP and the epoxy matrix being ~2.3 MPa [250], then the GNP pull-out length is estimated to be about 8.7 μm. This value is similar to the value determined from SEM observations of the length of GNPs bridging the crack, as shown in Figure 5-7a_1 and a_2. Substituting Eq. (5-8) into Eq. (5-6) gives the expression for the energy dissipated during pull-out of the GNPs:

$$\Delta G_{pull-out} = \frac{V_f\, t\, W\, \sigma^2}{2\,(t+W)\,\tau_G} \tag{5-9}$$

The increase in fracture energy due to crack bridging by the GNPs is equal to the energy required to pull-out the bridging GNPs from the epoxy, and is therefore accounted for by $\Delta G_{pull-out}$ [85]. However, the energy associated with the elastic deformation of the GNPs up to their tensile failure stress is given by:

$$\Delta G_{rupture} = \frac{V_f\, l\, \sigma\, \varepsilon_{max}}{2} = \frac{V_f\, l\, \sigma^2}{2\, E_G} \tag{5-10}$$

where E_G and ε_{max} are the Young's modulus and the tensile failure strain of the GNPs, respectively.

In addition, the GNPs debond from the epoxy prior to the pull-out process. The energy due to interfacial debonding can be derived using the same approach as that developed for debonding of fibres given by Hull [83]:

$$\Delta G_{db} = \frac{2V_f\,(t+W)\, l_{po}\, G_i}{t\, W} \tag{5-11}$$

where G_i is the interfacial fracture energy between the GNPs and epoxy.

Plastic void growth in the process zone ahead of the crack, which is initiated by debonding of the GNPs from the epoxy, increases the intrinsic toughness of the nanocomposites. The fracture energy contribution from the plastic void growth mechanism can be calculated by considering the model proposed by Huang and Kinloch [223]:

$$\Delta G_v = \left(1 + \frac{\mu_m}{\sqrt{3}}\right)^2 (V_{void} - V_f)\sigma_y r_{yu} K_{vm}^2 \quad (5\text{-}12)$$

where μ_m is a material constant allowing for the pressure dependency of the yield stress and K_{vm} is the maximum stress concentration for the von Mises stresses around a debonded GNP [106]. The parameters σ_y and r_{yu} are respectively the tensile yield stress and the plastic zone size at fracture of the unmodified epoxy. The plastic zone size is given by Eq. (3-10).

From SEM fractographic observations, the volume fraction of voids, V_{void}, is estimated by assuming their shape to be an ellipsoid with their semi-major axis being equal to average half the width of the GNPs and their semi-minor axis being equal to four times the average GNP thickness as follows:

$$\left(V_{void} - V_f\right) = \left(N A_{GNP} \frac{2\pi W t}{A_{GNP}} - V_f\right) = V_f\,(2\pi - 1) \quad (5\text{-}13)$$

By combining the analyses of the different energy terms given above, the fracture energy of the epoxy nanocomposites reinforced with 2-dimensional nano-reinforcements can be calculated from the following expression:

$$G_{Ic} = G_{CU} + \frac{V_f\, t\, W\, \sigma^2}{2\,(t+W)\,\tau_G} + \frac{V_f\, l\, \sigma^2}{2\,E_G} + \frac{2V_f\,(t+W)\,l_{po}\,G_i}{t\,W} + \left(1 + \frac{\mu_m}{\sqrt{3}}\right)^2 [V_{void} - V_f]\sigma_y r_{yu} K_{vm}^2 \quad (5\text{-}14)$$

Similarly, the model for estimating the improvements in the fracture energy of the CNF-epoxy nanocomposites was presented in section 3.3.4. The expression to model the fracture energy, G_{Ic}, for one-dimensional CNF-epoxy nanocomposites (Eq. 5-15) is outlined here for comparison with the two-dimensional GNPs (Eq. 5-14):

$$G_{Ic} = G_{CU} + \frac{V_f \sigma_f^2 d_f}{8\tau_f} + \frac{V_f \sigma_f^2\, l_f}{2\,E_f} + \frac{V_f l_{po} G_i}{d_f} + \left(1 + \frac{\mu_m}{\sqrt{3}}\right)^2 [V_f \left(\frac{d_v^2}{3d_f^2} - 1\right)]\sigma_y r_{yu} K_{vm}^2 \quad (5\text{-}15)$$

Table 5-2 : List of values for the various parameters used in the analytical modelling studies.

Parameter	Symbol	Unit	Value	Source
CNF diameter	d_f	nm	70-200	[224]
GNP thickness	t	nm	1-20	[247]
GNP width	W	μm	25	[247]
CNF strength	σ_f	GPa	8.7	[224]
GNP strength	σ	GPa	5	[247]
Young's modulus of the CNF	E_f	GPa	320	[225]
Young's modulus of the GNP	E_G	GPa	1000	[247]
Density of the CNF	ρ_f	kg/m^3	1400	[224]
Density of the GNP	ρ	kg/m^3	2200	[247]
GNP/epoxy interface strength	τ_G	MPa	2.3	[250]
Density of unmodified epoxy	ρ_m	kg/m^3	1011	[226]
Tensile yield strength of unmodified epoxy	σ_y	MPa	50.5	[226]
Young's modulus of unmodified epoxy	E_m	GPa	3.17	[226]
Pressure dependent yield stress constant	μ_m	-	0.2	[223]
Maximum von Mises stress concentration	K_{vm}	-	2.11	[223]

Although the values for the interface strength τ_f between the CNF and epoxy are reported to be as high as 170 MPa [221], the value is in fact limited by the shear strength of the epoxy, which is approximately half that of the tensile yield stress using the Tresca yield criterion, giving a value of 25 MPa. The interfacial fracture energy G_i associated with debonding of the CNFs from the epoxy has been measured to be 3.3 J/m^2 [222]. At present there are no reports on the interfacial fracture energy between GNPs and epoxy. Therefore, a similar value for the interfacial fracture energy between CNFs and epoxy was used to estimate the energy dissipated during debonding of GNPs. The volume of the voids around the CNFs is assumed to be a truncated cone with the inner diameter equal to the diameter of the CNFs and the larger void diameter, d_v, is determined from the SEM images to be approximately seven times. The values of all other input parameters used to calculate the fracture energy of the epoxy

nanocomposites are given in Table 5-2. The predictions from the model and a comparison with the experimental results are discussed in the following section.

5.3.5 Results of the fracture energy modelling

A comparison of the theoretical model predictions with the experimentally measured values of the fracture energies is shown in Figure 5-8. Good agreement can be seen between the experimental results and the calculated fracture energies for the highest CNF diameter and GNP thickness. The model is particularly sensitive to the diameter or thickness of the nano-reinforcements. Since, nano-reinforcements with larger diameter or thickness would enable longer pull-out lengths (see Eq. 5-8) leading to a greater increase in the degree of extrinsic toughening. The results shown in Figure 5-8 confirm the primary toughening mechanisms proposed for the epoxy nanocomposites modified using randomly-oriented or aligned nano-reinforcements. The calculated contributions to the improvement in the fracture energy from each of the toughening mechanisms are given in Table 5-3. Pull-out of the nano-reinforcements and void growth are the two most dominant toughening mechanisms, accounting for the majority of the fracture energy enhancement for all the epoxy nanocomposites. A notable difference between the modelling results for the CNF- and GNP-epoxy nanocomposites was that the intrinsic toughening due to void growth was more pronounced in the CNF-epoxy nanocomposites. In contrast, the extrinsic toughening due to GNP pull-out was significantly more dominant in the GNP-epoxy nanocomposites, accounting for almost four times the intrinsic energy dissipation via void growth in the epoxy around the GNPs. This explains the transition to more stable fracture behaviour that was observed during DCB testing for the 1.5 wt% and 2.0 wt% GNP-epoxy nanocomposites. In these nanocomposites, the more pronounced extrinsic toughening in the form of pull-out and crack bridging by the GNPs was more effective at retarding crack growth leading to a more stable fracture process. By contrast, the CNF-epoxy nanocomposites absorbed a higher amount of energy in the process zone ahead of the crack via void growth, leading to a greater improvement in its intrinsic toughness. This is an interesting finding, as it enables the selection of the appropriate type of nano-reinforcement for the materials design of nano-reinforced polymers in order to achieve the desired fracture properties. One-dimensional nano-reinforcements such as CNFs may be more beneficial in resisting the initiation of fracture in the event of impact damage, whereas

two-dimensional nano-reinforcements such as GNPs may be more favourable for designing materials with a greater resistance to the unstable growth of cracks.

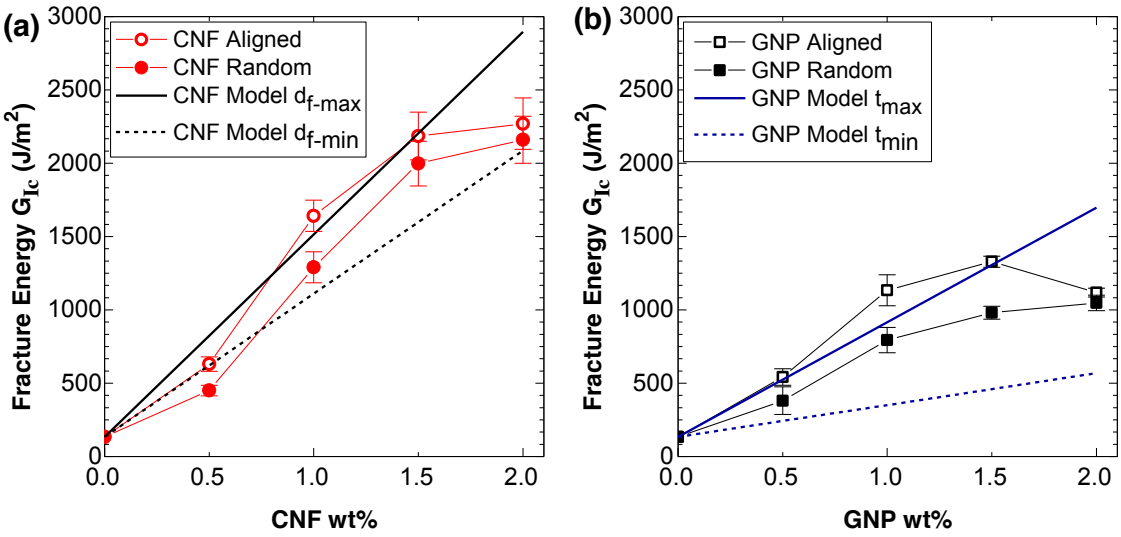

Figure 5-8 : Comparison of the experimental fracture energies and theoretically calculated fracture energies (for the aligned nano-reinforcements) as a function of (a) CNF and (b) GNP weight content in the epoxy nanocomposites.

Table 5-3 : Contributions to the fracture energy, G_{Ic}, of the epoxy nanocomposites for the various toughening mechanisms which were identified, as calculated from the analytical models for the highest values of the CNF diameter and GNP thickness.

Nano-reinforcement	**Concentration** (wt%)	$\Delta G_{pull\text{-}out}$ (J/m^2)	$\Delta G_{rupture}$ (J/m^2)	ΔG_{db} (J/m^2)	ΔG_{v} (J/m^2)
CNFs	0.5	311	10	1.2	369
	1.0	622	19	2.4	737
	1.5	933	29	3.5	1106
	2.0	1243	39	4.7	1474
GNPs	0.5	297	0.9	20	73
	1.0	595	1.7	39	146
	1.5	892	2.6	59	219
	2.0	1190	3.4	79	292

5.4 Conclusions

The effect of the carbon nano-reinforcement shape, orientation and concentration on the improvements observed in the electrical conductivity and fracture toughness of epoxy nanocomposite materials have been investigated. The application of an AC electric-field during the cure process of the resin can align CNFs or GNPs in the direction parallel to the external field. Compared to the unmodified epoxy, the improvements in electrical conductivity of the nanocomposites with aligned CNFs and GNPs were increased by about ten and seven orders of magnitude, respectively. Also, the percolation threshold of the nanocomposites containing aligned nano-reinforcements was about 50% lower that of their randomly-orientated counterparts. The values of the fracture energy, G_{Ic}, of the nanocomposites containing 0.5 wt% of randomly-oriented one-dimensional CNFs or two-dimensional GNPs was improved by up to about 200%, compared to the unmodified epoxy. An additional improvement in fracture energy of up to about 40% was achieved by aligning the nano-reinforcement transverse to the crack growth direction. The efficacy of the alignment of the nano-reinforcement on the improvement in the electrical conductivity and the fracture energies of the nanocomposites was found to diminish at higher concentrations of the nano-reinforcement.

The large improvements in the fracture energy of the epoxy nanocomposites were due to toughening mechanisms involving (a) debonding of the nano-reinforcements, (b) the energy associated with the frictional pull-out of the nano-reinforcements from the epoxy, (c) crack bridging and rupturing of the nano-reinforcements, and (d) void growth around the debonded nano-reinforcements in the process zone. Fracture energy modelling revealed that the one-dimensional CNFs are more effective at increasing the intrinsic toughness in the form of epoxy void growth, whereas the two-dimensional GNPs are efficient at extrinsic toughening through pull-out and crack bridging of the GNPs.

The results from the present modelling studies were in good agreement with the experimental results and will enable the materials design of polymer nanocomposites, thereby resulting in the more rapid and cost-effective development of such novel materials.

Chapter 6

Fatigue Resistance of Aligned Carbon Nanofibre Reinforced Epoxy Composites

Abstract

This chapter presents an investigation into the fatigue resistance of CNF-epoxy nanocomposites. The effects of the CNF weight content and orientation on the fatigue resistance of CNF-epoxy nanocomposite, and the toughening mechanisms are determined. The fatigue crack growth rate slowed rapidly with increasing CNF content, under mode I cyclic loading. The fatigue crack growth rate also slowed when the CNFs were aligned perpendicular to the crack growth direction up to a limiting concentration of about 0.7 wt%, above which no further improvement to the fatigue resistance was achieved due to their alignment. The fractographic analysis revealed a unique unravelling deformation mechanism in CNFs due to their double-layer microstructure. This unravelling mechanism only occurred when the CNFs are subjected to cyclic tension-compression fatigue loading. The fatigue loading causes the outer layer of the double-layer CNF to fracture and then the helical inner layer to unravel. This unravelling deformation mechanism also contributes to the significant improvement which is observed in the cyclic-fatigue resistance of CNF-epoxy nanocomposites.

The research presented in this chapter is currently under second review for publication in the following journal paper:

- Ladani RB, Wu S, Kinloch AJ, Mouritz AP, Wang CH. *The unravelling of carbon nanofibres under fatigue loading*, Small, 2016. (under review)

6.1 Introduction

Existing airworthiness regulations prescribe that delamination cracks or disbonds within composites above a critical size must be repaired for continued service of aircrafts [8]. In addition, all safety critical composite structures must sustain the design ultimate load in the presence of damage above a critical size [9]. The critical size depends on several parameters including the loading and geometry of the structure, the location of the damage, and the properties of the structural material. The Federal Aviation Administration's damage tolerant regulations permit short delamination cracks to be left unrepaired within aircraft structures provided they do not grow during service of the aircraft over a specified period of time [8]. However, aircraft composite structures are prone to rapid fatigue cracking under relatively low cyclic-fatigue loads due to the low fracture toughness and fatigue resistance of epoxy composites. This severely limits the allowable damage size for aircraft composite structures in comparison to their metallic counterparts. Several studies have reported an improvement in the fracture toughness of epoxy composites reinforced with carbon nano-reinforcements [106, 107]. However, very few studies have investigated the fatigue performance of epoxy composites containing carbon nano-reinforcements [106, 210, 251, 252], and these studies have been mostly focused on the use of CNTs. At present there are no reported studies on the mode I fatigue resistance of CNF-reinforced epoxy composites.

In this chapter, the mode I fatigue resistance of CNF-reinforced epoxy composites are studied. The study compares the fatigue performance of epoxy composite containing various concentrations of CNFs with random and aligned orientations. Detailed fractographic analysis is performed to understand the underlying toughening mechanisms promoted by CNFs when subjected to cyclic loading. Upon discovering a unique fatigue induced failure mechanism for CNFs on the fracture surface of fatigued epoxy nanocomposite specimens, additional *in-situ* tests were performed on individual CNFs to further investigate this failure mechanism. The influence of this unique CNF failure mechanism on the bridging traction behaviour of the CNF is evaluated using a mechanistic traction model.

6.2 Experimental Methodology

Fatigue testing of the epoxy nanocomposite

The fatigue testing was performed on samples similar to that fabricated to study the fracture energy of epoxy nanocomposites containing 0.4, 0.7 and 1.0 wt% of CNF in Chapter 3. The details of the sample fabrication process are outlined in section 3.2. Mode I cyclic-fatigue testing was performed by applying a constant amplitude sinusoidal cyclic load at a frequency of 10 Hz. The tests were performed using a computer-controlled Instron E3000 system with a 3 kN load cell under displacement control with a constant cyclic ratio (*R*-ratio). The ratio between the minimum and the maximum applied displacement in one load cycle was kept constant at 0.5. A sharp crack tip was achieved by carefully wedging the crack opening from the tip of the Teflon film. The specimens were then subjected to cyclic fatigue loading with the maximum crack opening displacement being chosen such that the initial value of the applied strain-energy release-rate was about 80% of the mode I fracture energy determined from the quasi-static test results in section 3.3.2. Delamination fatigue growth rates were measured at crack growth intervals of ~1 mm, in accordance with the load-shedding scheme prescribed in ASTM E647 [253]. The load-shedding process was continued until the crack growth rates reached the threshold value and no further delamination growth occurred.

In-situ fatigue testing of the CNF

In order to understand the sequence of the unique CNF deformation mechanisms, *in-situ* fatigue testing was conducted on a single CNF in a SEM (model FEI Scios) equipped with a focused ion beam (FIB) and a manipulator needle. The *in-situ* fatigue testing was conducted on a CNF which was pulled out on the fracture surface of an epoxy nanocomposite specimen tested under static loading. As shown in Figure 6-1, the free end of the CNF was welded to the tungsten manipulator tip using platinum deposition. Then, the CNF was loaded under tension until the CNF/epoxy interface had failed and it had just begun to pull-out from the epoxy matrix. Then, the CNF was fatigue cycled under displacement control with an amplitude equal to ~25% of the free

length of the CNF. The CNF was fatigued for a total of 200 cycles and then the remaining embedded length of the CNF was pulled out of the epoxy matrix and it transferred on to a TEM grid for observation.

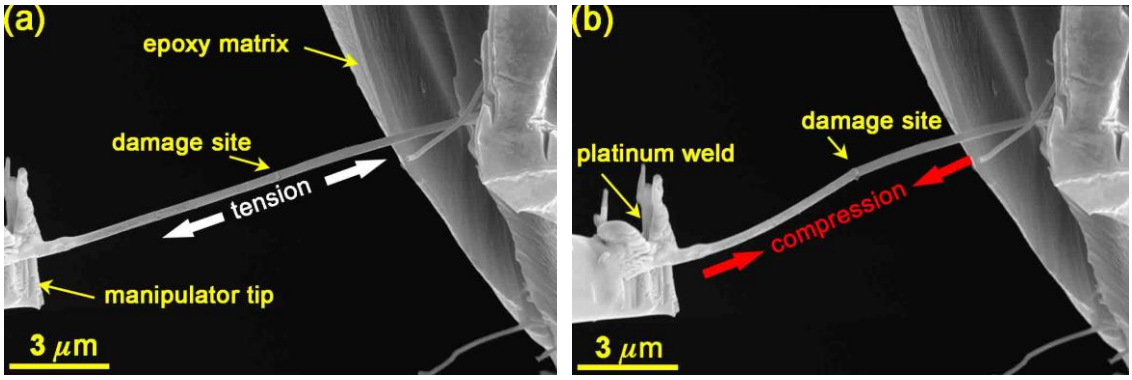

Figure 6-1 : SEM images of the *in-situ* fatigue test setup showing the deformation of the CNF at (a) maximum and (b) minimum displacement amplitude.

In-situ pull-out testing of the CNF

In order to investigate the load carrying capability of CNF during the unravelling process, additional *in-situ* CNF pull-out tests were conducted in a SEM (model Quanta 3D FEG) equipped with a focused ion beam (FIB) and a micro-manipulator, as shown in Figure 6-2. The *in-situ* pull-out testing was conducted on CNFs which were present on the fracture surface of an epoxy nanocomposite specimen tested under fatigue loading. The epoxy nanocomposite sample was mounted on a spring table with two parallel flat springs supplied by Kleindiek Nanotechnik which was fixed on to the SEM stage. The stiffness of the spring used was 125 N/m, which was calibrated prior to testing. The force exerted on the CNF was controlled via a constant displacement rate of the micro-manipulator needle. The micro-manipulator needle was kept orthogonal to the fixation of the flat springs during the pull-out tests. The pull-out force was calculated by using Hooke's law (Eq. 6-1), with the displacement of the deflected spring-table being determined via image-processing of the SEM movie clips 1 and 2:

$$P = k \cdot \Delta x \tag{6-1}$$

The Force Measurement Analysis software, STFMA (supplied by Kleindiek Nanotechnik) was used to process the image files to yield a force-extension curve. The

deflection of the spring, Δx, and the extension, Δl, of the CNF were determined by measuring the average displacement of the group of pixels in boxes B and T, respectively. As shown in Figure 6-2, the changes in position of the group of pixels in boxes B and T may be determined with respect to their initial position according to the following relationships:

$$\Delta x = l_{B2} - l_{B1} \tag{6-2}$$

$$\Delta l = (l_{T2} - l_{B2}) - (l_{T1} - l_{B1}) \tag{6-3}$$

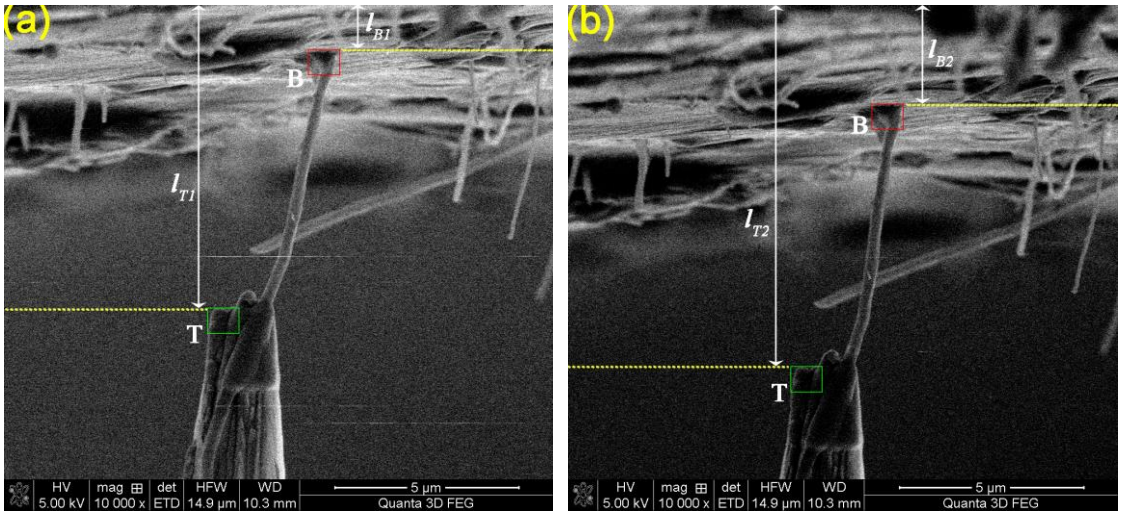

Figure 6-2 : (a-b) SEM images of the CNF pull-out test used to characterise the load versus extension behaviour of the CNF.

6.3 Results and Discussion

6.3.1 Fatigue Crack Growth Resistance

Figure 6-3 shows the fatigue crack-growth rate (*da*/*dN*) plotted against the maximum value of the cyclic strain-energy release rate (G_{max}) in the fatigue cycle for both the unmodified ('neat') epoxy polymer and the CNF epoxy nanocomposite. The measured crack growth rate exhibit the well-known Paris curve as a function of strain energy range as given by

$$\frac{da}{dN} = C(G_{max})^m \tag{6-4}$$

There is a small improvement in the cyclic fatigue resistance for the nanocomposite containing 0.4 wt% CNFs. This may be seen from Figure 6-3 where the fatigue crack growth rate curve for the nanocomposite is further to the right compared to that of the unmodified epoxy polymer. There by indicating that the rate of fatigue crack growth for the CNF nanocomposite is much less than that for the unmodified epoxy polymer at the same value of G_{max}. Similarly, a much greater improvement to the fatigue resistance was observed for the epoxy nanocomposites containing 0.7 wt% CNFs. However, the highest level of improvement to the fatigue resistance was observed for the epoxy nanocomposite containing 1 wt% CNFs. The apparent threshold cyclic strain energy release range ($\Delta G_{eq,th}$) required to start fatigue cracking from the pre-existing delamination was taken at a crack growth rate of 10^{-10} m/cycle. Using this growth rate to define the start of fatigue crack growth, then the threshold strain energy required to initiate fatigue cracking for the unmodified epoxy was about 20 J which is typical of brittle epoxies [254]. The reinforcement of the epoxy with 0.4 wt% CNFs lead to an increase in the threshold strain energy to 25 J. In addition, there was no apparent improvement in the threshold strain energy of the epoxy nanocomposite reinforced with 0.4 wt% of the aligned CNFs. In comparison, a somewhat greater improvement to the threshold strain energy was observed for the epoxy nanocomposite reinforced with 0.7 and 1.0 wt% CNFs. In comparison to the unmodified epoxy, the threshold strain energy for the epoxy nanocomposites containing 0.7 and 1.0 wt% CNFs increased by ~200% and ~400% respectively. However, similar to the 0.4 wt% samples, the alignment of CNFs perpendicular to the crack growth path led to no further improvement to the threshold strain energy for the epoxy nanocomposite containing 0.7 wt% CNFs. In addition, the fatigue crack growth rate for the 1.0 wt% aligned and random CNF samples were very similar for the applied strain energy range. Therefore, the results for the fatigue crack growth for the 1.0 wt% random samples are not included in Figure 6-3.

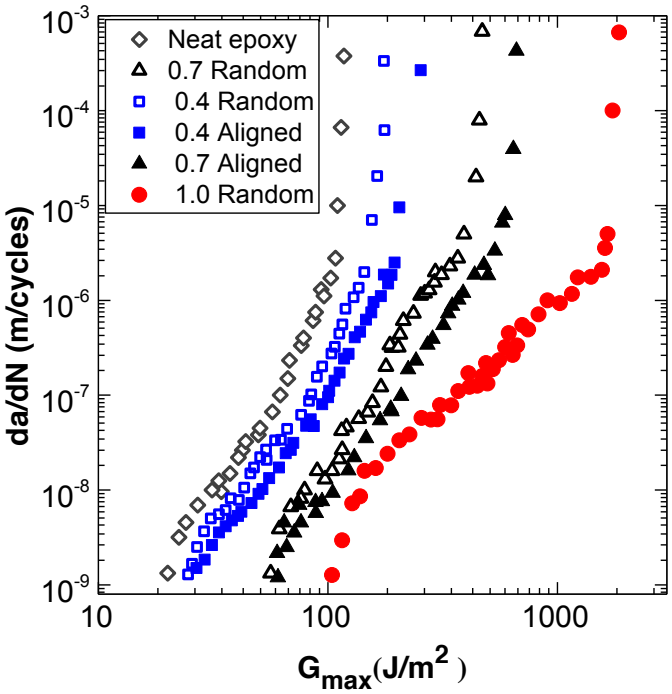

Figure 6-3 : Fatigue crack growth results showing the effect of the addition of CNFs on the cyclic-fatigue resistance of an epoxy nanocomposite

Similar to the quasi-static loading, the toughening due to CNF reinforcements led to the improvement in fatigue resistance of the epoxy nanocomposites. As can be seen in Figure 6-4a-c, fractographic studies revealed toughening mechanisms identical to the quasi-static test condition, namely, (a) interfacial debonding of the CNFs from the epoxy, (b) the pull-out of CNFs from the epoxy, (c) void growth of the epoxy which initiates from the hole created by the debonded CNFs, and (d) the CNFs then bridging and finally rupturing across the crack faces, behind the advancing crack tip. Nevertheless, a notable difference was that, a stable crack propagation mode was observed when the specimens were subjected to cyclic loading, in comparison to the unstable stick-slip crack growth observed during quasi-static loading conditions. In addition, the fracture surface of the epoxy nanocomposites subjected to cyclic loading revealed numerous CNFs had experienced a unique unravelling deformation. It can be seen in Figure 6-4a-d that the inner layer of the double-layer CNFs unravelled from the outer layer at multiple locations only when subjected to the fatigue loading. By contrast, under quasi-static loading the double-layer CNFs were observed to fracture without unravelling as shown in Figure 3-8 in section 3.3.3.

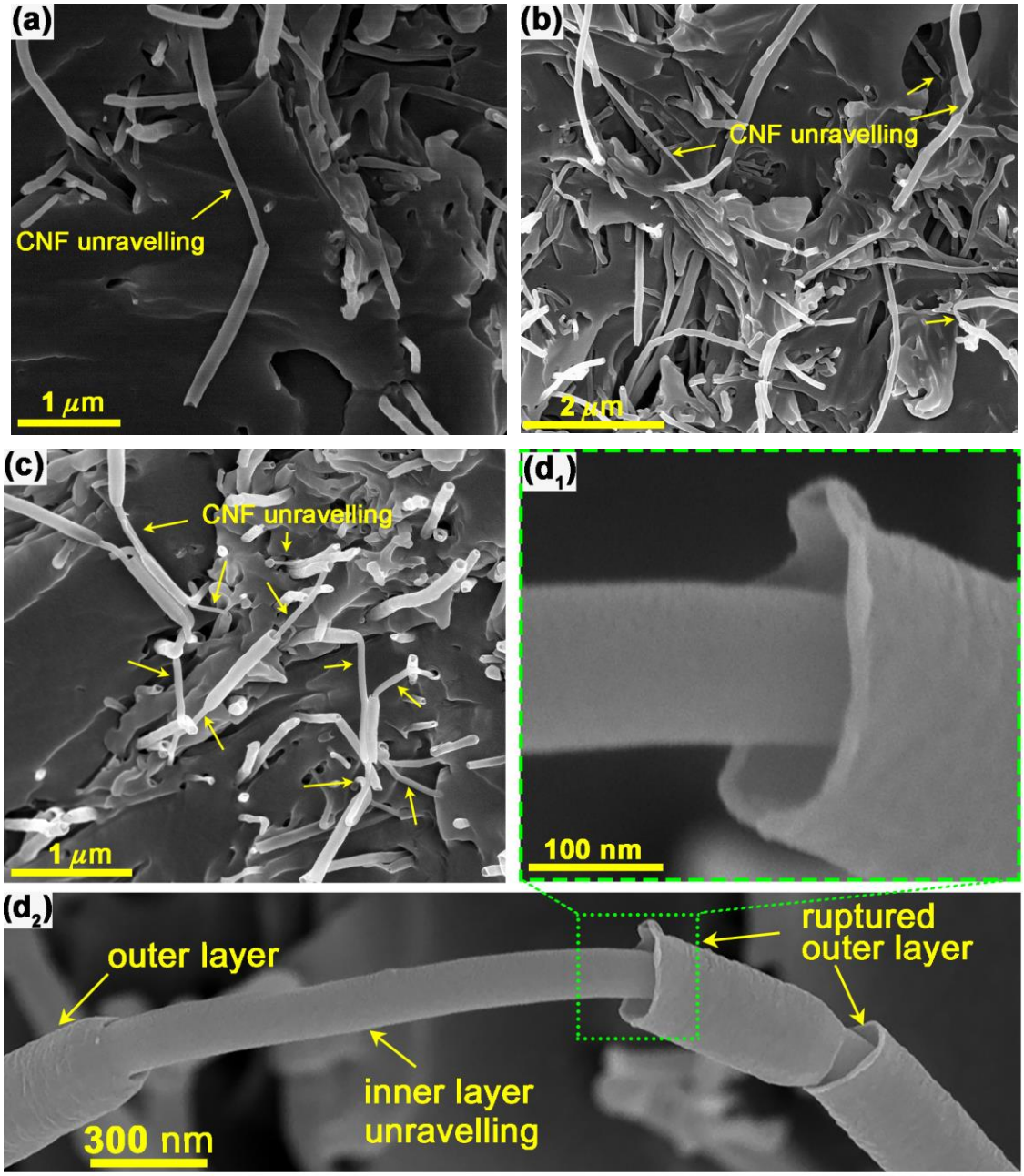

Figure 6-4 : SEM micrograph showing unravelling of CNFs on fatigue failure surface of epoxy nanocomposite containing randomly oriented (a) 0.4 wt%, (b) 0.7 wt% and (c) 1.0 wt% CNFs. (d) High magnification SEM image of an unravelling CNF observed on a fatigue failure surface.

Although the outer layer of the CNF is the primary load-bearing structure owing to its relatively higher stiffness and strength [255], the high magnification scanning electron microscope (SEM) (see Figure 6-4d) observations indeed confirmed that under fatigue loading the outer layer tended to fail prior to the uncoiling of the inner layer. This unravelling deformation mechanism was observed for about a quarter of the CNFs

pulled-out from the fracture surfaces. In most cases, the length of the inner layer being unravelled from the outer layer was ~30% of the entire length of the double-layer CNF.

6.3.2 Fatigue Induced Unravelling of Carbon Nanofibres

In contrast to CNTs which have a tubular structure, CNFs have a unique hybrid multilayer structure which consists of both conical and tubular graphene elements. There are two main types of CNFs: the first type has a single helical graphene layer, which are typically denoted as cone-helix CNFs, whilst the second type features a hollow-core with a double-layer microstructure [256]. These second type of double-layer CNFs are composed of an inner layer with a perfect cone-helix structure and an outer layer resembling a multiwall nanotube [62, 255]. Under quasi-static loading, the first type of CNFs with the cone-helix structure have been reported to undergo an unravelling deformation mechanism under increasing strain as they pull-out from the matrix [112].

The pull-out of the CNFs from the epoxy leads to the formation of a crack-bridging zone behind the tip (see Figure 6-5a) which provides further resistance to fatigue cracking. However, during fatigue loading, the CNFs within the crack bridging zone (see Figure 6-1 and Figure 6-5b-c) experience, sequentially, cyclic tension (crack opening) and compression (crack closing) loading. Under compression, the CNFs can bend and this causes micro-buckling of the outer layer (see the inset in Figure 6-5a). *In-situ* observations within the SEM of the fatigue process of a double-layer CNF have indeed confirmed that this unusual failure mechanism likely initiates from the inherent imperfection sites of the outer layer of the CNF due to the cyclic bending and unbending, as shown in Figure 6-5b-d. It is noteworthy, that although, the outer layer has a significantly higher stiffness and strength than that of the inner layer, its failure strain is much lower than that of the inner layer [255, 257]. Indeed, molecular-dynamic simulations have shown that the outer layer of such CNFs would fail in a brittle-like manner at much lower strains (i.e. of ~19%) than the inner layer which can sustain strains exceeding ~64% [257].

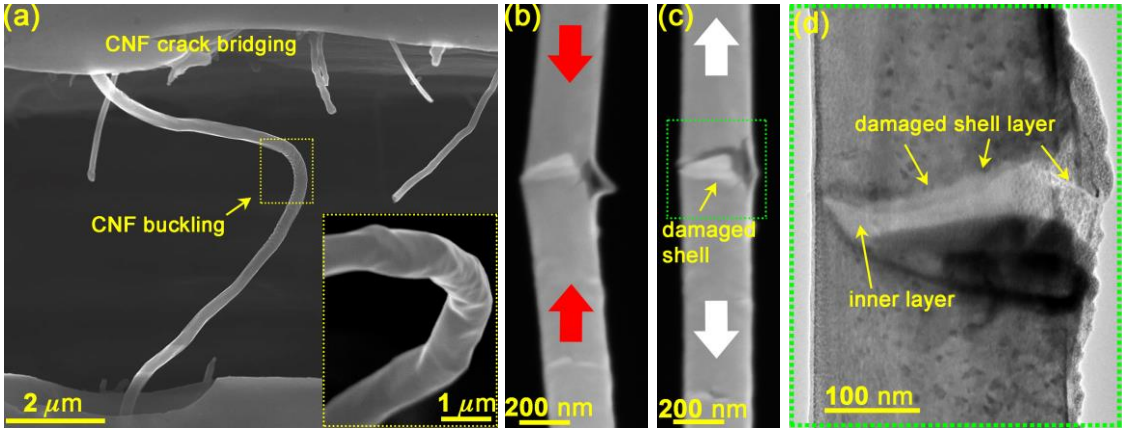

Figure 6-5 : (a) SEM observation of the fatigue cracks formed in DCB specimen showing the side view of the CNF crack bridging process zone immediately behind the crack tip and at minimum crack opening displacement. (b-c) SEM observation of the initiation and propagation of the fatigue damage during *in-situ* fatigue testing of the CNF shown under (b) compression and (c) tension loading. (d) TEM observation of the damaged outer shell of the CNF subjected to fatigue loading of the CNF shown in image (b-c).

As can be seen in Figure 6-6a, in some instances, the onset of such fatigue damage of the outer layer occurred simultaneously at multiple sites along the CNFs which led to the progressive unravelling of the inner layer at these sites (see Figure 6-6a-b). The unravelling of the inner layer causes the CNFs to thin in diameter, as can be observed in Fig 2c. Therefore, as shown schematically in Fig 2d, the cyclic-fatigue loading of the CNFs behind the crack tip leads to the fracture of the outer layer, thus causing an increase in the stress on the inner layer which then begins to unravel under tension. This unravelling deformation mechanism can be attributed to the existence of secondary bonds between each graphene cone within the inner layer [257]. The secondary bonds form during the heat treatment of these high heat-treated CNFs [258]. In particular, when heat-treated at 3000°C, the outer layer becomes thinner and attains an ordered graphitic structure resembling that of multi-wall nanotubes [259], as shown in Figure 6-7a-b. Whereas the inner layer attains the stacked-cup morphology with the open edges of its graphene cups coalesced via the secondary bonds in the form of loops [62, 258], as can be seen in Figure 6-7c-d. Molecular-dynamic simulation of the thermal-treatment of such CNFs has shown that these loops are the result of sp^2 bonding between adjacent graphene layers which form above a heat-treatment temperature of 725°C. In addition, the density of the secondary bonds increases with

temperature, resulting in a higher elastic strain limit for the inner layer of these high heat-treated CNFs [260].

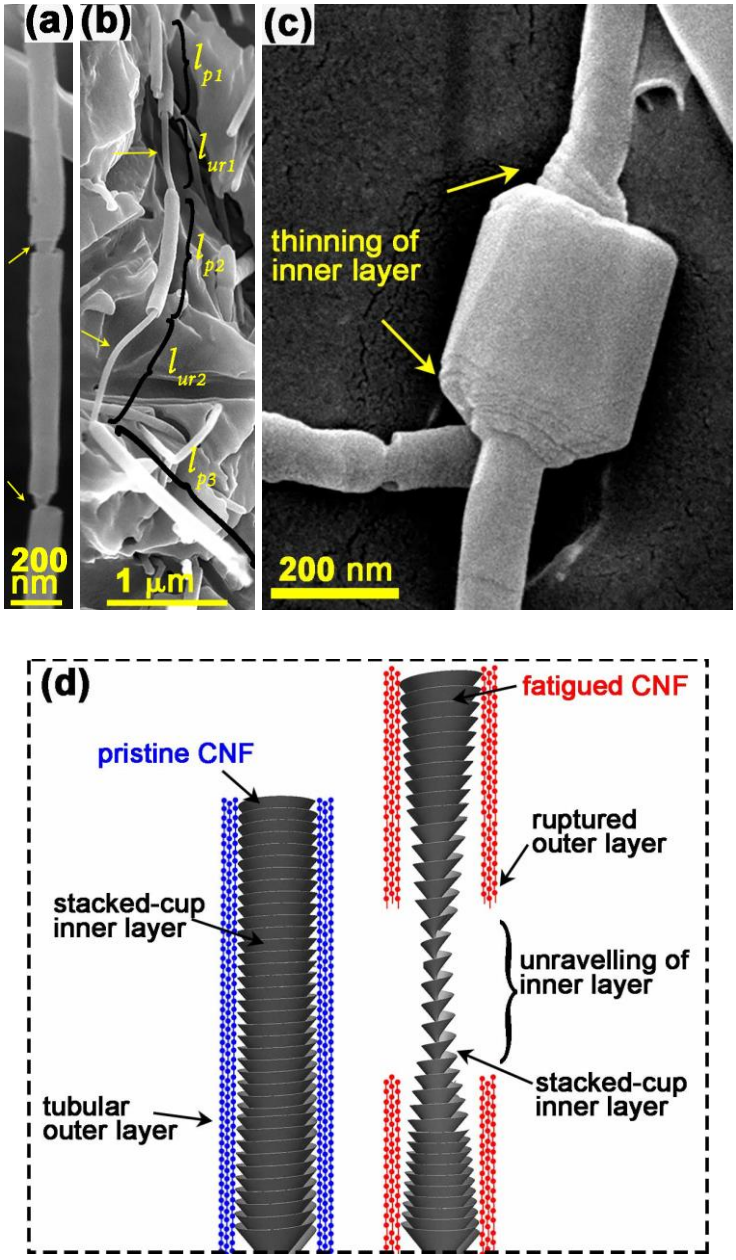

Figure 6-6 : (a-b) SEM micrographs of the unravelling type deformation of the double-layer CNFs observed on the fracture surface of the epoxy nanocomposite specimen tested under fatigue loading showing (a) the onset and (b) propagation of unravelling type deformation at multiple locations along the length of a CNF. (c) SEM observation of the thinning behaviour of the inner layer of an unravelled CNF. (d) Schematic illustration of the CNF microstructure demonstrating the unravelling type deformation of the inner CNF layer induced by the fatigue damage to the outer layer.

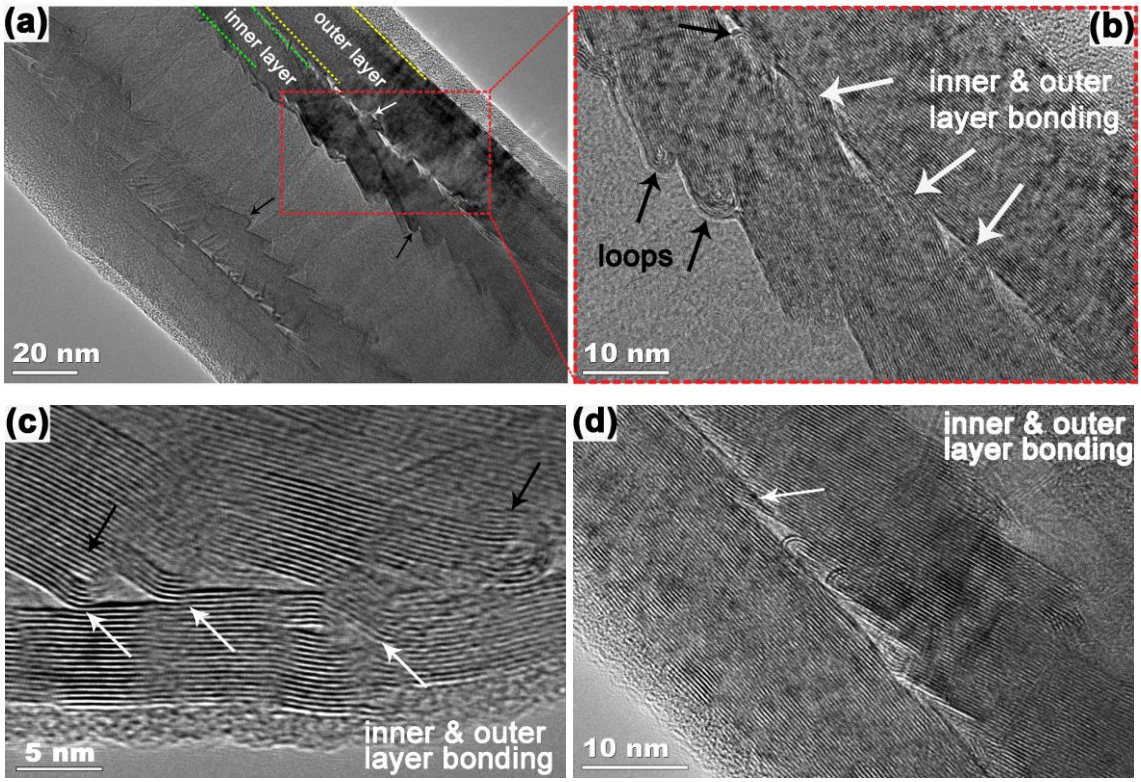

Figure 6-7 : (a-d) High-resolution TEM images of the double-layer CNFs in their as-supplied form showing the double layer structure consisting of an inner stacked-cup layer and an outer layer resembling multi-walled nanotube structure. The black arrows indicate the secondary bonding in form of loops between the graphene cups of the inner layer, and the white arrows indicate the bonding between the inner and outer layers.

However, as can be seen in Figure 6-7c-d**,** secondary bonds were also observed between the outer and inner layers in the form of continuous graphene sheets. A previous study on microstructural changes of CNFs induced by heat-treatment processes has also reported similar continuous graphene sheets linking the inner and outer layers [261]. These secondary bonds between the two layers would enable an effective load transfer from the outer layer to the inner layer during the unravelling deformation mechanism. In order to assess the load-bearing capability of an unravelling CNF, additional *in-situ* CNF pull-out tests were performed as shown in Figure 6-2 and Figure 6-8a. The results of the load versus extension test for a CNF are given in Figure 6-8b**.** This curve shows an unusual type of stick-slip behaviour during the load-extension test and this arises from there being three separate stages in the unravelling deformation mechanism of the CNF, as shown in Figure 6-8. Firstly, the load increases linearly up to point A. Secondly, this is followed by a drop in the load to point B due to the rupture of the

outer layer causing sudden unravelling and a dramatic extension of the CNF. The stiffness of the CNF prior to unravelling (measured from line OA) is about 86 GPa which is similar in value to previous reports of experimentally-measured stiffnesses of the CNFs [255]. Thirdly, upon continuing the extension of the CNF, the load increases linearly to point C followed by another sudden drop in load due to a second unravelling event as shown in Figure 6-8a. The unravelled portion of the CNF appears bright white in the SEM image in Figure 6-8a. The increase in load to point E led to additional unravelling of the CNF with its total length suddenly becoming greater than the applied displacement. This causes the complete unloading of the CNF due to the displacement controlled *in-situ* test set-up used for this investigation.

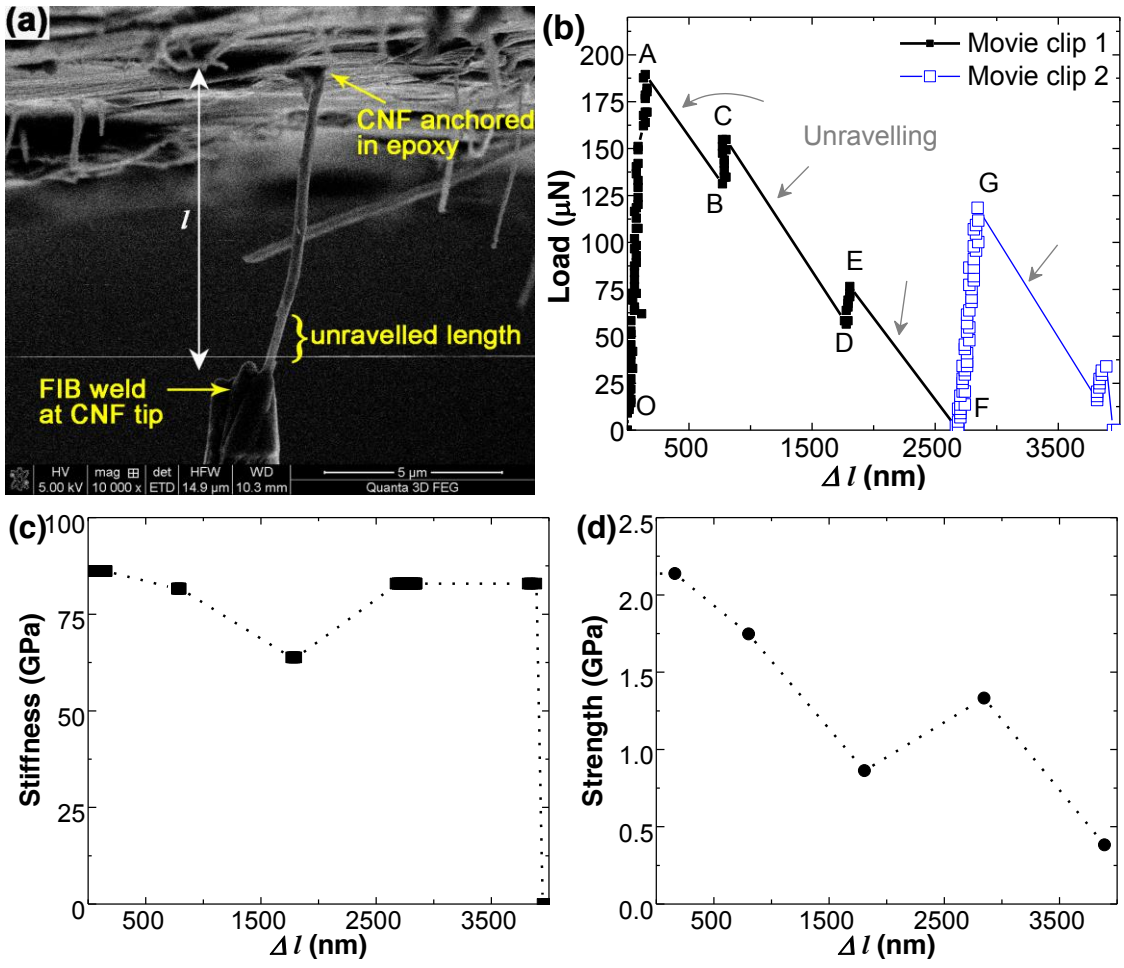

Figure 6-8 : (a) SEM image acquired during the *in-situ* CNF pull-out test used to characterise the (b) load versus extension behaviour for an unravelling CNF. (Note: This image corresponds to the point D of the load-extension curve in (b)). (c) The stiffness and (d) the strength of the CNF calculated at various stages of the unravelling process.

However, restarting the extension of CNF led to a linear increase in the load to point G which is higher than the previous peak load at point E. Thus, despite the fracture of the outer layer, the inner layer of the CNF possesses excellent load-carrying capability due to secondary sp^2 bonds formed during its heat treatment. In addition, as shown in Figure 6-8c, a very similar stiffness was retained by the unravelled CNFs (corresponding to load lines BC, DE and FG in Figure 6-8b) in comparison to the stiffness of the CNF prior to its unravelling. However, as shown in Figure 6-8d, the strength of the CNF decreased after the fracture of the outer layer, as would be expected. In addition, there was a gradual reduction in strength of the CNF with each unravelling stage. This is attributed to the gradual rupture of the sp^2 bonds and a subsequent reduction in the bond density during each unravelling stage. Nevertheless, the average strength of the unravelled CNF was measured to be about 50% of its strength prior to unravelling (i.e. a strength corresponding to load point A). Moreover, the results of stiffness and strength given in Figure 6-8 are in good agreement with previous molecular-dynamic simulations of the unravelling deformation mechanism of the CNF [257, 260]. Furthermore, the energy dissipated during the unravelling mechanism given by the area under the load-extension curve in Figure 6-8b is about 700% higher than the energy estimated for the rupture of the CNFs using Eq. (3-7) with a value of CNF strength (i.e. 3.34 GPa) measured in a previous study [225] and the stiffness (i.e. 86 GPa) measured in the current study. This is in good agreement with molecular-dynamic simulation that shows a 600% increase in energy dissipated due to the unravelling mechanism in comparison to the energy required to rupture the CNFs [257].

6.3.3 Traction Load-Displacement Curve for Unravelling CNF

From Figure 6-4 and Figure 6-6, it can be seen that the CNFs have undergone frictional pull-out after unravelling. Despite the damage to the outer layer, the unravelling of the inner layer structure of the double-layer CNFs continue to promote the crack-bridging mechanism under fatigue loading as shown in Figure 6-9a-b. The crack bridging by the unravelled CNFs provides the traction load which reduces the stress concentration at the crack-tip, and a larger applied force is thus required to achieve a given fatigue crack-growth rate, da/dN. This combination of the frictional pull-out and unravelling of

the CNFs would continue to bridge the crack even at a relatively high crack opening displacement, and thereby effectively retard the fatigue crack growth. Figure 6-9c shows the expected bridging traction load-displacement curve behaviour in the presence of multiple unravelling deformations for the double-layer CNF shown in Figure 6-6b. The load required to pull-out a fibre from the matrix is given by Hull [83] as,

$$P = \pi d \tau_i l_p \tag{6-5}$$

where τ_i, d and l_p are the interface strength, the diameter and the total pull-out length of the CNF shown in Figure 6-6b. The total frictional pull-out length of the CNF is equal to

$$l_p = l_{p1} + l_{p2} + l_{p3} \tag{6-6}$$

where, l_{p1}, l_{p2} and l_{p3} are the lengths corresponding to length of frictional pull-out segments. The peak static pull-out traction load given by Eq. (6-5) for the CNF shown in Figure 6-6b is plotted as a function of the pull-out length in Figure 6-9c. The values of the model parameters used to calculate the traction load are listed in Table 6-1.

For the pull-out process involving the unravelling deformation, we assume the following sequence of events, firstly, the CNF undergoes a partial frictional pull-out equal to the length l_{p1} followed by unravelling of the first core segment equal to a length l_{ur1}. It is then followed by a subsequent frictional pull-out (with length l_{p2}) and the second unravelling equal to the length l_{ur2}. Finally, the pull-out of the remaining embedded segment of length l_{p3}. The values for the length of the unravelling segments of the CNF shown in Figure 6-6b are also listed in Table 6-1. Then the load sustained during the unravelling of the first and the second core segments is given by Eq. (6-7) and (6-8).

For displacement $l_{p1} \leq l_{ur1} \leq l_{p2}$

$$P = \pi d \tau_i (l_p - l_{p1}) \tag{6-7}$$

and for displacement $l_{p2} \leq l_{ur2} \leq l_{p3}$

$$P = \pi d \tau_i (l_p - l_{p1} - l_{p2}) \quad (6\text{-}8)$$

Table 6-1 : List of values for the various parameters used in the analytical modelling of the traction load-displacement curves.

Parameter	Symbol	Unit	Value
CNF diameter	d	nm	125
Interface strength	τ_i	MPa	25
Pull-out length	l_p	µm	5.3
1st segment length	l_{p1}	µm	1.1
2nd segment length	l_{p2}	µm	1.5
3rd segment length	l_{p3}	µm	2.7
1st unravelling length	l_{ur1}	µm	0.95
2nd unravelling length	l_{ur2}	µm	1.85

The additional contribution to the energy dissipation during the pull-out of CNFs due to the unravelling is estimated to be ~60%, which is consistent with the extra enhancement in fatigue resistance in comparison to the improvement in the quasi-static fracture toughness of the epoxy nanocomposites.

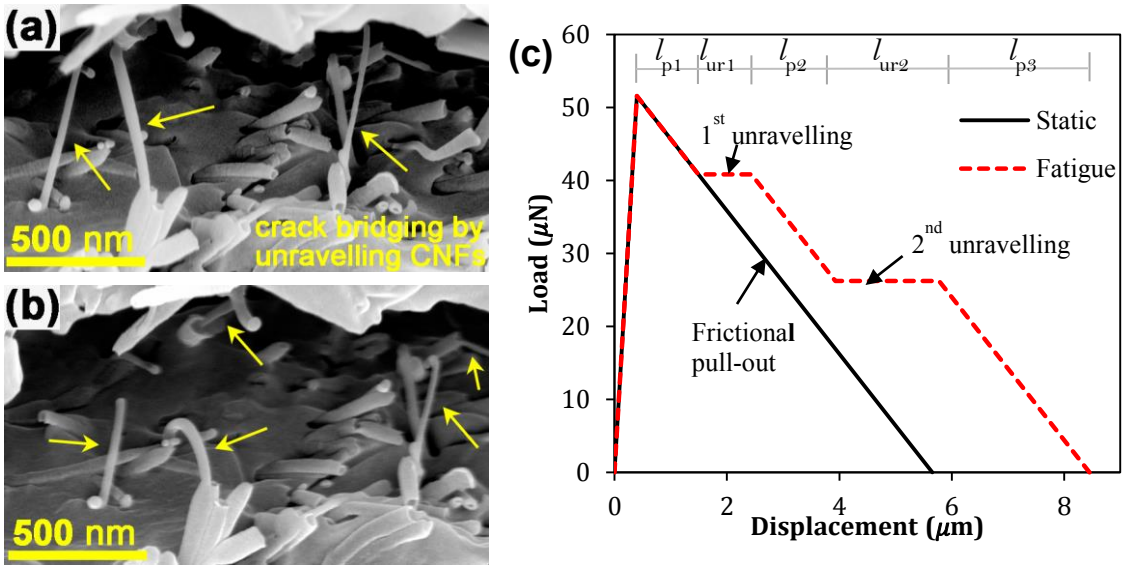

Figure 6-9 : (a-b) SEM observations of the double-layer CNFs bridging the fatigue cracks via superplastic deformation of their inner layer at (a) a low and (b) a slightly higher crack-opening displacement. (c) Effect of the double-layer CNF unravelling on the bridging traction load-displacement behaviour during pull-out from the epoxy matrix.

6.4 Conclusions

The cyclic fatigue crack growth resistance of the epoxy composites improves significantly with the inclusion of CNF reinforcements. The maximum cyclic critical strain energy release rate as well as the threshold strain energy of the CNF-epoxy nanocomposites increases with the CNF content. A similar improvement also occurs due to the alignment of CNFs perpendicular to the crack growth path up to a limiting concentration of about 0.7 wt%, above which no further improvement to the fatigue resistance was achieved due to their alignment. The main toughening mechanisms which led to the increase in the fatigue resistance for the CNF toughened epoxy nanocomposite were similar to those observed for quasi-static tests including (a) interfacial debonding of the CNFs from the epoxy, (b) the frictional energy associated with the CNFs now pulling-out from the epoxy, (c) void growth of the epoxy which initiates from the hole created by the debonded CNFs, and (d) the CNFs bridging and finally rupturing across the crack faces, behind the advancing crack tip. In addition, a unique energy-dissipative deformation mechanism of double-layer CNFs was observed under cyclic fatigue loading. This deformation mechanism, which has been rarely observed in previous quasi-static tests, contributes to the improvement observed in the cyclic-fatigue resistance of such epoxy nanocomposites.

Chapter 7

Disbond Detection in Composite Joints using Aligned Carbon Nanofibre Network and DC Potential Drop Technique

Abstract

This chapter investigates the ability of carbon nanofibre (CNF) networks for *in situ* monitoring of fatigue induced disbond damage in adhesive bonded composite joints. The inclusion of CNFs in the epoxy adhesive increases its conductivity while simultaneously retarding the delamination growth rate. The improved electrical conductivity is utilized to evaluate the ability of the CNF networks to monitor and detect the fatigue induced disbond damage via *in situ* electrical resistance changes measured using a DC potential drop technique. The changes in total resistance was a function of the bulk electrical resistivity of the adhesive and the bond dimensions, which were related to the disbond length to model and determine the size of the disbond. Good agreement were found between the optical disbond measurements and the calculated disbond length using the *in situ* resistance measurements, therefore proving the ability of CNFs to not only detect disbond in composite bonded joints but also retard its growth rate.

The research presented in this chapter has been published in the following conference paper:

- Ladani RB, Wu S, Mouritz AP, Kinloch AJ, Ghorbani K, Wang CH. *Disbond Monitoring of Composite Adhesive Joints with DC Resistance Technique using Carbon Nanofibre Network*. In Proceeding of the 26th International Conference on Composite Materials, Copenhagen, Denmark, 2015.

7.1 Introduction

One of the key challenge for using composites as superstructure material is the need for joining during initial modular construction and repair of damaged articles while in service. These joining interfaces generally involve discontinuity of the reinforcing fibres resulting in higher stress concentration regions. For joining composite parts, adhesively bonded joints provide many advantages such as low cost, high strength to weight ratio, low stress concentration, fewer processing requirements and good environmental resistance [262]. However, their inability to be disassembled for periodic inspection provides a major drawback. Therefore, bolted joints are preferred for joining composite parts, in spite of their low bearing strength [263]. Existing airworthiness regulations prescribe that safety critical structures must sustain the design ultimate load in the presence of damage larger than the detection limit of chosen non-destructive inspection methods [9]. Detection of damage in bonded joints is currently limited to ultrasonic, radiography and acoustic emission techniques during scheduled maintenance intervals. Potential drop and eddy current technique cannot be used in the absence of through-thickness conductivity in bonded joint due to the dielectric property of the epoxy adhesives [96]. Since regular visual inspection are limited to the detection of flaws that lie near the surface, there is a strong demand for additional repeatable and reliable non-destructive inspection techniques that could be applied on field to ensure the integrity of bonded joints.

Carbon nano-reinforcements can form conductive networks in polymeric materials at extremely low weight fractions while simultaneously improving the fracture toughness. Numerous studies have investigated their use for detecting damage in composites [35, 64, 203-206]. Other studies have utilized the conductive nano-reinforcement networks for *in-situ* health monitoring of disbond in composite joints [36, 207]. Lim et al. [36] reported the use of CNT networks to monitor the initiation of damage in epoxy bonded lap joints under quasi-static and dynamic tensile loading. Mactabi et al. [207] studied the electromechanical response of CNT networks incorporated in bonded lap joints under tensile fatigue loading. While a short communication by Zhang et al. [210] is the only study reported on utilizing CNT networks in epoxy polymer to monitor and predict the fatigue crack growth during mode I cyclic loading. The study successfully demonstrated that changes in resistance

induced by mode I fatigue crack growth in bulk epoxy samples could be used to determine the size of the underlying damage. The potential application of this technique to monitor and detect fatigue crack growth in epoxy bonded composite joints has never been studied.

This chapter focuses on utilizing the improved electrical conductivity of an epoxy nanocomposite adhesive containing aligned CNFs for monitoring and detection of fatigue crack growth in epoxy bonded composite joints. The chaining is accomplished by applying an external AC electric-field whilst the adhesive is liquid prior to crosslinking. The electrical response of the nanocomposite adhesive is measured *in-situ* during cyclic-fatigue testing using a DC potential drop technique. The *in-situ* resistance measurements are used to determine the size of the fatigue cracks. A simple resistivity model is used to evaluate the disbond size based on the resistance measurements.

7.2 Materials and Experimental Methodology

The fatigue testing was performed on the same samples that were fabricated to study the fracture energy of epoxy nanocomposites containing 0.4, 0.7 and 1.0 wt% of CNFs in Chapter 3. The details of the sample fabrication process are outlined in section 3.2. As shown in Figure 7-1a, two electrical contacts were established on the outer surface of the composite adherends. The adherends were lightly sanded to expose the conductive carbon fibres and a conductive silver paste was used to bond the contact wires for resistance measurements. The silver paste was allowed to cure for at least 24 hours prior to conducting the *in-situ* resistance measurement and mode I fatigue test. Mode I cyclic-fatigue testing was performed by applying a constant amplitude sinusoidal cyclic load at a frequency of 5 Hz. The tests were performed using a computer-controlled Instron E3000 system with a 3 kN load cell under displacement control with a constant cyclic ratio (*R*-ratio). The ratio between the minimum and the maximum applied displacement in one load cycle was kept constant at 0.5. As shown in Figure 7-1a, non-conductive grips made of Bakelite were used to isolate the samples from the fatigue rigs. The specimens were subjected to cyclic fatigue loading with the maximum crack opening displacement being chosen such that the initial value of the

applied strain-energy release-rate was about 250 J/m^2. A datataker (Delloger model 80) with a four probe setup was used for *in-situ* resistance measurements during mode I fatigue tests. The fatigue crack growth was measured from the 50 mm pre-crack (i.e. Teflon insert) using a travelling microscope.

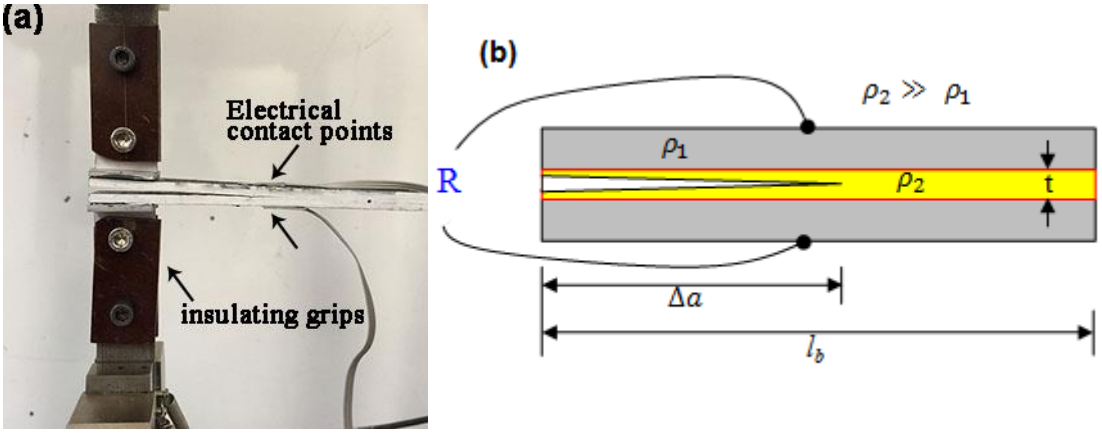

Figure 7-1 : (a) Photograph of the experimental setup for *in situ* resistance measurements during mode I fatigue testing; and (b) schematic illustration of the *in-situ* resistance measurement setup for the DCB joint.

7.3 Results and Discussion

7.3.1 Electrical resistance response to disbond in joints

Figure 7-2a. shows the transient resistance changes measured in-situ during cyclic loading of DCB joints at stress intensity ratio of 0.5 and applied fracture energy of 250 J/m^2. The resistance increased monotonically with increasing number of cycles. Figure 7-2b shows the effect of displacement on the transient resistance measurements obtained during cycling. The resistance increased at the maximum and decreased at the minimum crack opening displacement, such that there was an irreversible increase in resistance after each cycle. The increase in resistance likely corresponds to the disbond of adhesive, since the joint failure was cohesive in the adhesive, as shown in Figure 7-3. The effect of disbond length on the resistance measurements are shown in Figure 7-4a. There was a significant increase in resistance with increasing disbond length. For 1 wt % samples with aligned CNFs, the resistance had almost doubled as the length of disbond reached 50% of the intact bond ligament length. The results show that the crack

growth modifies the charge conduction pathways within the CNF modified adhesive resulting in a resistance change.

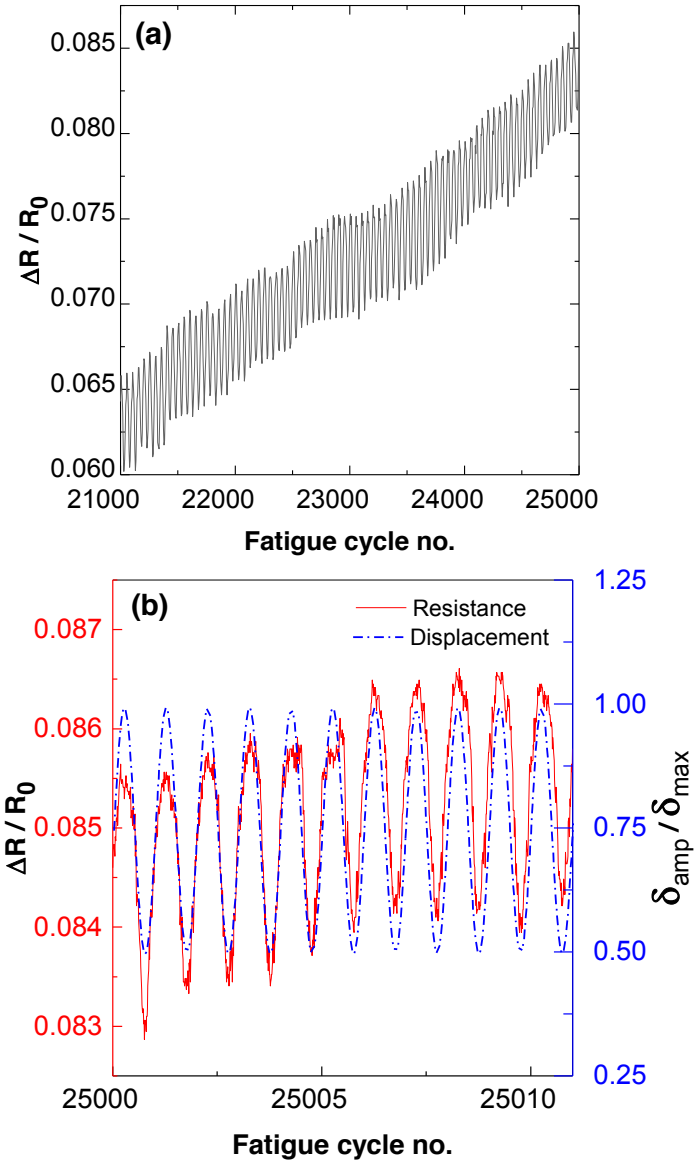

Figure 7-2 : In situ resistance response during mode I cyclic fatigue testing (a) at 5 Hz, (b) at 0.01 Hz fatigue cycling.

The change in the total resistance is due to the shortening of the un-cracked bond ligament ahead of the crack as shown in the schematic in Figure 7-1b. Since the total resistance is a function of the electrical resistivity of the adhesive and structure's dimensions (width and length), the disbond length, Δa can be explicitly related to the measured resistance by,

$$R = \frac{\rho_2 t}{(l_b - \Delta a) b} \tag{7-1}$$

where ρ_2, l_b, t, b, and R denote the electric resistivity of the CNF modified adhesive, the length, thickness and width of the adhesive, and the total resistance, respectively.

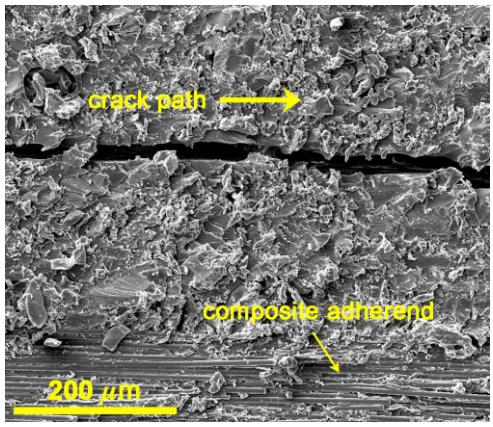

Figure 7-3 : SEM micrograph of the side view of a fatigue tested sample containing 0.4 wt% aligned CNFs.

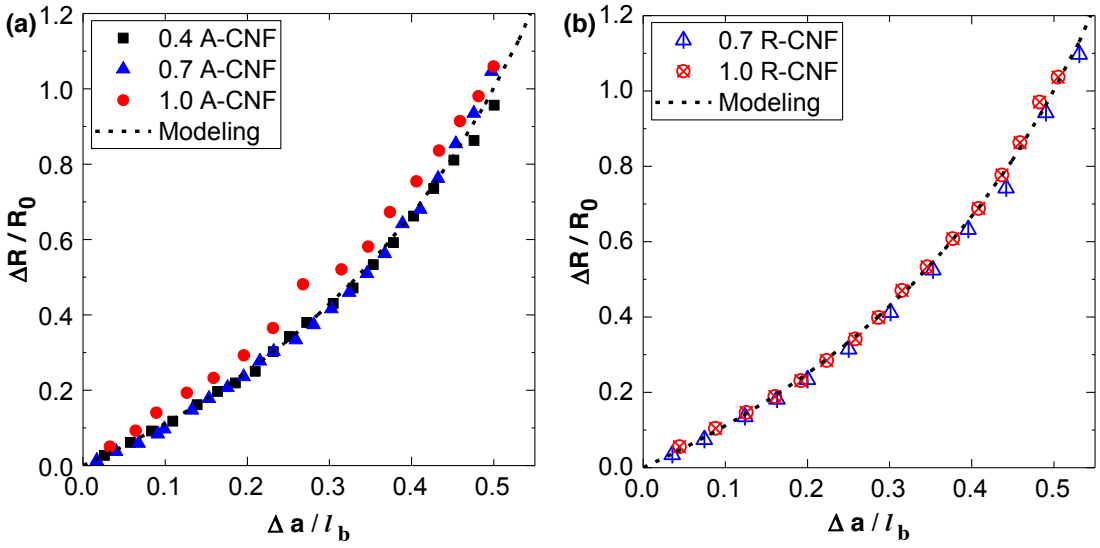

Figure 7-4 : Increase in resistance as a function of disbond length for samples containing (a) aligned CNFs and (b) random CNFs.

For comparison, the above relationship is plotted in Figure 7-4a. For the samples containing aligned or randomly-oriented CNFs, the change in resistance due to fatigue crack growth is in good agreement with the model given by Eq. (7-1). However, for the

epoxy nanocomposite samples containing 0.4 wt% randomly-oriented CNFs, the resistivity was too high to be measured with the four probe setup used to perform the *in-situ* resistance measurements during mode I fatigue testing. This was due to the CNF content in the epoxy being lower than the percolation threshold (i.e. 0.43 wt%) for the randomly-oriented CNF-epoxy nanocomposite. As discussed in section 5.3.1, the DC conductivity could only be measured at CNF content greater than the corresponding percolation threshold.

7.3.2 Determining disbond size from resistance measurement

Crack growth results in a decrease in the effective cross-sectional area of the bondline causing the resistance across the bond interface to increase. For a constant width joint, the change in resistance can be used to calculate the increase in the crack length by rearranging Eq. (7-1) as follows:

$$\Delta a = l_b - \frac{\rho_2 t}{Rb} \tag{7-2}$$

Figure 7-5a1 & b1 shows the comparison of the measured and calculated disbond length from the in-situ resistance measurements taken during cyclic loading. The calculated crack length is in good agreement with the optically observed crack length. Therefore a conductive adhesive could be effectively used for in-situ monitoring of crack growth in a composite bonded joint. Furthermore, to distinguish between permanent resistance changes due to crack growth and any reversible change which occurs due to contact of crack face upon unloading, the joints were unloaded intermittently to measure the resistance corresponding to closed cracks. Figure 7-5 a2 & b2 shows the calculated crack length from the resistance corresponding to closed cracks upon unloading of the DCB samples. There was a small reduction in the resistance upon unloading of the samples, indicating the sensitivity of resistance to crack closure phenomenon. The crack length calculated from the resistance measurement corresponding to the unloaded state was almost 10 % lower than the optical crack measurements. The effect of crack closure was more prominent for the more conductive 0.7 and1.0 wt% samples, irrespective of the alignment of the CNFs. The discrepancy between the observed crack length and the calculated crack length increased with the

length of disbond. In contrast, for the 0.4 wt% aligned samples, the effect of crack closure on the calculated crack length was almost negligible. This was due to the permanent damage of the conduction path length with the progression of damage. In highly conductive adhesive for e.g. 0.7 and 1.0 wt% samples in this study, a significantly larger number of CNFs were exposed on the crack face (see Figure 3-9). The exposed CNFs come into random contact upon closure of the crack, leading to reestablishment of conduction pathways causing a drop in the measured resistance.

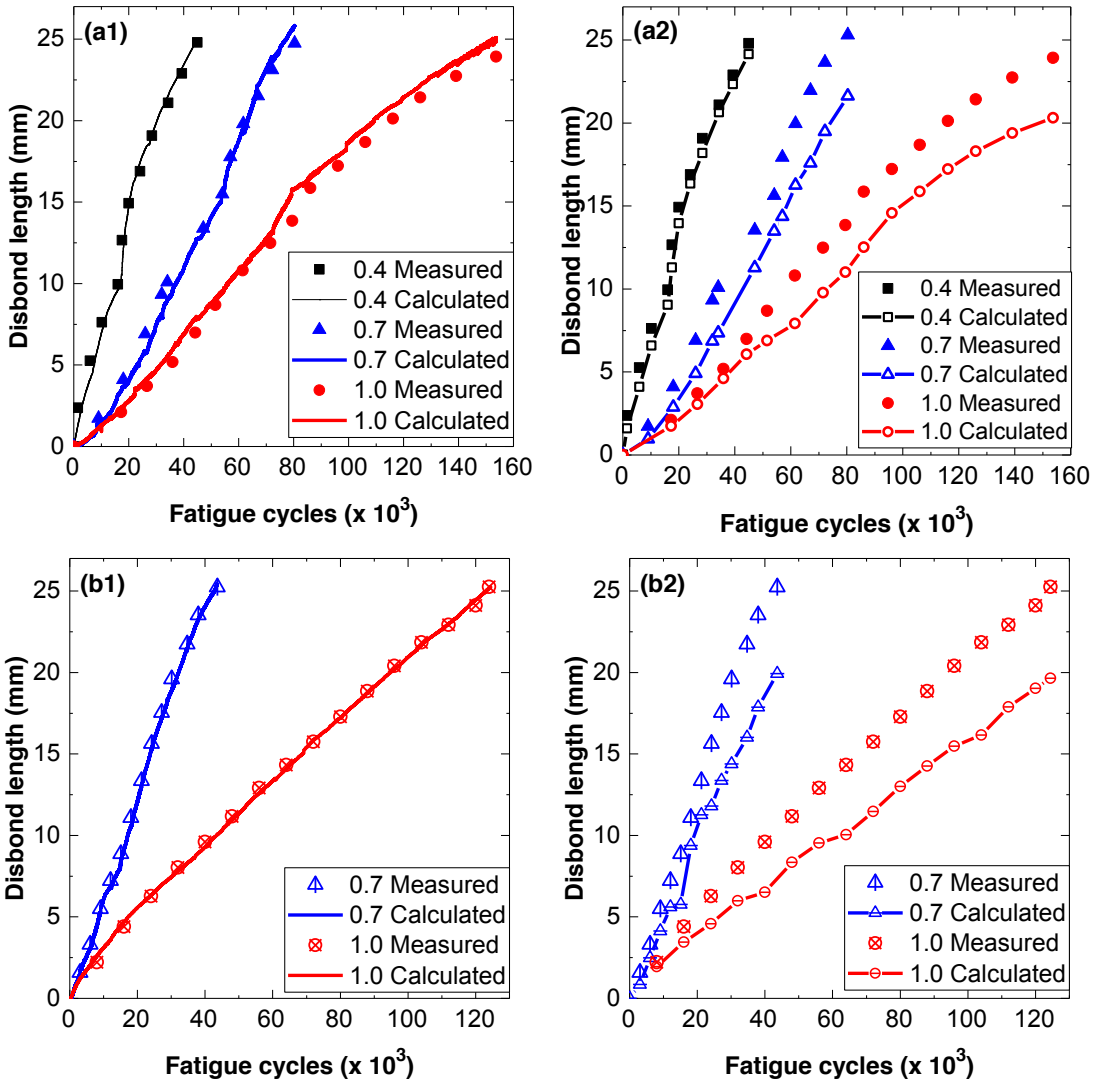

Figure 7-5 : Comparison of the optical observations and the calculated disbond length from Eq. (7-2); (a) using *in situ* resistance measurements (b) upon unloading the samples

However, for the 0.4 wt% sample containing aligned CNFs, the promotion of percolating networks by the electric-field induced chaining leads to a limited number of

conduction pathways, as shown in Figure 7-6. The damage caused to these conductive pathways due to the rupture or pull-out of CNFs during the crack propagation process cannot be reversed upon unloading of the cracked faces. Therefore, for 0.4 wt% aligned samples, the crack lengths calculated from the electrical resistance corresponding to a closed crack were in good agreement with the optically measured crack lengths. Therefore, the alignment of a low content of CNFs in an epoxy adhesive could be beneficial for detecting closed cracks.

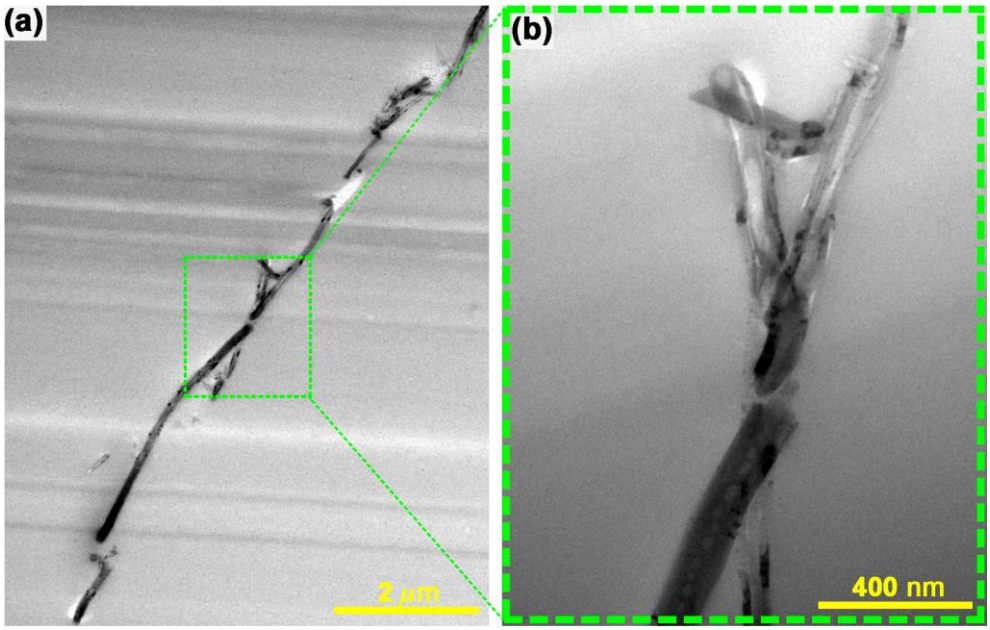

Figure 7-6 : TEM images of the CNF-epoxy nanocomposites containing 0.4 wt% of CNFs aligned via the application of the AC electric-field. Image (b) is an inset of image (a) showing the various contact points within a chain formed by several CNFs.

7.4 Conclusion

Real-time *in-situ* electrical resistance measurements are performed during mode I cyclic loading of CNF-reinforced adhesive bonded composite joints to evaluate the effect of fatigue induced disbond on electrical resistance changes. The through-thickness electrical resistance of the adhesively bonded joints increased monotonically with the disbond length. The electrical resistance had almost doubled when the disbond length reached half the value of the initial bond length. A simple model is then used to correlate the changes in resistance to the material resistivity and its geometry. The changes in resistance measured due to fatigue induced disbond are in good agreement

with the resistivity model. This model is then used to calculate the disbond length from the change in resistance measured during fatigue testing. The disbond length calculated from the *in-situ* resistance measurements is in good agreement with the optically observed disbond length. The alignment of CNFs in the through-thickness direction of the epoxy adhesive layer showed no obvious advantages over their random counterparts. However, the sample containing 0.4 wt% aligned CNFs showed the best prospects for detecting closed cracks. Whereas, for the samples containing 0.7 and 1.0 wt% CNFs (random or aligned), there occurred a reduction in the measured resistance upon unloading of the sample due to the contact between the cracked faces. Therefore, highly conductive adhesive are less effective for detecting closed disbonds or cracks. This electrical resistance based technique can be used in real-time for *in-situ* detection and monitoring of disbond damage in adhesively bonded composite joints and offers an alternative to traditional non-destructive inspection techniques.

Chapter 8

Improving the Toughness and Electrical Conductivity of Epoxy Composites using Magnetic Field Aligned Magnetite-Carbon Nanofibres

Abstract

In this chapter, magnetite-carbon nanofibre hybrids (denoted by "Fe_3O_4@CNFs") have been used to facilitate the alignment of CNFs in epoxy using a relatively weak magnetic-field. Experimental results have shown that a weak magnetic-field (~50 mT) can align these newly-developed nanofibre hybrids to form a chain-like structure in the epoxy resin. Upon curing, the epoxy nanocomposites containing the aligned Fe_3O_4@CNFs show (i) greatly improved electrical conductivity in the alignment direction and (ii) significantly higher fracture toughness when the Fe_3O_4@CNFs are aligned normal to the direction of crack growth, compared to the nanocomposites containing randomly-oriented Fe_3O_4@CNFs. The mechanisms underpinning the significant improvements in the fracture toughness have been identified, including interfacial debonding, pull-out, crack bridging and rupture of the Fe_3O_4@CNFs, and plastic void growth in the polymer matrix.

The research presented in this chapter has been conducted in collaboration with Dr. Shuying Wu which was published in the following journal and conference papers:

- Wu S, Ladani RB, Zhang J, Kinloch AJ, Zhao J, Ma J, Zhang X, Mouritz AP, Ghorbani K, Wang CH. *Epoxy Nanocomposites Containing Magnetite-Carbon Nanofibres Aligned Using a Weak Magnetic Field*. Polymer (United Kingdom). 2015; 68:25-34.
  The open access journal article from Polymer (United Kingdom) is attached in Appendix A.III.

- Ladani RB, Wu S, Kinloch AJ, Mouritz AP, Wang CH. *The unravelling of carbon nanofibres under fatigue loading*, Carbon, 2016. (submitted)

8.1 Introduction

Different approaches for aligning carbon nano-reinforcements have been reported in the literature, mainly based on mechanical stretching [264, 265] or the application of an electric-field [53, 266] or magnetic-field [54, 165, 186, 187, 267, 268]. Although using an electric-field is recognized as an effective method, this technique is typically restricted to materials with very low electrical conductivity, since the field strength is usually limited to avoid dielectric breakdown of the polymer [268]. Moreover, due to their low magnetic susceptibility [54, 165, 186, 187], an extremely strong magnetic-field (e.g. of several Teslas) is usually required to align carbon-based nano-reinforcements. For instance, Camponeschi and co-workers [54] employed a magnetic-field of up to 25 T to orientate and align CNTs in an epoxy resin and found that the properties of the resulting nanocomposites were superior to those prepared in the absence of a magnetic-field. Another similar attempt was reported by Mahfuz and co-workers [186] who used magnetic-fields of up to 28 T to align CNFs in a two-phase toughened epoxy resin system and achieved 21% and 3% increases in the compressive strength and modulus compared to randomly-oriented CNFs. The necessity to employ such high magnetic-fields limits the practical application of this method. Therefore, various methods have been reported to functionalise carbon nano-reinforcements with magnetic nanoparticles, especially iron-based nanoparticles, so as to align the nano-reinforcement in a polymer matrix without needing to employ high magnetic-fields [55, 188, 189]. For instance, magnetite (Fe_3O_4) decorated single-walled CNTs have been developed using a sonochemical oxidation process and these hybrid nano-reinforcements were successfully aligned in an epoxy using a relatively weak magnetic-field [188].

However, at present there is no report on aligning iron oxide-CNFs in an epoxy resin using a relatively low magnetic-field to selectively reinforce the epoxy polymer in a preferred orientation. Therefore, the aim of the present chapter is to explore the magnetic-field induced alignment of CNFs functionalised with iron oxide and its effects on the fracture and electrical properties of the epoxy nanocomposites. The functionalised carbon nanofibres, denoted by Fe_3O_4@CNFs, are first dispersed into a liquid epoxy resin which is then cured under a relatively weak magnetic-field of ~50 mT. The electrical conductivity and fracture toughness of the cured epoxy

nanocomposites containing Fe_3O_4@CNFs are measured and compared. Finally, the toughening mechanisms are identified from fractographic studies.

8.2 Materials and Experimental Methodology

Materials

Vapour grown carbon nanofibres (VGCNFs) (Pyrograf®-III, grade PR-24-XT-HHT) used in the earlier work presented in Chapter 3 were also used in the present study. The details of the CNFs are given in section 3.2. The CNFs were functionalised with Fe_3O_4 nanoparticles using co-precipitation method, to improve their magnetic susceptibility. The CNF functionalisation was conducted by Dr. Shuying Wu as part of the broader research project under the Australian Research Grant Program (DP140100778). Further details on the preparation and characterisation of the magnetic Fe_3O_4@CNFs can be found in the published paper which is attached in Appendix A.III.

Preparation of the bulk epoxy nanocomposites with Fe_3O_4@CNFs

The Fe_3O_4@CNFs were firstly dispersed in a small amount of acetone by bath sonication for 15 minutes (the typical concentration being 20 mg/mL). Epoxy resin was then added and the sonication process was continued for 1 h. The acetone was then removed under reduced pressure. Subsequently, a stoichiometric amount of hardener was added and the mixture was poured into a rubber mold for curing. To align the Fe_3O_4@CNFs, the mixture was subjected to a weak magnetic-field of ~50 mT generated by a pair of permanent magnets whilst it was being cured. Using a gaussmeter, the intensity of the magnetic-field was measured to be approximately 50 mT at a distance of 4 cm between a pair of ferrite magnets which were 150 × 50 × 25.4 mm in size. Initial, exploratory, experiments were carried out using different intensities of magnetic-field, ranging from 20 mT to 50 mT by changing the gap between the magnets. Since the alignment of the Fe_3O_4@CNFs needs to be completed prior to gelation of the epoxy (the gel time of the epoxy is around 20-30 minutes at 25 ^oC), a magnetic-field strength of 50 mT was finally selected so that the Fe_3O_4@CNFs could

be highly aligned within approximately 10 minutes from the application of the magnetic-field. Epoxy nanocomposites containing various weight contents (i.e. 0.0, 0.2, 0.4, and 0.6 wt%) of the Fe_3O_4@CNFs were prepared.

Preparation of epoxy nanocomposite joints with Magnetic-field

The fabrication and pre-treatment of the carbon fibre composite substrates was performed according to the procedure outlined in section 3.2. The alignment of the Fe_3O_4@CNFs was achieved by placing the bonded joints (prior to the curing of the epoxy) between two permanent magnets, as shown in Figure 8-1. The magnetic-field direction is perpendicular to the bonding surfaces. The joints were cured at room temperature for 48 hours. Once cured, the samples were cut into double-cantilever beam (DCB) specimens for mode I fracture toughness testing in accordance with IS) 25217 [217]. Further details of the DCB testing procedure are given in section 3.2. The samples for electrical conductivity measurements were fabricated and tested using the methodology presented earlier in section 3.2.

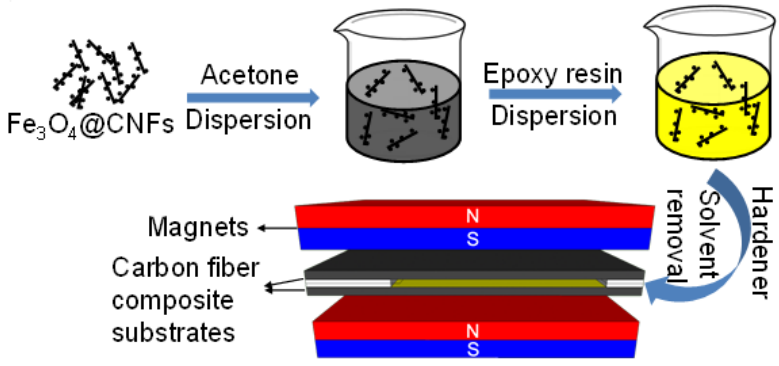

Figure 8-1: Schematic of composite join preparation with magnetic-field.

8.3 Results and Discussion

8.3.1 Alignment of Fe_3O_4@CNFs in epoxy nanocomposites

The alignment of the Fe_3O_4@CNFs in the liquid epoxy resin was observed using optical microscopy. Figure 8-2a shows a typical optical micrograph of an epoxy resin that was

not subjected to the external magnetic-field. Clearly, the Fe_3O_4@CNFs are randomly-oriented in the epoxy resin. This micrograph also reveals that the nanofibre hybrids are well dispersed. Figure 8-2b shows a typical optical micrograph of the liquid epoxy resin containing Fe_3O_4@CNFs subjected to the applied magnetic-field. This micrograph confirms the alignment and chain-like structure of the nanofibre hybrids in the direction of the applied magnetic-field, as indicated by the arrow.

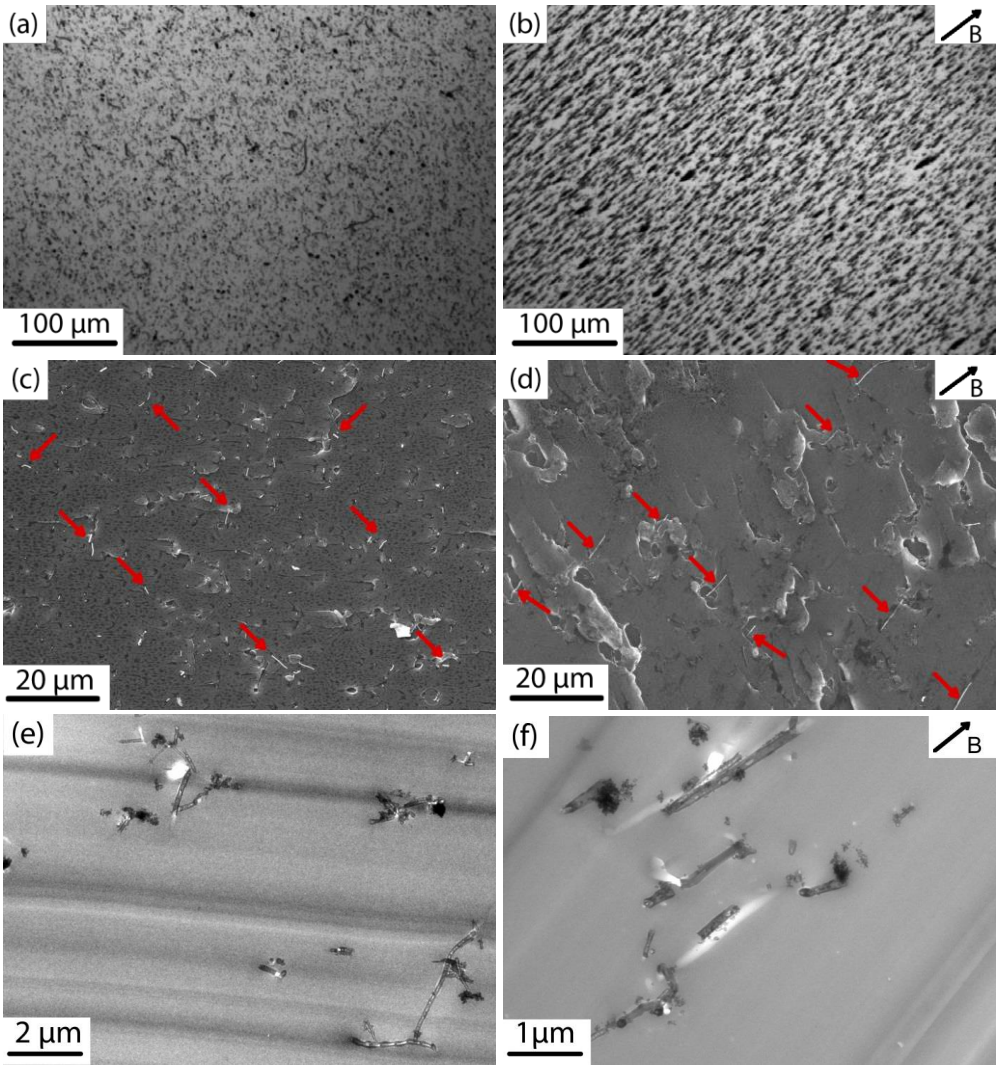

Figure 8-2: Representative optical micrographs (a and b), SEM images (c and d), and TEM (e and f) images of epoxy nanocomposites containing 0.6 wt% of randomly-oriented Fe_3O_4@CNFs (i.e. (a), (c), and (e)) and Fe_3O_4@CNFs aligned under the 50mT magnetic-field (i.e. (b), (d), and (f)). The black arrows in (b), (d), and (f) indicate the direction of the applied magnetic-field (B). The red arrows in (c) and (d) indicate the nanofibre hybrids.

The alignment and chain-like structure of the Fe_3O_4@CNFs may be ascribed to the anisotropic nature of the dipolar interactions of the iron oxide nanoparticles close to the

ends of the Fe_3O_4@CNFs [191, 192]. Without an externally applied magnetic-field, the magnetic moments of the iron oxide nanoparticles are randomly oriented leading to vanishing net magnetization. However, upon the application of a sufficiently large magnetic-field, the magnetic moments of the nanoparticles align along the external field direction and the resultant dipolar interactions orient the Fe_3O_4@CNFs. Attraction of the north and south poles of the magnetic carbon nanofibres resulted in the formation of the chain-like structure.

After the epoxy was cured, the orientation of the CNFs was further verified using SEM (see Figure 8-2c,d) and TEM (see Figure 8-2e,f) to view 90 nm thick slices (obtained through ultramicrotomy) of the epoxy nanocomposite. For comparison, Figure 8-2c shows a SEM image of the epoxy nanocomposite without being subjected to any applied magnetic-field. As expected, the Fe_3O_4@CNFs (i.e. the bright spots) are uniformly dispersed and randomly-oriented in the epoxy polymer (i.e. the grey continuous area). For the epoxy nanocomposites subjected to the magnetic-field during curing, Figure 8-2d reveals that the Fe_3O_4@CNFs are aligned parallel to the direction of the magnetic-field, consistent with the observed alignment in the liquid epoxy resin prior to cure (see Figure 8-2b). The TEM images (see Figure 8-2e & f) further support the above conclusions on the orientation of the nanofibre hybrids, parallel to the applied magnetic-field, in the epoxy nanocomposites.

8.3.2 Electrical conductivity studies

Figure 8-3 shows the conductivity of the epoxy nanocomposites with different contents of randomly-oriented and aligned Fe_3O_4@CNFs. The electrical conductivities of the Fe_3O_4@CNF-epoxy nanocomposites subjected to the magnetic-field were measured in two directions, namely, parallel and perpendicular to the direction of the externally applied magnetic-field. The unmodified epoxy exhibits a conductivity of ~ 10^{-13} S/m which increases to ~10^{-12} S/m and ~10^{-10} S/m for the epoxy nanocomposites containing 0.2 wt% and 0.6 wt% of randomly-oriented Fe_3O_4@CNFs, respectively. For the epoxy nanocomposites cured under the applied magnetic-field, a higher electrical conductivity is observed when measured in the direction parallel to the magnetic-field. Indeed, the conductivity in the direction parallel to the magnetic-field is consistently over one order

of magnitude higher than that for the nanocomposites containing randomly-oriented Fe_3O_4@CNFs.

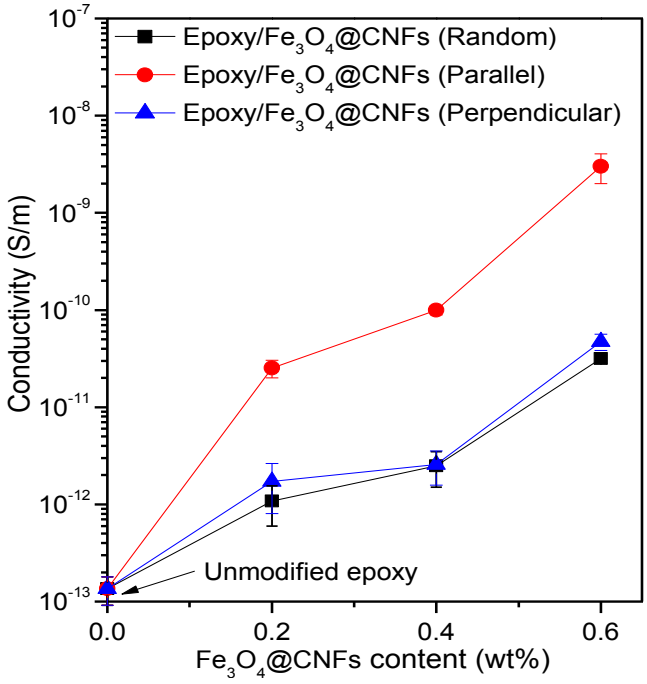

Figure 8-3: Electrical conductivity of the epoxy nanocomposites containing 0.0, 0.2, 0.4, and 0.6 wt% of Fe_3O_4@CNFs. (The orientation of the Fe_3O_4@CNFs with respect to the direction of measurement is indicated.)

This is similar to the reported increase from the use of CNTs aligned by a magnetic-field of 25 T [179, 185]. By contrast, the electrical conductivity measured normal to the magnetic-field shows no significant increase compared to the nanocomposites containing randomly-oriented Fe_3O_4@CNFs. This demonstrates that the application of the magnetic-field leads to the resultant epoxy nanocomposites possessing anisotropic electrical properties. However, the improvement of the electrical conductivities was not that remarkable. Greater improvements in the electrical conductivities were observed for the electric-field aligned CNF-epoxy nanocomposites reported in section 5.3.1. It has been shown that higher the oxygen concentration present in the CNFs, then higher is the content of CNFs required to reach the percolation threshold [269]. During the preparation of the Fe_3O_4@CNFs, a strong acid was employed to treat the CNFs, which might have introduced some defects and some oxidative surface groups. This partially may account for the relatively low electrical conductivity of the epoxy nanocomposites. Additionally, coating the surface of CNFs with iron oxide nanoparticles, which have a

relatively high resistivity, would further reduce the electrical conductivity of the nanocomposite [55, 192].

8.3.3 Fracture toughness

The effects of the alignment of the nanofibre hybrids on the fracture toughness of the epoxy nanocomposites were studied by investigating the mode I fracture behaviour of the carbon fibre composite joints bonded using the epoxy nanocomposites (or the unmodified epoxy polymer). The unmodified epoxy polymer and all the epoxy nanocomposites exhibited unstable, stick-slip, crack growth behaviour similar to that observed for CNF-epoxy nanocomposites in section 3.3.3. Figure 8-4 presents the values of G_{Ic} of the unmodified epoxy polymer and the epoxy nanocomposites containing either randomly-oriented or aligned nanofibre hybrids.

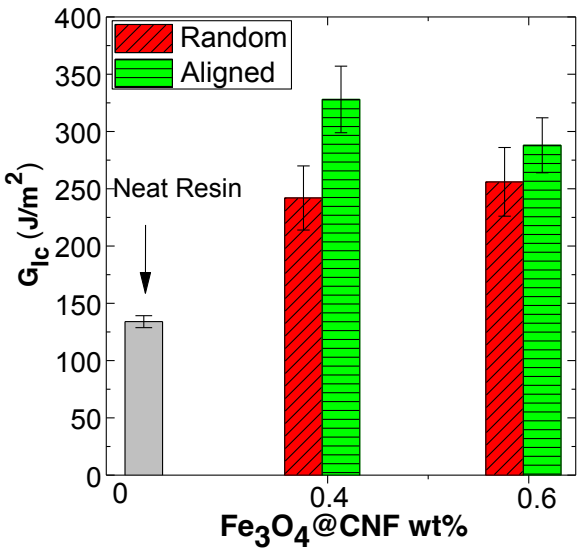

Figure 8-4: The mode I fracture energy, G_{Ic}, of the epoxy nanocomposites as a function of the content of Fe_3O_4@CNFs. (The orientation of the Fe_3O_4@CNFs was either random or aligned normal to the crack growth direction, as indicated.)

The addition of 0.4 wt% of randomly-oriented nanofibre hybrids, the fracture energy increased to 242 J/m^2. The application of the external magnetic-field, which oriented the Fe_3O_4@CNFs in a direction normal to the direction of crack growth, further improved the fracture energy to 328 J/m^2. It can be seen from Figure 8-4 that increasing the content of the Fe_3O_4@CNFs beyond 0.4 wt% did not yield any further significant

improvements in G_{Ic} of the epoxy nanocomposites containing either the randomly-oriented or aligned nanofibre hybrids.

8.3.4 Toughening mechanisms

An examination of the hybrid epoxy nanocomposite fracture surface revealed patterns of tear marks which were indicative of the plastic deformation of the epoxy that had occurred in the stress-whitened regions, either just ahead of the crack tip or due to some extent of slow crack growth occurring prior rapid crack growth taking place. Such an observation is typically associated with an enhanced toughness. In contrast, as shown in Figure 8-5a a typical featureless and smooth fracture surface was observed for the unmodified epoxy which was indicative of a very brittle fracture. The primary toughening mechanisms for Fe_3O_4@CNF-epoxy nanocomposites were identical to those observed for the electric-field aligned CNF-epoxy nanocomposite reported in section 3.3.3. As shown in Figure 8-5b-e, the primary toughening mechanisms leading to the increase in the fracture energy of –epoxy nanocomposite were identified to be, (a) an increase in the plastic deformation of the epoxy in the presence of Fe_3O_4@CNFs, (b) interfacial debonding and (c) pull-out of Fe_3O_4@CNFs from the epoxy, (d) epoxy void growth around the debonded Fe_3O_4@CNFs, and (e) the Fe_3O_4@CNFs bridging and rupturing across the crack face. The alignment of the Fe_3O_4@CNFs in the direction normal to the crack growth path increases the possibility of such interactions between the advancing crack tip and the Fe_3O_4@CNFs, leading to a significantly higher G_{Ic}.

However, the overall improvements in the fracture energy of the Fe_3O_4@CNF-epoxy nanocomposites were somewhat lower in comparison to the unmodified CNF-epoxy nanocomposites studied in Chapter 3. A possible reason for this was the damage to the CNFs caused by the strong acid treatment employed during the functionalisation of CNFs with Fe_3O_4. In addition, the use of multiple ultrasonication treatment employed during (i) the dispersion of the CNFs in distilled water for the functionalisation process and (ii) for dispersion of the Fe_3O_4@CNFs in the epoxy resin for fabricating DCB joints would lead to shortening of their length. The ultrasonication process has been shown to cause damage to the carbon nano-reinforcements [63]. Since, the fracture energy due to nanofibres pull-out given by Eq. (3-4) decreases as the square of the reinforcement length, any reduction in the length of the carbon nano-

reinforcements caused by their damage during dispersion process would lead to a significant reduction in the energy dissipation via the pull-out mechanism. This phenomenon was also demonstrated by Thostenson et al. [107], who reported a reduction in the fracture toughness of CNT-epoxy nanocomposites prepared by employing a high shear rate during the dispersion process.

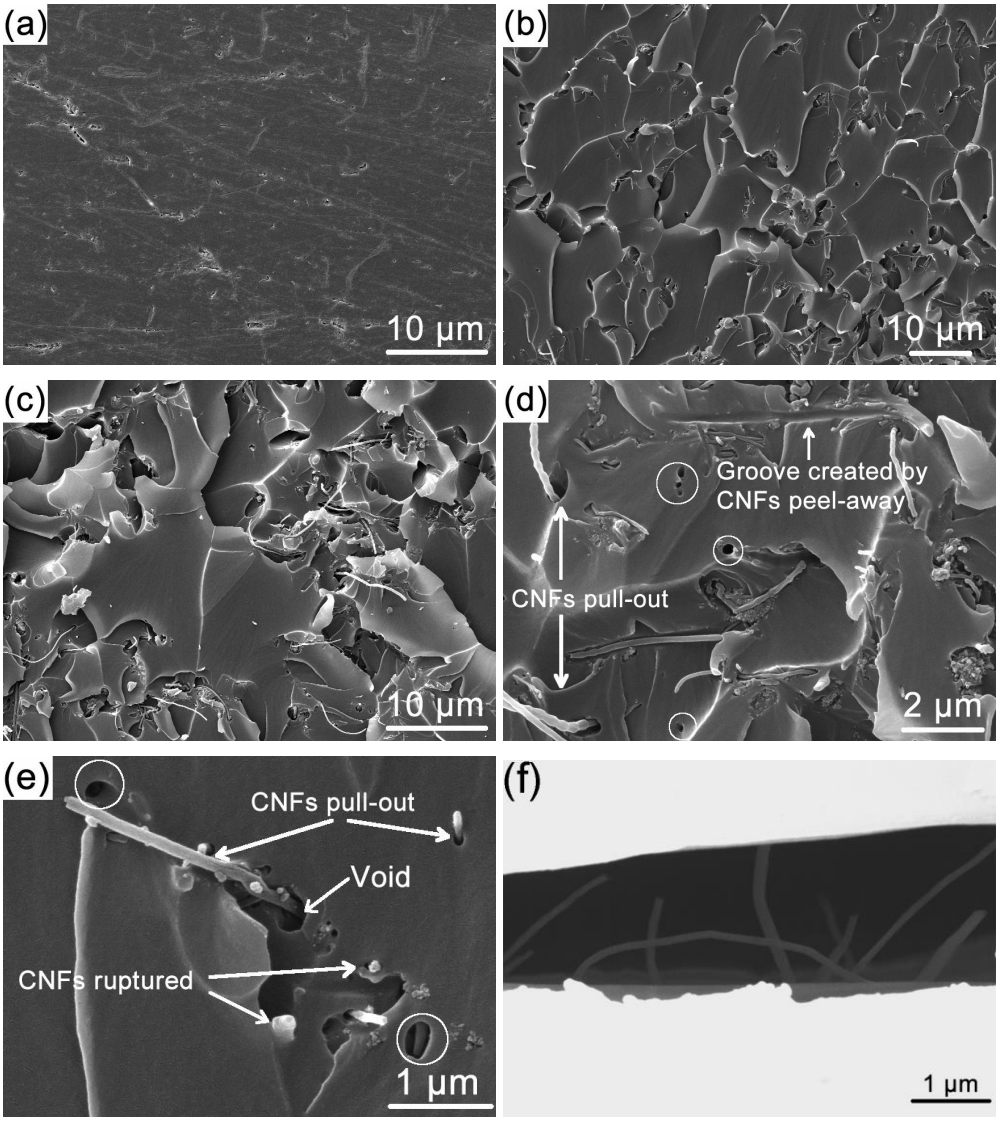

Figure 8-5: SEM micrographs of the fracture surfaces of (a) the unmodified epoxy polymer and (b–e) the epoxy nanocomposites containing 0.6 wt% of aligned Fe_3O_4@CNFs. (f) SEM micrograph of the cross-section (i.e. side view) of the crack tip of a DCB specimen bonded with the epoxy nanocomposites containing 0.6 wt% of aligned Fe_3O_4@CNFs. The white circles in (d) and (e) indicate the cavities created by pull-out of the Fe_3O_4@CNFs.

8.4 Conclusions

Fe_3O_4@CNFs hybrids can be aligned in the liquid epoxy resin by the application of a relatively weak magnetic-field (~ 50 mT), and that this alignment of the nanofibre hybrids is maintained whilst the epoxy nanocomposites are cured. Compared to the unmodified epoxy polymer, the epoxy nanocomposites exhibit a higher electrical conductivity, especially along the direction of the alignment. In addition, alignment of the Fe_3O_4@CNFs further enhances the toughening efficiency. For example, the addition of 0.4 wt% of aligned Fe_3O_4@CNFs increases the fracture energy of the epoxy nanocomposites by about 150% above that of the unmodified epoxy polymer. By contrast, randomly-oriented Fe_3O_4@CNFs at the same content only give about an 80% improvement. Based on fractographic analyses, the main toughening mechanisms induced by the nanofibre hybrids include interfacial debonding, pull-out, crack bridging and rupture of the Fe_3O_4@CNFs, and plastic void growth in the epoxy polymer. The alignment of the Fe_3O_4@CNFs in the direction normal to the crack growth increases their propensity to interact with the advancing crack tip, leading to more effective toughening. However, the damage to the Fe_3O_4@CNFs during the functionalisation process and subsequent shortening of lengths as a result of multiple ultrasonication processes led to somewhat lower improvements in the fracture energy of the Fe_3O_4@CNF-epoxy nanocomposites in comparison to the unmodified CNF-epoxy nanocomposites studied earlier. Moreover, the use of co-precipitation technique for synthesis of Fe_3O_4@CNF using current facilities yields a very low volume production (less than 0.5 gm/day) which is insufficient for manufacturing fibre-reinforced composite laminates for further studies. Therefore, additional through-thickness aligned reinforcement techniques will be employed in subsequent study on improving the delamination resistance of carbon-fibre composite laminates.

Chapter 9

Multi-scale toughening of fibre composites using carbon nanofibres and z-pins

Abstract

The present chapter investigates a multi-scale approach to synergistically toughen composites by combining nano- and macro-scale reinforcements inspired by natural composite materials. Carbon reinforcements with two different length scales are used: nano-scale carbon nanofibres (~100 nm diameter) and macro-scale carbon z-pins (~280 μm diameter) to reinforce continuous carbon-fibre composites in the through-thickness direction. The resultant composite, featuring three-dimensional reinforcement architecture, possesses triple toughening mechanisms at three different scales, thus yielding a synergistic effect. At the nano-scale, the carbon nanofibres alone promote high mode I delamination resistance (~70% increase in interlaminar fracture energy) by multiple intrinsic and extrinsic toughening processes around the crack tip. The macro-size carbon z-pins, together with the crossover continuous fibres, promote a strong extrinsic toughening mechanism (~200% increase in the interlaminar fracture energy) behind the crack tip and over a larger length-scale via both the z-pins and crossover fibres bridging the crack faces. When used concurrently, the nano-reinforcements and z-pins promote a higher toughness under quasi-static loading (~400% increase in fracture energy) than when used separately due to a multiplicative effect from the interplay between intrinsic and extrinsic toughening processes operative ahead of, and behind, the crack tip. Under mode I interlaminar cyclic-fatigue loading, the multi-scale laminates show a strong improvement in resistance against fatigue delamination growth. Similar to the synergistic increase in fracture energy, a greater increase in the delamination fatigue resistance occurs when both are active together. However, the results indicate that the synergistic effect of the multi-scale toughening is statistically

significant under quasi-static loading but not under fatigue loading. A very small reduction (~2%) in the tensile strength is observed for the multi-scale reinforced laminates.

The research presented in this chapter has been published in the following journal and conference papers:

- Ladani RB, Ravindran AR, Wu S, Pingkarawat K, Kinloch AJ, Mouritz AP, Kinloch AJ, Mouritz AP, Ritchie RO, Wang CH. *Multi-scale toughening of fibre composites using carbon nanofibres and z-pins,* Composite Science and Technology, 2016. (under review)

9.1 Introduction

Natural composite materials, such as bone and nacre, have evolved elaborate hierarchical architectures to achieve structures that are both strong and tough, using weak but readily available building blocks [270]. Natural composite materials that combine the desirable properties of their sub-components often perform significantly better than the sum of their parts, representing a major synergistic improvement through the confluence of mechanisms that interact at multiple length scales [271]. This has led to the current interest in bioinspired composite design ideas [271-273]. However, very few examples of practical synthetic versions of the complex hierarchical architecture of natural composites have been reported [274]. Almost all natural materials comprise of a relatively small number of polymeric (proteins) and ceramic (for instance calcium oxide) components or building blocks which have relatively poor intrinsic properties [272]. The superior traits of natural composites stem from naturally-occurring complex architectures utilizing different structures or structural orientations of constituents spanning nano- to macro-scales [274]. For instance, in natural composites, such as nacre or bone, the ceramic phase is often in the form of nanometre grains, nanofibres or nanoplatelets, all of which increase flaw tolerance and strength [270]. In contrast, most human-engineered composites have been developed through the formulation and synthesis of new compounds, for instance, different fibres or polymeric matrices, and with structural control primarily at the micrometre scale [275].

The purpose of the research presented in this chapter is to demonstrate a novel approach for toughening fibre-reinforced composite architecture with structural reinforcements spanning multiple length scales and orientations as shown in Figure 9-1. In the absence of the wide availability of CNFs, CNTs or GNPs with high magnetic susceptibility that can be aligned in the through-thickness direction of the carbon fibre-epoxy composites using relatively weak magnetic-fields, carbon z-pins aligned in the through-thickness direction are used to reinforce the laminates. Carbon fibre-epoxy composites studied in this chapter are reinforced in the through-thickness direction using a combination of nano-scale carbon nanofibres (CNFs) and macro-scale carbon z-pins. CNFs of 1.0 wt% with random orientation are incorporated in the epoxy matrix

while z-pins of 1.0 wt% are inserted in the through-the-thickness direction of the laminate. The focus of this chapter is to investigate the hybridisation effect of concurrent reinforcements by CNFs and z-pins on the mode I interlaminar fracture toughness and fatigue properties of carbon-fibre epoxy laminates. To this end, the toughening mechanisms of multi-scale reinforcements are characterised experimentally, including the impact of CNFs in the matrix on the z-pin bridging traction load under mode I static and fatigue loadings. The experimental data and fractographic observations presented in this paper provide new insights into the microstructure and parameters that control the fracture toughness and fatigue properties of multi-scale composites.

9.2 Materials and Experimental Methodology

Multi-scale material designs

As a prime example of a damage-tolerant natural composite material, bone combines strength with toughness via a multitude of deformation and toughening mechanisms operating at different length scales [270, 276, 277]. The fracture resistance in bone can be separated into intrinsic mechanisms that promote ductility and extrinsic mechanisms that act to 'shield' a growing crack [274]. In bone, the intrinsic toughness originates at the nanometre length scales through various processes, including stable uncoiling of the mineralized collagen components and the process of collagen fibrils (of ~1.5 nm diameter and ~300 nm long) sliding as shown in Figure 9-1a. The fibrillar sliding mechanism promotes plasticity near the crack tip at nano- and micro-length scales [270]. This intrinsic toughening mechanism results in relatively large energy dissipation within the plastic zones and serves to blunt crack tips, while reducing the driving force for cracking. Recent nanocomposite research has demonstrated that similar intrinsic toughening can be realised in polymeric matrices at the nano-scale via nano-reinforcements such as carbon nanofibres (CNFs) [278-280], carbon nanotubes (CNTs) [31, 281] and graphene nanoplatelets (GNPs) [280, 282]. The inclusion of nano-

reinforcements in polymeric matrices may significantly enhance energy-dissipative deformation mechanisms of the polymer in the form of void growth, for example, which promotes the formation of plastic zones as shown in Figure 9-1b.

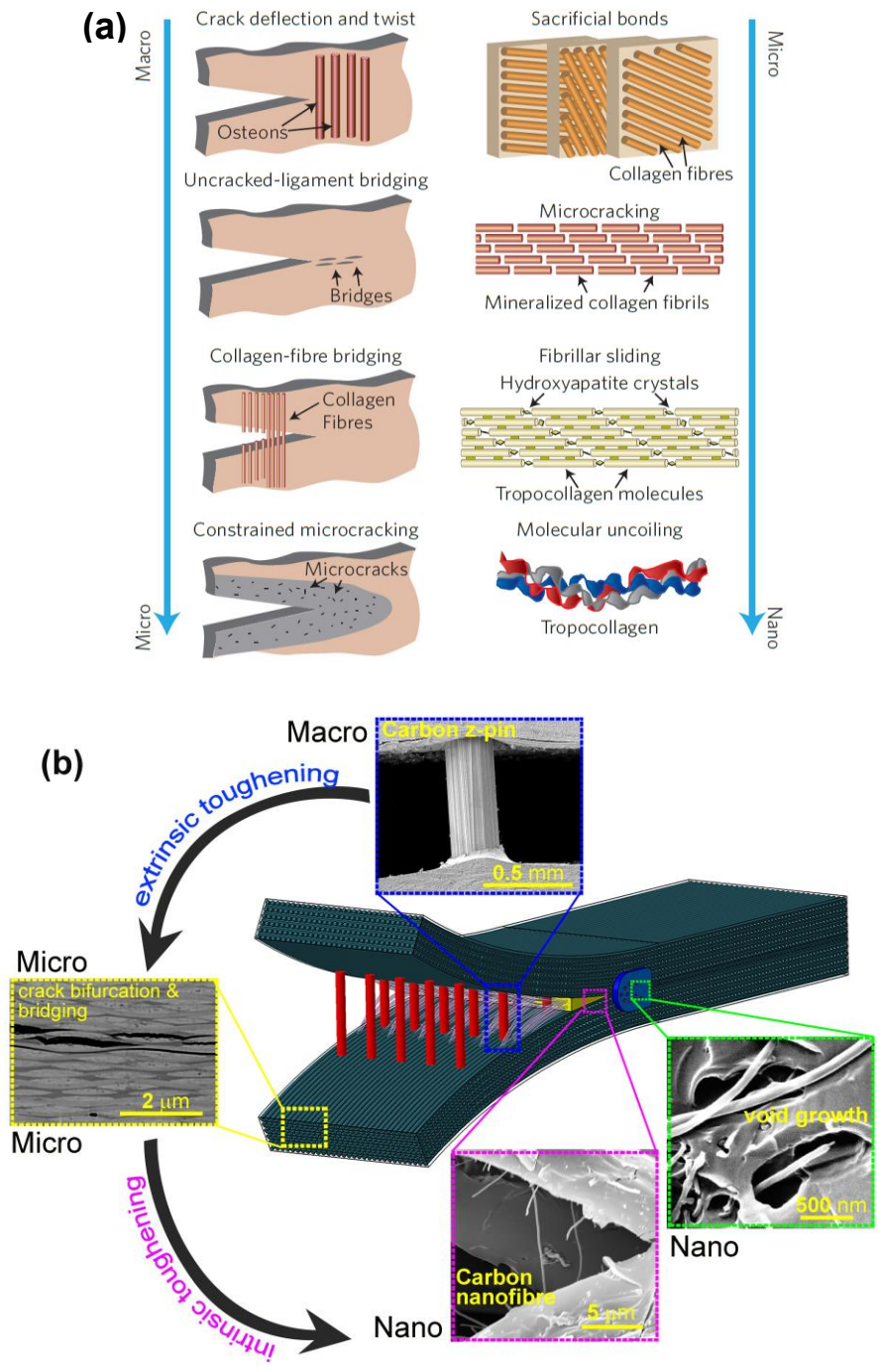

Figure 9-1 : (a) The various level of hierarchical toughening mechanisms prevailing in a bone. Adapted from [16] with permission from Macmillan Publishers Ltd Copyright 2014. (b) Schematic representation of the multi-scale carbon-fibre epoxy composite with toughening processes operating at various scales.

In addition, an even greater improvement to the polymer toughening occurs via the pull-out of nano-reinforcements from the polymer matrix which dissipates energy through frictional sliding [219]. The nano-reinforcement pull-out process also leads to the formation of a crack-bridging zone near the tip, which opposes the applied stress for cracking. As shown in Figure 9-1a-b, this frictional sliding process in human-engineered composites is analogous to the fibrillar sliding mechanism observed in bone. However, an even greater contribution to the fracture resistance of bone arises from an extrinsic toughening mechanism that occur behind the crack tip at longer length scales, in the range of 10-100 μm [276]. Specifically, once the crack begins to grow, mechanisms within the crack wake are activated in the form of crack bridging by the osteons to inhibit further cracking [283]. As the crack continues to grow, the regions between microcracks formed at the osteonal interfaces form the uncracked-ligament bridges, which act as intact regions spanning the crack wake to inhibit its progress. Any pull-out of the osteons from the bone matrix that may occur will promote toughening once crack propagation has begun. Such crack bridging toughens normal bone by decreasing the crack-tip stress intensity, and a larger applied force is required to propagate the crack further. This type of extrinsic toughening mechanism can be realised using z-pinning technique, where thin carbon-fibre z-pins (of ~280 μm diameter) are inserted in the thickness direction (see Figure 9-1b) of a laminate [40, 284]. However, the advent of nanotubes and nanofibres has opened possibilities of attaining additional intrinsic toughening mechanisms at previously unattainable scales in combination with the extrinsic toughening, as is shown in Figure 9-1b. The present work will focus on understanding and demonstrating the synergistic toughening of fibre composites through the use of nano-scale (*i.e*. CNFs), micro-scale (*i.e*. carbon fibres) and macro-scale (*i.e*. z-pins) reinforcements forming a three-dimensional architecture mimicking tough natural composites.

Composite materials and reinforcement process

Four different types of composites were manufactured for testing. The first configuration comprised the baseline laminate, which was fabricated using 20 plies of a 200 gsm plain woven T300 carbon fabric (AC220127 supplied by Colan Ltd.) and a

bisphenol-A based epoxy resin (Resin-105 and Hardener-206 supplied by Westsystem®). The plies were oriented such that the weft and warp tows were along the length and width of the laminate, respectively. The chosen Westsystem-105 resin is widely used for marine applications where the operating temperature of its fibre composite system is typically limited by the glass transition temperature (i.e. ~70^{o}C) of the cured epoxy resin [226]. (However, the information on the moisture absorption rate of this resin system is currently unavailable from the supplier or the published literature.) The carbon-fibre epoxy laminate was made using a wet hand-layup process. The laminate was cured at room temperature with 350 kPa overpressure in a hydraulic press for 24 hours, and then post-cured at room temperature for 48 hours to allow the epoxy to reach its working strength in accordance with the epoxy supplier's recommendations [226].

The second type of composite material consisted of a CNF-reinforced laminate made by incorporating commercially available CNFs (Pyrograf® - III, grade PR-24-XT-HHT supplied by Applied Sciences Inc.), which have a diameter of about 70-200 nm and a length of 50-200 μm. The addition of CNF to the epoxy resin leads to a significant increase in its viscosity [136]. Therefore, a moderate CNF weight content (i.e. 1 wt%) was chosen to keep the resin viscosity low enough to allow the infiltration of carbon fibre preforms during the wet layup process. Nevertheless, in our previous investigations on the optimum loading of CNF in epoxy, we observed that addition of just 1 wt% CNFs can promote large improvements to the fracture energy of epoxy matrices with only a moderate increase in its viscosity [285, 286]. Firstly, 1 wt% (*i.e.* 0.82 vol%) of the CNFs were hand-mixed with the epoxy resin (without the hardener) and solvent-free acrylate copolymers, namely Disperbyk-191 and -192 (supplied by BYK®), to aid the dispersion of the CNFs. The dispersive surfactants that were added to the CNFs were equal to the weight of CNFs, resulting in a mixture of CNFs:D-191:D-192 at a weight ratio of 1:1:1. The addition of the dispersion aiding surfactants was found to have no effect on the fracture toughness of the bulk epoxy. The CNF/epoxy mixture was then passed four times through the three-roll mill at 150 rpm with progressively smaller gap size until the smallest gap setting of 20 μm had been reached. The hardener was then added to this mixture followed by a wet hand layup to

produce the carbon-fibre laminate, which was processed and cured under the same conditions as the control material described above.

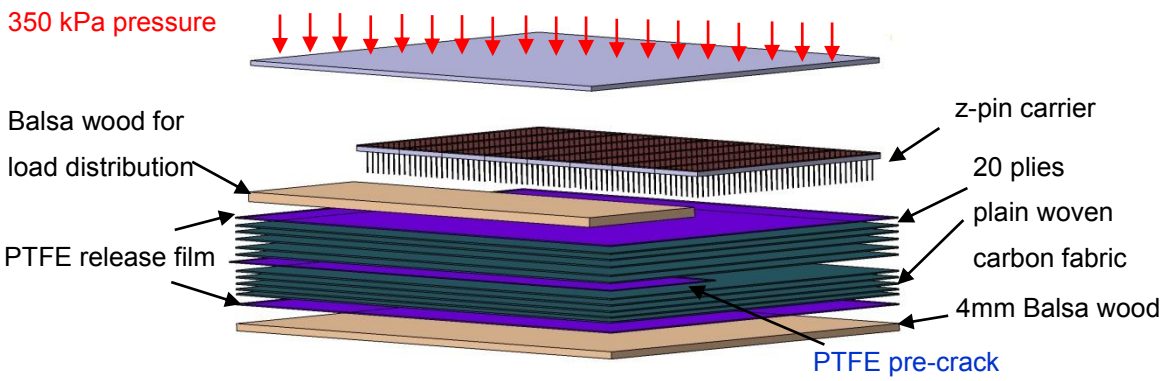

Figure 9-2 : Schematic illustration of the z-pin reinforced carbon-epoxy laminate layup.

As shown in Figure 9-2, the third and fourth types of composites were made by z-pinning the baseline material (i.e. without any CNFs present) and the CNF-reinforced carbon-fibre epoxy laminates, respectively. They were then cured in the hydraulic press. The z-pins used were 280 μm diameter pultruded rods of unidirectional carbon fibre-bismaleimide (supplied by Albany Engineered Composites Pty Ltd.). By controlling the average spacing to 3.5 mm, the volume content of the z-pins was set to be 0.5 vol%. The in-plane strength and stiffness of z-pinned laminate decrease approximately linearly with increasing volume content of the pins [20, 287]. Thus, a low 0.5 vol% of z-pins was chosen for through-thickness reinforcement of the laminate and the presence of 0.5 vol% of z-pins is reported to cause less than 2% and 4% reduction in the compressive and tensile strengths of the laminate, respectively [20]. The same layup procedure and processing conditions were applied to the z-pinned laminate and the laminate reinforced with both CNFs and z-pins. Although the length of the as-supplied z-pins within its carrier was 9 mm, the length of the z-pins within the laminate was controlled by the actual thickness of the carbon-epoxy laminate, which was 5 mm. As shown in Figure 9-2, an additional layer of balsa wood with 4 mm thickness was placed at the base of the wet layup laminate in order to accommodate the excess length of the z-pins during the z-pinning process. The traditional ultrasonically-assisted pinning process used for the carbon-epoxy prepreg system was not necessary

due to the soft nature of the wet layup laminate. Instead, z-pinning in the through-thickness direction was achieved by simply compressing the z-pin laminate assembly within the hydraulic press with a pressure of 350 kPa. The excess z-pin length within the carrier and the base balsa wood were trimmed with a vibrating saw blade after the laminates were fully cured.

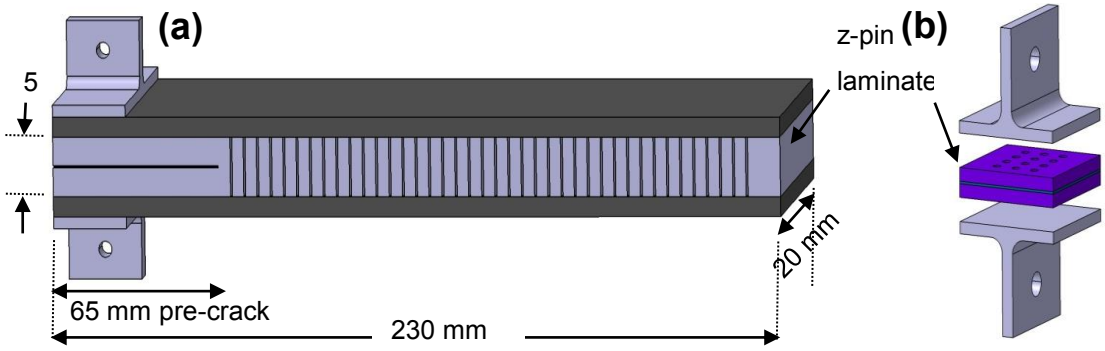

Figure 9-3 : Schematic illustrations of (a) double cantilever beam (DCB) specimen used for mode I quasi-static and fatigue interlaminar fracture toughness testing; and (b) z-pin pin pull-out test specimen used for measuring the z-pin bridging traction load.

Double cantilever beam (DCB) specimens were employed for the tests described in the following sections; they consisted of 230 mm long, 20 mm wide rectangular-shaped coupons. The DCB specimens consisted of a central region made from wet layup plain woven carbon-epoxy laminate and outer regions that were used to provide additional stiffening and strengthening, as shown schematically in Figure 9-3a. One end of the specimen contained loading tabs as well as a 50 mm long, and 25 μm thick polytetrafluoroethylene (PTFE) film was placed between the two middle plies to act as a pre-crack for initiation of the delamination crack. To prevent the sub-laminate arms of the DCB specimens from breaking during testing, each specimen was bonded with two 12-ply unidirectional carbon-epoxy composite strips using an epoxy-paste adhesive (Araldite 420 supplied by Huntsman®).

Fracture toughness and cyclic-fatigue testing procedures

Both the static fracture toughness and the delamination cyclic-fatigue growth properties of all four types of composite laminates were measured using the DCB specimens described above. Mode I fracture toughness testing was conducted under displacement

controlled using a screw-driven Instron testing machine with a 10 kN load cell. The mode I interlaminar fracture toughness was measured by monotonically loading the arms of the specimen (via the bonded-on end blocks) using a displacement rate of 2 mm/min, in accordance with the ASTM Standard D5528 [288]. The crack length was measured using a travelling optical microscope located at one side of the DCB specimen. A white correction fluid was applied to one side of the DCB facing the travelling microscope in order to improve the visibility of the delamination crack growth. During loading the delamination crack grew uniformly across the width of the specimen, so measurement was only needed on one edge. Four specimens were tested for each of the four materials.

Mode I interlaminar cyclic-fatigue testing was performed by applying a constant amplitude sinusoidal cyclic load at a frequency of 10 Hz. The tests were performed using a computer-controlled Instron E3000 system with a 3 kN load cell under displacement control with a constant cyclic ratio (*R*-ratio). The ratio between the minimum and the maximum applied displacement in one load cycle was kept constant at 0.5. Initially, the specimens were subjected to quasi-static loading and the delamination was allowed to grow by ~15 mm from the initial flaw in order to achieve a naturally sharp crack. The specimens were then subjected to cyclic fatigue loading with the maximum crack opening displacement being chosen such that the initial value of the applied strain-energy release-rate was about 80% of the mode I interlaminar fracture toughness determined from the quasi-static tests. Delamination fatigue growth rates were measured at crack growth intervals of ~1 mm, in accordance with the load-shedding scheme prescribed in ASTM E647 [253]. The load-shedding process was continued until the crack growth rates reached the threshold value and no further delamination growth occurred.

Static and fatigue z-pin pull-out tests

Z-pin pull-out tests were performed to assess the influence of the CNF reinforcement of the matrix on the crack-bridging traction law of the z-pins. Figure 9-3b shows the schematic of the z-pin pull-out test specimens, which were manufactured from the same carbon-fibre epoxy laminate and with similar curing conditions as discussed earlier.

Two separate batches of specimens were manufactured with one using CNF-reinforced matrix and the other without the CNFs being present. The specimens were z-pinned at 0.5 vol% in a 4 x 3 configuration. A thin film of polytetrafluoroethylene was placed between the two middle plies to keep the two laminates unbonded to facilitate the z-pin pull-out. The quasi-static z-pin pull-out tests were conducted by loading the specimen in the through-thickness direction at a rate of 0.5 mm/min until the laminates became separated. The separation of the samples was measured using a crack-opening displacement gauge. The z-pin bridging traction load was determined by dividing the measured load by the number of pins within the specimens.

The degradation to the z-pin friction traction load under fatigue cycling was investigated using the test procedure outlined by Zhang *et al*. [21]. The fatigue z-pin pull-out testing was performed under displacement control by applying a triangular waveform with a frequency of 0.05 Hz. A monotonic increasing load was first applied until the z-pins fully debond from the laminate. Then the displacement at which the z-pins fully debond from the matrix was used as the minimum cyclic displacement (δ_{min}) for fatigue testing. The maximum cyclic displacement was to found to follow the relationship,

$$\delta_{max} = \delta_{min} + 0.2l \tag{9-1}$$

where l is the z-pin length (= 5 mm). The z-pin bridging traction load was measured up to a total of 5000 fatigue cycles.

Tensile testing procedure

Tensile tests were performed to assess the influence of z-pin and CNF reinforcement on the strength and stiffness of the laminates. Dog-bone shaped tensile test coupons with a 14 mm wide gauge section were fabricated using water-lubricated precision grinding machine. Tensile test was performed on a MTS testing machine with a 100 kN load cell. The tensile test was performed using a displacement rate of 2 mm/min in accordance with the ASTM standard D3039 [253]. Four tensile specimens were tested

parallel to the warp tows to determine the average tensile strength and stiffness of each laminate type.

9.3 Results and Discussion

9.3.1 Quasi-static tests

Figure 9-4a shows the typical effect of the through-thickness reinforcements on the mode I crack growth resistance (R-curve) behaviour of the carbon-fibre epoxy laminates under quasi-static loading, and shows the effect of the through-thickness reinforcement size on the interlaminar fracture toughness. The R-curve for the control laminate increased slightly over the initial 10 mm of delamination extension, and this is due to the carbon fibres crossing over and bridging the crack faces [254]. As shown in Figure 9-4, the R-curve for the CNF-reinforced laminate increased rapidly during the initial 15-20 mm phase of crack growth and then reached a steady-state.

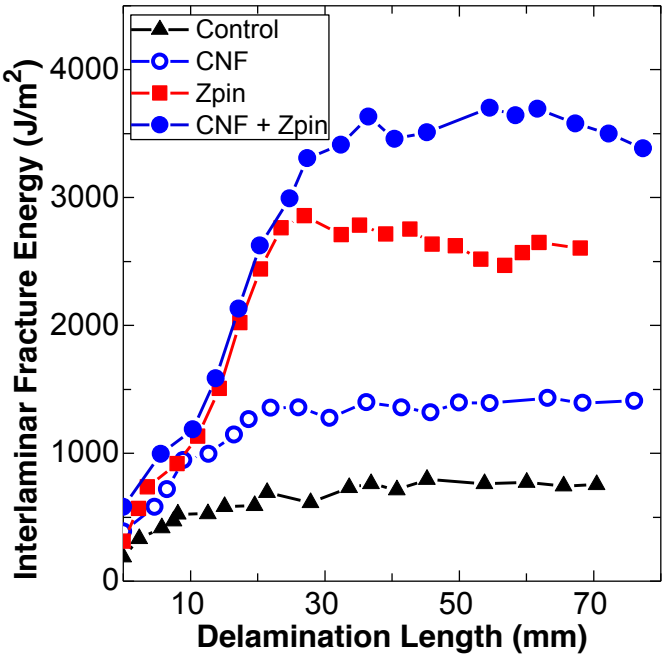

Figure 9-4 : Crack growth resistance (R-) curves for the unreinforced and through-thickness reinforced laminates containing 1.0 wt% CNFs and/or 1.0 wt% z-pins under quasi-static loading.

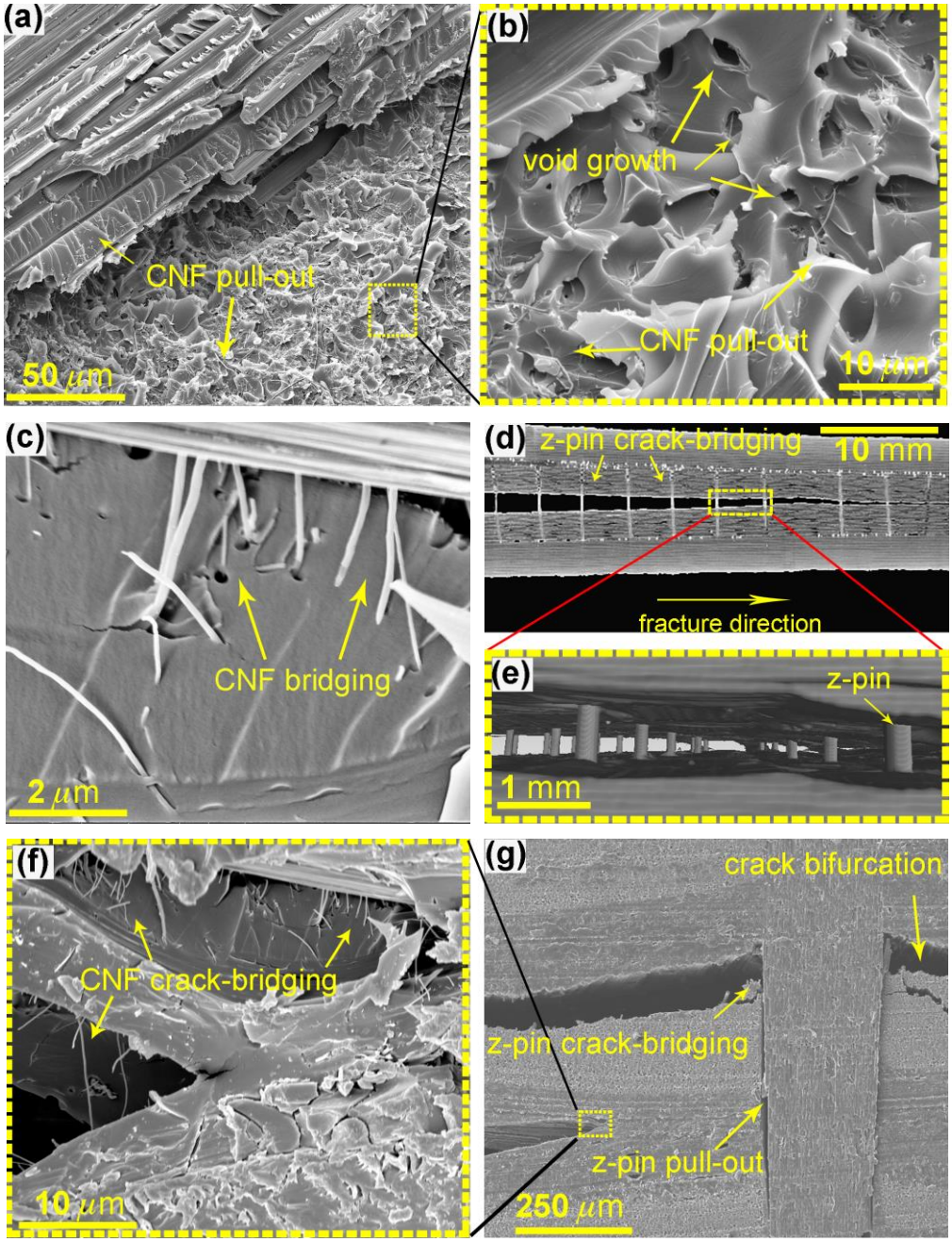

Figure 9-5 : (a-c) SEM micrographs of the 0.82 vol% CNF-reinforced laminates. (d-e) X-ray computed tomography images showing a side view of a z-pinned DCB test specimen. (f-g) SEM micrographs of the delamination front in a side view for the DCB test specimen containing CNF and z-pin reinforcements.

This toughness increase was due to the intrinsic toughening in the form of CNF debonding and subsequent matrix void growth (see Figure 9-5a-b) as well as the extrinsic toughening in the form of CNF pull-out and crack bridging, as shown in Figure 9-5a,c. These toughening mechanisms are commonly observed in nanofiller-reinforced laminates [289, 290]. In comparison, the R-curve for the z-pinned laminate

increased at a much faster rate than the unpinned laminates. This was due primarily to the evolution of a z-pin bridging-zone which spanned ~30 mm of the crack, as shown in Figure 9-5d-e. Most importantly, from Figure 9-4a it is seen that the steady-state interlaminar fracture toughness measured for the laminates reinforced concurrently with CNFs and z-pins was much higher than when these reinforcements were used separately. This was due to the synergistic combination of toughening by CNFs at the crack tip and the extrinsic toughening in the crake wake via a long z-pin crack-bridging process zone, as shown in Figure 9-5f-g. This synergistic toughening is discussed in detail below.

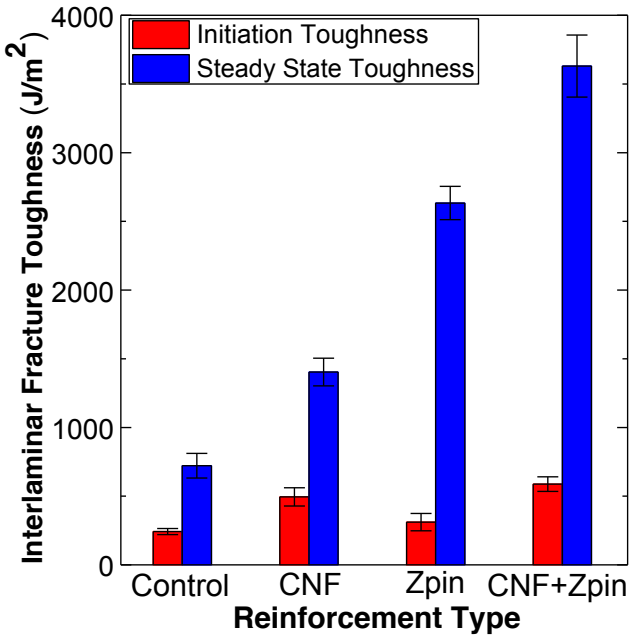

Figure 9-6 : Mode I interlaminar fracture toughness under quasi-static loading results for initiation and propagation of delamination in the control laminate and the laminates reinforced with 0.82 vol% CNF and/or 0.5 vol% z-pins.

Figure 9-6 shows the effects of using CNF and z-pin reinforcements concurrently and separately on the initiation, G_{Ii} and steady-state interlaminar fracture toughness, G_{Ic} of the laminate. The initiation fracture toughness of the laminate reinforced with z-pins was slightly greater (by ~30%) than the unreinforced (i.e. 'control') laminate. The Z-pins promote very little resistance to crack initiation at relatively low volume fractions (~ 0.5 vol%) [40]. This is due to the much greater inter-pin distance (~3.5 mm as seen in Figure 9-5d-e) in comparison to the small-scale length

of the crack initiation process zone: z-pins are only effective when the delamination crack is much longer than the inter-pin distance. However, the initiation toughness of the CNF-reinforced laminate was about 100% greater than the control laminate. Similarly, when CNF and z-pin reinforcements are used concurrently, the initiation fracture toughness was even higher (by ~150%). CNFs promote high delamination resistance by multiple toughening processes near the crack tip, including intrinsic (i.e. crack bifurcation and matrix void growth, see Figure 9-5a-b) and extrinsic (i.e. crack bridging and pull-out of the CNFs, see Figure 9-5c,f). In the process zone ahead of the crack tip, CNFs debond from the matrix due to the presence of triaxial tensile stresses. The debonded CNFs then act as voids within the matrix, enabling the matrix to deform plastically and dissipate energy while enlarging these voids. Matrix void growth around nano-reinforcements is commonly observed to promote intrinsic toughness in nanocomposites [31, 278]. However, in laminated composites, the size of the process zone cannot develop to its full extent, since it is constrained in a thin layer of matrix by plies of fibre on either side [291]. Therefore, relatively less energy is dissipated in the form of matrix void growth. Instead, the majority of the strain energy is dissipated via CNF pull-out and the formation of the crack-bridging process zone behind the tip (see Figure 9-5c,f). During CNF pull-out and crack-bridging process zone formation, a large amount of energy is dissipated in the form of interfacial frictional sliding between the CNF and the matrix. Once the CNF bridging process zone is fully developed, the fracture toughness reaches the steady-state value and remains approximately constant. The CNF reinforcement increased the steady-state fracture toughness by ~70%, which agrees with other studies [39, 290, 292]. Even greater improvements to the steady-state fracture toughness were measured (by ~200%) for the laminates reinforced with z-pins. The z-pins promote a strong extrinsic toughening mechanism behind the crack tip and over a longer length-scale via a long crack-bridging process zone (see Figure 9-5d-e). The major improvement to the fracture toughness is due to the frictional energy dissipated during the pull-out of z-pins from the laminate. This leads to the formation of the z-pin bridging process-zone in the crack wake, which provides the necessary traction force to shield the crack tip from the applied stresses. Importantly, when CNFs and z-pins were used concurrently, they produced a much greater improvement to the

steady-state fracture toughness (by ~400%) due to toughening processes operative ahead of the tip (via the CNFs) and behind the crack tip (via the z-pins). Furthermore, the overall improvement to the fracture toughness is greater than the expected simple additive effect from the toughening due to CNFs and z-pin separately. This is indicative of a synergistic toughening effect. This synergism in the fracture toughness can be evaluated as follows:

$$\text{Synergy} = \frac{G_{Ic(CNF+zpin)} - G_{Ic(Control)}}{(G_{Ic(zpin)} - G_{Ic(Control)}) + (G_{Ic(CNF)} - G_{Ic(Control)})} - 1 \qquad (9\text{-}2)$$

where G_{Ic} denotes the mode I steady-state fracture toughness, and the subscripts "control", "CNF", "zpin", and "CNF+zpin" denote the quantities pertinent to the four types of composites. Using the average values of G_{Ic} from Figure 9-6, the level of synergy in the steady-state fracture toughness was calculated to be about 11% using Eq. (9-2). The statistical significance of this low level of synergy was determined using a two-way analysis of variance (ANOVA). The two-way ANOVA test calculates the probability of interaction while considering the standard deviation of each sample population. Each sample population had a size of 38, comprised of all G_{Ic} values corresponding to the delamination length greater than 30 mm in Figure 9-4. The corresponding values of *p* and *f* for interaction were 0.003 and 10.36 respectively which suggests a 99% probability of synergy when the CNF and z-pins are used concurrently. A possible major reason for this synergy is that the presence of CNFs in the matrix enhances the energy dissipation during the debonding and pull-out of the z-pins. This was further examined by determining the mode I bridging traction load using the z-pin pull-out test. Figure 9-8a shows shows the comparison between a representative bridging traction load-displacement behaviour during the pull-out of the z-pins from laminates with CNF-reinforced matrix and unmodified matrix. The initial portion of this curve represents the elastic deformation of the z-pin/matrix interface up to the maximum traction load necessary to fully debond the z-pin. The debonding is followed by the subsequent pull-out of the z-pin from the laminate. The area under the traction load-displacement curve defines the total amount of energy dissipated by the pull-out of z-pins. The maximum traction load necessary to fully debond the z-pin is increased by

the presence of CNFs in the matrix. The maximum traction load is limited by the z-pin/matrix interface or the shear strength of the matrix, whichever is the lesser. Several recent fibre pull-out studies have reported up to 30% improvement in the interfacial strength [293, 294] between micro-scale fibres and the matrix, when the latter was reinforced with nanofillers due to the better flow of the matrix. Other studies have also reported improvements in the interlaminar shear strength in composites with CNF-reinforced matrices [26, 141]. The z-pin/matrix interface strength can be determined from the maximum traction load, P_{max} using [295]:

$$\tau_i = \frac{P_{max}}{\pi d l_{po}} \tag{9-3}$$

where d and l_{po} ($\sim l/2$) are the z-pin diameter and pull-out length, respectively. By using an average value for the maximum traction load measured from five different z-pin pull-out samples, the z-pin interface strength for the unmodified matrix was calculated to be 16.4 MPa. This value is very similar to that previously reported for z-pin interface strength measurements [295]. Similarly, the z-pin interface strength for the CNF-reinforced matrix was calculated to be 22.1 MPa. A similar enhancement to the z-pin interface strength may be achieved by either using a stronger matrix or by improving the interfacial adhesion via, for example, functionalising the surface of the z-pin. However, simply increasing the interfacial adhesion may not necessarily lead to a greater toughness improvement, because the energy associated with the elastic deformation of the z-pin and its subsequent debonding is much lower than that dissipated during the pin pull-out process. The energy dissipated during the pull-out process for the z-pin is due to the interfacial frictional stress, τ_{if}, between the z-pin and the laminate. By using the average peak friction load corresponding to the z-pin pull-out stage (see Figure 9-7a) in Eq. (9-3), the interfacial frictional stress for the unmodified matrix was calculated to be 7.85 MPa. The interfacial frictional stress for the CNF-reinforced matrix was slightly higher at 9.89 MPa. Thus, as generally reported [295], the interfacial frictional stress is indeed lower than the z-pin interface strength.

The energy dissipated during the z-pin pull-out process can be determined from the interfacial frictional stress using Eq. (2-5) [82]. Figure 9-7b shows the effect of

CNF reinforcement on the energy dissipated during the z-pin pull-out process determined from Eq. (2-5) and its comparison to the experimentally measured energy from the area under the curve in Figure 9-7a. Using Eq. (2-5) the z-pin pull-out energy for various pull-out lengths can be calculated, as shown in Figure 9-7b. It can be seen that the model predictions correlate well with the experimental results pertinent to a pin density of 0.5 vol%. Furthermore, the calculated pull-out energy is in agreement with the improvement of the steady-state value of G_{Ic} due to the presence of the z-pins, compared to the control laminate, i.e. about 2 kJ/m^2 as shown in Figure 9-6. Moreover, the energy dissipation during the z-pin pull-out from the CNF-reinforced matrix was found to be ~25% greater than the unmodified matrix. This suggests interactions occur between the CNFs and z-pins which lead to significant toughness enhancements. Therefore, the presence of CNFs in the matrix delays the onset of z-pin debonding process and also increases the frictional energy dissipated during the subsequent pull-out of the z-pin, which is due to the pull-out of additional CNFs at the z-pin/matrix interface, as shown in Figure 9-8. This enhancement to the energy dissipation during the pull-out of the z-pins in the presence of the CNFs in the matrix leads to the synergistic improvement in the fracture toughness of the laminate that is observed.

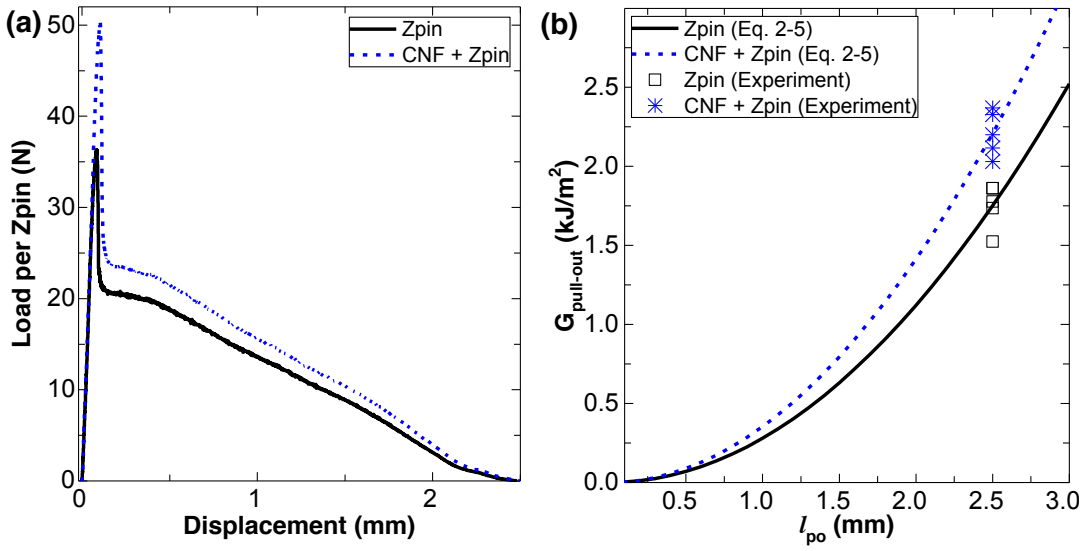

Figure 9-7: Effects of the CNF-reinforced matrix on (a) the z-pin traction load-crack opening displacement curve and (b) the z-pin pull-out energy calculated from (i) the area under the load-displacement curve in (a) and (ii) Eq. (2-5).

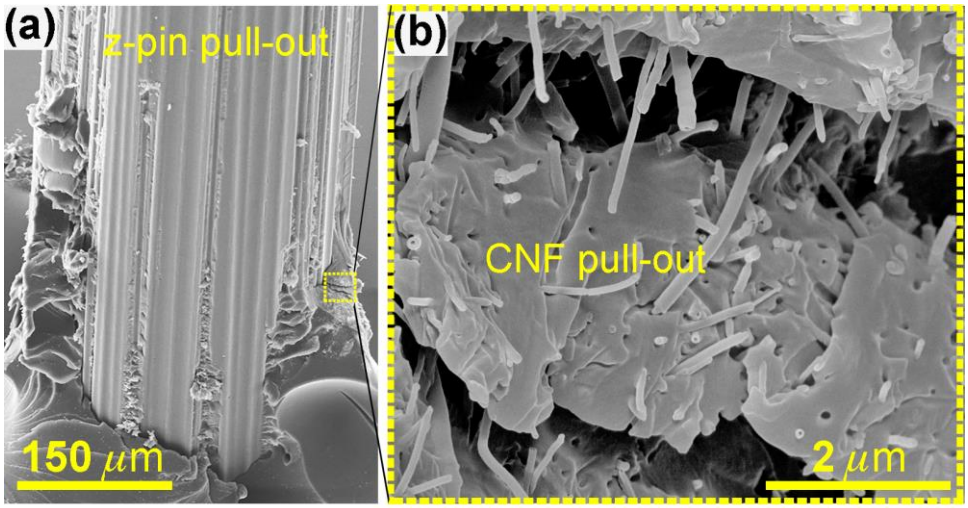

Figure 9-8 : SEM micrographs of the z-pin surface (a) at low magnification and (b) at high magnification, as observed for the pin pull-out specimens reinforced with CNFs and z-pins concurrently.

9.3.2 Cyclic-fatigue tests

Figure 9-9 presents the fatigue delamination growth, *da*/*dN*, per load cycle against the cyclic strain-energy release-rate range (SERR) for the unreinforced laminate and laminates reinforced with CNFs and/or z-pins. The measured *da*/*dN* versus ΔG_{eq} curves exhibit the typical Paris relationship, where the term ΔG_{eq} is defined by [254, 296, 297]:

$$\Delta G_{eq} = \left(\sqrt{G_{max}} - \sqrt{G_{min}}\right)^2 \tag{9-5}$$

The above relationship can be extended by using the Forman equation [292] to account for the effects of the threshold and fracture toughness on the crack growth rate, as given by the following relationship [296]:

$$\frac{da}{dN} = \frac{C[\Delta G_{eq} - \Delta G_{eq,th}]^m}{(1-R)[\sqrt{G_{Ic}} - \sqrt{\Delta G_{eq}}]} \tag{9-6}$$

where $\Delta G_{eq,th}$ is the threshold value of ΔG_{eq} and R is the crack opening displacement ratio during fatigue loading. With the values of $\Delta G_{eq,th}$ and the fracture energy listed in Table 9-1, the parameters C and m in Eq. (9-6) can be obtained by curve-fitting the

measured fatigue crack growth rates using Eq. (9-6). (The value of $\Delta G_{eq,th}$, below which no cyclic-fatigue crack will occur from the pre-existing delamination, was taken at a crack growth rate of 10^{-9} m/cycle.)

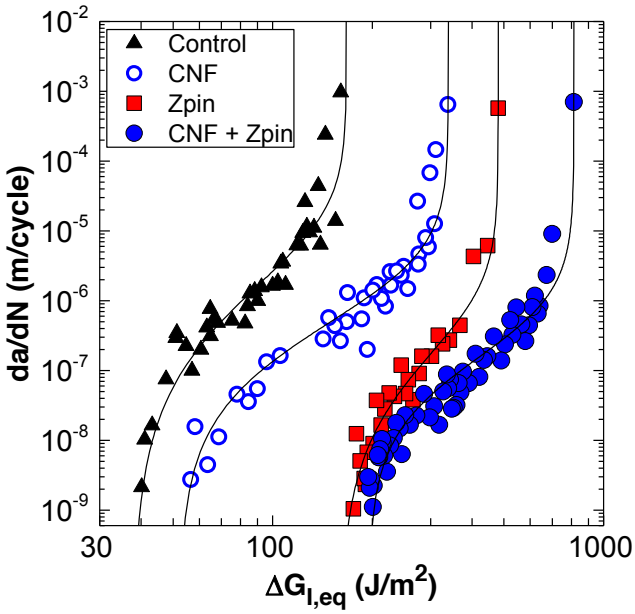

Figure 9-9 : Paris curve plots showing the effect of the applied strain energy release range ($\Delta G_{I,eq}$) on the fatigue crack growth rate (da/dN) for the control laminate and the laminates reinforced with 0.82 vol% CNFs and/or 0.5 vol% z-pins.

Table 9-1: Tensile and fatigue delamination properties of the laminates.

Specimen	G_{Ic} (J/m^2)	$\Delta G_{eq,th}$ (J/m^2)	G_{Ic} (J/m^2)	m	C	E_{11} (GPa)	σ_{11} (MPa)
Control	670	40	670	2.2	4×10^{-7}	49.6 (0.1)	447.5 (3.7)
CNF	1123	56	1123	1.7	2×10^{-7}	50.1 (0.5)	452.9 (4.1)
z-pin	1922	165	1922	2	3.6×10^{-8}	49.3 (0.1)	427.6 (2.3)
CNF + z-pin	3255	200	3255	1.4	9×10^{-8}	49.3 (0.2)	436.7 (6.5)

Note: The value of the crack opening displacement ratio during fatigue loading was 0.5. The values in the bracket indicate standard deviations.

Similar to the results for the quasi-static interlaminar tests, the resistance to fatigue loading was much greater for the laminate reinforced with CNFs and z-pins concurrently. Indeed, the value of $\Delta G_{eq,th}$ increased by ~40% for the CNF-reinforced and ~300% for the z-pin reinforced laminates. However, when the laminate was reinforced together with both CNFs and z-pins concurrently, the value of $\Delta G_{eq,th}$ was

much greater and increased by ~400% compared to the control laminate. Similarly there was a much greater reduction in the gradient of the crack growth rate, as defined by the Paris exponent *m* (see Eq. 9-6 and values given in Table 9-1) for the laminate reinforced with CNFs and z-pins concurrently. The value of the exponent, *m*, defines the sensitivity of the crack growth rate of a material to variations in the applied range of cyclic SERR. A lower value of *m*, in part, indicates a greater resistance to fatigue crack growth. In contrast, the value of *m* measured for the laminates reinforced with CNFs and z-pins separately, was only slightly lower than the control laminate. Similar to the quasi-static interlaminar tests, the toughening due to CNF pull-out and crack bridging near the tip caused the improvement to the cyclic fatigue delamination resistance in the CNF-reinforced laminate. For the z-pinned laminate, the fatigue-induced delamination growth caused the formation of a large-scale z-pin bridging zone along the crack wake. This z-pin bridging zone generated traction loads that slowed the fatigue crack growth rate under cyclic loading. However, for the laminate reinforced with CNFs, the improvement in the value of $\Delta G_{eq,th}$ was somewhat lower than the improvement seen in the fracture energy during quasi-static loading of this laminate. This was due to the degradation of the CNF bridging zone near the crack tip caused by the fatigue-induced damage of the CNFs. For example, Figure 9-10 shows the fatigue-induced damage of the CNFs on the fracture surface of the CNF-reinforced laminate tested under fatigue loading. The outer primary load-bearing CNF wall appears to have been damaged by the fatigue loading which resulted in the smaller diameter inner-core carrying low load, due to its lower stiffness. Most notably, when CNF and z-pin reinforcements are used concurrently, the improvement to $\Delta G_{eq,th}$ is much greater than the expected additive effect from the toughening due to CNFs and z-pin, representing a major synergistic toughening mechanism.

Next, the question arises of whether, when CNF and z-pin reinforcements are used concurrently, is the improvement to ΔG_{eq} much greater than expected simply from an additive effect from the toughening due to the CNFs and z-pin acting independently? Since, the former would represent a major synergistic toughening mechanism. Here the apparent synergy in fatigue resistance can be calculated by replacing G_{Ic} in Eq. (9-2) with ΔG_{eq}:

$$\text{Synergy}_{Fatigue} = \frac{\Delta G_{eq(CNF+zpin)} - \Delta G_{eq(Control)}}{(\Delta G_{eq(zpin)} - \Delta G_{eq(Control)}) + (\Delta G_{eq(CNF)} - \Delta G_{eq(Control)})} - 1 \qquad (9\text{-}7)$$

This possible fatigue synergy refers to the SERR range, ΔG_{eq}, necessary to cause a given fatigue crack growth rate of *da*/*dN*. The results are presented in Figure 9-11. When the CNF and z-pin reinforcements are used concurrently, the level of improvement to the ΔG_{eq} near the threshold range (~13%) is very similar to the synergistic improvement observed in the quasi-static fracture toughness of this laminate, which was 11%. The apparent synergistic improvement was, however, much greater (~35%) at higher growth rates and, hence, at higher values of ΔG_{eq}, i.e. when the crack growth rate exceeded ~10^{-6} m/cycle (see Figure 9-11). However, this apparent synergy in the fatigue resistance has been found to be statistically insignificant by using a two-way analysis of variance (ANOVA). The large scatter of about one order of magnitude observed in the crack growth rates leads to a high *p*-value of 0.679, which implies that the interaction is statistically improbable.

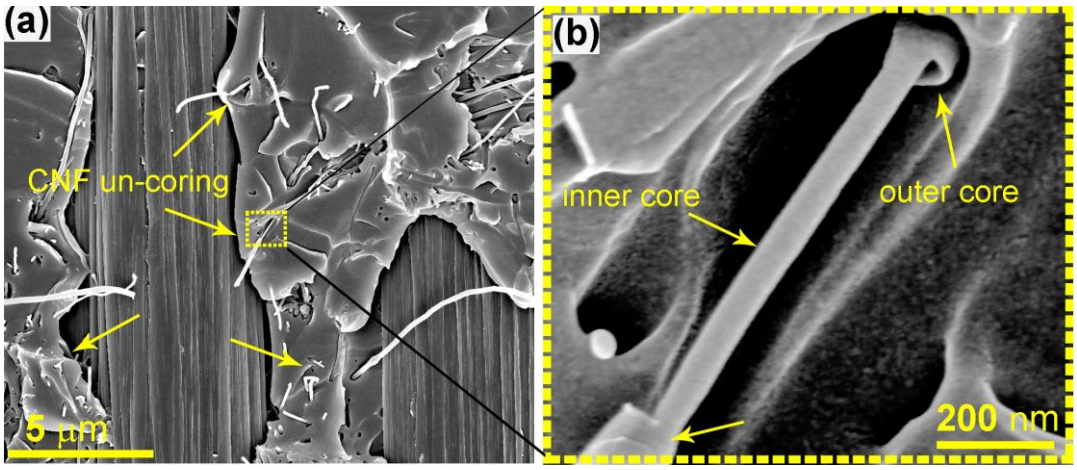

Figure 9-10 : CNF un-coring type damage as observed on the fracture surface of the CNF-reinforced laminate tested under fatigue loading.

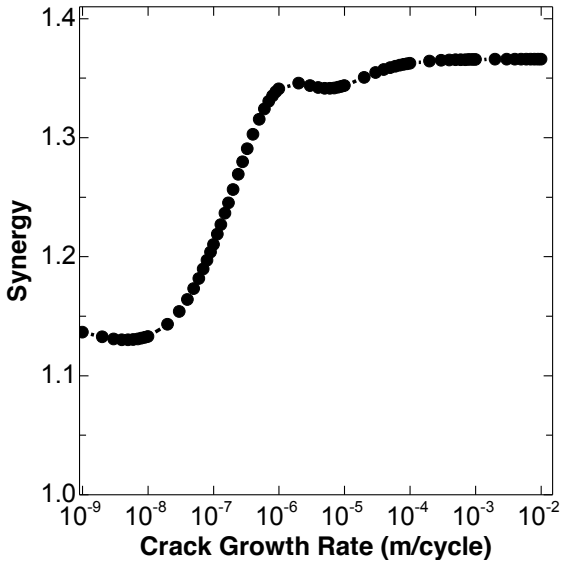

Figure 9-11 : The level of synergistic improvement to the strain energy release range (ΔG_{eq}) for the laminate reinforced with CNFs and z-pins concurrently.

Studies have shown that fatigue damage of the z-pin/laminate interface can result in early onset of interfacial debonding of z-pins which eventually leads to their failure by pull-out [21, 40]. To further investigate the influence of CNFs on the z-pin/laminate interface properties, additional cyclic-loading pin pull-out tests were conducted. Figure 9-12 shows the influence of CNFs on the friction traction load generated during the cyclic pull-out of z-pins, and a comparison to quasi-static test results. As seen in Figure 9-12a, there is a progressive reduction in the friction traction load generated by z-pins with increasing number of displacement cycles. This reduction is due to the wearing of the z-pin/laminate interface caused by the cyclic pull-out of the pins [28]. For instance, Figure 9-13 shows images taken inside the holes created from z-pin pull-out in the specimens tested under quasi-static or fatigue loading. The hole-wall surface was relatively smooth when the pins were pulled-out under quasi-static loading. Under cyclic loading there was significant wearing of the hole surface, since during cyclic loading the z-pins slid back and forth against the laminate with each load cycle. This resulted in a fretting-type wear process which caused widening of the hole around the debonded z-pin. This then led to the progressive reduction in the friction traction stress generated by the z-pins with increasing number of load cycles as shown in Figure 9-12a. A comparison of the peak z-pin friction traction load for the unreinforced and CNF-reinforced matrix is presented in Figure 9-12b. This figure shows that similar to

quasi-static loading, a higher z-pin bridging traction is generated due to CNF reinforcement of the z-pin/laminate interface under cyclic loading.

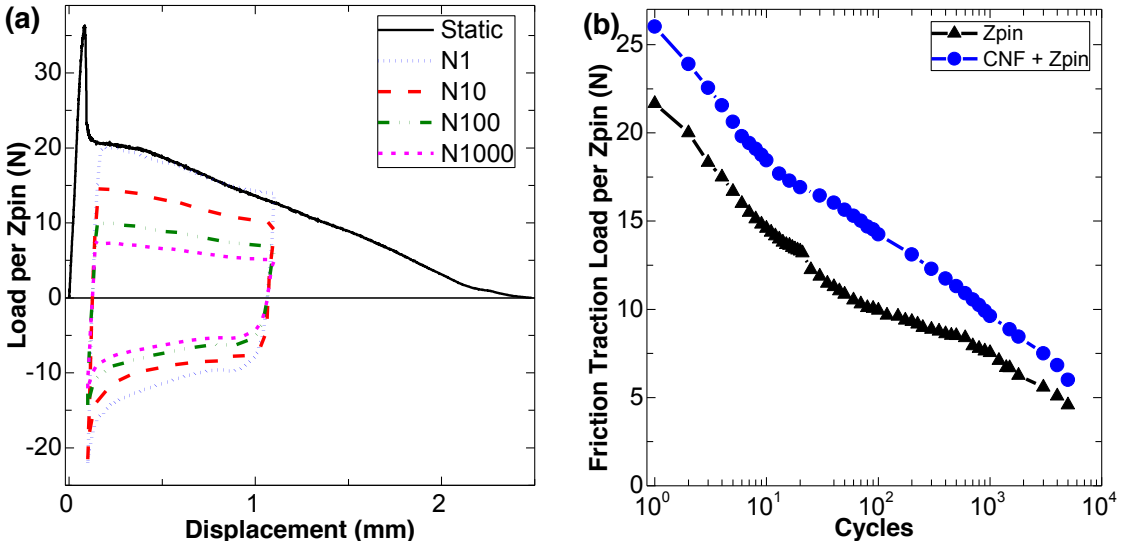

Figure 9-12 : (a) Effect of cyclic loading on the z-pin friction traction load-displacement curve with increasing number of load cycles as measured for the pin pull-out specimen reinforced with 0.5 vol% z-pins. N is the number of load cycles. (b) The peak z-pin friction traction load measured with increasing number of load cycles for the pin pull-out specimen reinforced with pins only and the specimen reinforced with CNFs and z-pins concurrently.

As seen in Figure 9-13c, the fretting-type wear process is less severe for the z-pin/laminate interface reinforced by CNFs. This is because the CNF nano-reinforcements acts to improve the shear strength of the composite matrix [26, 141]. For example, Figure 9-13d shows that the CNFs bridge the micro-cracks that form during the shear deformation of the z-pin/matrix interface due to a cyclic pull-out process and reduce the fretting-type wear action. In z-pinned DCB laminates, the severity of the fretting-wear was observed to increase with ΔG_{eq}. Since at higher ΔG_{eq} values, the sliding distance in each cycle increases, this can lead to a greater amount of fretting-type wear of the z-pin/laminate interface. However, at such high ΔG_{eq} values, the CNF reinforcement to the z-pin/laminate interface demonstrated a greater influence on the fatigue performance of the z-pins. This explains the greater level of improvement observed at higher ΔG_{eq} values for the laminate reinforced with both CNFs and z-pins. The rupturing or 'un-coring' type of cyclic damage to the CNFs which caused the degradation of the crack-bridging zone of the CNFs was rarely observed on the fracture

surface of the laminate reinforced with CNFs and z-pins concurrently. This suggests that, under fatigue loading, the z-pin bridging zone and the resultant traction load shields the CNF bridging zone at the crack tip, leading to the significantly greater improvement in the value of $\Delta G_{eq,th}$ that was observed when CNFs and z-pins were used concurrently, see Table 9-1.

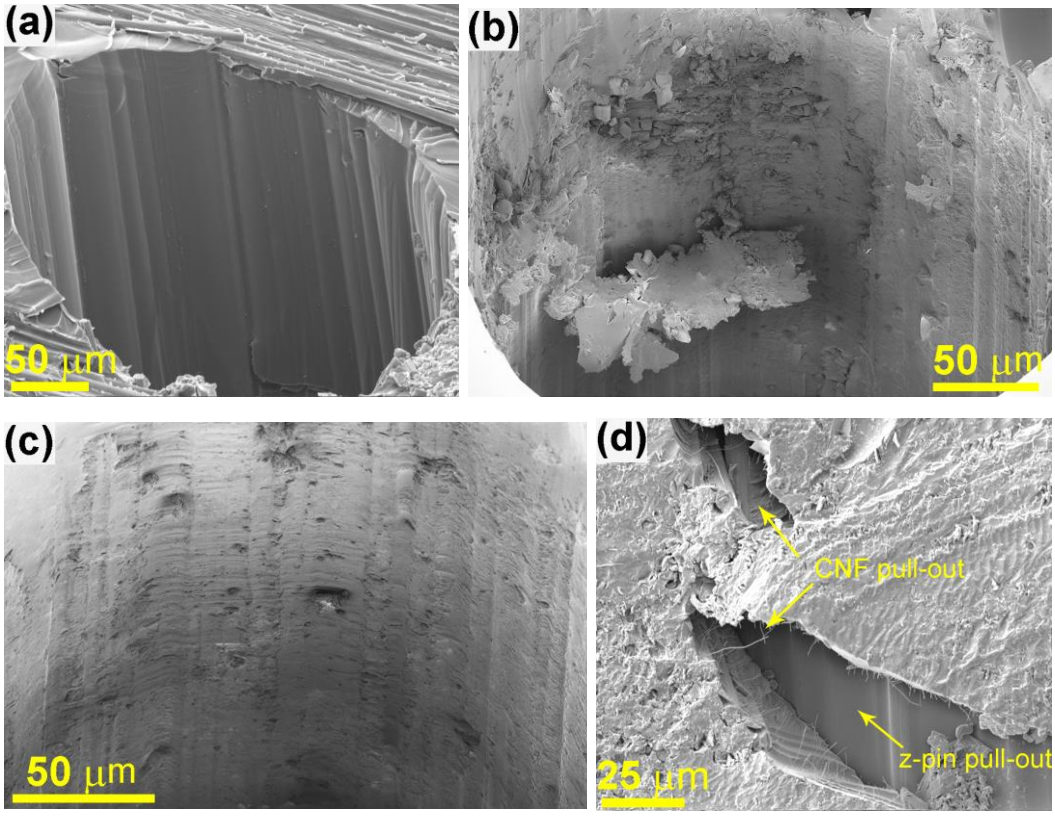

Figure 9-13 : SEM micrographs of the hole walls formed by z-pin pull-out under (a) static interlaminar loading, (b) fatigue loading; and (c-d) for specimen reinforced with CNFs and tested under fatigue loading.

In addition, tensile tests were performed to assess the influence of through-thickness reinforcement on the in-plane properties of the laminates. The tensile strength (σ_{11}) and Young's modulus (E_{11}) of the laminates are listed in Table 9-1. The stiffness of the through-thickness reinforced laminates is very similar to the control laminate. However, the tensile strength of the z-pinned laminates decreased by 2 to 4%. Previous studies have also reported that a greater reduction occurs in the tensile strength of z-pinned laminates in comparison to the reduction in their stiffness [287]. The magnitude of the reduction in the strength of laminates reinforced with 0.5 vol% z-pins is similar to that reported in other studies [20]. The reduction in strength is attributed to the

crimping of in-plane fibres caused by the inserted z-pins, which increases the stress concentration around these regions of the laminate [20, 298]. As a result, all z-pinned tensile specimens were observed to fail along the z-pin region. The CNF reinforcements caused a marginal improvement in the strength of the laminates. But this improvement was not sufficient to offset the degradation in strength due to the z-pins.

9.4 Conclusions

The effects of multi-scale toughening of carbon-epoxy laminates using carbon nanofibres and z-pins spanning multiple length scales have been investigated. The results show that CNFs are effective at improving the interlaminar fracture toughness under quasi-static loading by intrinsic (i.e. crack bifurcation or branching and epoxy void growth) and extrinsic (i.e. crack bridging and pull-out of the CNFs) mechanisms. By comparison, z-pins generate significant extrinsic toughening primarily behind the crack tip and over a larger length-scale via crack bridging. When used concurrently, the interaction between the CNFs and z-pins has been shown to yield a greater toughness than when the two reinforcements are used separately. In particular, the presence of CNFs in the matrix enhanced the energy dissipation during the pull-out of the z-pins; indeed, this represented a major synergy suggesting a multiplicative toughening effect. The presence of a synergistic effect was indeed confirmed for the quasi-static toughness results via a statistical analysis. However, the tensile strength of the z-pinned laminates was slightly lower than that of the control laminates. The addition of the CNF reinforcement to the z-pinned laminates was insufficient to recover this loss of strength.

The multi-scale reinforcement to the laminate via CNFs and z-pins also leads to a strong improvement in the resistance to cyclic-fatigue delamination growth over the entire range of crack growth rates from the threshold regime to instability. The improvement in the fatigue delamination resistance has been found to increase with delamination growth, due to the greater effects of the CNF reinforcement on the z-pin/laminate interface under fatigue loading at relatively high cyclic loads. Although there was an initial suggestion of synergistic improvement to the fatigue resistance

when the laminate was reinforced by both CNFs and z-pins, it was statistically insignificant and therefore the overall improvement was largely additive from these two reinforcements.

A new class of multi-scale fibre composites has been described which offers a unique opportunity to markedly enhance the fracture toughness and fatigue resistance of polymer matrix fibre composites, and hence significantly increase the damage tolerance of such composites over multiple length-scales of delamination cracking from sub-micron to sub-meter scales, which has previously not been possible. It is feasible that other types of carbon nano-reinforcements (e.g. CNTs, grapheme) and z-pins (e.g. metals) promote similar or even greater interlaminar strengthening, and this is currently under investigation.

CHAPTER 10

Concluding Remarks

10.1 Major Conclusions

10.1.1 Electrical conductivity and fracture energy of aligned CNF and GNP-reinforced epoxy composites

This PhD study investigated the effects of the carbon nano-reinforcement shape, orientation and concentration on the electrical conductivity and fracture energy of epoxy composites. The experimental study shows that both the one-dimensional CNFs and two-dimensional GNPs are effective reinforcements for improving the electrical conductivity and fracture energy of thermoset epoxy polymer. The AC electric-field was found to be very effective in aligning CNFs and GNPs to form a chain-like structure in epoxy. The AC electric-field induced alignment and chaining of CNFs and GNPs led to the formation of a percolating network at low nano-reinforcement content, thus yielding a measurable DC conductivity. The epoxy composites containing aligned nano-reinforcements showed a lower (by ~50%) electrical percolation threshold in comparison to the epoxy composites containing randomly-oriented nano-reinforcements. Compared to the unmodified epoxy, the improvement in electrical conductivity of the epoxy composites containing aligned CNFs and GNPs were increased by about then and seven orders of magnitude, respectively.

The fracture energy of the epoxy composites reinforced with just 1 wt% of CNFs and GNPs increased by about 850% and 500%, respectively. An additional improvement in the fracture energy of up to about 40% was achieved by aligning the nano-reinforcements transverse to the crack growth direction. However, the efficacy of the alignment of nano-reinforcements on the improvement in the electrical conductivity and fracture energies of the epoxy composites was found to diminish at higher

concentrations of nano-reinforcements. The fractographic analysis revealed that the large improvement in the fracture energy of the nano-reinforced epoxy composites was due to a combination of intrinsic and extrinsic toughening mechanisms, including (i) debonding of the nano-reinforcements, (b) the energy associated with the frictional pull-out of the nano-reinforcements, (c) crack bridging and rupturing of the nano-reinforcements, and (d) void growth around the debonded nano-reinforcements in the process zone. The alignment of the nano-reinforcements perpendicular to the crack path generally led to a higher fraction of nano-reinforcements participating in these aforementioned toughening mechanisms, and thus accounted for the relatively higher values of fracture energy. The mechanistic fracture model developed to estimate the fracture energy contribution from each of the above toughening mechanism was in good agreement with the experimental results. The fracture energy modelling results showed that the one-dimensional CNFs are efficient at increasing the intrinsic toughness of epoxy in the form of epoxy void growth, whereas the two-dimensional GNPs are more effective at extrinsic toughening through pull-out and crack bridging of the GNPs.

In addition to the use of electric-field to align CNFs, the PhD project investigated the alignment of CNFs using a magnetic-field. The functionalisation of CNFs with Fe_3O_4 nanoparticles significantly enhanced their magnetic susceptibility. A low magnetic-field of just 50 mT was found to be sufficient to cause the alignment of the Fe_3O_4 functionalised CNFs in a liquid epoxy resin. The curing of the Fe_3O_4@CNF epoxy composites in the presence of a magnetic-field was found to maintain the alignment of Fe_3O_4@CNFs along the external field direction in the cured epoxy composite samples. The improvement in the electrical conductivity and fracture energy of the epoxy composites reinforced with magnetic-field aligned Fe_3O_4@CNFs was greater than their random counterparts. However, the overall improvements for the epoxy composites reinforced with Fe_3O_4 functionalised CNFs was lower than that reinforced with the unfunctionalised CNFs. This was attributed to the damage to the CNFs caused by the acid treatments used for the synthesis of Fe_3O_4 functionalised CNFs as well as the severe shear forces experienced during their dispersion via multiple ultrasonication treatments. This study showed that the synthesis of high quality nano-reinforcements with high susceptibility to magnetic-field and at higher volume production remains a challenging task. In this PhD study, the as supplied CNF

reinforcement of the epoxy composites showed the highest level of improvement in their electrical conductivity and fracture energy compared to the GNP and Fe_3O_4 functionalised CNF reinforcements.

10.1.2 Fatigue resistance of epoxy composite reinforced with aligned CNFs

A further experimental investigation explored the effectiveness of electric-field aligned CNFs at improving the fatigue resistance of epoxy composites. Under cyclic loading, the CNF-reinforced epoxy composites showed improved resistance to fatigue cracking. The critical and threshold strain energy of the CNF-reinforced epoxy composites was much greater than unmodified epoxy. The improvement in the critical strain energy measured under cyclic loading was similar to the level of improvement observed in the fracture energy of these epoxy composites tested under monotonic loading. Similar to the quasi-static fracture energy tests, a somewhat greater improvement to the fatigue resistance was measured for the epoxy composites reinforced with aligned CNFs. The increase in the fatigue resistance of the CNF-reinforced epoxy composites was due to the same underlying toughening mechanisms observed during the quasi-static fracture energy tests. However, the fractographic analysis revealed that CNFs undergo a unique fatigue induced damage mechanism when subjected to cyclic loading. The inner layer of double-layer CNFs can unravel under cyclic fatigue loading, following the fracture of the outer layer. This deformation mechanism, which has not been observed previously in quasi-static tests, contributes to the substantial improvements observed in the cyclic-fatigue resistance of such epoxy nanocomposites.

10.1.3 Disbond detection in bonded composite joints using aligned CNFs

Next, the aligned CNF-reinforced epoxy composites were used as adhesive for bonded carbon fibre-epoxy joints to investigate the effectiveness of CNF networks for detecting disbond in composite joints. Real-time *in-situ* resistance measurements through-the-thickness of such composite joints during cyclic loading revealed a large increase in the resistance due to fatigue cracking of the CNF-reinforced adhesive layer. The increase in resistance due to the propagation of fatigue cracks was in good agreement with the simple resistivity model used in the investigation. The disbond length calculated from

the *in-situ* resistance measurement using the resistivity model was in good agreement with the optically observed disbond length. The alignment of the CNFs in the through-thickness direction of the adhesive joints showed no obvious advantage over their randomly-oriented counterparts for detecting disbond in joint. However, the *in-situ* resistance based disbond detection technique demonstrated in this PhD study offers excellent alternative to other traditional non-destructive inspection techniques currently used for detecting disbond in adhesively bonded composite joints.

10.1.4 Multi-scale composites reinforced with CNFs and z-pins

In addition, the multi-scale toughening effects of CNF and z-pin reinforcements on the interlaminar delamination resistance of carbon fibre-epoxy laminates was investigated under quasi-static and cyclic loading. For the laminate reinforced concurrently with CNFs and z-pins, the CNFs promote high delamination resistance by multiple intrinsic (i.e. crack bifurcation or branching and epoxy void growth) and extrinsic (i.e. crack bridging and pull-out of the CNFs) toughening mechanisms. In addition, an even greater contribution to toughness occurred from z-pins through an extrinsic toughening primarily behind the crack tip and over a larger length-scale via crack bridging. The presence of CNFs in the matrix enhanced the energy dissipation during the pull-out of the z-pins; indeed, this represented a major synergy suggesting a multiplicative toughening effect. Therefore, when used concurrently, the interaction between the CNFs and z-pins was shown to yield a greater toughness than when the two reinforcements were used separately. In particular, the presence of CNFs in the matrix enhanced the energy dissipation during the pull-out of the z-pins; which represented a major synergistic toughening effect. The multi-scale reinforcement to the laminate via CNFs and z-pins also led to a strong improvement in the resistance to cyclic-fatigue delamination growth over the entire range of crack growth rates from the threshold regime to instability. While there was an initial suggestion of synergistic improvement to the fatigue resistance when the laminate was reinforced by both CNFs and z-pins, it was found to be statistically insignificant. The multi-scale fibre composite offers a unique opportunity to markedly enhance the fracture toughness and fatigue resistance of advanced fibre-reinforced composites, and thus improving their damage tolerance.

10.2 Recommendations and Future Research Area

This PhD project has researched the efficacy of the aligned carbon nano-reinforcements in improving the electrical properties and fracture resistance of an epoxy polymer and its composites. The research has highlighted the advantages of aligning carbon nano-reinforcements for achieving the optimum performance in epoxy composites. However, there remain key challenges in achieving the alignment of carbon nano-reinforcements in the through-thickness direction of advanced fibre-reinforced composites. This section briefly describes several research topics worthy of investigation to advance the science and technology of nano-reinforced composites.

10.2.1 Further Assessment of the Fracture Resistance of Nano-reinforced Composites

This project investigated the fracture resistance of epoxy composites and fibre-reinforced epoxy composites containing carbon nano-reinforcements when subjected to mode I static and fatigue loading. However, additional investigation into the fracture properties of nano-reinforced composites under different loading conditions is needed. Although, the alignment of the carbon nano-reinforcements along the primary loading direction (i.e. mode I) leads to optimum improvement to its fracture resistance. The effect of alignment on the fracture resistance of composites under other loading conditions such as mode II and mixed I/II needs to be evaluated. This could result in the fracture resistance of carbon nano-reinforced composites under mode II and mixed-mode conditions being different to the high level of improvement observed in this PhD project for mode I loading.

In addition, the level of improvements observed in the fracture toughness and fatigue crack growth resistance of CNF-reinforced epoxy, if used as an adhesive, may depend on the bond line thickness. The possible effect of the adhesive bond line thickness on the fracture and fatigue resistance of CNF-reinforced epoxy composites can be investigated. Moreover, the mechanistic fracture modeling studies showed that the respective contribution from the primary toughening mechanisms, namely nano-reinforcements pull-out, debonding, void growth and their rupture depends largely on the nano-reinforcement/polymer interface properties. Thus, the effect of modulating the

nano-reinforcement/polymer interface on the fracture toughness and the toughening mechanisms of nano-reinforced composites could be investigated. The effects of modulating the nano-reinforcement/polymer interface could be further investigated using molecular dynamic simulations to obtain a comprehensive model of the fracture mechanisms of the nano-reinforced composites which cannot be captured using the mechanistic model proposed in this PhD.

10.2.2 Aligning Carbon Nano-reinforcements in Carbon Fibre-Epoxy Composites

This project investigated the alignment of CNFs in epoxy composites using electric- and magnetic-field. The use of electric-field was found to be more effective at improving electrical conductivity and fracture properties of CNF-epoxy composites in comparison to the Fe_3O_4@CNF-epoxy composites prepared with magnetic-field. Although, magnetic-field can be used to align CNFs in carbon fibre-epoxy composites, the use of co-precipitation technique to synthesis Fe_3O_4 functionalised CNFs with improved magnetic susceptibility was found to cause structural damage of CNFs. The resulting Fe_3O_4@CNF-reinforced epoxy composites possessed lower fracture resistance. This combined with the very low volume yield of Fe_3O_4@CNF functionalisation process makes it impractical for reinforcing carbon fibre-epoxy composite laminates for further investigations. Therefore, any future study needs to overcome this dilemma of improving the magnetic susceptibility of carbon nano-reinforcements without adversely affecting their reinforcing capability. Recently, the deposition of ferromagnetic metals on CNTs using electron-beam evaporation has been shown to increase their magnetic susceptibility with good prospects for scalable manufacturing of such carbon nano-materials without adversely affecting its inherent properties [299]. Furthermore, the use of aligned CNFs in the adhesive joints showed no obvious advantage over their randomly-oriented counterparts for detecting disbond in joint. The use of CNF-reinforced adhesives enabled the detection of small damage size of about 5 percent of the bond area. However, the ability to detect the damage may also depend on the size of the samples, the conductivity of the composite adherends as well as the location of the electrodes used to measure the potential drop. These effects need to be investigated before the proposed detection technique could be used for actual structural health monitoring application.

Bibliography

[1] Wang CH, Duong CN. Bonded Joints and Repairs to Composite Airframe Structures: Academic Press; 2015.

[2] Hexcel. 2015 annual report. 2015.

[3] Baker AAB. Composite materials for aircraft structures: AIAA; 2004.

[4] Tong L, Mouritz AP, Bannister M. 3D fibre reinforced polymer composites: Elsevier; 2002.

[5] Airbus. Airbus composite training : Evolution composite application at Airbus. VPO Conference, Frankfurt2007.

[6] EASA. Composite damage metrics and inspection - EASA.2010.C13. 2012.

[7] Ostrower J. Delamination prompts Boeing to inspect 787 fleet. vol. 2013 Washington DC: Flight Global; 2012.

[8] FAA. Damage tolerance and fatigue evaluation of structure AC 25.571-1D. 2001.

[9] FAA. Composite Aircraft Structure AC 20-107B. 2009.

[10] Boeing. Lightning strikes: Protection, inspection, and repair. Aeromagazine. 2012(48).

[11] Boeing. Special damage cases : Lightning strikes. Aeromagazine. 2014(56).

[12] Garg AC, Mai YW. Failure mechanisms in toughened epoxy resins-A review. Composites Science and Technology. 1988;31(3):179-223.

[13] Bucknall CB, Partridge IK. Phase separation in epoxy resins containing polyethersulphone. Polymer. 1983;24(5):639-644.

[14] Hourston DJ, Lane JM. The toughening of epoxy resins with thermoplastics: 1. Trifunctional epoxy resin-polyetherimide blends. Polymer. 1992;33(7):1379-1383.

[15] Bascom WD, Cottington RL, Jones RL, Peyser P. The fracture of epoxy- and elastomer-modified epoxy polymers in bulk and as adhesives. J Appl Polym Sci. 1975;19:2545-2562.

[16] Kinloch AJ, Shaw SJ, Tod DA, Hunston DL. Deformation and fracture behaviour of a rubber-toughened epoxy: 1. Microstructure and fracture studies. Polymer. 1983;24(10):1341-1354.

[17] Kinloch AJ, Mohammed RD, Taylor AC, Eger C, Sprenger S, Egan D. The effect of silica nano particles and rubber particles on the toughness of multiphase thermosetting epoxy polymers. Journal of Materials Science. 2005;40(18):5083-5086.

[18] Kinloch AJ, Taylor AC. Mechanical and fracture properties of epoxy/inorganic micro- and nano-composites. Journal of Materials Science Letters. 2003;22(20):1439-1441.

[19] Kinloch AJ, Taylor AC. The mechanical properties and fracture behaviour of epoxy-inorganic micro- and nano-composites. Journal of Materials Science. 2006;41(11):3271-3297.

[20] Mouritz AP. Review of z-pinned composite laminates. Composites Part A: Applied Science and Manufacturing. 2007;38(12):2383-2397.

[21] Zhang AY, Liu HY, Mouritz AP, Mai YW. Experimental study and computer simulation on degradation of z-pin reinforcement under cyclic fatigue. Composites Part A: Applied Science and Manufacturing. 2008;39(2):406-414.

[22] Bekyarova E, Thostenson ET, Yu A, Kim H, Gao J, Tang J, Hahn HT, Chou TW, Itkis ME, Haddon RC. Multiscale carbon nanotube-carbon fiber reinforcement for advanced epoxy composites. Langmuir. 2007;23(7):3970-3974.

[23] Kim HS, Hahn HT. Graphite fiber composites interlayered with single-walled carbon nanotubes. Journal of Composite Materials. 2011;45(10):1109-1120.

[24] Hu N, Masuda Z, Yan C, Yamamoto G, Fukunaga H, Hashida T. The electrical properties of polymer nanocomposites with carbon nanotube fillers. Nanotechnology. 2008;19(21).

[25] Bortz DR, Merino C, Martin-Gullon I. Mechanical characterization of hierarchical carbon fiber/nanofiber composite laminates. Composites Part a-Applied Science and Manufacturing. 2011;42(11):1584-1591.

[26] Palmeri MJ, Putz KW, Ramanathan T, Brinson LC. Multi-scale reinforcement of CFRPs using carbon nanofibers. Composites Science and Technology. 2011;71(2):79-86.

[27] Park JK, Do I-H, Askeland P, Drzal LT. Electrodeposition of exfoliated graphite nanoplatelets onto carbon fibers and properties of their epoxy composites. Composites Science and Technology. 2008;68(7–8):1734-1741.

[28] Shin MK, Lee B, Kim SH, Lee JA, Spinks GM, Gambhir S, Wallace GG, Kozlov ME, Baughman RH, Kim SJ. Synergistic toughening of composite fibres by self-alignment of reduced graphene oxide and carbon nanotubes. Nature Communications. 2012;3.

[29] Mannov E, Schmutzler H, Chandrasekaran S, Viets C, Buschhorn S, Tölle F, Mülhaupt R, Schulte K. Improvement of compressive strength after impact in fibre reinforced polymer composites by matrix modification with thermally reduced graphene oxide. Composites Science and Technology. 2013;87:36-41.

[30] Shen M-Y, Chang T-Y, Hsieh T-H, Li Y-L, Chiang C-L, Yang H, Yip M-C. Mechanical Properties and Tensile Fatigue of Graphene Nanoplatelets Reinforced Polymer Nanocomposites. Journal of Nanomaterials. 2013;2013:1-9.

[31] Fiedler B, Gojny FH, Wichmann MHG, Nolte MCM, Schulte K. Fundamental aspects of nano-reinforced composites. Composites Science and Technology. 2006;66(16):3115-3125.

[32] Termonia Y. Structure–property relationships in nanocomposites. Polymer. 2007;48(23):6948-6954.

[33] Sandler JKW, Kirk JE, Kinloch IA, Shaffer MSP, Windle AH. Ultra-low electrical percolation threshold in carbon-nanotube-epoxy composites. Polymer. 2003;44(19):5893-5899.

[34] Bauhofer W, Kovacs JZ. A review and analysis of electrical percolation in carbon nanotube polymer composites. Composites Science and Technology. 2009;69(10):1486-1498.

[35] Thostenson ET, Chou TW. Real-time in situ sensing of damage evolution in advanced fiber composites using carbon nanotube networks. Nanotechnology. 2008;19(21).

[36] Lim AS, Melrose ZR, Thostenson ET, Chou TW. Damage sensing of adhesively-bonded hybrid composite/steel joints using carbon nanotubes. Composites Science and Technology. 2011;71(9):1183-1189.

[37] Hu N, Itoi T, Akagi T, Kojima T, Xue J, Yan C, Atobe S, Fukunaga H, Yuan W, Ning H, et al. Ultrasensitive strain sensors made from metal-coated carbon nanofiller/epoxy composites. Carbon. 2013;51:202-212.

[38] Hu N, Karube Y, Arai M, Watanabe T, Yan C, Li Y, Liu Y, Fukunaga H. Investigation on sensitivity of a polymer/carbon nanotube composite strain sensor. Carbon. 2010;48(3):680-687.

[39] Lubineau G, Rahaman A. A review of strategies for improving the degradation properties of laminated continuous-fiber/epoxy composites with carbon-based nanoreinforcements. Carbon. 2012;50(7):2377-2395.

[40] Pingkarawat K, Mouritz AP. Improving the mode I delamination fatigue resistance of composites using z-pins. Composites Science and Technology. 2014;92:70-76.

[41] Mirjalili V, Hubert P. Modelling of the carbon nanotube bridging effect on the toughening of polymers and experimental verification. Composites Science and Technology. 2010;70(10):1537-1543.

[42] Veedu VP, Cao AY, Li XS, Ma KG, Soldano C, Kar S, Ajayan PM, Ghasemi-Nejhad MN. Multifunctional composites using reinforced laminae with carbon-nanotube forests. Nature Materials. 2006;5(6):457-462.

[43] Zhang Q, Liu J, Sager R, Dai L, Baur J. Hierarchical composites of carbon nanotubes on carbon fiber: Influence of growth condition on fiber tensile properties. Composites Science and Technology. 2009;69(5):594-601.

[44] Monti M, Natali M, Torre L, Kenny JM. The alignment of single walled carbon nanotubes in an epoxy resin by applying a DC electric field. Carbon. 2012;50(7):2453-2464.

[45] Shi D, He P, Lian J, Chaud X, Bud'Ko SL, Beaugnon E, Wang LM, Ewing RC, Tournier R. Magnetic alignment of carbon nanofibers in polymer composites and anisotropy of mechanical properties. Journal of Applied Physics. 2005;97(6).

[46] Xie XL, Mai YW, Zhou XP. Dispersion and alignment of carbon nanotubes in polymer matrix: A review. Materials Science and Engineering R: Reports. 2005;49(4):89-112.

[47] Chen G, Wang H, Zhao W. Fabrication of highly ordered polymer/graphite flake composite with eminent anisotropic electrical property. Polymers for Advanced Technologies. 2008;19(8):1113-1117.

[48] Kim GH, Shkel YM. Polymeric composites tailored by electric field. Journal of Materials Research. 2004;19(4):1164-1174.

[49] Wang H, Zhang H, Chen G. Preparation of unsaturated polyester/graphite nanosheet conducting composite under electric field. Composites Part A: Applied Science and Manufacturing. 2007;38(10):2116-2120.

[50] Wang H, Zhang H, Zhao W, Zhang W, Chen G. Preparation of polymer/oriented graphite nanosheet composite by electric field-inducement. Composites Science and Technology. 2008;68(1):238-243.

[51] Ma C, Zhang W, Zhu Y, Ji L, Zhang R, Koratkar N, Liang J. Alignment and dispersion of functionalized carbon nanotubes in polymer composites induced by an electric field. Carbon. 2008;46(4):706-710.

[52] Prasse T, Cavaillé JY, Bauhofer W. Electric anisotropy of carbon nanofibre/epoxy resin composites due to electric field induced alignment. Composites Science and Technology. 2003;63(13):1835-1841.

[53] Martin CA, Sandler JKW, Windle AH, Schwarz MK, Bauhofer W, Schulte K, Shaffer MSP. Electric field-induced aligned multi-wall carbon nanotube networks in epoxy composites. Polymer. 2005;46(3):877-886.

[54] Camponeschi E, Vance R, Al-Haik M, Garmestani H, Tannenbaum R. Properties of carbon nanotube-polymer composites aligned in a magnetic field. Carbon. 2007;45(10):2037-2046.

[55] Prolongo SG, Meliton BG, Del Rosario G, Urena A. New alignment procedure of magnetite-CNT hybrid nanofillers on epoxy bulk resin with permanent magnets. Composites Part B-Engineering. 2013;46:166-172.

[56] Thostenson ET, Li C, Chou TW. Nanocomposites in context. Composites Science and Technology. 2005;65(3-4):491-516.

[57] Kim H, Abdala AA, MacOsko CW. Graphene/polymer nanocomposites. Macromolecules. 2010;43(16):6515-6530.

[58] Sengupta R, Bhattacharya M, Bandyopadhyay S, Bhowmick AK. A review on the mechanical and electrical properties of graphite and modified graphite reinforced polymer composites. Progress in Polymer Science (Oxford). 2011;36(5):638-670.

[59] Al-Saleh MH, Sundararaj U. A review of vapor grown carbon nanofiber/polymer conductive composites. Carbon. 2009;47(1):2-22.

[60] Thostenson ET, Ren Z, Chou TW. Advances in the science and technology of carbon nanotubes and their composites: A review. Composites Science and Technology. 2001;61(13):1899-1912.

[61] Compton OC, Nguyen ST. Graphene oxide, highly reduced graphene oxide, and graphene: Versatile building blocks for carbon-based materials. Small. 2010;6(6):711-723.

[62] Ramos A, Cameán I, García AB. Graphitization thermal treatment of carbon nanofibers. Carbon. 2013;59:2-32.

[63] Ma PC, Siddiqui NA, Marom G, Kim JK. Dispersion and functionalization of carbon nanotubes for polymer-based nanocomposites: A review. Composites Part a-Applied Science and Manufacturing. 2010;41(10):1345-1367.

[64] Pandey G, Thostenson ET. Carbon nanotube-based multifunctional polymer nanocomposites. Polymer Reviews. 2012;52(3-4):355-416.

[65] Zhao MQ, Zhang Q, Huang JQ, Wei F. Hierarchical nanocomposites derived from nanocarbons and layered double hydroxides - Properties, synthesis, and applications. Advanced Functional Materials. 2012;22(4):675-694.

[66] Hernandez FJ, Ozalp VC. Graphene and other nanomaterial-based electrochemical aptasensors. Biosensors. 2012;2(1):1-14.

[67] Chou TW, Gao L, Thostenson ET, Zhang Z, Byun JH. An assessment of the science and technology of carbon nanotube-based fibers and composites. Composites Science and Technology. 2010;70(1):1-19.

[68] Kardos JL, Halpin JC. Short predicting the strength and toughness of fiber composites. Macromolecular Symposia. 1999;147:139-153.

[69] Kelly A, Macmillan NH. Strong Solids. Oxford: Clarendon Press; 1986.

[70] Cox HL. The elasticity and strength of paper and other fibrous materials. British Journal of Applied Physics. 1952;3(3):72-79.

[71] Kelly A, Tyson WR. Tensile properties of fibre-reinforced metals: Copper/tungsten and copper/molybdenum. Journal of the Mechanics and Physics of Solids. 1965;13(6):329-338,in321-in322,339-350.

[72] Hancock P, Cuthbertson RC. The effect of fibre length and interfacial bond in glass fibre-epoxy resin composites. Journal of Materials Science. 1970;5(9):762-768.

[73] Riley VR, Reddaway JL. Tensile strength and failure mechanics of fibre composites. Journal of Materials Science. 1968;3(1):41-46.

[74] Bowyer WH, Bader MG. On the re-inforcement of thermoplastics by imperfectly aligned discontinuous fibres. Journal of Materials Science. 1972;7(11):1315-1321.

[75] Fukuda H, Chou TW. A probabilistic theory of the strength of short-fibre composites with variable fibre length and orientation. Journal of Materials Science. 1982;17(4):1003-1011.

[76] Hui CY, Shia D. Simple formulae for the effective moduli of unidirectional aligned composites. Polymer Engineering and Science. 1998;38(5):774-782.

[77] Ajayan PM, Stephan O, Colliex C, Trauth D. Aligned carbon nanotube arrays formed by cutting a polymer resin-nanotube composite. Science. 1994;265(5176):1212-1214.

[78] Cheng Q, Bao J, Park J, Liang Z, Zhang C, Wang B. High mechanical performance composite conductor: Multi-walled carbon nanotube sheet/bismaleimide nanocomposites. Advanced Functional Materials. 2009;19(20):3219-3225.

[79] Cheng Q, Li M, Jiang L, Tang Z. Bioinspired layered composites based on flattened double-walled carbon nanotubes. Advanced Materials. 2012;24(14):1838-1843.

[80] Cheng Q, Wang B, Zhang C, Liang Z. Functionalized carbon-nanotube sheet/bismaleimide nanocomposites: Mechanical and electrical performance beyond carbon-fiber composites. Small. 2010;6(6):763-767.

[81] Wang X, Yong Z, Li Q, Bradford PD, Liu W, Tucker DS, Cai W, Wang H, Yuan F-G, Zhu Y. Ultrastrong, stiff and multifunctional carbon nanotube composites. Materials Research Letters. 2013;1(1):19-25.

[82] Kim JK, Mai Yw. High strength, high fracture toughness fibre composites with interface control-A review. Composites Science and Technology. 1991;41(4):333-378.

[83] Hull D. An introduction to composite materials. Cambridge: Cambridge University Press; 1996.

[84] Wagner HD, Lustiger A. Optimized toughness of short fiber-based composites: The effect of fiber diameter. Composites Science and Technology. 2009;69(7-8):1323-1325.

[85] Blanco J, García EJ, Guzmán De Villoria R, Wardle BL. Limiting mechanisms of mode i interlaminar toughening of composites reinforced with aligned carbon nanotubes. Journal of Composite Materials. 2009;43(8):825-841.

[86] Wetherhold RC, Jain LK. Effect of fiber orientation on the fracture toughness of brittle matrix composites. Acta Metallurgica Et Materialia. 1992;40(6):1135-1143.

[87] Wetherhold RC, Jain LK. The toughness of brittle matrix composites reinforced with discontinuous fibers. Materials Science and Engineering: A. 1992;151(2):169-177.

[88] Fu SY, Lauke B. The fibre pull-out energy of misaligned short fibre composites. Journal of Materials Science. 1997;32(8):1985-1993.

[89] Piggott MR. Toughness in obliquely-stressed fibrous composites. Journal of Mechanics and Physics of Solids. 1974;22(6):457-458.

[90] Khatibzadeh M, Piggott MR. The effect of fibre alignment on composite strength: I. Single-fibre studies. Composites Science and Technology. 1996;56(12):1435-1442.

[91] Hwang S-F, Mao C-P. Failure of delaminated interply hybrid composite plates under compression. Composites Science and Technology. 2001;61(11):1513-1527.

[92] Wang S-X, Wu L-Z, Ma L. Low-velocity impact and residual tensile strength analysis to carbon fiber composite laminates. Materials & Design. 2010;31(1):118-125.

[93] Cappello F, Tumino D. Numerical analysis of composite plates with multiple delaminations subjected to uniaxial buckling load. Composites Science and Technology. 2006;66(2):264-272.

[94] Wang S, Zhang Y. Buckling, post-buckling and delamination propagation in debonded composite laminates Part 2: Numerical applications. Composite Structures. 2009;88(1):131-146.

[95] Zhang Y, Wang S. Buckling, post-buckling and delamination propagation in debonded composite laminates. Part 1: Theoretical development. Composite Structures. 2009;88(1):121-130.

[96] Adams RD, Cawley P. A Review of Defect Types and Nondestructive Testing Techniques for Composites and Bonded Joints. Ndt International. 1988;21(4):208-222.

[97] Yan C, Xiao K, Ye L, Mai YW. Numerical and experimental studies on the fracture behavior of rubber-toughened epoxy in bulk specimen and laminated composites. Journal of Materials Science. 2002;37(5):921-927.

[98] Kinloch AJ, Yuen ML, Jenkins SD. Thermoplastic-toughened epoxy polymers. Journal of Materials Science. 1994;29(14):3781-3790.

[99] Hsieh TH, Kinloch AJ, Masania K, Sohn Lee J, Taylor AC, Sprenger S. The toughness of epoxy polymers and fibre composites modified with rubber microparticles and silica nanoparticles. Journal of Materials Science. 2010;45(5):1193-1210.

[100] Guild FJ, Kinloch AJ. Modelling the properties of rubber-modified epoxy polymers. Journal of Materials Science. 1995;30(7):1689-1697.

[101] Johnsen BB, Kinloch AJ, Mohammed RD, Taylor AC, Sprenger S. Toughening mechanisms of nanoparticle-modified epoxy polymers. Polymer. 2007;48(2):530-541.

[102] Gojny FH, Wichmann MHG, Fiedler B, Schulte K. Influence of different carbon nanotubes on the mechanical properties of epoxy matrix composites – A comparative study. Composites Science and Technology. 2005;65(15–16):2300-2313.

[103] Rafiee MA, Rafiee J, Wang Z, Song HH, Yu ZZ, Koratkar N. Enhanced Mechanical Properties of Nanocomposites at Low Graphene Content. ACS Nano. 2009;3(12):3884-3890.

[104] Sun L, Warren GL, O'Reilly JY, Everett WN, Lee SM, Davis D, Lagoudas D, Sue HJ. Mechanical properties of surface-functionalized SWCNT/epoxy composites. Carbon. 2008;46(2):320-328.

[105] Gojny FH, Wichmann MHG, Köpke U, Fiedler B, Schulte K. Carbon nanotube-reinforced epoxy-composites: enhanced stiffness and fracture toughness at low nanotube content. Composites Science and Technology. 2004;64(15):2363-2371.

[106] Hsieh TH, Kinloch AJ, Taylor AC, Kinloch IA. The effect of carbon nanotubes on the fracture toughness and fatigue performance of a thermosetting epoxy polym. Journal of Materials Science. 2011;46(23):7525-7535.

[107] Thostenson ET, Chou T-W. Processing-structure-multi-functional property relationship in carbon nanotube/epoxy composites. Carbon. 2006;44(14):3022-3029.

[108] Sumfleth J, Prehn K, Wichmann MHG, Wedekind S, Schulte K. A comparative study of the electrical and mechanical properties of epoxy nanocomposites reinforced by CVD- and arc-grown multi-wall carbon nanotubes. Composites Science and Technology. 2010;70(1):173-180.

[109] Tang LC, Zhang H, Han JH, Wu XP, Zhang Z. Fracture mechanisms of epoxy filled with ozone functionalized multi-wall carbon nanotubes. Composites Science and Technology. 2011;72(1):7-13.

[110] Yu N, Zhang ZH, He SY. Fracture toughness and fatigue life of MWCNT/epoxy composites. Materials Science and Engineering: A. 2008;494(1–2):380-384.

[111] Zhang G, Karger-Kocsis J, Zou J. Synergetic effect of carbon nanofibers and short carbon fibers on the mechanical and fracture properties of epoxy resin. Carbon. 2010;48(15):4289-4300.

[112] Palmeri MJ, Putz KW, Brinson LC. Sacrificial bonds in stacked-cup carbon nanofibers: Biomimetic toughening mechanisms for composite systems. ACS Nano. 2010;4(7):4256-4264.

[113] Chatterjee S, Nafezarefi F, Tai NH, Schlagenhauf L, Nuesch FA, Chu BTT. Size and synergy effects of nanofiller hybrids including graphene nanoplatelets and carbon nanotubes in mechanical properties of epoxy composites. Carbon. 2012;50(15):5380-5386.

[114] Bortz DR, Heras EG, Martin-Gullon I. Impressive fatigue life and fracture toughness improvements in graphene oxide/epoxy composites. Macromolecules. 2012;45(1):238-245.

[115] Ma J, Meng Q, Michelmore A, Kawashima N, Zaman I, Bengtsson C, Kuan HC. Covalently bonded interfaces for polymer/graphene composites. Journal of Materials Chemistry A. 2013;1(13):4255-4264.

[116] Zaman I, Phan TT, Kuan HC, Meng Q, Bao La LT, Luong L, Youssf O, Ma J. Epoxy/graphene platelets nanocomposites with two levels of interface strength. Polymer. 2011;52(7):1603-1611.

[117] Olowojoba G, Sathyanarayana S, Caglar B, Kiss-Pataki B, Mikonsaari I, Hubner C, Elsner P. Influence of process parameters on the morphology, rheological and dielectric properties of three-roll-milled multiwalled carbon nanotube/epoxy suspensions. Polymer. 2013;54(1):188-198.

[118] Mukhopadhyay K, Dwivedi CD, Mathur GN. Conversion of carbon nanotubes to carbon nanofibers by sonication. Carbon. 2002;40(8):1373-1376.

[119] Hsieh TH, Kinloch AJ, Masania K, Taylor AC, Sprenger S. The mechanisms and mechanics of the toughening of epoxy polymers modified with silica nanoparticles. Polymer. 2010;51(26):6284-6294.

[120] Vera-Agullo J, Varela-Rizo H, Conesa JA, Almansa C, Merino C, Martin-Gullon I. Evidence for growth mechanism and helix-spiral cone structure of stacked-cup carbon nanofibers. Carbon. 2007;45(14):2751-2758.

[121] Liu Q, Fujigaya T, Nakashima N. Graphene unrolled from 'cup-stacked' carbon nanotubes. Carbon. 2012;50(15):5421-5428.

[122] Weisenberger M, Martin-Gullon I, Vera-Agullo J, Varela-Rizo H, Merino C, Andrews R, Qian D, Rantell T. The effect of graphitization temperature on the structure of helical-ribbon carbon nanofibers. Carbon. 2009;47(9):2211-2218.

[123] Qian D, Dickey EC, Andrews R, Rantell T. Load transfer and deformation mechanisms in carbon nanotube-polystyrene composites. Applied Physics Letters. 2000;76(20):2868-2870.

[124] Williams JG. Particle toughening of polymers by plastic void growth. Composites Science and Technology. 2010;70(6):885-891.

[125] Jang K, Cho WJ, Ha CS. Influence of processing method on the fracture toughness of thermoplastic-modified, carbon-fiber-reinforced epoxy composites. Composites Science and Technology. 1999;59(7):995-1001.

[126] Naffakh M, Dumon M, Gérard JF. Study of a reactive epoxy-amine resin enabling in situ dissolution of thermoplastic films during resin transfer moulding for toughening composites. Composites Science and Technology. 2006;66(10):1376-1384.

[127] Van Velthem P, Ballout W, Daoust D, Sclavons M, Cordenier F, Henry E, Dumont D, Destoop V, Pardoen T, Bailly C. Influence of thermoplastic diffusion on morphology gradient and on delamination toughness of RTM-manufactured composites. Composites Part A: Applied Science and Manufacturing. 2015;72:175-183.

[128] Wang CH, Sidhu K, Yang T, Zhang J, Shanks R. Interlayer self-healing and toughening of carbon fibre/epoxy composites using copolymer films. Composites Part A: Applied Science and Manufacturing. 2012;43(3):512-518.

[129] Kinloch AJ, Mohammed RD, Taylor AC, Sprenger S, Egan D. The interlaminar toughness of carbon-fibre reinforced plastic composites using 'hybrid-toughened' matrices. Journal of Materials Science. 2006;41(15):5043-5046.

[130] Wichmann MHG, Sumfleth J, Gojny FH, Quaresimin M, Fiedler B, Schulte K. Glass-fibre-reinforced composites with enhanced mechanical and electrical properties – Benefits and limitations of a nanoparticle modified matrix. Engineering Fracture Mechanics. 2006;73(16):2346-2359.

[131] Karapappas P, Vavouliotis A, Tsotra P, Kostopoulos V, Paipetis A. Enhanced Fracture Properties of Carbon Reinforced Composites by the Addition of Multi-Wall Carbon Nanotubes. Journal of Composite Materials. 2009;43(9):977-985.

[132] Tugrul Seyhan A, Tanoglu M, Schulte K. Mode I and mode II fracture toughness of E-glass non-crimp fabric/carbon nanotube (CNT) modified polymer based composites. Engineering Fracture Mechanics. 2008;75(18):5151-5162.

[133] Warrier A, Godara A, Rochez O, Mezzo L, Luizi F, Gorbatikh L, Lomov SV, VanVuure AW, Verpoest I. The effect of adding carbon nanotubes to glass/epoxy composites in the fibre sizing and/or the matrix. Composites Part A: Applied Science and Manufacturing. 2010;41(4):532-538.

[134] Godara A, Mezzo L, Luizi F, Warrier A, Lomov SV, van Vuure AW, Gorbatikh L, Moldenaers P, Verpoest I. Influence of carbon nanotube reinforcement on the processing and the mechanical behaviour of carbon fiber/epoxy composites. Carbon. 2009;47(12):2914-2923.

[135] Zhu Y, Bakis CE, Adair JH. Effects of carbon nanofiller functionalization and distribution on interlaminar fracture toughness of multi-scale reinforced polymer composites. Carbon. 2012;50(3):1316-1331.

[136] Sadeghian R, Gangireddy S, Minaie B, Hsiao KT. Manufacturing carbon nanofibers toughened polyester/glass fiber composites using vacuum assisted resin transfer molding for enhancing the mode-I delamination resistance. Composites Part A: Applied Science and Manufacturing. 2006;37(10):1787-1795.

[137] Kostopoulos V, Tsotra P, Karapappas P, Tsantzalis S, Vavouliotis A, Loutas TH, Paipetis A, Friedrich K, Tanimoto T. Mode I interlaminar fracture of CNF or/and PZT doped CFRPs via acoustic emission monitoring. Composites Science and Technology. 2007;67(5):822-828.

[138] Li Y, Hori N, Arai M, Hu N, Liu Y, Fukunaga H. Improvement of interlaminar mechanical properties of CFRP laminates using VGCF. Composites Part A: Applied Science and Manufacturing. 2009;40(12):2004-2012.

[139] Yokozeki T, Iwahori Y, Ishiwata S, Enomoto K. Mechanical properties of CFRP laminates manufactured from unidirectional prepregs using CSCNT-dispersed epoxy. Composites Part A: Applied Science and Manufacturing. 2007;38(10):2121-2130.

[140] Yokozeki T, Iwahori Y, Ishibashi M, Yanagisawa T, Imai K, Arai M, Takahashi T, Enomoto K. Fracture toughness improvement of CFRP laminates by dispersion of cup-stacked carbon nanotubes. Composites Science and Technology. 2009;69(14):2268-2273.

[141] Khan SU, Kim JK. Improved interlaminar shear properties of multiscale carbon fiber composites with bucky paper interleaves made from carbon nanofibers. Carbon. 2012;50(14):5265-5277.

[142] Garcia EJ, Wardle BL, John Hart A. Joining prepreg composite interfaces with aligned carbon nanotubes. Composites Part A: Applied Science and Manufacturing. 2008;39(6):1065-1070.

[143] Guo J, Lu C. Continuous preparation of multiscale reinforcement by electrophoretic deposition of carbon nanotubes onto carbon fiber tows. Carbon. 2012;50(8):3101-3103.

[144] An Q, Rider AN, Thostenson ET. Hierarchical composite structures prepared by electrophoretic deposition of carbon nanotubes onto glass fibers. ACS Appl Mater Interfaces. 2013;5(6):2022-2032.

[145] Li K-z, Li L, Li H-j, Song Q, Lu J-h, Fu Q-g. Electrophoretic deposition of carbon nanotubes onto carbon fiber felt for production of carbon/carbon composites with improved mechanical and thermal properties. Vacuum. 2014;104:105-110.

[146] Rodriguez AJ, Guzman ME, Lim C-S, Minaie B. Mechanical properties of carbon nanofiber/fiber-reinforced hierarchical polymer composites manufactured with multiscale-reinforcement fabrics. Carbon. 2011;49(3):937-948.

[147] Schaefer JD, Rodriguez AJ, Guzman ME, Lim C-S, Minaie B. Effects of electrophoretically deposited carbon nanofibers on the interface of single carbon fibers embedded in epoxy matrix. Carbon. 2011;49(8):2750-2759.

[148] Lee S-H, Kim H, Hang S, Cheong S-K. Interlaminar fracture toughness of composite laminates with CNT-enhanced nonwoven carbon tissue interleave. Composites Science and Technology. 2012;73:1-8.

[149] Wang Q, Dai J, Li W, Wei Z, Jiang J. The effects of CNT alignment on electrical conductivity and mechanical properties of SWNT/epoxy nanocomposites. Composites Science and Technology. 2008;68(7-8):1644-1648.

[150] Khan SU, Pothnis JR, Kim JK. Effects of carbon nanotube alignment on electrical and mechanical properties of epoxy nanocomposites. Composites Part A: Applied Science and Manufacturing. 2013;49:26-34.

[151] Jiao W, Shioya M, Wang R, Yang F, Hao L, Niu Y, Liu W, Zheng L, Yuan F, Wan L, et al. Improving the gas barrier properties of Fe3O4/graphite nanoplatelet reinforced nanocomposites by a low magnetic field induced alignment. Composites Science and Technology. 2014;99:124-130.

[152] Yan H, Tang Y, Long W, Li Y. Enhanced thermal conductivity in polymer composites with aligned graphene nanosheets. Journal of Materials Science. 2014;49(15):5256-5264.

[153] Vigolo B, Penicaud A, Coulon C, Sauder C, Pailler R, Journet C, Bernier P, Poulin P. Macroscopic fibers and ribbons of oriented carbon nanotubes. Science. 2000;290(5495):1331-1334.

[154] Fan Z, Advani SG. Characterization of orientation state of carbon nanotubes in shear flow. Polymer. 2005;46(14):5232-5240.

[155] Sulong A, Park J. Alignment of multi-walled carbon nanotubes in a polyethylene matrix by extrusion shear flow: mechanical properties enhancement. Journal of Composite Materials. 2011;45(8):931-941.

[156] Haggenmueller R, Gommans HH, Rinzler AG, Fischer JE, Winey KI. Aligned single-wall carbon nanotubes in composites by melt processing methods. Chemical Physics Letters. 2000;330(3-4):219-225.

[157] Thostenson ET, Chou TW. Aligned multi-walled carbon nanotube-reinforced composites: processing and mechanical characterization. Journal of Physics D-Applied Physics. 2002;35(16):L77-L80.

[158] Akima N, Iwasa Y, Brown S, Barbour AM, Cao J, Musfeldt JL, Matsui H, Toyota N, Shiraishi M, Shimoda H, et al. Strong anisotropy in the far-infrared absorption spectra of stretch-aligned single-walled carbon nanotubes. Advanced Materials. 2006;18(9):1166-1169.

[159] Chen D, Liu T, Zhou X, Tjiu WC, Hou H. Electrospinning fabrication of high strength and toughness polyimide nanofiber membranes containing multiwalled carbon nanotubes. Journal of Physical Chemistry B. 2009;113(29):9741-9748.

[160] Sen R, Zhao B, Perea D, Itkis ME, Hu H, Love J, Bekyarova E, Haddon RC. Preparation of single-walled carbon nanotube reinforced polystyrene and polyurethane nanofibers and membranes by electrospinning. Nano Letters. 2004;4(3):459-464.

[161] Oliva-Avilés AI, Avilés F, Sosa V, Oliva AI, Gamboa F. Dynamics of carbon nanotube alignment by electric fields. Nanotechnology. 2012;23(46).

[162] Steinert BW, Dean DR. Magnetic field alignment and electrical properties of solution cast PET-carbon nanotube composite films. Polymer. 2009;50(3):898-904.

[163] Mahfuz H, Zainuddin S, Parker MR, Al-Saadi T, Rangari VK, Jeelani S. Reinforcement of SC-15 epoxy with CNT/CNF under high magnetic field: An investigation of mechanical and thermal response. Journal of Materials Science. 2009;44(4):1113-1120.

[164] Fragouli D, Das A, Innocenti C, Guttikonda Y, Rahman S, Liu L, Caramia V, Megaridis CM, Athanassiou A. Polymeric films with electric and magnetic anisotropy due to magnetically assembled functional nanofibers. ACS Applied Materials and Interfaces. 2014;6(6):4535-4541.

[165] Abdalla M, Dean D, Theodore M, Fielding J, Nyairo E, Price G. Magnetically processed carbon nanotube/epoxy nanocomposites: Morphology, thermal, and mechanical properties. Polymer. 2010;51(7):1614-1620.

[166] Fishbine BH. Carbon nanotube alignment and manipulation using electrostatic fields. Fullerene Science and Technology. 1996;4(1):87-100.

[167] Yamamoto K, Akita S, Nakayama Y. Orientation of carbon nanotubes using electrophoresis. Japanese Journal of Applied Physics, Part 2: Letters. 1996;35(7 SUPPL. B):L917-L918.

[168] Yamamoto K, Akita S, Nakayama Y. Orientation and purification of carbon nanotubes using ac electrophoresis. Journal of Physics D: Applied Physics. 1998;31(8):L34-L36.

[169] Jones TB. Electromechanics of Particles. New York: Cambridge University Press; 1995.

[170] Benedict LX, Louie SG, Cohen ML. Static polarizabilities of single-wall carbon nanotubes. Physical Review B. 1995;52(11):8541-8549.

[171] Kozinsky B, Marzari N. Static dielectric properties of carbon nanotubes from first principles. Physical Review Letters. 2006;96(16).

[172] Hughes MP. AC electrokinetics: Applications for nanotechnology. Nanotechnology. 2000;11(2):124-132.

[173] Romyen N, Thongyai S, Praserthdam P. Alignment of carbon nanotubes in polyimide under electric and magnetic fields. Journal of Applied Polymer Science. 2012;123(6):3470-3475.

[174] Larijani MM, Khamse EJ, Asadollahi Z, Asadi M. Effect of aligned carbon nanotubes on electrical conductivity behaviour in polycarbonate matrix. Bulletin of Materials Science. 2012;35(3):305-311.

[175] Park C, Wilkinson J, Banda S, Ounaies Z, Wise KE, Sauti G, Lillehei PT, Harrison JS. Aligned single-wall carbon nanotube polymer composites using an electric field. Journal of Polymer Science, Part B: Polymer Physics. 2006;44(12):1751-1762.

[176] Felisberto M, Arias-Durán A, Ramos JA, Mondragon I, Candal R, Goyanes S, Rubiolo GH. Influence of filler alignment in the mechanical and electrical properties of carbon nanotubes/epoxy nanocomposites. Physica B: Condensed Matter. 2012;407(16):3181-3183.

[177] Kim GH. Thermo-physical responses of polymeric composites tailored by electric field. Composites Science and Technology. 2005;65(11-12):1728-1735.

[178] Domingues D, Logakis E, Skordos AA. The use of an electric field in the preparation of glass fibre/epoxy composites containing carbon nanotubes. Carbon. 2012;50(7):2493-2503.

[179] Kimura T, Ago H, Tobita M, Ohshima S, Kyotani M, Yumura M. Polymer composites of carbon nanotubes aligned by a magnetic field. Advanced Materials. 2002;14(19):1380-1383.

[180] Wang XK, Chang RPH, Patashinski A, Ketterson JB. Magnetic susceptibility of buckytubes. Journal of Materials Research. 1994;9(6):1578-1582.

[181] Ramirez AP, Haddon RC, Zhou O, Fleming RM, Zhang J, McClure SM, Smalley RE. Magnetic susceptibility of molecular carbon: Nanotubes and fullerite. Science. 1994;265(5168):84-86.

[182] Lu JP. Novel magnetic properties of carbon nanotubes. Physical Review Letters. 1995;74(7):1123-1126.

[183] Takahashi T, Yonetake K, Koyama K, Kikuchi T. Polycarbonate crystallization by vapor-grown carbon fiber with and without magnetic field. Macromolecular Rapid Communications. 2003;24(13):763-767.

[184] Garmestani H, Al-Haik MS, Dahmen K, Tannenbaum R, Li D, Sablin SS, Yousuff Hussaini M. Polymer-Mediated Alignment of Carbon Nanotubes under High Magnetic Fields. Advanced Materials. 2003;15(22):1918-1921.

[185] Choi ES, Brooks JS, Eaton DL, Al-Haik MS, Hussaini MY, Garmestani H, Li D, Dahmen K. Enhancement of thermal and electrical properties of carbon nanotube polymer composites by magnetic field processing. Journal of Applied Physics. 2003;94(9):6034-6039.

[186] Mahfuz H, Zainuddin S, Parker M, Al-Saadi T, Rangari V, Jeelani S. Reinforcement of SC-15 epoxy with CNT/CNF under high magnetic field: an investigation of mechanical and thermal response. Journal of Materials Science. 2009;44(4):1113-1120.

[187] Steinert BW, Dean DR. Magnetic field alignment and electrical properties of solution cast PET–carbon nanotube composite films. Polymer. 2009;50(3):898-904.

[188] Malkina O, Mahfuz H, Sorge K, Rondinone A, Chen J, More K, Reeves S, Rangari V. Magnetic alignment of SWCNTs decorated with Fe3O4 to enhance mechanical properties of SC-15 epoxy. AIP Advances. 2013;3(4):042104.

[189] Jiao WC, Shioya M, Wang RG, Yang F, Hao LF, Niu Y, Liu WB, Zheng L, Yuan F, Wan L, et al. Improving the gas barrier properties of Fe3O4/graphite nanoplatelet reinforced nanocomposites by a low magnetic field induced alignment. Composites Science and Technology. 2014;99:124-130.

[190] Prolongo SG, Meliton BG, Del Rosario G, Ureña A. New alignment procedure of magnetite-CNT hybrid nanofillers on epoxy bulk resin with permanent magnets. Composites Part B: Engineering. 2013;46:166-172.

[191] Correa-Duarte MA, Grzelczak M, Salgueiriño-Maceira V, Giersig M, Liz-Marzán LM, Farle M, Sierazdki K, Diaz R. Alignment of carbon nanotubes under low magnetic fields through attachment of magnetic nanoparticles. Journal of Physical Chemistry B. 2005;109(41):19060-19063.

[192] Kim IT, Tannenbaum A, Tannenbaum R. Anisotropic conductivity of magnetic carbon nanotubes embedded in epoxy matrices. Carbon. 2011;49(1):54-61.

[193] Baughman RH, Cui C, Zakhidov AA, Iqbal Z, Barisci JN, Spinks GM, Wallace GG, Mazzoldi A, De Rossi D, Rinzler AG, et al. Carbon nanotube actuators. Science. 1999;284(5418):1340-1344.

[194] Fiedler B, Gojny FH, Wichmann MHG, Bauhofer W, Schulte K. Can carbon nanotubes be used to sense damage in composites? Annales de Chimie: Science des Materiaux. 2004;29(6):81-94.

[195] Kuronuma Y, Takeda T, Shindo Y, Narita F, Wei Z. Electrical resistance-based strain sensing in carbon nanotube/polymer composites under tension: Analytical modeling and experiments. Composites Science and Technology. 2012;72(14):1678-1682.

[196] Lipomi DJ, Vosgueritchian M, Tee BCK, Hellstrom SL, Lee JA, Fox CH, Bao Z. Skin-like pressure and strain sensors based on transparent elastic films of carbon nanotubes. Nature Nanotechnology. 2011;6(12):788-792.

[197] Yamada T, Hayamizu Y, Yamamoto Y, Yomogida Y, Izadi-Najafabadi A, Futaba DN, Hata K. A stretchable carbon nanotube strain sensor for human-motion detection. Nature Nanotechnology. 2011;6(5):296-301.

[198] Zhang R, Deng H, Valenca R, Jin J, Fu Q, Bilotti E, Peijs T. Strain sensing behaviour of elastomeric composite films containing carbon nanotubes under cyclic loading. Composites Science and Technology. 2013;74:1-5.

[199] Rocha JG, Paleo AJ, Van Hattum FWJ, Lanceros-Mendez S. Polypropylene-carbon nanofiber composites as strain-gauge sensor. IEEE Sensors Journal. 2013;13(7):2603-2609.

[200] Toprakci HAK, Kalanadhabhatla SK, Spontak RJ, Ghosh TK. Polymer nanocomposites containing carbon nanofibers as soft printable sensors exhibiting strain-reversible piezoresistivity. Advanced Functional Materials. 2013;23(44):5536-5542.

[201] Chiacchiarelli LM, Rallini M, Monti M, Puglia D, Kenny JM, Torre L. The role of irreversible and reversible phenomena in the piezoresistive behavior of graphene epoxy nanocomposites applied to structural health monitoring. Composites Science and Technology. 2013;80:73-79.

[202] Hwang S-H, Park HW, Park Y-B, Um M-K, Byun J-H, Kwon S. Electromechanical strain sensing using polycarbonate-impregnated carbon nanotube–graphene nanoplatelet hybrid composite sheets. Composites Science and Technology. 2013;89:1-9.

[203] Naghashpour A, Hoa SV. In situ monitoring of through-thickness strain in glass fiber/epoxy composite laminates using carbon nanotube sensors. Composites Science and Technology. 2013;78:41-47.

[204] Monti M, Natali M, Petrucci R, Kenny JM, Torre L. Carbon nanofibers for strain and impact damage sensing in glass fiber reinforced composites based on an unsaturated polyester resin. Polymer Composites. 2011;32(5):766-775.

[205] Gao L, Chou TW, Thostenson ET, Zhang Z. A comparative study of damage sensing in fiber composites using uniformly and non-uniformly dispersed carbon nanotubes. Carbon. 2010;48(13):3788-3794.

[206] Gao L, Thostenson ET, Zhang Z, Chou TW. Coupled carbon nanotube network and acoustic emission monitoring for sensing of damage development in composites. Carbon. 2009;47(5):1381-1388.

[207] Mactabi R, Rosca ID, Hoa SV. Monitoring the integrity of adhesive joints during fatigue loading using carbon nanotubes. Composites Science and Technology. 2013;78:1-9.

[208] Thostenson ET, Chou TW. Carbon nanotube networks: Sensing of distributed strain and damage for life prediction and self healing. Advanced Materials. 2006;18(21):2837-2841.

[209] Gao L, Thostenson ET, Zhang Z, Chou TW. Sensing of damage mechanisms in fiber-reinforced composites under cyclic loading using carbon nanotubes. Advanced Functional Materials. 2009;19(1):123-130.

[210] Zhang W, Sakalkar V, Koratkar N. In situ health monitoring and repair in composites using carbon nanotube additives. Applied Physics Letters. 2007;91(13).

[211] Cui S, Kinloch IA, Young RJ, Noé L, Monthioux M. The effect of stress transfer within double-walled carbon nanotubes upon their ability to reinforce composites. Advanced Materials. 2009;21(35):3591-3595.

[212] Blighe FM, Young K, Vilatela JJ, Windle AH, Kinloch IA, Deng L, Young RJ, Coleman JN. The effect of nanotube content and orientation on the mechanical properties of polymer-nanotube composite fibers: Separating intrinsic reinforcement from orientational effects. Advanced Functional Materials. 2011;21(2):364-371.

[213] Gong L, Young RJ, Kinloch IA, Riaz I, Jalil R, Novoselov KS. Optimizing the reinforcement of polymer-based nanocomposites by graphene. ACS Nano. 2012;6(3):2086-2095.

[214] Vallés C, Kinloch IA, Young RJ, Wilson NR, Rourke JP. Graphene oxide and base-washed graphene oxide as reinforcements in PMMA nanocomposites. Composites Science and Technology. 2013;88:158-164.

[215] Young RJ, Kinloch IA, Gong L, Novoselov KS. The mechanics of graphene nanocomposites: A review. Composites Science and Technology. 2012;72(12):1459-1476.

[216] Odegard GM, Gates TS, Wise KE, Park C, Siochi EJ. Constitutive modeling of nanotube-reinforced polymer composites. Composites Science and Technology. 2003;63(11):1671-1687.

[217] ISO25217. Determination of the Mode i Adhesive Fracture Energy of Structural Adhesive Joints Using Double Cantilever Beam and Tapered Double Cantilever Beam Specimens. Geneva. 2009.

[218] Li VC, Wang Y, Backer S. A micromechanical model of tension-softening and bridging toughening of short random fiber reinforced brittle matrix composites. Journal of the Mechanics and Physics of Solids. 1991;39(5):607-625.

[219] Wagner HD, Ajayan PM, Schulte K. Nanocomposite toughness from a pull-out mechanism. Composites Science and Technology. 2013;83:27-31.

[220] Fu SY, Chen ZK, Hong S, Han CC. The reduction of carbon nanotube (CNT) length during the manufacture of CNT/polymer composites and a method to simultaneously determine the resulting CNT and interfacial strengths. Carbon. 2009;47(14):3192-3200.

[221] Manoharan MP, Sharma A, Desai AV, Haque MA, Bakis CE, Wang KW. The interfacial strength of carbon nanofiber epoxy composite using single fiber pullout experiments. Nanotechnology. 2009;20(29).

[222] Ozkan T, Chen Q, Chasiotis I. Interfacial strength and fracture energy of individual carbon nanofibers in epoxy matrix as a function of surface conditions. Composites Science and Technology. 2012;72(9):965-975.

[223] Huang Y, Kinloch AJ. Modelling of the toughening mechanisms in rubber-modified epoxy polymers - Part II A quantitative description of the microstructure-fracture property relationships. Journal of Materials Science. 1992;27(10):2763-2769.

[224] SIGMA-ALDRICH. Properties and Application of Carbon Nanofibers (CNFs) Synthesized Using Vapor Grown Carbon Fiber (VGCF) Manufacturing Technology http://www.sigmaaldrich.com/china-mainland/zh/materials-science/nanomaterials/carbon-nanofibers.html. 2015.

[225] Ozkan T, Naraghi M, Chasiotis I. Mechanical properties of vapor grown carbon nanofibers. Carbon. 2010;48(1):239-244.

[226] Westsystem. 105 Resin Engineering Data http://www.westsystem.com/ss/assets/Product-Data-PDFs/TDS%20105_206.pdf. 2015.

[227] Liu W, Kong J, Toh WE, Zhou R, Ding G, Huang S, Dong Y, Lu X. Toughening of epoxies by covalently anchoring triazole-functionalized stacked-cup carbon nanofibers. Composites Science and Technology. 2013;85:1-9.

[228] Lonjon A, Demont P, Dantras E, Lacabanne C. Electrical conductivity improvement of aeronautical carbon fiber reinforced polyepoxy composites by insertion of carbon nanotubes. Journal of Non-Crystalline Solids. 2012;358(15):1859-1862.

[229] Song SH, Park KH, Kim BH, Choi YW, Jun GH, Lee DJ, Kong BS, Paik KW, Jeon S. Enhanced thermal conductivity of epoxy-graphene composites by using non-oxidized graphene flakes with non-covalent functionalization. Advanced Materials. 2013;25(5):732-737.

[230] Rafiee MA, Rafiee J, Srivastava I, Wang Z, Song H, Yu ZZ, Koratkar N. Fracture and fatigue in graphene nanocomposites. Small. 2010;6(2):179-183.

[231] Stankovich S, Dikin DA, Dommett GHB, Kohlhaas KM, Zimney EJ, Stach EA, Piner RD, Nguyen ST, Ruoff RS. Graphene-based composite materials. Nature. 2006;442(7100):282-286.

[232] Schwarz MK, Bauhofer W, Schulte K. Alternating electric field induced agglomeration of carbon black filled resins. Polymer. 2002;43(10):3079-3082.

[233] Tomer V, Randall CA, Polizos G, Kostelnick J, Manias E. High- and low-field dielectric characteristics of dielectrophoretically aligned ceramic/polymer nanocomposites. Journal of Applied Physics. 2008;103(3).

[234] Knaapila M, Pinheiro JP, Buchanan M, Skjeltorp AT, Helgesen G. Directed assembly of carbon nanocones into wires with an epoxy coating in thin films by a combination of electric field alignment and subsequent pyrolysis. Carbon. 2011;49(10):3171-3178.

[235] Tang LC, Wan YJ, Yan D, Pei YB, Zhao L, Li YB, Wu LB, Jiang JX, Lai GQ. The effect of graphene dispersion on the mechanical properties of graphene/epoxy composites. Carbon. 2013;60:16-27.

[236] Meng Q, Jin J, Wang R, Kuan HC, Ma J, Kawashima N, Michelmore A, Zhu S, Wang CH. Processable 3-nm thick graphene platelets of high electrical conductivity and their epoxy composites. Nanotechnology. 2014;25(12).

[237] Jia J, Sun X, Lin X, Shen X, Mai YW, Kim JK. Exceptional electrical conductivity and fracture resistance of 3D interconnected graphene foam/epoxy composites. ACS Nano. 2014;8(6):5774-5783.

[238] Park YT, Qian YQ, Chan C, Suh T, Nejhad MG, Macosko CW, Stein A. Epoxy Toughening with Low Graphene Loading. Advanced Functional Materials. 2015;25(4):575-585.

[239] Chandrasekaran S, Sato N, Tölle F, Mülhaupt R, Fiedler B, Schulte K. Fracture toughness and failure mechanism of graphene based epoxy composites. Composites Science and Technology. 2014;97:90-99.

[240] Chandrasekaran S, Seidel C, Schulte K. Preparation and characterization of graphite nano-platelet (GNP)/epoxy nano-composite: Mechanical, electrical and thermal properties. European Polymer Journal. 2013;49(12):3878-3888.

[241] Wang X, Jin J, Song M. An investigation of the mechanism of graphene toughening epoxy. Carbon. 2013;65:324-333.

[242] Huang J, Rodrigue D. The effect of carbon nanotube orientation and content on the mechanical properties of polypropylene based composites. Materials & Design. 2014;55:653-663.

[243] Lionetto F, Calo E, Di Benedetto F, Pisignano D, Maffezzoli A. A methodology to orient carbon nanotubes in a thermosetting matrix. Composites Science and Technology. 2014;96:47-55.

[244] Jonscher AK. The 'universal' dielectric response. Nature. 1977;267(5613):673-679.

[245] Jonscher AK. A new understanding of the dielectric relaxation of solids. Journal of Materials Science. 1981;16(8):2037-2060.

[246] Tibbetts GG, Lake ML, Strong KL, Rice BP. A review of the fabrication and properties of vapor-grown carbon nanofiber/polymer composites. Composites Science and Technology. 2007;67(7-8):1709-1718.

[247] XG-Sciences. xGnP Grade M Product Characteristics. http://xgsciencescom/wp-content/uploads/2012/10/10-15-13_xGnP-M_Data-Sheetpdf. 2015.

[248] Zheng W, Wong SC. Electrical conductivity and dielectric properties of PMMA/expanded graphite composites. Composites Science and Technology. 2003;63(2):225-235.

[249] Zheng W, Lu XH, Wong SC. Electrical and mechanical properties of expanded graphite-reinforced high-density polyethylene. Journal of Applied Polymer Science. 2004;91(5):2781-2788.

[250] Gong L, Kinloch IA, Young RJ, Riaz I, Jalil R, Novoselov KS. Interfacial Stress Transfer in a Graphene Monolayer Nanocomposite. Advanced Materials. 2010;22(24):2694-+.

[251] Zhang W, Picu RC, Koratkar N. The effect of carbon nanotube dimensions and dispersion on the fatigue behavior of epoxy nanocomposites. Nanotechnology. 2008;19(28).

[252] Jones R, Pitt S, Hui D, Brunner A. Fatigue crack growth in nano-composites. Composite Structures. 2013;99:375-379.

[253] ASTM-D3039-14. Standard test method for tensile properties of polymer matrix composite materials. ASTM International; 2014.

[254] Donough MJ, Gunnion AJ, Orifici AC, Wang CH. Plasticity induced crack closure in adhesively bonded joints under fatigue loading. International Journal of Fatigue. 2015;70:440-450.

[255] Lawrence JG, Berhan LM, Nadarajah A. Elastic properties and morphology of individual carbon nanofibers. ACS Nano. 2008;2(6):1230-1236.

[256] Lawrence JG, Berhan LM, Nadarajah A. Structural transformation of vapor grown carbon nanofibers studied by HRTEM. Journal of Nanoparticle Research. 2008;10(7):1155-1167.

[257] Gu J, Sansoz F. Superplastic deformation and energy dissipation mechanism in surface-bonded carbon nanofibers. Computational Materials Science. 2015;99:190-194.

[258] Endo M, Kim YA, Hayashi T, Yanagisawa T, Muramatsu H, Ezaka M, Terrones H, Terrones M, Dresselhaus MS. Microstructural changes induced in “stacked cup” carbon nanofibers by heat treatment. Carbon. 2003;41(10):1941-1947.

[259] Shioyama H. The production of a sheath around a stacked-cup carbon nanofiber. Carbon. 2005;43(1):203-205.

[260] Gu J, Sansoz F. An atomistic simulation study of the mechanisms and kinetics of surface bond strengthening in thermally-treated cone-stacked carbon nanofibers. Carbon. 2013;56:351-357.

[261] Ci L, Zhu H, Wei B, Xu C, Liang J, Wu D. Graphitization behavior of carbon nanofibers prepared by the floating catalyst method. Materials Letters. 2000;43(5–6):291-294.

[262] Deng SQ, Djukic L, Paton R, Ye L. Thermoplastic-epoxy interactions and their potential applications in joining composite structures - A review. Composites Part a-Applied Science and Manufacturing. 2015;68:121-132.

[263] Thoppul SD, Finegan J, Gibson RF. Mechanics of mechanically fastened joints in polymer-matrix composite structures - A review. Composites Science and Technology. 2009;69(3-4):301-329.

[264] Wang Q, Dai JF, Li WX, Wei ZQ, Jiang JL. The effects of CNT alignment on electrical conductivity and mechanical properties of SWNT/epoxy nanocomposites. Composites Science and Technology. 2008;68(7-8):1644-1648.

[265] Bradford PD, Wang X, Zhao HB, Maria JP, Jia QX, Zhu YT. A novel approach to fabricate high volume fraction nanocomposites with long aligned carbon nanotubes. Composites Science and Technology. 2010;70(13):1980-1985.

[266] Schwarz M-K, Bauhofer W, Schulte K. Alternating electric field induced agglomeration of carbon black filled resins. Polymer. 2002;43(10):3079-3082.

[267] Shi D, He P, Lian J, Chaud X, Bud'ko SL, Beaugnon E, Wang LM, Ewing RC, Tournier R. Magnetic alignment of carbon nanofibers in polymer composites and anisotropy of mechanical properties. Journal of Applied Physics. 2005;97(6):064312.

[268] Fragouli D, Das A, Innocenti C, Guttikonda Y, Rahman S, Liu L, Caramia V, Megaridis CM, Athanassiou A. Polymeric Films with Electric and Magnetic Anisotropy Due to Magnetically Assembled Functional Nanofibers. Acs Applied Materials & Interfaces. 2014;6(6):4535-4541.

[269] Lim CS, Rodriguez AJ, Guzman ME, Schaefer JD, Minaie B. Processing and properties of polymer composites containing aligned functionalized carbon nanofibers. Carbon. 2011;49(6):1873-1883.

[270] Wang RZ, Gupta HS. Deformation and fracture mechanisms of bone and nacre. Annual Review of Materials Research, Vol 41. 2011;41:41-73.

[271] Studart AR. Towards high-performance bioinspired composites. Advanced Materials. 2012;24(37):5024-5044.

[272] Li L, Ortiz C. A natural 3D interconnected laminated composite with enhanced damage resistance. Advanced Functional Materials. 2015;25(23):3463-3471.

[273] Chen PY, McKittrick J, Meyers MA. Biological materials: Functional adaptations and bioinspired designs. Progress in Materials Science. 2012;57(8):1492-1704.

[274] Wegst UGK, Bai H, Saiz E, Tomsia AP, Ritchie RO. Bioinspired structural materials. Nature Materials. 2014;14(1):23-36.

[275] Mouritz AP, Bannister MK, Falzon PJ, Leong KH. Review of applications for advanced three-dimensional fibre textile composites. Composites Part A: Applied Science and Manufacturing. 1999;30(12):1445-1461.

[276] Launey ME, Buehler MJ, Ritchie RO. On the mechanistic origins of toughness in bone. Annual Review of Materials Research, vol. 402010. p. 25-53.

[277] Ritchie RO. The conflicts between strength and toughness. Nature Materials. 2011;10(11):817-822.

[278] Wu S, Ladani RB, Zhang J, Kinloch AJ, Zhao Z, Ma J, Zhang X, Mouritz AP, Ghorbani K, Wang CH. Epoxy nanocomposites containing magnetite-carbon nanofibers aligned using a weak magnetic field. Polymer (United Kingdom). 2015;68:25-34.

[279] Bortz DR, Merino C, Martin-Gullon I. Carbon nanofibers enhance the fracture toughness and fatigue performance of a structural epoxy system. Composites Science and Technology. 2011;71(1):31-38.

[280] Ladani RB, Wu S, Kinloch AJ, Ghorbani K, Zhang J, Mouritz AP, Wang CH. Multifunctional properties of epoxy nanocomposites reinforced by aligned nanoscale carbon. Materials & Design 2015 http://dxdoiorg/101016/jmatdes201601052.

[281] Hsieh TH, Kinloch AJ, Taylor AC, Kinloch IA. The effect of carbon nanotubes on the fracture toughness and fatigue performance of a thermosetting epoxy polymer. Journal of Materials Science. 2011;46(23):7525-7535.

[282] Wu S, Ladani RB, Zhang J, Bafekrpour E, Ghorbani K, Mouritz AP, Kinloch AJ, Wang CH. Aligning multilayer graphene flakes with an external electric field to improve multifunctional properties of epoxy nanocomposites. Carbon. 2015;94:607-618.

[283] Koester KJ, Ager Iii JW, Ritchie RO. The true toughness of human cortical bone measured with realistically short cracks. Nature Materials. 2008;7(8):672-677.

[284] Pegorin F, Pingkarawat K, Mouritz AP. Comparative study of the mode I and mode II delamination fatigue properties of z-pinned aircraft composites. Materials and Design. 2015;65:139-146.

[285] Ladani RB, Wu S, Kinloch AJ, Ghorbani K, Zhang J, Mouritz AP, Wang CH. Improving the toughness and electrical conductivity of epoxy nanocomposites by using aligned carbon nanofibres. Composites Science and Technology. 2015;117:146-158.

[286] Ladani RB, Wu S, Kinloch AJ, Ghorbani K, Zhang J, Mouritz AP, Wang CH. Multifunctional properties of epoxy nanocomposites reinforced by aligned nanoscale carbon. Materials & Design. 2016;94:554-564.

[287] Mouritz AP, Chang P, Isa MD. Z-pin composites: Aerospace structural design considerations. Journal of Aerospace Engineering. 2011;24(4):425-432.

[288] ASTM-D5528-01. Standard test method for mode I interlaminar fracture toughness of unidirectional fiber-reinforced polymer matrix composites. ASTM International; 2007.

[289] Wicks SS, Wang W, Williams MR, Wardle BL. Multi-scale interlaminar fracture mechanisms in woven composite laminates reinforced with aligned carbon nanotubes. Composites Science and Technology. 2014;100:128-135.

[290] Tang Y, Ye L, Zhang Z, Friedrich K. Interlaminar fracture toughness and CAI strength of fibre-reinforced composites with nanoparticles - A review. Composites Science and Technology. 2013;86:26-37.

[291] Wang CH. On the fracture of constrained layers. International Journal of Fracture. 1998;93(1-4):227-246.

[292] Forman RG, Kearney VE, Engle RM. Numerical analysis of crack propagation in cyclic-loaded structures. Journal of Basic Engineering. 1967;89(3):459-463.

[293] Park JM, Wang ZJ, Jang JH, Gnidakoung JRN, Lee WI, Park JK, DeVries KL. Interfacial and hydrophobic evaluation of glass fiber/CNT-epoxy nanocomposites using electro-micromechanical technique and wettability test. Composites Part A: Applied Science and Manufacturing. 2009;40(11):1722-1731.

[294] Pedrazzoli D, Pegoretti A, Kalaitzidou K. Synergistic effect of exfoliated graphite nanoplatelets and short glass fiber on the mechanical and interfacial properties of epoxy composites. Composites Science and Technology. 2014;98:15-21.

[295] Mouritz AP, Koh TM. Re-evaluation of mode i bridging traction modelling for z-pinned laminates based on experimental analysis. Composites Part B: Engineering. 2014;56:797-807.

[296] Donough MJ, Gunnion AJ, Orifici AC, Wang CH. Scaling Parameter for Fatigue Delamination Growth in Composites under Varying Load Ratios. Composites Science and Technology. 2015;120(4):39-48.

[297] Rans C, Alderliesten R, Benedictus R. Misinterpreting the results: How similitude can improve our understanding of fatigue delamination growth. Composites Science and Technology. 2011;71(2):230-238.

[298] Mouritz AP, Chang P. Tension fatigue of fibre-dominated and matrix-dominated laminates reinforced with z-pins. International Journal of Fatigue. 2010;32(4):650-658.

[299] Yamamoto N, Manohara H, Platzman E. Magnetically anisotropic additive for scalable manufacturing of polymer nanocomposite: Iron-Coated carbon nanotubes. Materials Research Express. 2016;3(2).

Appendix

A. I. Journal Article: Improving the Toughness and Electrical Conductivity of Epoxy Nanocomposites by using Aligned Carbon Nanofibres

Composites Science and Technology 117 (2015) 146–158

Contents lists available at ScienceDirect

Composites Science and Technology

journal homepage: http://www.elsevier.com/locate/compscitech

Improving the toughness and electrical conductivity of epoxy nanocomposites by using aligned carbon nanofibres

Raj B. Ladani [a], Shuying Wu [a], Anthony J. Kinloch [b], Kamran Ghorbani [a], Jin Zhang [c], Adrian P. Mouritz [a], Chun H. Wang [a, *]

[a] Sir Lawrence Wackett Aerospace Research Centre, School of Aerospace, Mechanical & Manufacturing Engineering, RMIT University, GPO Box 2476, Melbourne, VIC 3001, Australia
[b] Department of Mechanical Engineering, Imperial College London, South Kensington Campus, London SW7 2AZ, UK
[c] Institute for Frontier Materials, Deakin University, Geelong Waurn Ponds Campus, VIC 3220, Australia

ARTICLE INFO

Article history:
Received 5 April 2015
Received in revised form
6 June 2015
Accepted 9 June 2015
Available online 18 June 2015

Keywords:
A. Adhesive joints
B. Fracture toughness
C. Modelling
C. Fibre bridging
Fibre pull-out

ABSTRACT

There is an increasing demand for high performance composites with enhanced mechanical and electrical properties. Carbon nanofibres offer a promising solution but their effectiveness has been limited by difficulty in achieving directional alignment. Here we report the use of an alternating current (AC) electric field to align carbon nanofibres in an epoxy. During the cure process of an epoxy resin, carbon nanofibres (CNFs) are observed to rotate and align with the applied electric field, forming a chain-like structure. The fracture energies of the resultant epoxy nanocomposites containing different concentrations of CNFs (up to 1.6 wt%) are measured using double cantilever beam specimens. The results show that the addition of 1.6 wt% of aligned CNFs increases the electrical conductivity of such nanocomposites by about seven orders of magnitudes to 10^{-2} S/m and increases the fracture energy, G_{Ic}, by about 1600% from 134 to 2345 J/m^2. A modelling technique is presented to quantify this major increase in the fracture energy with aligned CNFs. The results of this research open up new opportunities to create multi-scale composites with greatly enhanced multifunctional properties.

1. Introduction

Thermosetting epoxy polymers are widely used in aerospace and automotive applications as matrices for manufacturing fibre reinforced composites and as adhesives for joining structural components. Despite offering many desirable properties, thermosetting polymers typically exhibit a low electrical conductivity and a low fracture toughness, which leads to poor resistance to lightning strike and crack growth [1]. In the absence of any through-thickness reinforcement, fibre composites and bonded joints are susceptible to delamination or debonding [2]. The low electrical conductivity of composites and bonded structures, especially along the thickness direction, present challenges in protecting of aircraft against lightning strikes and electromagnetic interference. Also, good electrical conductivity is needed to meet fire retardant antistatic regulations for mining equipment, and oil-gas storage and transportation. Hence, improving the through-thickness toughness and electrical conductivity of fibre composites is of great importance.

Traditional techniques to improve the through-thickness properties and damage tolerance of epoxy polymers are to form a polymeric alloy via the addition of thermoplastics [3,4] or rubber tougheners [5,6]. Although these methods provide significant improvements to the toughness, the electrical conductivity remains unchanged because such additives are dielectric. More recently, studies on conductive carbon-based nanofillers, such as carbon nanotubes (CNTs) [7–9], carbon nanofibres (CNFs) [10–12] and graphene nanosheets (GNSs) [13,14], have shown significant promise to increase the toughness of epoxy polymers, as well as the ability to improve their electric conductivity. A number of studies have reported good improvements in toughness of epoxy nanocomposites by the addition of CNTs [15–18] or CNFs [12,19,20]. For example, Tang et al. [21] reported that the addition of 1 wt% CNTs increased the fracture energy of an epoxy by about 130%. Palmeri et al. [22] showed that the addition of just 0.68 wt% CNFs improved the fracture toughness of an epoxy by about 43–112%. Similarly, other studies have reported fracture toughness improvements

* Corresponding author.
E-mail address: chun.wang@rmit.edu.au (C.H. Wang).

http://dx.doi.org/10.1016/j.compscitech.2015.06.006

between 40 and 80 % for CNT or CNF modified epoxy nanocomposites. While these improvements are impressive, they are significantly lower than the nine fold increase in fracture toughness reported for nano-silica [23] and rubber-toughened modified epoxy polymers [24]. But the use of carbon based nanofillers can simultaneously increase the electric conductivity and mechanical properties, unlike nano-silica and rubber particles.

One major factor limiting the property improvements achieved to date in epoxy nanocomposites has been the fact that the carbon nanofillers are typically randomly-oriented, which arises naturally from the dispersion process using ultrasonication and/or mechanical mixing [25]. Unsurprisingly, the improvements achieved in many important properties of the epoxy nanocomposites containing randomly-oriented carbon-based nanofillers are significantly lower than what would be predicted had the nanofillers been aligned in the desired direction, albeit that the properties are now of course anisotropic. Theoretical modelling and computational simulations suggest that aligning nano-scale structures (e.g. CNTs and CNFs) in a certain direction should lead to substantial advantages compared with randomly-oriented nanofillers. Indeed, numerical analyses have confirmed that 1.0 vol% aligned CNTs should increase the stiffness of an epoxy by about 300% [26] in the alignment direction. Similarly, the alignment of 3.0 vol% CNTs in epoxy normal to the crack growth plane is predicted to enhance the toughness by up to 400% [27]. Unfortunately, there is a dearth of suitable processes to align carbon nanofillers along the through-thickness direction of composites. However, recently the use of electric- and magnetic-fields to align nanoparticles in liquid resins, prior to curing, has been reported [28–32]. The present authors have shown that by attaching nano-magnetite (Fe_3O_4), CNFs can be aligned by using a very weak (0.05T) magnetic field [32]. Under the application of an electric field between a pair of parallel plate electrodes, the nanofillers may align to form a chain-like network in the direction of the electric field [33]. This mechanism of the self-aligning of conductive carbon nanofillers in polymers offers a new opportunity to create multi-scale structures. Since thermosetting resins, such as epoxy resins, may typically possess a relatively low viscosity prior to cure, the application of an electric- and/or magnetic-field will be able to transform the randomly-oriented carbon-based nanofillers to give a highly aligned structure. Upon curing, the aligned nanofillers will remain in place in the resulting epoxy nanocomposite.

The alignment of CNFs [33] and CNTs [16] using an electric field has indeed been reported to improve the electrical conductivity of polymers through the formation of a percolating network at extremely low weight fractions of the added CNFs or CNTs. Khan et al. [16] has reported an additional 30% increase in the fracture toughness of CNT modified epoxy nanocomposites due to the alignment of the CNTs normal to the crack growth plane using a direct current (DC) electric field. Although randomly aligned CNFs have also been reported [22] to improve the fracture toughness of nanocomposites, the effect of their alignment on the fracture energy has never been studied.

Considering that CNFs may be an excellent alternative to CNTs due to their wide availability and lower cost [34], the present study focuses on dual improvements in the electrical conductivity and fracture toughness of an epoxy nanocomposite containing aligned CNFs. The alignment is accomplished by applying an external AC electric-field whilst the resin is liquid prior to crosslinking. Upon curing the epoxy resin, the resultant epoxy nanocomposite contains aligned CNFs. The effects of alignment of the CNFs on the fracture toughness and electrical conductivity of the epoxy nanocomposite are measured and theoretical modelling studies are undertaken to quantify the increase in the fracture toughness due to the alignment of the CNFs. The results are then compared to the values pertinent to the unmodified epoxy and the epoxy nanocomposites containing randomly-oriented CNFs.

2. Materials and experimental methodology

2.1. Materials

The epoxy resin used was a liquid blend of bisphenol A and bisphenol F ('105' from West System) and the hardener ('206' from West System) was a blend of aliphatic amines and aliphatic amine adducts based on diethylenetriamine and triethylenetetramine. Commercially-available vapour-grown carbon nanofibres, Pyrograf® – III PR-24-HHT and supplied by Applied Sciences Inc., USA, were employed as the nanofiller. The CNFs had a diameter of about 70–200 nm and a length of 50–200 μm [35]. Carbon fibre composite substrates were manufactured using 12 plies of unidirectional T700 carbon-fibre/epoxy-prepreg (VTM 264 supplied by Applied Composites Group). The substrates, with dimensions of 300 mm × 250 mm × 2.5 mm, were cured and consolidated in an autoclave at 120° C for 1 h, in accordance with the manufacturer's recommended cure process. The substrate surfaces were abraded using 320 grit aluminium oxide abrasive paper, cleaned under running tap water for about 2 min, degreased with acetone, and finally cleaned with distilled water to remove any surface impurities. The substrates were then used as the electrodes between which the liquid epoxy resin mixed with the CNFs, prepared according the procedure described below, acted as an adhesive layer.

2.2. Dispersion and in-situ alignment of the CNFs in the liquid epoxy resin

A three-roll mill (Dermamill 100) was used to disperse the CNFs in the liquid epoxy resin. Firstly, 1.0 wt% of the CNFs were hand mixed with dispersion-aiding additives based upon solvent-free acrylate copolymers, namely Disperbyk-191 and -192 (supplied by BYK®). The dispersive surfactants that were added to the CNFs were equal to the weight of the CNFs, resulting in a mixture of CNFs:D-191:D-192 at weight ratio of 1:1:1. The CNF-surfactant mixture was then added to the epoxy resin, with no curing agent yet added, and hand mixed for 5 min. This mixture was then passed four times through the three-roll mill at 150 rpm with varying gap sizes. In order to achieve a homogeneous dispersion of CNFs, with each subsequent pass the mill gap size was gradually reduced until the smallest gap setting of 20 μm had been reached. The 1.0 wt% CNF/epoxy mixture was then diluted by adding epoxy resin, to achieve the desired weight fraction of CNFs (0.1%, 0.4%, and 0.7%) in the epoxy resin. A batch of 1.6 wt% CNFs was mixed and dispersed separately following the above procedure, due to its relatively higher weight fraction in the epoxy resin.

To observe the AC electric-field induced alignment of the CNFs, a 0.1 wt% CNF/epoxy resin mixture was placed on a glass slide between two parallel carbon electrodes with a 2.0 mm separation distance. VTM264 carbon fibre-epoxy prepreg strips were used as electrodes. An AC signal generator (Tektronix CFG250) in combination with a wideband amplifier (Krohnhite 7602M) was used to apply 60 V AC at 10 kHz to generate the AC electric field of 30 V/mm strength. The *in-situ* alignment of the CNFs in the liquid epoxy resin was observed using a Leica optical microscope. Time-lapsed images of the CNFs were acquired using a Leica DC 300 digital camera to observe the alignment of the CNFs in the epoxy resin. The distribution of the orientation angles of the CNFs was ascertained using the Leica image processing software.

2.3. Joint manufacturing and testing

The surface-treated carbon-fibre composite substrates (150 × 250 × 2.5 mm) were placed between glass fibre frames which were used as a dam to prevent the epoxy mixture from flowing out of the joint. Spacers, 2 mm in thickness made of glass slides, were placed at both ends of the joint to control the thickness of the epoxy layer between the substrates. Teflon-coated tape about 30 mm long and 11 μm thick was placed at an approximately equal distance between the two substrates, at one end of the joint, to act as a crack starter. The amine-based curing agent was added to the dispersed CNF/epoxy resin mixture and hand-mixed for approximately 5 min. This CNF-modified epoxy resin mixture was then poured between the substrates. Such bonded joints were prepared using the epoxy nanocomposite as the adhesive layer for six different concentrations of CNFs (i.e. 0.0, 0.1, 0.4, 0.7, 1.0 and 1.6 wt %). Studies were undertaken for two different orientations of the CNFs (i.e. randomly-oriented and aligned). In order to achieve a highly aligned network of CNFs in the through-thickness direction of the epoxy nanocomposite layer, an AC electric field of 30 V/mm at 10 kHz was applied between the carbon-fibre composite substrates during the initial 1 h period of the curing cycle of the epoxy resin. The epoxy resin was then cured at room temperature (i.e. 25 °C) for 48 h in total to form the epoxy nanocomposite. After this time period, the CNF epoxy nanocomposite is referred to as 'n Random' or 'n Aligned', where 'n' refers to the amount of CNF by percentage weight of the total epoxy resin followed by the orientation. The joints were then cut into 20 mm wide double-cantilever beam (DCB) adhesively-bonded specimens. The electrical conductivity of the cured joints was tested using an impedance analyser (HP4192A). Fig. 1 shows a schematic of the DCB specimen. A sharp crack tip was achieved by carefully wedging the crack opening from the tip of the Teflon film. A minimum of five DCB specimens were tested in a 10 kN Instron machine at a crosshead speed of 1 mm/min in accordance with ISO 25217 [36]. The load versus displacement curves were recorded continuously, and a travelling optical microscope was used to observe the crack length in the epoxy nanocomposite layer. The mode I fracture energy, G_{Ic}, was calculated based on 'corrected beam theory' [36]. The crack was always found to propagate cohesively through the epoxy nanocomposite layer itself.

3. Results and discussion

3.1. Dispersion and in-situ alignment studies

The as-supplied CNFs were in the form of agglomerates, as shown in Fig. 2a. The use of the three-roll milling method was efficient at breaking up the agglomerates and dispersing the CNFs, as may be seen from Fig. 2b. The diameter of the as supplied CNFs was measured from five different SEM micrographs (see Fig. 2a) with a total CNF population equal to 510. As shown in Fig. 2c, the diameter distribution of the CNFs has a range from 60 nm to 200 nm with a lognormal peak of about 95 nm. The post-dispersion length of CNFs in the epoxy resin was measured using the Leica image processing software. Fig. 2d shows the length distribution of the CNFs after three-roll milling. The three-roll mill dispersion resulted in sizes of the CNFs ranging from 2 to 50 μm, with the majority of the CNFs having lengths of 16–24 μm. Dispersion using ultrasonication or three-roll milling would inevitably reduce the length of CNFs, however three-roll milling has been reported to be less damaging [25]. Retaining a relatively long length for the CNFs during their dispersion in the epoxy is considered to be important for obtaining an effective toughening of the epoxy nanocomposite, since the theoretical improvement in the fracture energy of the epoxy, from a fibre pull-out mechanism, will be proportional to the square of half the embedded length of the CNFs [37].

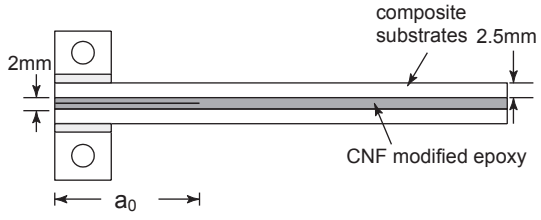

Fig. 1. Schematic of the double-cantilever beam (DCB) joint configuration.

The response of the CNFs in the liquid epoxy resin to the AC electric field was verified through *in-situ* optical microscopy. An AC electric field with an amplitude of 30 V/mm at 10 kHz was applied to 0.1 wt% of CNFs dispersed in the epoxy resin (i.e. containing no curing agent). Observations using the optical microscope were made to measure the time to achieve alignment. Fig. 3a shows an optical micrograph for t = 0 min (i.e. before the application of the AC electric field) and, therefore, the CNFs are randomly-oriented. Upon application of the AC electric field the CNFs rotated to align in the direction parallel to the electric field, as shown in Fig. 3b. For a 30 V/mm electric-field strength, the time needed to complete the alignment process was found to be about 5 min; beyond which no further improvement in the degree of alignment was observed. Fig. 3c shows a comparison of the angle distribution between the randomly-oriented CNFs (i.e. no electric field was applied) and the CNFs where the AC electric field was applied for 5 min. The use of the AC electric field has resulted in 85% of the CNF population of being aligned within ±15° of the applied electric-field direction. As shown in Fig. 4, the orientation of the CNFs was further verified using transmission electron microscopy to view 90 nm thick slices (obtained through ultramicrotomy) of the epoxy nanocomposite. The alignment of the CNFs can be attributed to the *dielectrophoresis* process, which is widely used for electrophoretic deposition of particles [38]. In the dielectrophoresis process, a particle immersed in a dielectric medium undergoes polarization when subjected to an externally applied electric field. This arises from the difference in the dielectric properties and the electrical conductivities between the particle and the medium. For one-dimensional particles, such as CNFs and CNTs, due to their shape anisotropy the longitudinal polarizability is at least an order of magnitude greater than the transverse polarizability [39,40]. Therefore, when subjected to an electric field, the difference in polarizability of the CNFs results in an induced dipole and its interaction with the electric-field gradient generates a torque resulting in rotation of the long axis of CNFs, so causing them to align along the external-field direction [41].

3.2. Electrical conductivity studies

Fig. 5a shows a logarithmetic versus logarithmetic plot of the electric conductivity (or specific conductance) as a function of frequency of the epoxy nanocomposite layer in the bonded joint in the direction normal to the substrate surfaces, i.e. in the through-thickness direction. The '0.1 random' epoxy nanocomposite (0.1 denotes the wt% of CNFs present) reveal an increase in the capacitive component with increasing frequency, similar to that of the unmodified (i.e. 'neat') epoxy polymer. While for the '0.1 aligned' case, there is always at least one order of magnitude improvement in the conductivity below about 1 kHz, independent of the frequency. This is then followed by a region of somewhat increasing conductivity which is similar in value to that of the '0.1 random' samples. A similar trend was also observed for the '0.4 random'

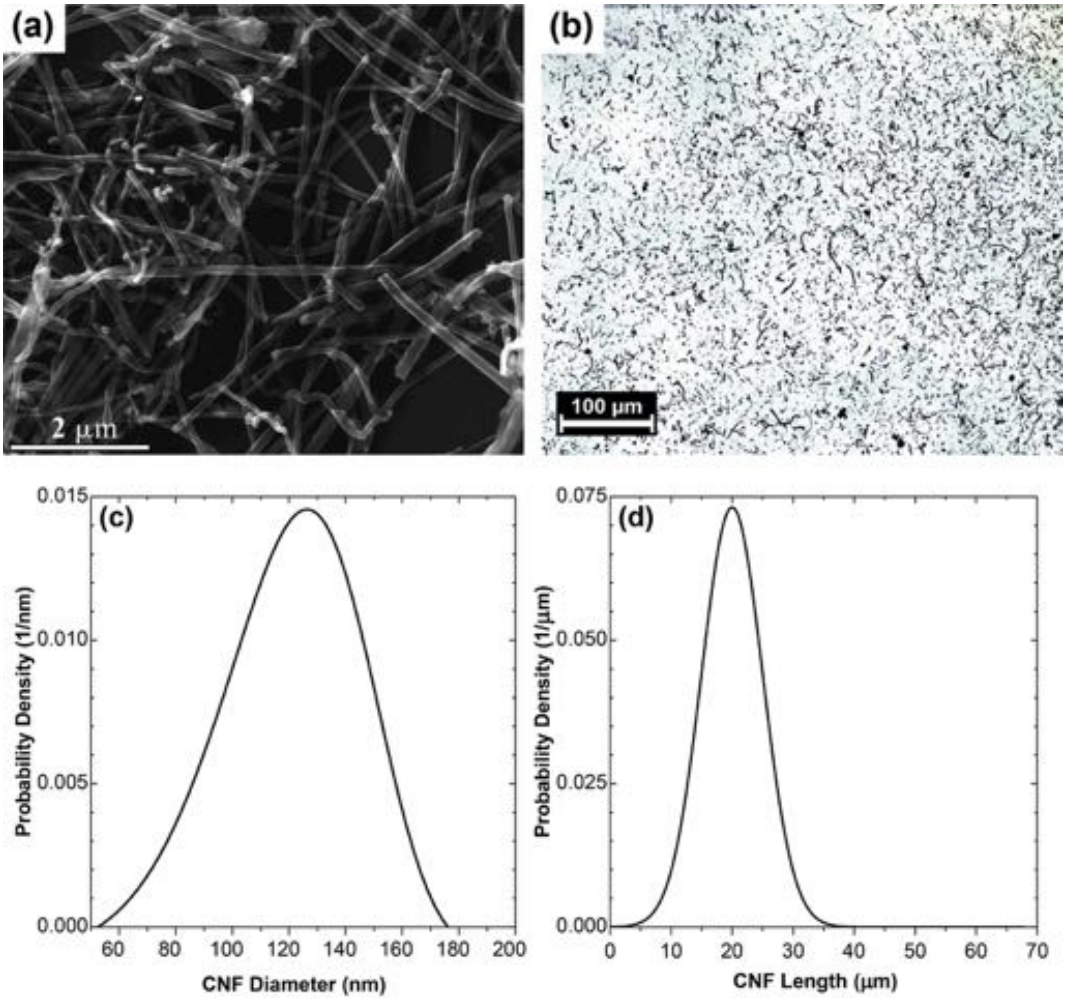

Fig. 2. (a) SEM micrograph of the as supplied CNF and (b) optical micrograph of the epoxy resin/0.1 wt% CNF mixtures after three-roll mill dispersing; (c) diameter probability density function of the as supplied CNFs measured from SEM micrograph and (d) length probability density function of the CNFs after the three roll-milling dispersion process from Fig. 2b.

epoxy nanocomposite with a frequency-independent conductivity up to about 10 kHz. This can be explained by considering the complex frequency dependent conductivity response of conductor-dielectric nanocomposites that are often analysed in terms of the *resistance-capacitance (R–C)* model,

$$\sigma(\omega) = \sigma_{dc} + \sigma_{ac} = \sigma_0 + A\omega^n \quad (1)$$

where σ_{dc} and σ_{ac} are the DC and AC conductivity respectively, ω is the angular frequency, A is a constant and the exponent n is in a range between 0 and 1 depending on the frequency range [42]. The AC component of the conductivity corresponds to the power-law frequency dependence and is well known for a wide range of materials which was noted by Jonscher [43] as the "Universal Dielectric Response". For each composition of nanocomposite containing a conductive filler, the above conductivity relationship is governed by a critical frequency,ω_c below which the conductivity becomes frequency-independent (i.e. DC conductivity, σ_{dc} when $\omega \rightarrow 0$), and beyond which the power-law is followed. Curve fitting the AC conductivity results of the neat epoxy composite using Eq. (1), the following values are obtained: $A = 1.5 \times 10^{-8}$ and $n = 1.0$, as shown in Fig. 5a. It is interesting to note that Eq. (1) with these two values is in good agreement with the other loadings of CNFs. The appearance of a DC plateau for the '0.1 aligned' and '0.4 random' samples below their critical frequencies of 1 kHz and 10 kHz, respectively, indicates a transition from an insulating to a conducting regime, which reflects the formation of some percolating CNF networks. However, for the '0.1 random' sample, the absence of the DC plateau region indicates that the conductivity is dominated entirely by the dielectric property of the epoxy. By contrast, the conductivity of '0.4 aligned' samples is significantly higher than that of the '0.4 random' samples and is independent of the frequency over the complete range of frequencies that were investigated. This indicates that the conductivity of the '0.4 aligned' nanocomposite is dominated by the conductor (i.e. the CNF networks) for most part. With further increases in the concentration of CNFs, the conductivity was found to be frequency-independent for both the randomly-oriented and the aligned nanocomposites, and increased to a maximum value of 10^{-2} S/m for the '1.6 aligned' epoxy nanocomposite. The measured increase in the DC conductivity of the epoxy as a function of the weight fraction of CNFs is shown in Fig. 5b.

From these results, the increases in the conductivity suggest that a network of percolated nanofibres formed at a concentration of CNFs above about 0.7 wt% when they were randomly-oriented. However, the application of the AC electric field during the curing of the epoxy resin resulted in alignment of the CNFs and it appears that the percolation network now formed at a concentration of

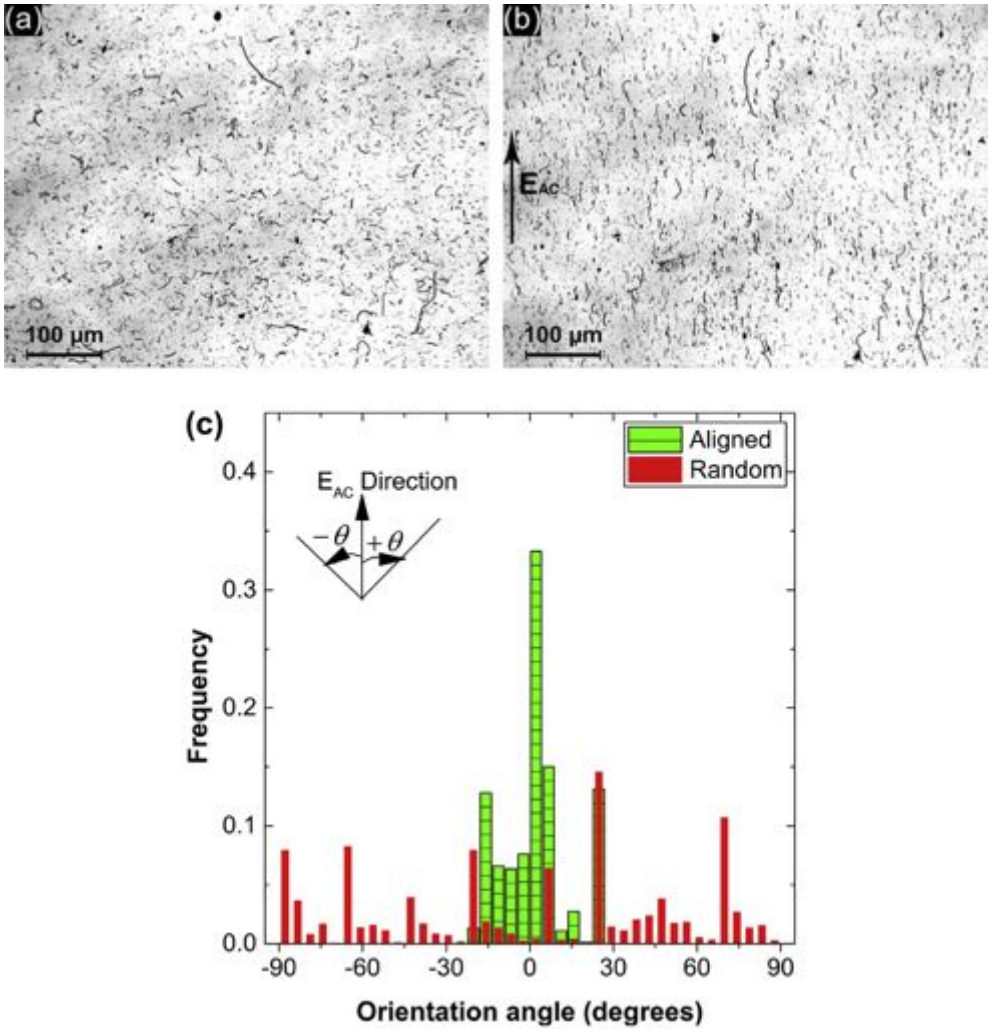

Fig. 3. *In-situ* alignment of 0.1 wt% CNFs in the epoxy resin using the AC electric field (a) t = 0 min (i.e. randomly-oriented CNFs) and (b) t = 5 min (i.e. aligned CNFs), the direction of the applied AC electric field is indicated by the arrow; (c) comparison of the angle distribution of the randomly-oriented CNFs (from Fig. 3a) and the CNFs aligned after being subjected to the AC electric field for 5 min (from Fig. 3b).

CNFs of about 0.4 wt%. A comparison of these results with the DC conductivity of these nanocomposites gave identical results. Indeed, the advantage of aligning the CNFs in the epoxy nanocomposites is clearly apparent from the '0.7 aligned' samples, which had a higher conductivity than the '1.0 random' samples. However, for the 1.6 wt% samples, the increase in the conductivity of the epoxy nanocomposites due to the alignment of CNFs was minimal. This is attributed to the lack of free space available for the

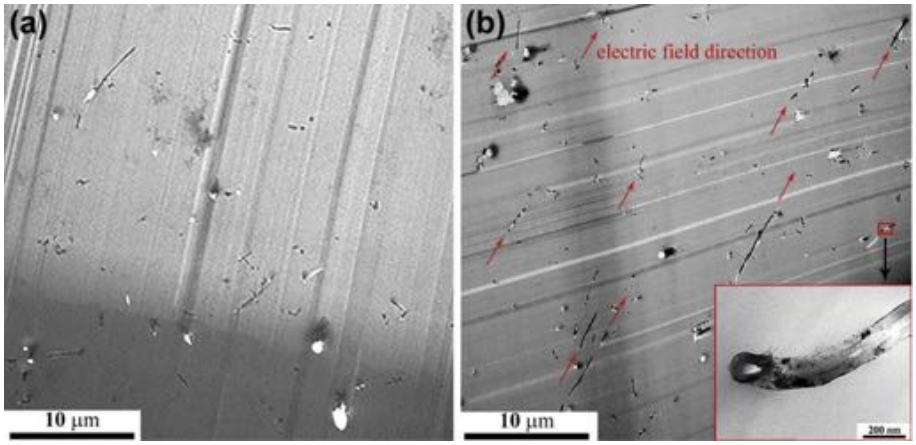

Fig. 4. TEM images of the epoxy nanocomposites. (a) 0.7 wt% of CNFs and randomly-oriented. (b) 0.7 wt% of CNFs and aligned via the application of the AC electric field for 5 min (The arrows indicate the direction of the applied AC electric field.) Inset shown in (b) gives a detailed view of CNF.

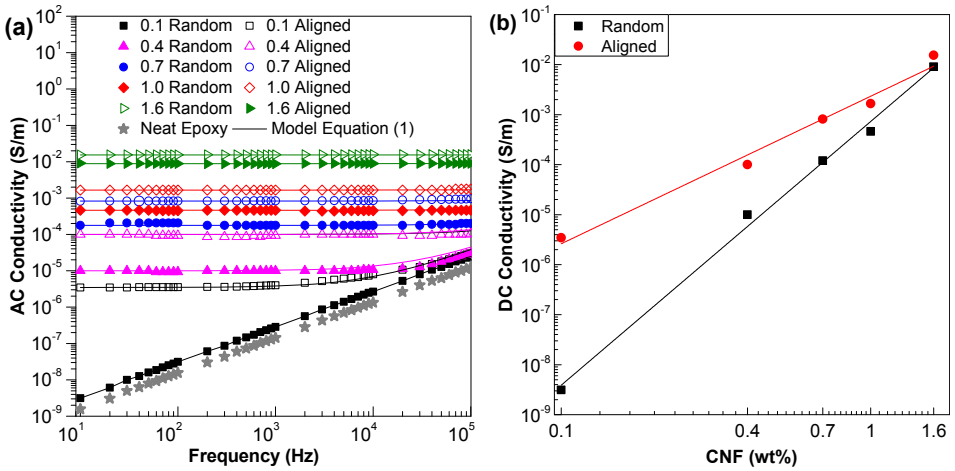

Fig. 5. (a) Electrical conductivity of the epoxy nanocomosites as a function of frequency. (a) AC conductivity as a function of frequency; all solid lines are calculated from Equation (1). (b) DC conductivity as a function of CNF concentration for both randomly-oriented or aligned CNFs in the epoxy nanocomposites; the lines represent a linear fit. (Note: The conductivity of the aligned nanocomposites was measured in the direction of alignment.)

CNFs to rotate in the direction of the electric field due to the resistance from the interaction between closely packed CNFs [44] and the likely formation of CNF agglomerates in the epoxy at these relatively high weight fractions of CNFs.

3.3. Fracture energy studies

As shown in Fig. 6, the applied load versus crack opening displacement curves for the DCB tests with the adhesive layer comprising of unmodified epoxy or epoxy nanocomposites containing randomly-oriented or aligned CNFs all revealed that the type of crack growth was unstable, i.e. stick-slip, in nature, with the distinct "saw-tooth" shaped load versus displacement curves typical of such failure. The maximum peak loads of these curves corresponded to the onset of crack growth, while the lower values of load corresponded to the arrest of the fast propagating crack. For the DCB specimens with a higher weight concentration of CNFs in the epoxy nanocomposite layer, the length of the unstable crack growth was much greater, due to the higher maximum loads for crack propagation that were attained. Therefore, the load versus displacement curves for these samples had fewer peaks. The values of G_{Ic} for the onset of crack propagation were calculated using the maximum loads that were measured [35]. The locus of failure was along the centre of the unmodified (i.e. neat) epoxy polymer or epoxy nanocomposite layer in all cases.

The results of the fracture toughness tests of the DCB tests with the adhesive layer comprising of unmodified epoxy or epoxy nanocomposites containing randomly-oriented or aligned CNFs are shown in Fig. 7. The average mode I fracture energy, G_{Ic}, of the unmodified epoxy layer for the DCB joint was found to be 134 J/m^2, as would be expected for a relatively brittle epoxy. An increase in the value of the fracture energy was observed for all the epoxy nanocomposites. For the nanocomposites, the fracture energy increases almost linearly with the concentration of CNFs. In addition, a somewhat greater improvement in the fracture energy was consistently measured for samples containing aligned CNFs, with their orientation of course normal to the direction of crack growth. The '1.6 aligned' specimen showed the highest improvement, with a sixteen fold increase in the fracture energy compared to the unmodified epoxy. Further, compared to the nanocomposites containing randomly-oriented CNFs, the alignment of the CNFs resulted in a consistent rise of about an additional 25% increase in the fracture energy for the concentrations investigated at, and below, 1.0 wt%. However, a further increase in the concentration of

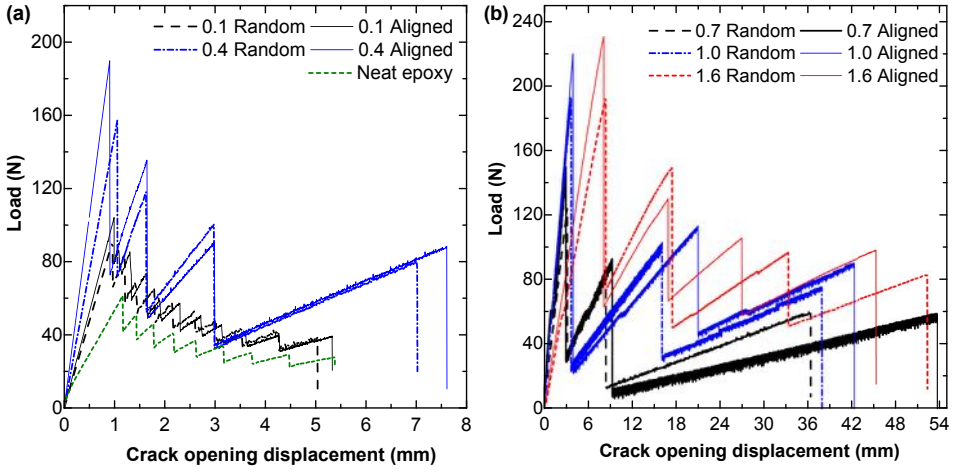

Fig. 6. Load versus displacement curves for the epoxy nanocomposites containing different concentrations of CNFs and for both randomly-oriented or aligned CNFs in the epoxy nanocomposite layer.

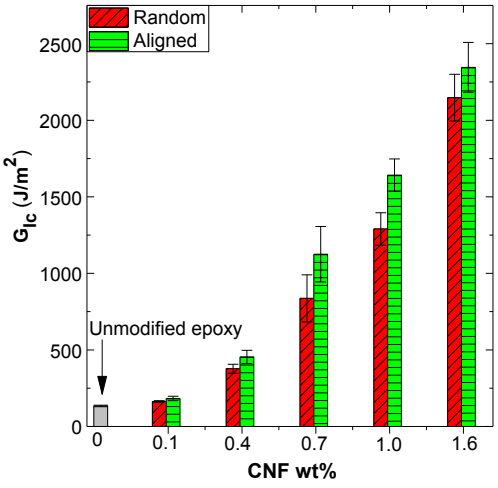

Fig. 7. Values of the fracture energy, G_{IC}, for the epoxy nanocomposites containing different concentrations of CNFs and for both randomly-oriented or aligned CNFs in the epoxy nanocomposite layer.

the CNFs to 1.6 wt% showed a relatively small difference between the fracture energies of the aligned and randomly-oriented CNF nanocomposites which was not statistically significant. Similar observations have been reported for CNT/epoxy nanocomposites at relatively high concentrations of CNTs, and were suggested to be due to the lack of free space available for the rotation and alignment of the CNTs in the epoxy when a relatively high concentration of nanofiller was present [16]. The toughening mechanisms responsible for these observed improvements in the measured toughness are discussed in the following section.

3.4. Toughening mechanisms

Post-failure examination of the fracture surfaces of the DCB samples gave an insight into the toughening mechanisms responsible for the improvements in the fracture energy of the epoxy nanocomposites. A typical featureless and smooth fracture surface was observed for the unmodified epoxy which was indicative of a very brittle fracture. Fig. 8 shows a photograph of the fracture surface for a nanocomposite sample where the regions of crack initiation and arrest are visible as curved lines across the width of the sample. In the epoxy layer of the DCB test, crack growth occurred under predominantly plane-strain conditions but with plane-stress conditions at the specimen edges of the specimen, causing the curved profile of the crack front. There is a distinct whitening of the polymer along these crack initiation/arrest lines. Examination of these regions using the SEM revealed a pattern of tear marks, which provides evidence of plastic deformation in the epoxy polymer along the line of crack initiation, which would have occurred immediately before the onset of the rapid growth of the crack. Further away from the stress-whitened regions, where the crack had propagated rapidly, there was very little evidence of ductile, plastic deformation, and the glassy fracture surface was representative of a very brittle fracture having occurred.

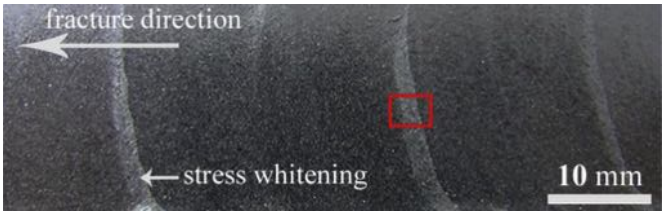

Fig. 8. Photograph of the crack fronts on the fracture surface of an epoxy nanocomposite with 1.0 wt% aligned CNFs.

Fig. 9 shows SEM micrographs of the stress-whitened region which correspond to the location of the onset of crack growth (i.e. the crack initiation location, see the inset in Fig. 8) in the epoxy nanocomposites containing different concentrations of aligned CNFs. Patterns of tear marks were observed in most of these images, revealing the plastic deformation of the epoxy that had occurred in the stress-whitened regions, either just ahead of the crack tip or due to some extent of slow crack growth occurring prior rapid crack growth taking place. The size and roughness of the stress-whitened region both increased with CNF concentration. The increase in the severity of the tear marks and the roughness with increasing CNF concentration is indicative of the increased plastic deformation of the epoxy in the process zone ahead of the crack tip due to the presence of the CNFs. As shown in Fig. 9, a significant number of CNFs were pulled out of the epoxy, leaving behind a void on the opposite crack surface. The areal density of the pulled-out regions of the CNFs increased with the increasing concentration of aligned CNFs. Moreover, some of the CNFs showed evidence of having experienced uncoiling and a cup-cone type of failure. This uncoiling phenomenon is unique to CNFs due to their stacked graphene cup morphology [22], which has been previously observed using TEM, revealing an uncoiled nanoribbon of graphene sheet [45]. The uncoiling and cup-cone type failure of CNFs was observed for both aligned and randomly-oriented CNF epoxy nanocomposites. However, the fibre pull-out mechanism is typically the most dominant mechanism in increasing the fracture energy [2]. The increase in the fracture energy during pull-out is due to the work of friction by the interfacial shear stress between the CNFs and the epoxy polymer. During this pull-out process the CNFs also formed a bridging zone behind the crack tip. This is evident from SEM observations of the crack bridging by CNFs, as shown in Fig. 10. The average length of the CNFs bridging the crack at its maximum opening displacement was about 8 μm. The bridging density of the CNFs decreased with decreasing concentration of CNFs, with almost no bridging being observed for the 0.1 wt% CNF epoxy nanocomposite samples. In order to pull-out and bridge the crack, the CNF must firstly debond from the epoxy. The strain energy absorbed in overcoming the adhesion of the epoxy/CNF interface during the debonding process would also increase the fracture energy, but to a lesser extent. If the interfacial bond strength exceeds the strength of the nanofibres, the CNFs would rupture prematurely before pull-out occurred. However, the rupture of the CNFs would result in smaller improvements in the values of the fracture energy, since the strain energy consumed during fibre rupture is reported to be significantly lower than that pertinent to pull-out [46].

Further, a significant number of relatively large voids are present around the CNFs (see Fig. 9c–f) and are indicative of plastic void growth of the epoxy polymer in the process zone, which leads to an additional increase in the fracture energy, compared to the unmodified epoxy. This arises because in the process zone ahead of the crack tip, where a triaxial stress-field exists, the CNFs debond from the epoxy as the local stresses increase at the crack tip. The debonded CNFs act as voids in the epoxy which allows the polymer to deform plastically, and so the voids increase in size. For rubber- and nanosilica-toughened epoxies, this plastic void growth mechanism has been shown to significantly increase the fracture toughness of the material [23,47].

Therefore, the aggregate increase in the fracture energy of the epoxy due to the addition of the CNFs is considered to be a combination of the energy dissipated by (a) the frictional energy associated with the CNFs now pulling-out from the epoxy, (b)

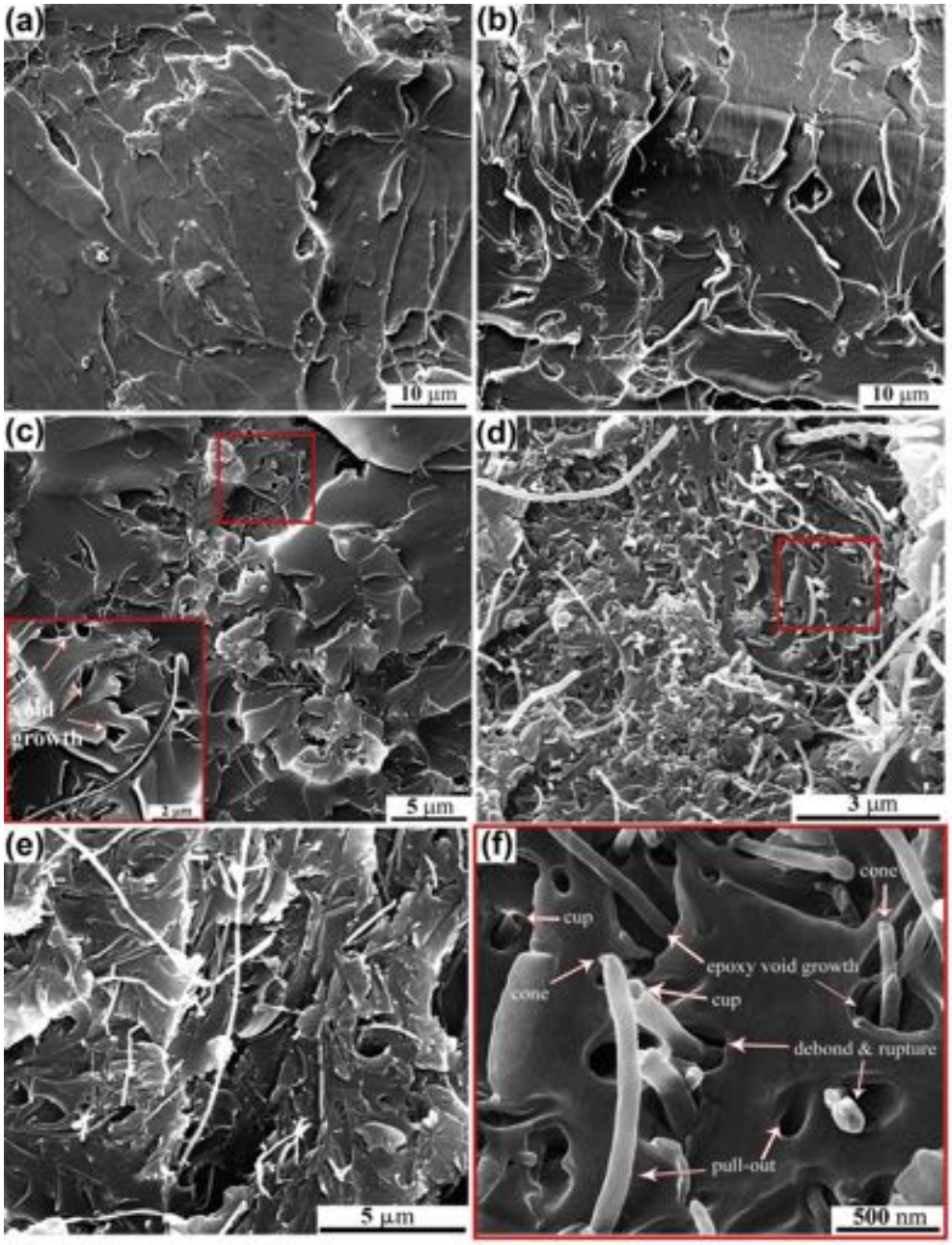

Fig. 9. SEM images of the crack initiation region of the fracture surfaces for the epoxy nanocomposites containing aligned CNFs of concentration; (a) 0.1 wt%; (b) 0.4 wt%; (c) 0.7 wt %; (d) 1.0 wt%; (e) 1.6 wt% and (f) is of the inset of (d) at a higher magnification for the 1.0 wt% nanocomposite.

rupture of CNFs, (c) interfacial debonding of the CNFs from the epoxy, and (d) void growth of the epoxy which initiates from the hole created by the debonded CNFs.

Considering the alignment of the CNFs perpendicular to the crack path in the nanocomposites, such alignment of the CNFs would lead to a higher fraction of CNFs participating in the above toughening mechanisms. For a random orientation of CNFs in the epoxy, the probability of the crack front encountering the CNFs depends on their orientation angle. For short fibre composites with a random fibre orientation, this probability is given by $\cos\theta$ (refer to Fig. 4 for the orientation axes), and for an orientation angle above 60° the probability is less than 50% [27,48]. This would lead to a lower fraction of CNFs involved in the pull-out, bridging and rupturing mechanisms for the epoxy nanocomposites containing the randomly-oriented CNFs. This is clearly evident for the randomly-oriented materials, as is shown in Fig. 11a, where a greater number of CNFs which were oriented parallel to the crack path have undergone debonding but without participating in the pull-out or void growth toughening mechanisms. While for the aligned epoxy nanocomposites, as shown in Fig. 11b, almost all the CNFs have now undergone debonding and pull-out, and hence led to the void growth mechanism being operative. In addition, if aligned normal to the direction of crack growth, the CNFs are far more likely to bridge the crack faces and undergo tensile rupture as the crack tip advances, as may be seen from comparing Fig. 10c and d.

3.5. Theoretical modelling of the fracture energy

As discussed in the previous section, the primary toughening mechanisms in the epoxy nanocomposites based on the

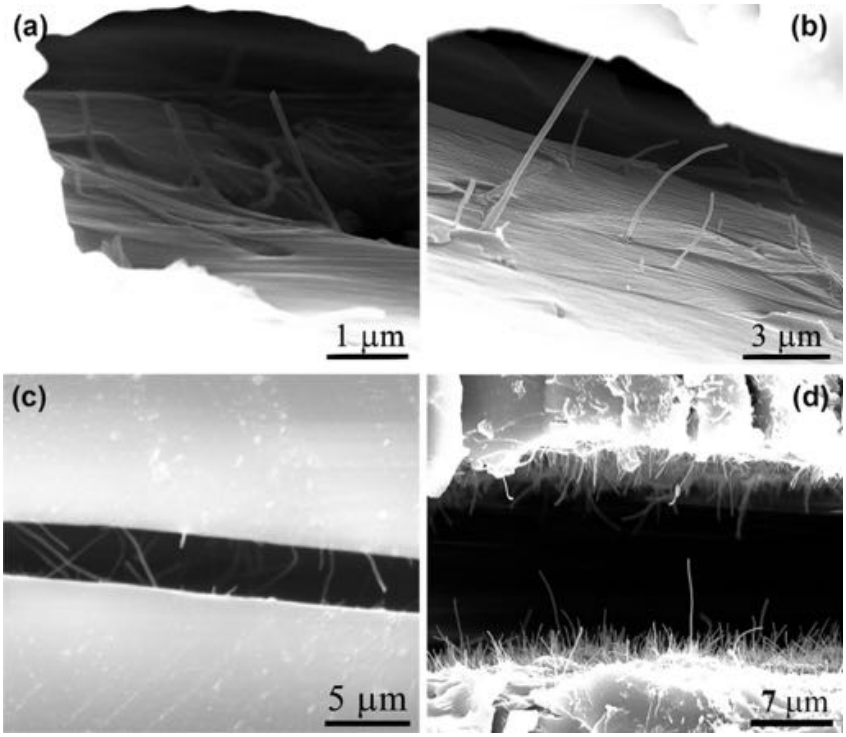

Fig. 10. SEM images of CNFs bridging the crack in epoxy nanocomposites. (a) '0.4 random'; (b) '0.4 aligned'; (c) '0.7 random'; and (d) '1.0 aligned'.

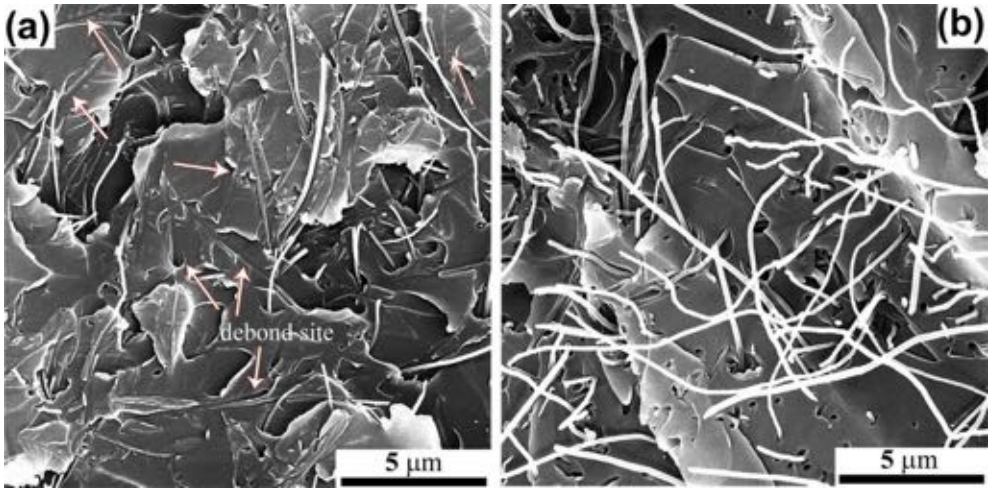

Fig. 11. Comparison of the pull-out of CNFs in the epoxy nanocomposites for (a) '1.0 random' and (b) '1.0 aligned' samples.

fractographic evidence were debonding and pull-out of the CNFs, plastic void growth of the epoxy initiated by the voids formed by the CNFs debonding and the CNFs bridging and finally rupturing across the crack faces behind the advancing crack tip. Assuming the application of continuum mechanics is valid at the nanoscale and the interfacial stress being constant [15,49], the energy dissipated by fibre pull-out based on the conventional expression from Hull [50] and Cottrell-Kelly [see 2] is given by:

$$\Delta G_{\text{pull-out}} = \frac{N_{\text{po}} \pi d_{\text{f}} \tau_{\text{i}} l_{\text{po}}^2}{2} \tag{2}$$

where l_{po} is the nanofibre pull-out length, d_f is the diameter of the CNF, τ_{i} is the interfacial shear strength and N_{po} is the total number of nanofibres per unit area of crack surface. N_{po} is related to the volume fraction, V_{fpo}, of CNFs which are pulled-out from the epoxy:

$$N_{\text{po}} = \frac{\text{nanofibre volume}}{\text{volume per nanofibre}} = \frac{l_{\text{f}} V_{\text{fpo}}}{l_{\text{f}} A_{\text{f}}} = \frac{V_{\text{fpo}}}{A_{\text{f}}} \tag{3}$$

where A_{f} is the nanofibre cross-sectional area and l_{f} is the nanofibre length. For a given weight fraction of CNFs in the epoxy, not all of the CNFs are involved in the pull-out process. Therefore, the volume fraction of CNFs pulled-out from the epoxy V_{fpo} has been determined by counting from the SEM micrographs the number of CNFs on the fracture surface. A total of sixteen SEM micrographs were used per sample type to determine the CNF pull-out volume fraction. Previous studies have successfully demonstrated the use of a similar approach to analytically calculate the strength [51] and

toughness [15] of CNT containing polymer composites. (Note: the CNF pull-out count from the fracture surfaces also includes the voids left behind by the CNFs pulled-out onto the opposite crack face). Substituting Eq. 3 into 2 gives:

$$\Delta G_{\text{pull-out}} = \frac{2V_{\text{fpo}}\tau_i l_{\text{po}}^2}{d_f} \quad (4)$$

The CNF pull-out length is difficult to determine with accuracy from SEM images of the fracture surfaces, particularly for samples with a relatively high volume fraction of CNFs. Also, relatively long CNFs are expected to rupture at the crack plane, since their embedded lengths on either side of the crack plane are long enough for the stress in the CNF to build up sufficiently to break them. Two outcomes are possible depending on the length of the embedded CNFs: (a) the CNFs pull-out when the length is shorter than the critical length given by the classical Kelly-Tyson [2,52] formula i.e. $l_c = \sigma_f d_f/2\tau_i$, or (b) the CNFs rupture when their length is longer than the critical length. The longest possible pull-out length of the CNFs is equal to half the critical length of the CNFs embedded in the nanocomposites as given by the Kelly-Tyson formula:

$$l_{\text{po}} = \frac{\sigma_f d_f}{4\tau_i} \quad (5)$$

where σ_f is the nanofibre strength. Substituting Eq. 5 into 4 gives the estimate of the pull-out energy in terms of the inherent properties of the nanocomposite as follows:

$$\Delta G_{\text{pull-out}} = \frac{V_{\text{fpo}}\sigma_f^2 d_f}{8\tau_i} \quad (6)$$

A wide range of values for the interfacial shear strength between CNFs and epoxies have been reported in the literature, [53,54]. However, the maximum possible interface strength between the epoxy and CNFs is limited by the shear strength of the epoxy polymer. From Table 1 the shear strength of the epoxy polymer may be taken to be half that of the tensile yield strength using Tresca yield criterion, giving a value of 25 MPa. This value is used to estimate the contribution to the fracture energy from pull-out of the CNFs.

The contribution to the fracture energy due to CNF bridging is from the energy required to pull-out the bridging CNFs from the epoxy, and is therefore accounted by $\Delta G_{\text{pull-out}}$ [46]. Whereas, the energy contribution due to the elastic deformation of the CNFs prior to rupturing, whether in the plastic zone ahead of the crack tip or in its wake, is given by Ref. [27]:

$$\Delta G_{\text{rupture}} = \frac{V_{\text{fpo}}\sigma_f\, l_f\, \varepsilon_{\max}}{2} = \frac{V_{\text{fpo}}\sigma_f^2\, l_f}{2\, E_f} \quad (7)$$

where E_f and $\varepsilon_{\max}$ are the Young's modulus and the tensile failure strain of the CNFs, respectively.

The CNFs undergo debonding prior to the pull-out process. The interfacial debonding of the CNFs is an essential process because it allows them to pull-out and initiates plastic void growth of the epoxy around the hole so created. The interfacial debonding energy, ΔG_{db}, is given by Refs. [15,50]:

$$\Delta G_{\text{db}} = \frac{V_f l_{\text{po}} G_i}{d_f} \quad (8)$$

where G_i is the interfacial fracture energy between the CNFs and the epoxy. Ozkan et al. [53]. measured the interfacial fracture energy between CNFs and an epoxy polymeric matrix to be 3.3 J/m^2, and this value was used in the present study.

In addition to the CNF pull-out mechanism, the plastic void growth of the epoxy matrix promoted by debonding of CNFs from the epoxy matrix would further increase the fracture energy. In previous studies [23,47], the plastic void growth mechanism was quantitatively shown to significantly improve the fracture toughness of a nanosilica modified epoxy polymer. Huang and Kinloch [55] have shown that the fracture energy, ΔG_v, contribution from the plastic void growth mechanism can be calculated as follows:

$$\Delta G_v = \left(1 + \frac{\mu_m}{\sqrt{3}}\right)^2 \left(V_{\text{void}} - V_{\text{fpo}}\right)\sigma_y r_{yu} K_{vm}^2 \quad (9)$$

where V_{void} is the volume fraction of the voids and μ_m is a material constant allowing for the pressure dependency of the yield stress. The parameter K_{vm} is the maximum stress concentration for the von Mises stresses around a debonded CNF, which lies between 2.11 and 2.12 [15]. The parameters σ_y and r_{yu} are respectively the tensile yield stress and the plastic zone size at fracture of the unmodified epoxy. The plastic zone size is given by:

$$r_{yu} = \frac{1}{6\pi}\frac{E_m G_{CU}}{(1-\nu^2)\sigma_y^2} \quad (10)$$

where G_{cu} is the fracture energy, E_m is the tensile modulus and ν is the Poisson's ratio of the unmodified epoxy polymer. Each void is assumed to be a truncated cone with the smaller diameter equal to the diameter of the CNFs and the larger void diameter is determined from the SEM micrographs which has a varying distribution depending on the size of the CNFs. In the present study the void diameter was estimated from SEM micrographs to be approximately seven times the diameter of the CNFs around which the void

Table 1
List of values for the various parameters used in the analytical modelling study.

Parameter	Symbol	Unit	Value	Source
CNF diameter	d_f	nm	135	[35]
CNF average length after dispersion	l_f	μm	20	This study
CNF strength	σ_f	GPa	8.7	[35]
Young's modulus of the CNF	E_f	GPa	320	[56]
Density of the CNF	ρ_f	kg/m^3	1400	[35]
Density of unmodified epoxy	ρ_m	kg/m^3	1011	[57]
CNF/epoxy interface fracture energy	G_i	J/m^2	3.3	[53]
Tensile yield strength of unmodified epoxy	σ_y	MPa	50.5	[57]
Young's modulus of unmodified epoxy	E_m	GPa	3.17	[57]
Pressure dependent yield stress constant	μ_m	–	0.2	[55]
Maximum von Mises stress concentration	K_{vm}	–	2.11	[15]

are formed. In other words, $V_{void} = 16V_{fpo}$ in the present case. Therefore, the fracture energy, G_{Ic}, of the CNF toughened epoxy can be expressed as:

$$G_{Ic} = G_{CU} + \Delta G_{rupture} + \Delta G_{pull\text{-}out} + \Delta G_{db} + \Delta G_{v} \quad (11)$$

The above model is used to estimate the fracture energy improvement by considering an average CNF diameter equal to 135 nm as supplied by the manufacturer [53].

Equations (6), (8) and (9) show that the energy contributions due to CNF pull-out, debonding and epoxy void growth depend strongly on the diameter of the nanofibres. The probability density function of CNF diameter is shown in Fig. 2c. The 135 nm diameter value provided by the manufacturer corresponds to the median of this distribution. By accounting for the distribution of the CNF diameter, the total fracture energy can be expressed in terms of the diameter probability function $\rho(d_f)$:

$$G_{Ic} = G_{CU} + \Delta G_{rupture} + \int_{d_{min}}^{d_{max}} \left(\Delta G_{pull\text{-}out} + \Delta G_{db} + \Delta G_{v}\right)\rho\left(d_f\right)\mathrm{d}d_f \quad (12)$$

where $\Delta G_{rupture}$ is independent of the CNF diameter as can be seen from Eq. (7). The fracture energy modelling results are calculated from the experimentally-determined values of V_{fpo} for the random and aligned nanocomposite, apart from the '1.6 aligned' nanocomposite. Due to the relatively high concentration of CNFs in the 1.6 wt% nanocomposite, it is excessively time consuming to count the number of CNFs pulled out on the crack surface.

The fracture energy is also calculated by assuming all the CNFs are pulled out, hence $V_{fpo} = V_f$. The V_f is estimated from the CNF weight fraction by considering the graphitic CNF wall density to be 1400 kg/m^3 [35]. This approach assumes that all the CNFs in a unit volume of epoxy are intersected by the advancing crack. The values of all the input parameters used to calculate the fracture energy of the epoxy polymers containing the CNFs are given in Tables 1 and 2 Model predictions and comparison with experimental results are presented in the following section.

3.6. Results of theoretical models

Fig. 12 shows the results from the theoretical modelling studies compared to the experimentally measured values of G_{Ic}. The figure shows two curves calculated using the model assuming that the CNFs have the mean diameter (Eq. (11)) or the diameter varies according to the probability density function (Eq. (12)). The toughness values are slightly higher when it is assumed that all the CNFs have the same (mean) diameter. Good agreement can be seen between the experimental results and the predicted fracture energies which supports the primary toughening mechanisms which have been proposed for the epoxy polymers modified using randomly-oriented or aligned CNFs. The CNF pull-out and the epoxy void growth were the two most dominant toughening mechanism, accounting for the majority of the fracture energy enhancement for all the epoxy nanocomposites.

Table 2
Measured values of the volume fraction, V_{fpo}, of CNFs which are pulled-out from the epoxy and the volume fraction, V_{void}, of the voids formed around the debonded CNFs.

CNFs (wt%)	V_f (%)	V_{fpo} (%)		V_{void} (%)	
		Aligned	Random	Aligned	Random
0.1	0.08	0.02	0.01	0.32	0.23
0.4	0.33	0.23	0.18	3.99	3.34
0.7	0.58	0.53	0.43	9.39	8.12
1.0	0.82	0.78	0.63	13.76	11.91
1.6	1.31	–	–	–	–

Table 3a shows a comparison of the highest fracture toughness improvements that have been reported in the literature for CNT and CNF modified epoxies against the nanocomposites studied here. It is noteworthy that the toughness improvements achieved in the present study are many times higher than those reported previously. These variations in the enhancement of the fracture energy may be mainly explained by the differences in the length of the CNFs, and its effect on the fracture energy due to pull-out of the CNFs as given by Eq. (4). For example, if the CNF length is reduced to 6 μm, as was the case in the study by Palmeri et al. [22], the fracture energy due to pull-out will be greatly reduced. In order to obtain a better estimate for such an effect, and for the purpose of comparison between the two studies, it has been assumed that the volume fraction of CNFs that are pulled-out is only dependent on the concentration of CNFs and is independent of the length. On this basis, for the 0.7 wt% of random CNF nanocomposite studied by Palmeri et al. [22], assuming that all the modelling parameters (besides the value of the nanofibre length, l_f) are similar in value to those used in the present work, the expected improvement in the value of the fracture energy, as given by Eq. (11) with a CNF length equal to 6 μm, would be about 116%. This is very similar to the measured improvement reported in their study, see Table 3a. The improvements in the fracture energy of epoxy polymer containing CNFs reported in some other studies can be similarly estimated and the data are given in Table 3b where the matrix properties are taken from Ref. [58]. Using Eqs. (11) or (12) and the relevant data in Tables 1 and 3b, the proposed model gives a reasonable estimate for the measured values of G_{Ic} reported previously in the literature, as may be seen from Table 3a. It is also clear that the improvement in the fracture energy of the epoxy due to the addition of the CNFs or CNTs is strongly dependent on the dimensions of the nanofiller, especially the fibre length. Thus, the use of longer CNFs, as in the present study, would indeed be expected to lead a better enhancement in the fracture energy of the epoxy nanocomposites.

4. Conclusions

The fracture energy and electrical conductivity of a thermoset epoxy polymer modified by the addition of carbon nanofibres (CNFs) have been investigated. The CNFs were dispersed in a liquid epoxy resin using a surfactant and then processed employing a three-roll mill to give a good degree of dispersion with the majority of the CNFs having lengths of between 16 and 24 μm. An AC electric field has been found to be very effective in aligning CNFs to form a chain-like structure in epoxy with the majority (85%) of the CNFs lying within ±15° of the applied electric field. The alignment of 0.4 wt% of CNFs in the epoxy nanocomposite led to the formation of a percolating network of CNFs which yielded a measurable DC conductivity, while simultaneously increasing the average fracture energy, G_{Ic}, from 134 J/m^2 to 453 J/m^2, compared to the unmodified epoxy polymer. The highest increases in toughness and conductivity were for the epoxy nanocomposites containing 1.6 wt% of aligned CNFs. The fracture energy and the electrical conductivity of this nanocomposite were increased by about 1600% (from 134 to 2345 J/m^2) and seven orders of magnitude above the unmodified epoxy. When compared to randomly-oriented CNFs, the alignment of the CNFs resulted in a 27% increase in the fracture energy and about a five-fold increase in the electrical conductivity at 1.0 wt% of CNFs. The main toughening mechanisms which led to the increase in the fracture

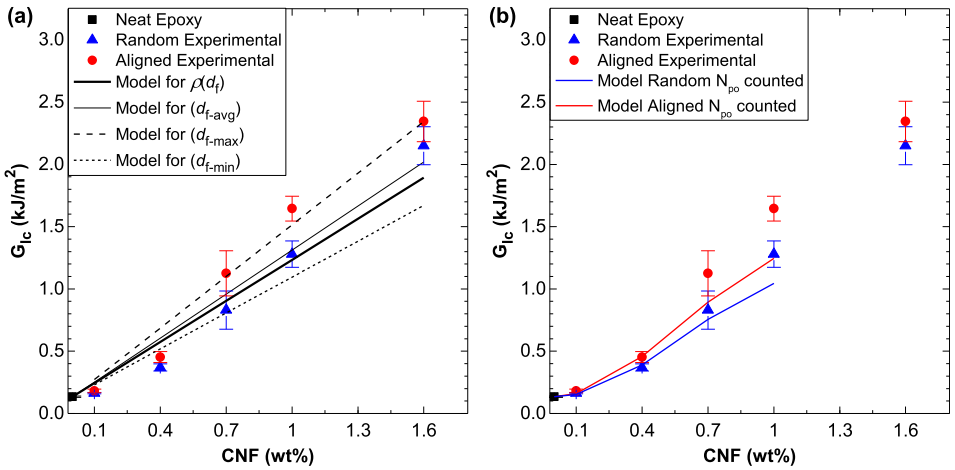

Fig. 12. Comparison of the experimental and theoretically calculated fracture energies as a function of the concentration of CNFs. (a) Model calculations based on total volume fraction ($V_{fpo} = V_f$) using minimum, mean, maximum, and probabilistic distribution of the CNF diameter; and (b) model calculations based on the experimentally measured V_{fpo} for random- and aligned-CNF nanocomposites.

Table 3a
Fracture toughness, G_{Ic}, values of epoxy polymers toughened with 1-D carbon nanofillers.

Source	Nanofiller	Nanofiller concentration (wt%)	Improvement (%)	Model prediction (%)
The present study	CNFs-Random	1.6	1500	1410
	CNFs-Random	1.0	850	880
	CNFs-Random	0.7	500	610
	CNFs-Random	0.4	180	350
Tang et al. [21]	MWCNTs*	1.0	130	–
Palmeri et al. [22]	CNFs	0.68	113	95
Liu et al. [19]	CNFs	0.4	80	140
Hsieh et al. [15]	CNTs	0.5	70	60

*Multiwall carbon nanotubes (MWCNTs).

Table 3b
Parameters used to calculate the fracture energy improvement in Table 3a using the theoretical model from Section 3.5 for the different studies from the literature.

Source	Nanofiller	τ_i (MPa)	l_f (μm)	d_f (nm)
Palmeri et al. [22]	CNFs	36 (Ref [58])	6	135
Liu et al. [19]	CNFs	36 (Ref [58])	20	135
Hsieh et al. [15]	CNTs	47	120	120

energy for the nanocomposites were identified to be (a) interfacial debonding of the CNFs from the epoxy, (b) the energy associated with the pull-out of CNFs from the epoxy, (c) void growth of the epoxy which initiates from the hole created by the debonded CNFs, and (d) the rupturing of CNFs. The alignment of CNFs perpendicular to the crack path generally led to a higher fraction of CNFs participating in the above toughening mechanisms, and thus accounted for the relatively higher values of G_{Ic} typically measured for these nanocomposites, compared to those containing randomly-oriented CNFs.

Acknowledgements

The authors kindly acknowledge Mr Geoffrey Thomas (RMIT) for providing access to the HP impedance analyzer and the technical assistance of Mr Peter Tkatchyk (RMIT) as well as the RMIT Microscopy and Microanalysis Facility (RMMF) team. The authors are thankful for the financial support received from the Australian Research Council's Discovery Grant Program (DP140100778).

References

[1] A.J. Kinloch, Adhesives in engineering, in: Proceedings of the Institution of Mechanical Engineers, 1997, pp. 307–336, http://dx.doi.org/10.1243/0954410971532703. Part G.
[2] J.K. Kim, Y.W. Mai, High strength, high fracture toughness fibre composites with interface control-a review, Compos. Sci. Technol. 41 (1991) 333–378.
[3] C. Bucknall, I. Partridge, Phase separation in epoxy resins containing polyethersulphone, Polymer 24 (1983) 639–644, http://dx.doi.org/10.1016/0032-3861(83)90120-9.
[4] D.J. Hourston, J.M. Lane, The toughening of epoxy resins with thermoplastics: 1. Trifunctional epoxy resin-polyetherimide blends, Polymer 33 (1992) 1379–1383.
[5] W.D. Bascom, R.L. Cottington, R.L. Jones, P. Peyser, The fracture of epoxy and elastomer modified epoxy polymers in bulk and as adhesives, J. Appl. Polym. Sci. 19 (1975) 2545–2562.
[6] A.J. Kinloch, S.J. Shaw, D.A. Tod, D.L. Hunston, Deformation and fracture behaviour of a rubber-toughened epoxy: 1. Microstructure and fracture studies, Polymer 24 (1983) 1341–1354, http://dx.doi.org/10.1016/0032-3861(83)90070-8.
[7] W. Bauhofer, J.Z. Kovacs, A review and analysis of electrical percolation in carbon nanotube polymer composites, Compos. Sci. Technol. 69 (2009) 1486–1498, http://dx.doi.org/10.1016/j.compscitech.2008.06.018.
[8] E.T. Thostenson, Z. Ren, T.-W. Chou, Advances in the science and technology of carbon nanotubes and their composites: a review, Compos. Sci. Technol. 61 (2001) 1899–1912, http://dx.doi.org/10.1016/S0266-3538(01)00094-X.
[9] M. Rahmat, P. Hubert, Carbon nanotube–polymer interactions in nanocomposites: a review, Compos. Sci. Technol. 72 (2011) 72–84, http://dx.doi.org/10.1016/j.compscitech.2011.10.002.
[10] M.H. Al-Saleh, U. Sundararaj, Review of the mechanical properties of carbon nanofiber/polymer composites, Compos. Part A Appl. Sci. Manuf. 42 (2011) 2126–2142, http://dx.doi.org/10.1016/j.compositesa.2011.08.005.
[11] G.G. Tibbetts, M.L. Lake, K.L. Strong, B.P. Rice, A review of the fabrication and properties of vapor-grown carbon nanofiber/polymer composites, Compos. Sci. Technol. 67 (2007) 1709–1718, http://dx.doi.org/10.1016/j.compscitech.2006.06.015.
[12] S. Shadlou, E. Alishahi, M.R. Ayatollahi, Fracture behavior of epoxy nanocomposites reinforced with different carbon nano-reinforcements, Compos.

Struct. 95 (2013) 577–581, http://dx.doi.org/10.1016/j.compstruct.2012.08.002.
[13] M.A. Rafiee, J. Rafiee, I. Srivastava, Z. Wang, H. Song, Z.-Z. Yu, et al., Fracture and fatigue in graphene nanocomposites, Small 6 (2010) 179–183, http://dx.doi.org/10.1002/smll.200901480 (Weinheim an Der Bergstrasse, Germany).
[14] S. Chatterjee, F. Nafezarefi, N.H. Tai, L. Schlagenhauf, F.A. Nüesch, B.T.T. Chu, Size and synergy effects of nanofiller hybrids including graphene nanoplatelets and carbon nanotubes in mechanical properties of epoxy composites, Carbon 50 (2012) 5380–5386, http://dx.doi.org/10.1016/j.carbon.2012.07.021.
[15] T.H. Hsieh, A.J. Kinloch, A.C. Taylor, I.A. Kinloch, The effect of carbon nanotubes on the fracture toughness and fatigue performance of a thermosetting epoxy polymer, J. Mater. Sci. 46 (2011) 7525–7535, http://dx.doi.org/10.1007/s10853-011-5724-0.
[16] S.U. Khan, J.R. Pothnis, J.-K. Kim, Effects of carbon nanotube alignment on electrical and mechanical properties of epoxy nanocomposites, Compos. Part A Appl. Sci. Manuf. 49 (2013) 26–34, http://dx.doi.org/10.1016/j.compositesa.2013.01.015.
[17] B. Fiedler, F.H. Gojny, M.H.G. Wichmann, M.C.M. Nolte, K. Schulte, Fundamental aspects of nano-reinforced composites, Compos. Sci. Technol. 66 (2006) 3115–3125, http://dx.doi.org/10.1016/j.compscitech.2005.01.014.
[18] F. Gojny, M. Wichmann, B. Fiedler, K. Schulte, Influence of different carbon nanotubes on the mechanical properties of epoxy matrix composites – A comparative study, Compos. Sci. Technol. 65 (2005) 2300–2313, http://dx.doi.org/10.1016/j.compscitech.2005.04.021.
[19] W. Liu, J. Kong, W.E. Toh, R. Zhou, G. Ding, S. Huang, et al., Toughening of epoxies by covalently anchoring triazole-functionalized stacked-cup carbon nanofibers, Compos. Sci. Technol. 85 (2013) 1–9, http://dx.doi.org/10.1016/j.compscitech.2013.05.009.
[20] H. Miyagawa, L.T. Drzal, Effect of oxygen plasma treatment on mechanical properties of vapor grown carbon fiber nanocomposites, Compos. Part A Appl. Sci. Manuf. 36 (2005) 1440–1448, http://dx.doi.org/10.1016/j.compositesa.2005.01.027.
[21] L. Tang, H. Zhang, J. Han, X. Wu, Z. Zhang, Fracture mechanisms of epoxy filled with ozone functionalized multi-wall carbon nanotubes, Compos. Sci. Technol. 72 (2011) 7–13, http://dx.doi.org/10.1016/j.compscitech.2011.07.016.
[22] M.J. Palmeri, K.W. Putz, L.C. Brinson, Sacrificial bonds in stacked-cup carbon nanofibers: biomimetic toughening mechanisms for composite systems, ACS Nano 4 (2010) 4256–4264, http://dx.doi.org/10.1021/nn100661a.
[23] T.H. Hsieh, A.J. Kinloch, K. Masania, A.C. Taylor, S. Sprenger, The mechanisms and mechanics of the toughening of epoxy polymers modified with silica nanoparticles, Polymer 51 (2010) 6284–6294, http://dx.doi.org/10.1016/j.polymer.2010.10.048.
[24] T.H. Hsieh, A.J. Kinloch, K. Masania, J. Sohn Lee, A.C. Taylor, S. Sprenger, The toughness of epoxy polymers and fibre composites modified with rubber microparticles and silica nanoparticles, J. Mater. Sci. 45 (2009) 1193–1210, http://dx.doi.org/10.1007/s10853-009-4064-9.
[25] P.-C. Ma, N.A. Siddiqui, G. Marom, J.-K. Kim, Dispersion and functionalization of carbon nanotubes for polymer-based nanocomposites: A review, Compos. Part A Appl. Sci. Manuf. 41 (2010) 1345–1367, http://dx.doi.org/10.1016/j.compositesa.2010.07.003.
[26] G. Odegard, Constitutive modeling of nanotube–reinforced polymer composites, Compos. Sci. Technol. 63 (2003) 1671–1687, http://dx.doi.org/10.1016/S0266-3538(03)00063-0.
[27] V. Mirjalili, P. Hubert, Modelling of the carbon nanotube bridging effect on the toughening of polymers and experimental verification, Compos. Sci. Technol. 70 (2010) 1537–1543, http://dx.doi.org/10.1016/j.compscitech.2010.05.016.
[28] M. Monti, M. Natali, L. Torre, J.M. Kenny, The alignment of single walled carbon nanotubes in an epoxy resin by applying a DC electric field, Carbon 50 (2012) 2453–2464, http://dx.doi.org/10.1016/j.carbon.2012.01.067.
[29] A.I. Oliva-Avilés, F. Avilés, V. Sosa, A.I. Oliva, F. Gamboa, Dynamics of carbon nanotube alignment by electric fields, Nanotechnology 23 (2012) 465710, http://dx.doi.org/10.1088/0957-4484/23/46/465710.
[30] D. Shi, P. He, J. Lian, X. Chaud, S.L. Bud'ko, E. Beaugnon, et al., Magnetic alignment of carbon nanofibers in polymer composites and anisotropy of mechanical properties, J. Appl. Phys. 97 (2005) 064312, http://dx.doi.org/10.1063/1.1861143.
[31] X. Xie, Y. Mai, X. Zhou, Dispersion and alignment of carbon nanotubes in polymer matrix: a review, Mater. Sci. Eng. R Rep 49 (2005) 89–112, http://dx.doi.org/10.1016/j.mser.2005.04.002.
[32] S. Wu, R.B. Ladani, J. Zhang, A.J. Kinloch, Z. Zhao, J. Ma, et al., Epoxy nanocomposites containing magnetite-carbon nanofibers aligned using a weak magnetic field, Polymer (2015), http://dx.doi.org/10.1016/j.polymer.2015.04.080.
[33] T. Prasse, J.-Y. Cavaille, W. Bauhofer, Electric anisotropy of carbon nanofibre/epoxy resin composites due to electric field induced alignment, Compos. Sci. Technol. 63 (2003) 1835–1841, http://dx.doi.org/10.1016/S0266-3538(03)00019-8.
[34] M.H. Al-Saleh, U. Sundararaj, A review of vapor grown carbon nanofiber/polymer conductive composites, Carbon 47 (2009) 2–22, http://dx.doi.org/10.1016/j.carbon.2008.09.039.
[35] SIGMA-ALDRICH, Properties and Application of Carbon Nanofibers (CNFs) Synthesized Using Vapor Grown Carbon Fiber (VGCF) Manufacturing Technology, 2015. http://www.sigmaaldrich.com/china-mainland/zh/materials-science/nanomaterials/carbon-nanofibers.html (accessed 08.05.15).
[36] ISO. 25217:2009, Determination of the Mode I Adhesive Fracture Energy of Structural Adhesive Joints Using Double Cantilever Beam and Tapered Double Cantilever Beam Specimens, 2009. Geneva.
[37] H.D. Wagner, A. Lustiger, Optimized toughness of short fiber-based composites: the effect of fiber diameter, Compos. Sci. Technol. 69 (2009) 1323–1325, http://dx.doi.org/10.1016/j.compscitech.2009.03.008.
[38] T.B. Jones, Electromechanics of Particles, Cambridge University Press, New York, 1995, http://dx.doi.org/10.1017/CBO9780511574498.
[39] L. Benedict, S. Louie, M. Cohen, Static polarizabilities of single-wall carbon nanotubes, Phys. Rev. B 52 (1995) 8541–8549, http://dx.doi.org/10.1103/PhysRevB.52.8541.
[40] B. Kozinsky, N. Marzari, Static dielectric properties of carbon nanotubes from first principles, Phys. Rev. Lett. 96 (2006) 166801, http://dx.doi.org/10.1103/PhysRevLett.96.166801.
[41] M.P. Hughes, AC electrokinetics: applications for nanotechnology, Nanotechnology 11 (2000) 124–132, http://dx.doi.org/10.1088/0957-4484/11/2/314.
[42] A.K. Jonscher, A new understanding of the dielectric relaxation of solids, J. Mater. Sci. 16 (1981) 2037–2060, http://dx.doi.org/10.1007/BF00542364.
[43] A.K. Jonscher, The "universal" dielectric response, Nature 267 (1977) 673–679.
[44] B.M. Tyson, R.K. Abu Al-Rub, A. Yazdanbakhsh, Z. Grasley, A quantitative method for analyzing the dispersion and agglomeration of nano-particles in composite materials, Compos. Part B Eng. 42 (2011) 1395–1403, http://dx.doi.org/10.1016/j.compositesb.2011.05.020.
[45] J. Vera-Agullo, H. Varela-Rizo, J.A. Conesa, C. Almansa, C. Merino, I. Martin-Gullon, Evidence for growth mechanism and helix-spiral cone structure of stacked-cup carbon nanofibers, Carbon 45 (2007) 2751–2758, http://dx.doi.org/10.1016/j.carbon.2007.09.040.
[46] J. Blanco, E.J. Garcia, R. Guzman de Villoria, B.L. Wardle, Limiting mechanisms of mode I interlaminar toughening of composites reinforced with aligned carbon nanotubes, J. Compos. Mater. 43 (2009) 825–841, http://dx.doi.org/10.1177/0021998309102398.
[47] J.G. Williams, Particle toughening of polymers by plastic void growth, Compos. Sci. Technol. 70 (2010) 885–891, http://dx.doi.org/10.1016/j.compscitech.2009.12.024.
[48] V.C. Li, Y. Wang, S. Backer, A micromechanical model of tension-softening and bridging toughening of short random fiber reinforced brittle matrix composites, J. Mech. Phys. Solids 39 (1991) 607–625, http://dx.doi.org/10.1016/0022-5096(91)90043-N.
[49] H.D. Wagner, P.M. Ajayan, K. Schulte, Nanocomposite toughness from a pull-out mechanism, Compos. Sci. Technol. 83 (2013) 27–31, http://dx.doi.org/10.1016/j.compscitech.2013.04.017.
[50] D. Hull, An Introduction to Composite Materials. Cambridge Solid State Science Series, second ed., Cambridge University Press, Cambridge, 1996.
[51] S.-Y. Fu, Z.-K. Chen, S. Hong, C.C. Han, The reduction of carbon nanotube (CNT) length during the manufacture of CNT/polymer composites and a method to simultaneously determine the resulting CNT and interfacial strengths, Carbon 47 (2009) 3192–3200, http://dx.doi.org/10.1016/j.carbon.2009.07.028.
[52] A. Kelly, W.R. Tyson, Tensile properties of fibre-reinforced metals: copper/tungsten and copper/molybdenum, J. Mech. Phys. Solids 13 (1965) 329–350, http://dx.doi.org/10.1016/0022-5096(65)90035-9.
[53] T. Ozkan, Q. Chen, I. Chasiotis, Interfacial strength and fracture energy of individual carbon nanofibers in epoxy matrix as a function of surface conditions, Compos. Sci. Technol. 72 (2012) 965–975, http://dx.doi.org/10.1016/j.compscitech.2012.03.004.
[54] M.P. Manoharan, A. Sharma, A. Desai, M.A. Haque, C.E. Bakis, K.W. Wang, The interfacial strength of carbon nanofiber epoxy composite using single fiber pullout experiments, Nanotechnology 20 (2009) 295701–295706, http://dx.doi.org/10.1088/0957-4484/20/29/295701.
[55] Y. Huang, A.J. Kinloch, Modelling of the toughening mechanisms in rubber-modified epoxy polymers, J. Mater. Sci. 27 (1992) 2763–2769, http://dx.doi.org/10.1007/BF00540703.
[56] T. Ozkan, M. Naraghi, I. Chasiotis, Mechanical properties of vapor grown carbon nanofibers, Carbon 48 (2010) 239–244, http://dx.doi.org/10.1016/j.carbon.2009.09.011.
[57] WESTSYSTEM, 105 Resin Engineering Data, 2015. http://www.westsystem.com.au/files/products.resin_and_hardeners/west_system_r105_eng_data.pdf (accessed 18.02.15).
[58] HUNTSMAN, Araldite MY 721 Data Sheet, 2010. https://apps.huntsmanservice.com/WebFolder/ui/browse.do?pFileName=/opt/TDS/HuntsmanAdvanced Materials/English US/Long/Araldite MY721_US_e.pdf (accessed 10.05.15).

A. II. Journal Article: Aligning Multilayer Graphene Flakes with an External Electric Field to Improve Multifunctional Properties of Epoxy Nanocomposites

CARBON 94 (2015) 607–618

Contents lists available at ScienceDirect

CARBON

journal homepage: www.elsevier.com/locate/carbon

Aligning multilayer graphene flakes with an external electric field to improve multifunctional properties of epoxy nanocomposites

Shuying Wu [a], Raj B. Ladani [a], Jin Zhang [b], Ehsan Bafekrpour [c], Kamran Ghorbani [d], Adrian P. Mouritz [a], Anthony J. Kinloch [e], Chun H. Wang [a,*]

[a] Sir Lawrence Wackett Aerospace Research Centre, School of Aerospace, Mechanical & Manufacturing Engineering, RMIT University, GPO Box 2476, Melbourne, VIC 3001, Australia
[b] Australian Future Fibres Research and Innovation Centre, Institute for Frontier Materials, Deakin University, VIC 3220, Australia
[c] School of Fashion and Textiles, RMIT University, 25 Dawson Street, Brunswick, Melbourne 3056, Australia
[d] School of Electrical and Computer Engineering, RMIT University, GPO Box 2476, Melbourne 3001, Australia
[e] Department of Mechanical Engineering, Imperial College London, London SW7 2BX, UK

ARTICLE INFO

Article history:
Received 27 March 2015
Received in revised form 29 June 2015
Accepted 6 July 2015
Available online 7 July 2015

ABSTRACT

The increasing demand for multifunctional polymer nanocomposites calls for new technologies to simultaneously enhance mechanical, electrical, and thermal properties. This paper presents the use of an alternating-current electric field to align graphene nanoplatelets (GnPs) in an epoxy polymer. Theoretical modeling of the alignment process has identified the key parameters that control the rotation and chain-formation of the GnPs. Experimental results reveal that the resulting nanocomposites exhibit anisotropic properties with significantly improved electrical and thermal conductivities in the alignment direction, and dramatically increased fracture toughness when the GnPs are aligned transverse to the crack growth direction. In particular, compared to the unmodified epoxy polymer, the alignment of the GnPs yields up to about 7–8 orders of magnitude improvement in the electrical conductivity, up to approximately 60% increase in the thermal conductivity, and up to a nearly 900% increase in the mode I fracture toughness. The dramatic improvement in the fracture toughness is attributed to multiple intrinsic and extrinsic toughening mechanisms including microcracking, pinning, deflection and branching of the crack, and rupture and pull-out of the GnPs. Such major improvement in the toughness arises from GnPs being transversely aligned to the crack growth direction exhibiting increased interactions with the advancing crack tip.

1. Introduction

Improving the structural and functional properties of polymers and polymeric composites has been recognised as a key to dramatically increase their wide applications. Graphene shows great promise as a nanofiller in polymer composites due to its high physical aspect ratio, high strength and Young's modulus, and excellent thermal and electrical conductivities [1]. Substantial property improvements can be achieved using various graphene-based materials, such as graphene oxide (GO) [2,3], thermally expanded or reduced graphene [4,5], graphene foam [6], non-covalently functionalized graphene flakes [7] etc., even when such materials are used at low concentrations in the polymer. For instance, Stankovich et al. showed that by using graphene at a volume content as low as ~0.1 vol% an electrical percolation threshold could be reached within polystyrene [2]. Rafiee et al. showed that thermally exfoliated graphite oxide provided 53% additional increase in the mode I fracture toughness of an epoxy nanocomposite compared to single- or multi-walled carbon nanotubes [3]. Song et al. recently developed epoxy/graphene nanocomposites with remarkably enhanced thermal conductivities (e.g. 1.53 W/mK) using 10 wt% of 1-pyrenebutyric acid functionalized graphene flakes [7].

However, the property improvements achieved so far using such carbon nanofillers are still much lower than the theoretical predictions because a variety of factors have not yet been optimised. Such factors include the degree of dispersion and exfoliation, and critically, the orientation of the nanoplatelets [8]. Different approaches have been reported for orienting carbon nanofillers, based mainly on employing mechanical stretching [9], an electric field [10–15], and a magnetic field [16–18]. The use of an electric field has been reported to align carbon nanotubes [10,11], carbon nanofibers [12,13], and carbon black [14] to improve the electrical conductivity and mechanical properties of polymer nanocomposites. Recently, Kim et al. developed epoxy

* Corresponding author.
E-mail address: chun.wang@rmit.edu.au (C.H. Wang).

http://dx.doi.org/10.1016/j.carbon.2015.07.026
0008-6223/

nanocomposites with graphite aligned along the alternating-current (AC) electric field direction and found that these materials had anisotropic tensile modulus and strength [19,20]. Chen et al. prepared polyester resin nanocomposites with graphite nanosheets oriented along the applied AC electric field, and found that the electrical conductivity was greatly increased in the alignment direction [21–23]. In spite of these studies, very limited research has been reported on the mechanisms of aligning graphene nanoplatelets (GnPs) in polymers under an external electric field and its efficiency in improving the fracture toughness, as well as the electrical and thermal properties of the resultant nanocomposites.

Epoxy thermosets represent an important class of polymers due to their versatility and are widely used as coatings, electric encapsulates, fiber-optic sheathing, adhesives and matrices for fiber-reinforced composites, etc. However, their high degree of crosslinking makes them intrinsically brittle and prone to damage, thus holding back their increased application in aerospace, automotive and advanced electric applications [24]. Moreover, their extremely low thermal and electrical conductivities greatly limit their applications that demand good dissipation of heat and static electricity [6,7]. Furthermore, the low through-thickness electrical conductivity of fiber-reinforced epoxy composites, which is dominated by the polymeric matrix phase, makes such composite structures vulnerable to lightning strikes and unable to prevent electrostatic accumulation [25]. The low electrical conductivity also hinders the diagnosis of damage by electrical-based techniques, such as the eddy-current technique. Therefore, improving the electrical conductivity, thermal conductivity and fracture toughness of epoxy polymers is of major practical importance.

The present paper describes a technique to align GnPs in an epoxy by applying an AC electric field and focuses on experimental and theoretical investigations of the effects of alignment on the electrical and thermal conductivities, and fracture toughness of the epoxy nanocomposites. To the best of our knowledge, there is no report on (a) the mechanisms controlling the alignment of GnPs in an epoxy by an AC electric field and (b) the effects of alignment on the electrical and thermal conductivity, and fracture toughness of the resulting epoxy nanocomposites. The nanoplatelets used have a carbon-to-oxygen atomic ratio of 93-to-7 and an average platelet size and thickness of about 25 μm and 8 nm, respectively. Firstly, the electromechanical mechanisms controlling the rotation and chain formation of GnPs are investigated. Then, the improvements arising from the GnPs (both aligned and randomly-oriented) of different volume contents in the properties of the epoxy polymer are measured and compared. Finally, the mechanisms by which the GnPs improve these properties are investigated.

2. Experimental

2.1. Materials

The GnPs used in the present study were obtained from XG Science, having an average thickness of approximately 6–8 nm and an average particle diameter of 25 μm. The C:O ratio was determined to be 93:7 by using X-ray photoelectron spectroscopy (XPS) performed employing a Thermo K-alpha XPS instrument. The liquid epoxy resin ('105') and hardener ('206') were supplied by WEST SYSTEM®. The liquid epoxy resin used was a blend of bisphenol A and bisphenol F. The liquid hardener employed was a blend of aliphatic and aliphatic amine adducts based upon diethylenetriamine and triethylenetetramine. The carbon-fibre epoxy composite substrates were manufactured from T700 carbon-fibre/epoxy prepreg ('VTM 264') supplied by Applied Composites Group. Twelve plies of this unidirectional prepreg, with dimensions of 300 mm × 250 mm × 2.65 mm, were used to fabricate the substrates by curing in an autoclave at 120 °C and an overpressure of 98 kPa for 1 h.

2.2. Bulk epoxy nanocomposites fabrication

Epoxy nanocomposites with contents of 0.27, 0.54, 0.81, and 1.08 vol% of GnPs were fabricated by combining sonication and calendaring processes. The GnPs was first mixed with the liquid epoxy resin using a Hielscher UP200S ultrasonic homogenizer (operated at 0.5 cycles and 50% amplitude) for 30 min, which broke-up the graphene agglomerates. The mixture was then further processed by a three-roll mill (Dermamill 100) ten times at 150 rpm with a roller-gap distance of 20 μm. After this dispersion process, a stoichiometric amount of hardener was added. This mixture was then degassed and poured into a custom-made silicon rubber mold. The GnPs were aligned by using an AC electric field (25 V/mm, 10 kHz) supplied by an AC signal generator (Tektronix CFG250) in combination with a wideband amplifier (Krohnhite 7602 M). Two aluminum plates were used as the electrodes and a spacer was placed between them to prepare samples of required dimensions for the various tests. Fig. S1a in Supporting information illustrates the experimental apparatus for aligning the GnPs in the epoxy resin/GnPs/hardener mixture during curing.

2.3. Double-cantilever beam (DCB) specimen fabrication

The surfaces of the carbon-fibre epoxy composite substrates used for the DCB samples were grit-blasted and thoroughly degreased with acetone to promote strong bonding with the unmodified epoxy and the epoxy nanocomposites. A dam made of silicon rubber was placed between the two substrates to prevent the liquid epoxy resin mixtures from flowing out. Spacers (2 mm thick) made of two glass slides were placed between the substrates to control the bond-line thickness. A sharp pre-crack at the mid-plane of the epoxy layer was created using a 'Teflon' film (50 μm thick) placed between the two glass slides. The epoxy/GnPs/hardener mixtures were prepared following the procedure described above and then poured between the substrates. To align the GnPs in the through-thickness direction of the epoxy layer (i.e. transverse to the subsequent direction of crack growth), the carbon fibre-epoxy composite substrates (which are electrically conductive) were used as the electrodes. An AC electric field of 25 V/mm at 10 kHz was applied between the substrates during the initial one hour of curing at room temperature. The epoxy layer was further cured at room temperature (25 °C) for 48 h.

To prepare DCB specimens with the GnPs aligned parallel to the subsequent crack growth direction, bulk epoxy/GnPs nanocomposites (2 mm thick) were prepared following the procedures given in Section 2.2, but with the AC electric field applied across the width of the nanocomposite. These nanocomposites were then adhesively-bonded to the carbon-fibre epoxy composite substrates using an aerospace adhesive (Huntsman Araldite® 420 A/B). During the DCB fracture tests, the crack propagated in the epoxy nanocomposite layer, parallel to the alignment direction of the GnPs.

2.4. Investigation on the alignment of the GnPs

A Leica optical microscope was used to observe the response of the GnPs in the liquid epoxy resin to the AC electric field. A liquid epoxy resin/GnPs mixture, containing 0.054 vol% of GnPs, was placed on to a glass slide. Two parallel aluminum tapes were used as the electrodes to apply the AC electric field. The time-lapse images were acquired using a Leica DC 300 digital camera.

Furthermore, the orientation of the GnPs in the (cured) epoxy nanocomposites was investigated using a JEOL JEM 1010 transmission electron microscope (TEM) operated at 100 kV. TEM samples were prepared by cutting the epoxy nanocomposites into ultrathin sections of ~70 nm thick with a diamond knife using a Leica EM ultramicrotome. Scanning electron microscopy (SEM) analysis was performed using a FEI Nova NanoSEM operated at 15 kV and 5 mm working distance. For the SEM studies, the specimens were cryogenically fractured in liquid nitrogen and then surface-coated with a thin layer of gold prior to observation.

2.5. Characterization

The electrical conductivity was measured through-the-thickness of the unmodified epoxy polymer according to ASTM D257. For the epoxy nanocomposites containing aligned GnPs, measurements were made both parallel and transverse to the direction of alignment of the GnPs. Five measurements were taken of each material to obtain the average value and the variability. The thermal conductivity was measured using the C-Therm Thermal Conductivity Analyser employing the modified transient plane-source (MTPS) technique. Rectangular samples were placed on the thermal sensors and completely covered the measuring area. 'Type 120' thermal joint compound was applied between the sample and the sensor to improve the heat flow. The temperature was controlled in a TPS Tenney Junior thermal chamber. The measurements at room temperature (25 °C) were performed both parallel and transverse to the alignment direction of the GnPs. Ten measurements of each sample material were performed to determine the average and variability of the thermal conductivity.

DCB tests were performed using an Instron tensile testing machine to determine the mode I fracture energy (G_{Ic}) of the adhesive joints. The DCB joints had the dimensions illustrated in Fig. S1b in the Supporting information. A sharp crack tip was formed by carefully wedging the crack opening from the tip of the 'Teflon' film. The crack opening load was applied to the specimens at a crosshead speed of 1 mm/min in accordance with ISO 25217. The load versus displacement curves were recorded and a travelling optical microscope was used to measure the crack length (a). The value of the fracture toughness (G_{Ic}) for the onset of crack propagation was calculated using the 'corrected beam' theory [26]. At least five specimens were tested for each composition to get the average value of G_{Ic}. As described above, the values of G_{Ic} were determined using two types of specimens: one where the direction of crack growth was transverse to the aligned GnPs and one where the direction of crack growth was parallel to the aligned GnPs. Fracture surfaces from randomly selected failed DCB specimens were sectioned and sputter coated with a thin layer of gold for SEM examination. Side-views of the crack tips were also examined by SEM after polishing with a fine-grade sand-paper.

3. Results and discussion

3.1. Electric field-induced alignment of GnPs

The alignment of the GnPs within the liquid epoxy resin when exposed to an AC electric field was investigated experimentally and theoretically. In-situ optical microscopy observations were carried out on the movement of the GnPs within the liquid epoxy resin. The applied AC electric field had an amplitude of 25 V/mm and a frequency of 10 kHz. Time-lapse images for the epoxy resin containing 0.054 vol% of GnPs are presented in Fig. 1, showing the formation of a chain-like graphene network in the direction of the applied electric field. A network of aligned nanoplatelets began to visibly develop after exposure to the electric field for about four minutes. A well-defined chain-like structure of GnPs extending between the positive and negative electrodes formed after ~10 min, which then developed into relatively thick bundles upon further exposure to the electric field for ~20 min. This 'chaining' process is the result of dipole–dipole attractions between the nanoplatelets. Due to the opposite charges at their ends, they gradually move closer and connect end-to-end, forming chain-like structures. These structures were also observed for epoxy resin mixtures with higher contents of GnPs (see Fig. S2). Similar chained structures have been observed for other inclusions including ceramic ($BaTiO_3$) particles [27], carbon nanotubes [10,11], carbon nanofibers [12,13], carbon black [14], and carbon nanocones [28].

Fig. 2a and b show representative SEM and TEM images of the microstructure of the epoxy/GnPs (0.54 vol%) nanocomposite prepared without the application of the electric field. As expected, the GnPs were randomly-oriented and distributed in the epoxy polymer. Fig. 2c and d show the microstructure of the epoxy/GnPs (0.54 vol%) nanocomposite following exposure to the electric field, and most of the GnPs are aligned very close to being parallel to the applied electric field direction. Alignment of the GnPs was observed for all the different volume contents that were studied (i.e. 0.27, 0.54, 0.81 and 1.08 vol%). Voids and dispersed multi-layered GnPs are also observed in the TEM images, as indicated by the arrows in Fig. 2d. The appearance of the voids could be due to the relatively high stresses generated during the ultramicrotoming used to prepare the TEM samples [29,30]. To confirm this suggestion, selected area electron-diffraction (SAED) was employed to distinguish the GnPs from the amorphous epoxy polymer matrix, and Fig. S3 gives such an example. A well-defined diffraction spot pattern was obtained from the region close to the voids indicating the presence of crystalline GnPs.

3.2. Physical mechanisms of electric field-induced alignment of GnPs

3.2.1. Rotation

When subjected to a sinusoidal alternating electric field, a solid inclusion in a dielectric liquid is polarized and gains a dipole moment due to the different dielectric properties and electrical conductivity between the inclusion and the liquid [19]. The polarization moment, μ, is generally not aligned with the electric field for materials which are crystalline or show shape anisotropy and thus a torque $T^e = \vec{\mu} \times \vec{E}$ is induced to act on the inclusion. Two-dimensional GnPs have shape anisotropy and the polarization moment parallel to the platelet is much higher than that perpendicular to the platelet. GnPs can be considered as very thin oblate spheroids with semi-major and semi-minor axes a and b, corresponding to the radius and half thickness of a graphene nanoplatelet, respectively. The overall torque acting on an inclusion is the superposition of the torques induced by fields parallel and perpendicular to its axes:

$$T^e = \mu_{\parallel} \times E_{\perp} - \mu_{\perp} \times E_{\parallel} \tag{1}$$

where $E_{\perp} = E \cdot \sin\theta$ and $E_{\parallel} = E \cdot \cos\theta$ with θ being the angle between the electric field direction and the semi-major axis of the inclusion. The subscripts $\perp$ and $\parallel$ refer to the perpendicular and parallel to the surface of nanoplatelets, respectively.

When an inclusion is subjected to a sinusoidal alternating electric field ($E = E_0 \cdot \sin\omega t$), the torque acting on it is given by [31]:

$$T^e = \frac{2\pi a^2 b}{3} E_0^2 \sin^2\omega t \sin 2\theta \frac{\varepsilon_m(\varepsilon_i - \varepsilon_m)^2}{\left[\varepsilon_m + (\varepsilon_i - \varepsilon_m)L_{\parallel}\right]\varepsilon_i} \tag{2}$$

where $L_{\parallel}$ is the depolarization factor along the major axis, and $L_{\parallel} = \frac{b}{2a}\left(\frac{\pi}{2} - \frac{b}{a}\right)$ for an oblate-shaped inclusion. The subscripts i and m refer to the inclusion (i.e. the GnPs) and matrix, respectively. The term ε is the generalized dielectric constant. $\varepsilon_i = \varepsilon_i' + j(\varepsilon_i'' + \sigma_i/\omega)$, with ε_i', ε_i'', and σ denoting the real part and imaginary part of relative dielectric constant and the electrical

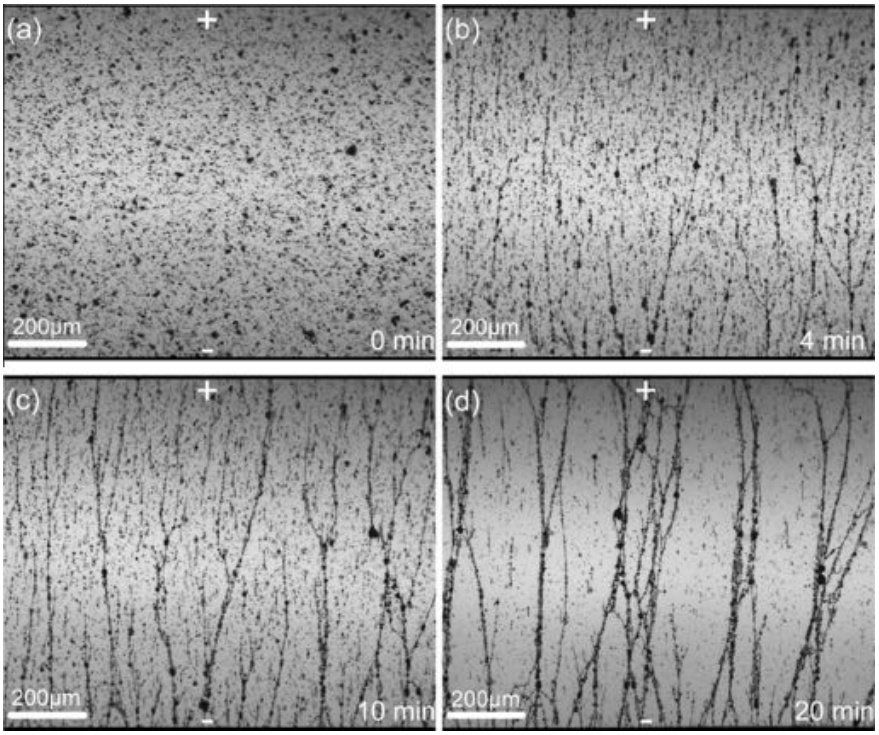

Fig. 1. Optical micrographs of GnPs in the liquid epoxy resin (0.054 vol%) during the application of the AC electric field (25 V/mm): (a) Randomly-oriented GnPs before the field was applied; (b), (c), and (d) after the field was applied for 4 min, 10 min, and 20 min, respectively. (The positive and negative electrodes are indicated by " + " and "−".)

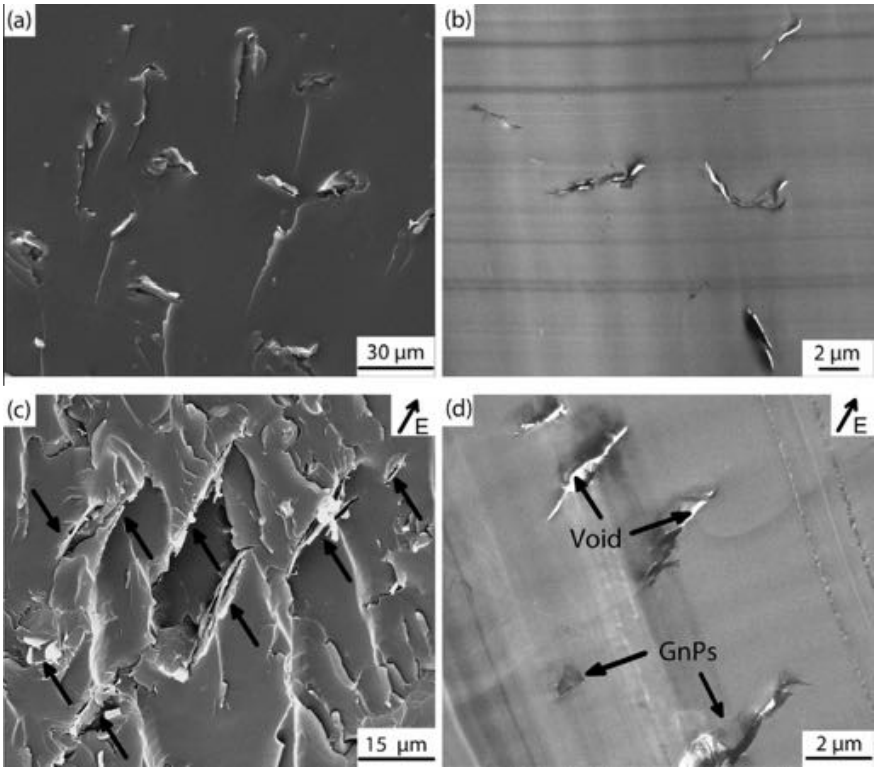

Fig. 2. SEM (a) and TEM (b) images of the epoxy nanocomposites with 0.54 vol% of randomly-oriented GnPs; SEM (c) and TEM (d) images of the epoxy nanocomposites with 0.54 vol% of aligned GnPs. The direction of the electric field (E) alignment is indicated in (c) and (d).

conductivity of the inclusions, respectively. The variables ω and E_0 denote the angular frequency and amplitude of the applied electric field, respectively.

For a GnP of relatively high electrical conductivity exposed to an AC electric field of a low to moderate frequency ($\omega \ll \sigma_i$), $\varepsilon_i/\varepsilon_m \to \infty$, the torque can be simplified to:

$$T^e = \frac{4\pi a^3}{3}\frac{\varepsilon_m}{\left(\frac{\pi}{2}-\frac{b}{a}\right)}E_0^2\sin^2\omega t\sin 2\theta \tag{3}$$

The electric field-induced torque is the driving force for the rotation of the GnPs in the liquid epoxy resin, which is resisted by viscous drag from the epoxy resin. The time needed to rotate GnPs from the initial angle θ_0 to an angular position θ can be estimated by balancing the electric field-induced torque with the viscous torque acting on the GnPs. The viscous torque T^v is proportional to the angular velocity $\dot{\theta}$ and viscosity η of the epoxy resin, and can be calculated using [10,32]:

$$T^v = -\eta\dot{\theta}k_r \tag{4}$$

where k_r is the rotational friction coefficient and $k_r = 32a^3/3$ [32]. Now the dynamic condition $T^e = T^v$ yields,

$$\dot{\theta} = -\frac{\pi}{8\eta}\frac{\varepsilon_m}{\left(\frac{\pi}{2}-\frac{b}{a}\right)}E_0^2\sin^2\omega t\sin 2\theta \tag{5}$$

from which the time to rotate (t_r) a GnP from the initial angle θ_0 to a generic angular position θ' can be solved from the following transcendental equation:

$$t_r - \frac{1}{2\omega}\sin 2\omega t_r = \frac{1}{A}\ln\frac{\tan\theta_0}{\tan\theta'} \tag{6}$$

where:

$$A = \frac{\pi}{8\eta}\frac{\varepsilon_m}{\left(\frac{\pi}{2}-\frac{b}{a}\right)}E_0^2 \tag{7}$$

By setting the final angle θ' close to zero, the corresponding t_r value is the rotation time for a GnP with an initial angle of θ_0. Eq. (6) reveals that the rotation time is dependent on the frequency of the AC electric field, but this effect diminishes rapidly as the frequency increases, with the rotation time approaching the following lower bound,

$$t_{r,\infty} = \frac{1}{A}\ln\frac{\tan\theta_0}{\tan\theta'}, \quad \omega\to\infty \tag{8}$$

It should be noted that numerical solutions for Eq. (6), referring to Fig. S4d, reveal that when the angular frequency of the AC electric field exceeds $1/t_{r,\infty}$, the rotation time approaches within 95% of that given by Eq. (8), as will be discussed Section 3.2.3.

3.2.2. End-to-end connection (i.e. 'chain' formation)

Once rotated, polarized GnPs tend to attract each other due to the opposite charges present at their ends. By balancing the electric force and the translational viscous friction, it is possible to estimate the time required to form an end-to-end connection between two platelets. The electric charge (q) present at the opposite ends was evaluated by considering the torque as the product of charges at the ends of nanoplatelets and the distance of $2a$ (i.e. the diameter) such that:

$$T^e = q * E * 2a\sin\theta \tag{9}$$

This torque induced by the applied field is given in Eq. (2), based on which the total electric charge at the end of a disk-shaped nanoplatelet is estimated by:

$$q = \frac{T^e}{E2a\sin\theta} = \frac{2\pi ab}{3}E_0\sin\omega t\cos\theta\frac{\varepsilon_m(\varepsilon_i-\varepsilon_m)^2}{\left[\varepsilon_m+(\varepsilon_i-\varepsilon_m)L_{||}\right]\varepsilon_i} \tag{10}$$

Thus, the electric force attracting adjacent nanoplatelets is:

$$F_{el} = \frac{q^2}{4\pi\varepsilon_0 x^2} = \frac{\pi(ab)^2}{9\varepsilon_0 x^2}E_0^2\sin^2\omega t\cos^2\theta\left(\frac{\varepsilon_m(\varepsilon_i-\varepsilon_m)^2}{\left[\varepsilon_m+(\varepsilon_i-\varepsilon_m)L_{||}\right]\varepsilon_i}\right)^2 \tag{11}$$

When a nanoplatelet becomes parallel to the electric field, i.e. $\theta = 0$, the electric force attracting two nanoplatelets separated by x is given by:

$$F_{el} = \frac{\pi(ab)^2}{9\varepsilon_0 x^2}E_0^2\sin^2\omega t\left(\frac{\varepsilon_m(\varepsilon_i-\varepsilon_m)^2}{\left[\varepsilon_m+(\varepsilon_i-\varepsilon_m)L_{||}\right]\varepsilon_i}\right)^2 \tag{12}$$

Coupling this electric force with the translational viscous friction, the equation representing the translational motion is:

$$\frac{\pi(ab)^2}{9\varepsilon_0 x^2}E_0^2\sin^2\omega t\left(\frac{\varepsilon_m(\varepsilon_i-\varepsilon_m)^2}{\left[\varepsilon_m+(\varepsilon_i-\varepsilon_m)L_{||}\right]\varepsilon_i}\right)^2 = -\eta k_t x \tag{13}$$

where k_t is the translational friction coefficient for an oblate spheroid particle [33,34], and is:

$$k_t = 6\pi(a^2b)^{1/3}\frac{\sqrt{|(b/a)^2-1|}}{\tan^{-1}\left(\frac{\sqrt{|(b/a)^2-1|}}{(b/a)}\right)} \tag{14}$$

The governing equation for the translation motion can be rewritten as:

$$\dot{x} = -\frac{B\sin^2\omega t}{x^2} \tag{15}$$

where:

$$B = \frac{4\pi a^4}{9\eta k_t\varepsilon_0}\frac{E_0^2\varepsilon_m^2}{\left(\frac{\pi}{2}-\frac{b}{a}\right)^2} \tag{16}$$

Solving the differential Eq. (15) yields the following solution:

$$x(t) = \sqrt[3]{-3B\left(\frac{t}{2}-\frac{\sin 2\omega t}{4\omega}\right)+x_0^3} \tag{17}$$

Similar to the solution of the rotation time described in Section 3.2.1, the lower-bound solution pertinent to the high frequency limit is:

$$x(t) = \sqrt[3]{-\frac{3}{2}Bt+x_0^3} \tag{18}$$

where x_0 is the initial distance from two opposite charged ends of graphene. The time required for the formation of an end-to-end connection (t_c) is:

$$t_c(x_0) = \frac{2x_0^3}{3B} \tag{19}$$

The influence of frequency diminishes when the frequency exceeds $1/t_c$. The initial distance (x_0) between the closest opposite charged ends of graphene can be evaluated by using similar method as that applied by Monti et al. for carbon nanotubes [10]. This distance depends on the content of the GnPs in the epoxy resin. Assuming the graphene is uniformly dispersed in the whole volume of the epoxy, the portion of this volume for each GnP (V_G) can be evaluated by:

$$V_G = \frac{1}{\rho}\frac{W_G}{m_G} \tag{20}$$

where ρ is the density of the epoxy, W_G is the weight fraction of graphene, and m_G is the mass of each GnP. The volume containing one GnP can be modeled as a square cuboid, with its two edges being equal to the average diameter ($2a$) of GnPs, and its third edge being the average initial distance x_0. In this case, the average initial distance can be obtained from the volume given by Eq. (20):

$$x_0 = \frac{V_G}{4a^2} = \frac{1}{\rho}\frac{W_G}{m_G}\frac{1}{4a^2} \tag{21}$$

3.2.3. Model results

Using the above analysis, it is possible to calculate the time required to rotate the GnPs and to form an end-to-end connection in the liquid epoxy resin in the direction of the electric field. In the calculation of the rotation time, the final angle was set at a value slightly greater than 0° (i.e. 1.0°), otherwise the calculated alignment time approaches an infinite value. The GnPs have an approximate thickness (b) of 8 nm and diameter (a) of 25 μm. The values of the viscosity and relative dielectric constant of the liquid epoxy resin were taken for the calculations to be $\eta = 0.725$ Pa·s and $\varepsilon_m = 3.6\varepsilon_0$, with ε_0 being the vacuum permittivity. Fig. 3d shows the calculated time required for the electric field to align the nanoplatelet from various initial angles (θ_0) to the final angle of $\theta' = 1.0°$. The calculated curve shows a similar trend to that recently reported by Monti et al. [10] for direct current field-induced alignment of carbon nanotubes. Fig. 3d shows that with the applied electric field strength of 25 V/mm, amplitude of 10 kHz, it takes up to ~15 min to closely align the majority of nanoplatelets upon applying the electric field.

In the calculation of the time required to form an end-to-end connection between two GnPs, the mass of a single GnP (2.65×10^{-14} kg) was estimated by calculating how many carbon atoms were present in the single sheet having the dimension of 25 μm × 25 μm and then multiplying this by the number of layers of sheets per nanoplatelet [10]. The GnPs are on average 8 nm thick which equates to about 18 single sheets of graphene based on the d-spacing (taken as 0.34 nm). For a liquid epoxy resin containing 0.1 wt% (0.054 vol%) of GnPs, the average initial separation distance x_0 between two platelets is ~36 μm. Fig. 3e shows the plot of Eq. (18). It can be seen that the time needed for a GnP to move a distance of 36 μm was about four minutes which is consistent with the optical microscopy observations shown in Fig. 1.

A thorough analysis of Eqs. (6) and (18) reveals the effects of different variables on the alignment of GnPs in a polymer. Firstly, as expected, it takes a shorter time to rotate GnPs and to translate a distance (x_0) to form end-to-end connection if the viscosity of the epoxy/GnPs mixture is lower and/or a stronger electric field is applied (see the plots in Figs. S4 and S5). The role of the aspect ratio (a/b) of the filler is presented in Figs. S4c and S5c. The contribution of this parameter seems to be negligible, i.e. the orientation time and end-to-end connection time does not change significantly as the aspect ratio of the GnPs is varied. Therefore, for GnPs of a given size (a), the thickness (i.e. the exfoliation state) does not significantly affect the alignment process. The influence of frequency of the electric field on the rotation time is presented in Fig. S4d. According to the model, the frequency will not have any noticeable effects provided that the frequency is moderately high (greater than 10 Hz in the present case), which is consistent with the experimental observations shown in Fig. 4. The DC conductivity was measured to monitor the degree of alignment during the alignment process every 60 s after the application of the electric field. As shown in Fig. 4, the electrical conductivity increases due to the formation of the GnP networks and reaches a plateau after around 600 s, irrespective of the frequency of the external electric field. Similar findings have been reported for epoxy/carbon black composites, i.e. the time-dependent evolution of the conductivities and final conductivity are nearly independent of frequency up to 10 kHz [14].

These experimental studies and theoretical modeling on the formation of aligned graphene platelets in both the liquid epoxy resin and the epoxy nanocomposites have indeed confirmed that a high degree of alignment of the GnPs may be achieved by using the process conditions described above. The electrical and thermal conductivities, and fracture toughness of the epoxy

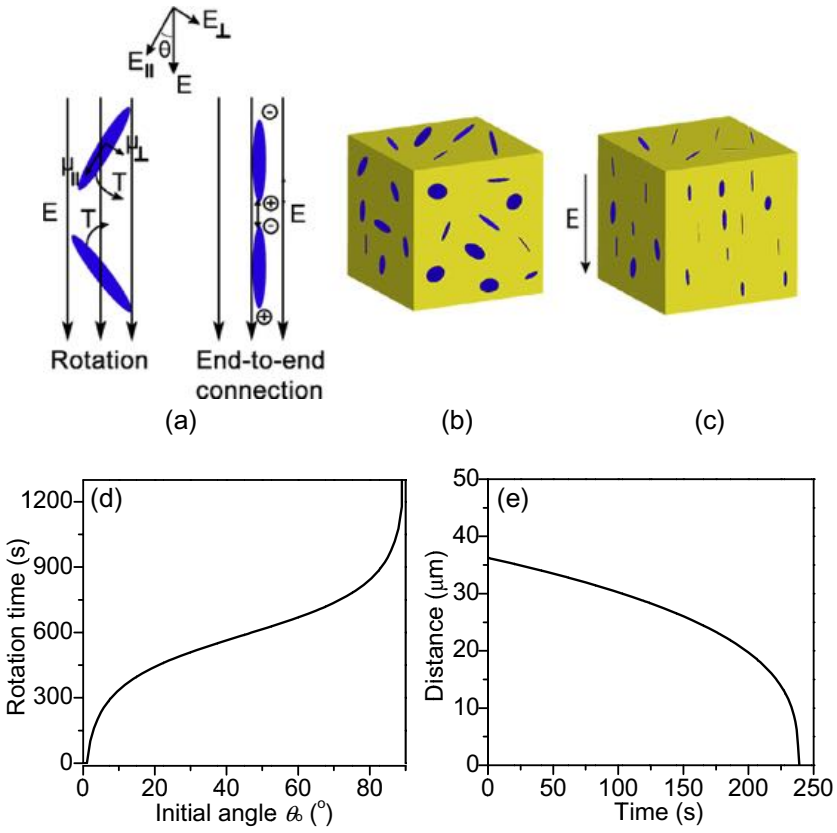

Fig. 3. Alignment mechanisms of the GnPs by the AC electric field: (a) rotation and end-to-end connection of polarized GnPs; (b) the initial random orientation in the epoxy resin; (c) GnPs oriented along the electric field direction in the epoxy resin; (d) plot of the rotation time as a function of the initial angle for the GnPs; (e) distance from two oppositely charged GnPs ends as a function of time. Note: the yellow region represents the epoxy resin and the blue regions are the GnPs.

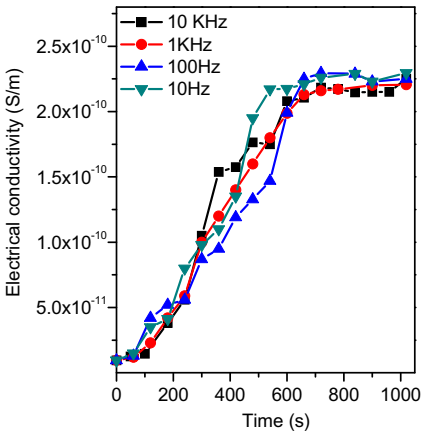

Fig. 4. Electrical conductivity (direct current) as a function of time for the liquid epoxy resin containing 0.054 vol% of GnPs during the application of the AC electric field.

nanocomposites containing aligned GnPs have been determined and are presented in the following sections.

3.3. Electrical conductivity

The electrical conductivity of the GnPs parallel to the surface is 10^7 S/m, which is much higher than that perpendicular to the surface (i.e. 10^2 S/m) [35]. Thus, the AC electric field-induced alignment was expected to increase significantly the conductivities of the epoxy/GnPs nanocomposites in the alignment direction. Electrical conductivities were measured in both the liquid epoxy resin/GnPs mixture during alignment and the cured epoxy nanocomposites.

Fig. 4 shows the change in the electrical conductivities of a liquid epoxy resin containing 0.054 vol% of GnPs when subjected to the electric field of different frequencies. The electrical conductivity increased rapidly over the initial ~10 min and then reached a constant value, by which time the in-situ observation of the liquid epoxy resin/GnPs mixture showed the formation of a well-defined chain-like graphene network aligned with the direction of the applied electric field (see Fig. 1d). The initial rapid rise in the electrical conductivity is attributed to the progressive rotation of the highly conductive nanoplatelets towards the direction of the applied electric field and the subsequent chaining to form continuous, electrically conductive pathways between the electrodes. After about 10 min the majority of the GnPs were closely aligned with the electric field direction, as predicted by the theoretical models presented in Sections 3.2.1 and 3.2.2, and therefore the electrical conductivities of the liquid epoxy resin/GnPs mixture reached a constant value.

Linear versus logarithmetic plots presented in Fig. 5 show the effects of alignment and volume content of the GnPs on the electrical conductivities of the epoxy nanocomposites. The electrical conductivities of the epoxy nanocomposites containing aligned GnPs were measured in two directions. For comparison, the electrical conductivity for the epoxy nanocomposites containing randomly-oriented GnPs are also included in Fig. 5. The results demonstrate that the electrical conductivities of the aligned and randomly-orientated nanocomposites increase rapidly with the content of GnPs. Moreover, the conductivities of the epoxy nanocomposites in the alignment direction of the GnPs are significantly higher than that of the nanocomposites containing randomly-oriented GnPs. Furthermore, the conductivities of the nanocomposites along the alignment direction are consistently 2–3 orders of magnitude higher than that along the transverse direction. Anisotropic electrical properties have also been recently reported by Kim and co-workers [36,37] for epoxy/graphene aerogel composites and epoxy/graphene oxide composites where a relatively high degree of alignment was observed when the graphene content was above a threshold.

By fitting the experimental data to a power-law equation (see Fig. 5b and c), a percolation threshold (Ψc) content of ~0.52 vol% was determined for the epoxy nanocomposite containing randomly-oriented GnPs. Electric field-induced alignment of the GnPs resulted in a much lower percolation threshold of ~0.22 vol% when the conductivity was measured in the alignment direction of the GnPs. This value is less than half that of the nanocomposites containing randomly-oriented GnPs. Thus, these results clearly demonstrate that aligning the GnPs significantly lowers the content of GnPs necessary to achieve percolation.

3.4. Thermal conductivity

Fig. 6 shows the effects of the volume content and alignment of the GnPs on the thermal conductivities of the epoxy nanocomposites. The thermal conductivities of the aligned epoxy nanocomposites were measured in two directions, i.e. parallel and transverse to the alignment direction of the GnPs, as indicated. The thermal conductivities of the epoxy nanocomposites containing randomly-oriented GnPs increased steadily with the content of

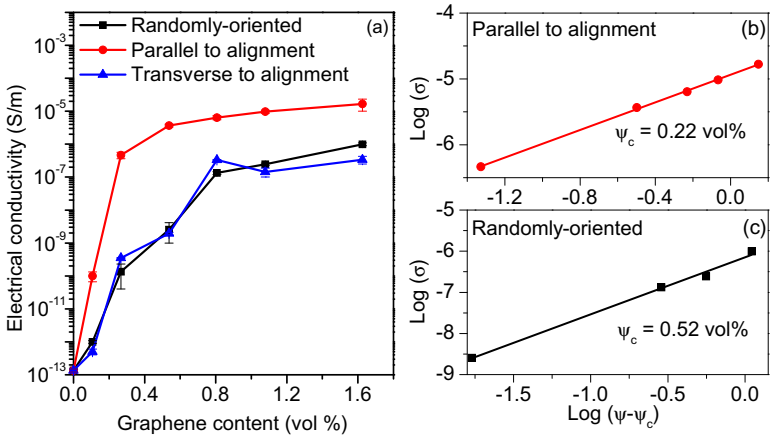

Fig. 5. (a) Effects of the volume content (Ψ) and alignment of GnPs on the electrical conductivities of the epoxy nanocomposites; (b) and (c) $\log\sigma$ plotted against $\log(\Psi - \Psi c)$ for the epoxy nanocomposites with randomly-oriented and aligned GnPs, respectively. (Ψc represents the critical content at the percolation threshold.) (The direction of the measured electrical conductivity with respect to the alignment direction of the GnPs is indicated.)

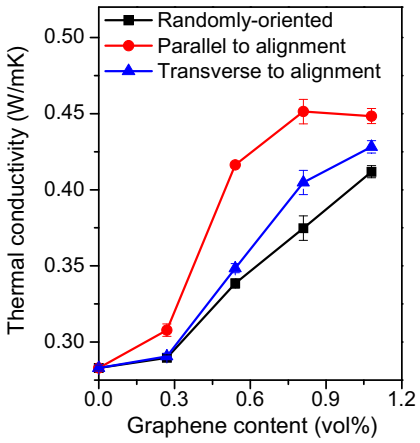

Fig. 6. Effects of the volume content and alignment of the GnPs on the thermal conductivities of the epoxy nanocomposites. (The direction of the measured thermal conductivity with respect to the alignment direction of the GnPs is indicated.)

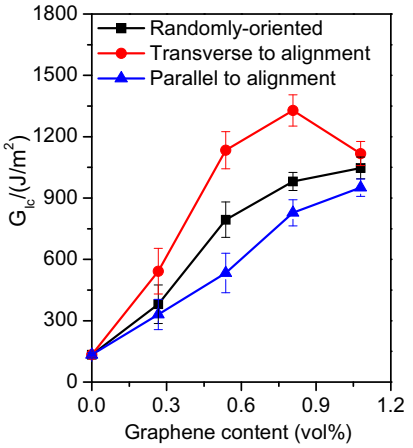

Fig. 7. Effects of the volume content and alignment of GnPs on the mode I fracture energy (G_{Ic}) of the epoxy nanocomposites. (The alignment direction of the GnPs with respect to the crack growth direction is indicated.)

GnPs and reached a value of 0.412 W/mK at the highest loading of 1.08 vol%. The value of 0.412 W/mK is about 50% higher than that of the unmodified epoxy polymer. This level of improvement is similar to that reported recently for other epoxy polymers with randomly-oriented GnPs [38].

Clearly, the thermal conductivities of the epoxy nanocomposites measured in alignment direction are much higher than that of nanocomposites containing randomly-oriented GnPs (see Fig. 6). Distinct differences were observed between the thermal conductivities measured with respect to the parallel and transverse directions of alignment of the GnPs, with the disparity increasing with the content of GnPs up to 0.8 vol%. The anisotropy in thermal conductivity of the present epoxy/GnPs composites is similar to that reported in a recent study on epoxy composites containing vertically-aligned and densely-packed multilayer graphene [39]. The planar thermal conductivity (i.e. 3000 W/mK) of the GnPs is significantly higher than the transverse (i.e. thickness direction) conductivity (i.e. 6 W/mK) [35], leading to a larger increase in the thermal conductivities of the epoxy nanocomposites in the alignment direction. The differences in the thermal conductivities measured in the orthogonal directions as well as the epoxy nanocomposites containing randomly-oriented GnPs decreased when the content of GnPs was further increased from 0.8 vol% to 1.08 vol%. The reason for this diminishing difference at relatively high loading levels is most likely due to the reduced degree of alignment and the likely agglomeration of the GnPs at concentrations above about 0.8 vol%.

3.5. Fracture toughness

The mode I fracture toughness of the unmodified epoxy polymer and the epoxy/GnPs nanocomposites were measured using the double cantilever beam (DCB) test. The materials were tested in the form of a thin, continuous epoxy polymer layer (2 mm thick) which was bonded between two carbon fibre-epoxy composite substrates (as illustrated in Fig. S1b in the Supporting information). In all the tests, the crack propagated through the epoxy polymer layer and did not grow along the epoxy polymer-substrate interface or within the carbon fibre-epoxy composite substrates.

The effects of alignment and volume concentration of the GnPs on the fracture toughness (G_{Ic}) of the epoxy nanocomposites are shown in Fig. 7. The fracture toughness of the nanocomposite containing randomly-oriented GnPs increased at a quasi-linear rate up to ~0.8 vol%, above which the rate of improvement tapered off. When the GnPs were aligned in the transverse direction with respect to the crack growth direction, the values of toughness increased linearly with the content of GnPs up to about 0.8 vol%. (It should be recalled that the electric field was applied transversely to the subsequent crack growth direction to make the GnPs align perpendicular to the crack growth.) Such alignment of the GnPs induces a significantly stronger toughening effect of about 40% compared to the randomly-oriented epoxy nanocomposites. By contrast, a lower toughness (of about 10–15% compared to the randomly-oriented materials) was measured when the GnPs were aligned parallel to the crack growth direction. Further, there was no statistically significant difference observed in the toughness of the epoxy nanocomposites containing randomly-oriented and aligned GnPs when the volume concentration of GnPs was increased from 0.8 vol% to 1.08 vol%. This may be ascribed to the reduced degree of alignment and the increased agglomeration of the GnPs at contents above about 0.8 vol%. Since, at relatively high contents of nanofillers, the viscosity of the epoxy mixture and the degree of filler packing increase. These factors make it more difficult for the GnPs to move and rotate in response to the applied electric field. Similar behaviour has been reported for multi-walled carbon nanotubes in an epoxy polymer matrix [40].

The improvement in fracture toughness gained by aligning the GnPs transverse to the crack growth direction, is superior to the toughening efficiency reported in the literature for various types of graphene when added to epoxy polymers. Table S1 summarizes the published values for the percentage increase in the mode I fracture toughness of epoxy polymers containing different randomly-oriented graphene-based materials (i.e. graphene oxide (GO), thermally expanded or reduced GO, chemically-modified graphene, or graphene foam) [4,6,29,30,41–47]. The maximum percentage increase in the fracture toughness (i.e. of up to ~900%) from the present studies is the highest recorded improvement. This demonstrates the very high toughening efficiency gained by the AC electric field-induced alignment of the GnPs, while at the same time providing the additional functionalities of increased electrical and thermal conductivities.

3.6. Toughening mechanisms

Fractographic analysis of the DCB specimens was performed to determine the toughening mechanisms induced by both the randomly-orientated and aligned GnPs. Fig. 8 shows a side-view of the main crack front in the unmodified epoxy polymer and in an epoxy nanocomposite containing randomly-oriented and

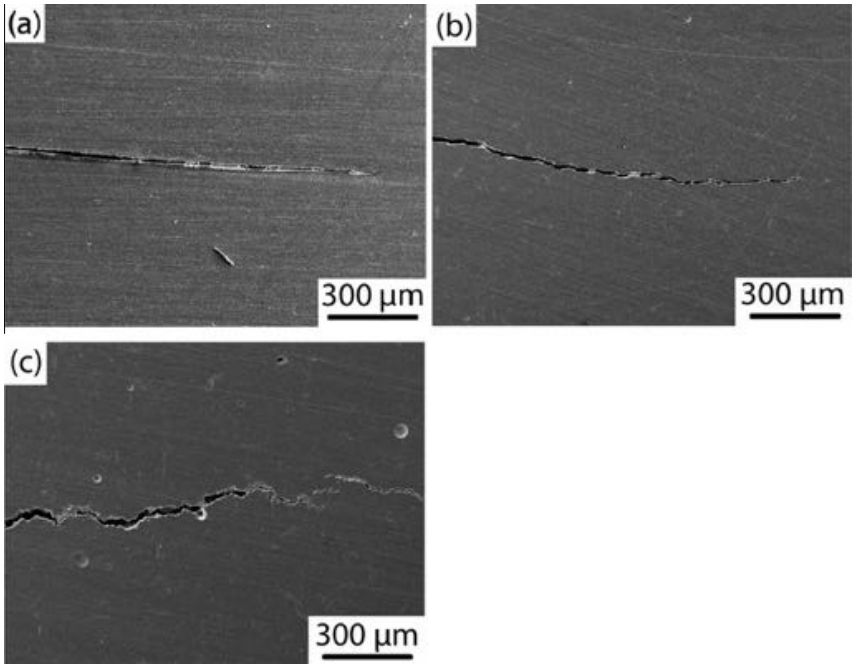

Fig. 8. SEM images of the crack tip region (side-view) of the (a) unmodified epoxy polymer; (b) epoxy nanocomposite containing randomly-oriented GnPs; and (c) epoxy nanocomposite containing 0.81 vol% of GnPs aligned transverse to the crack growth direction.

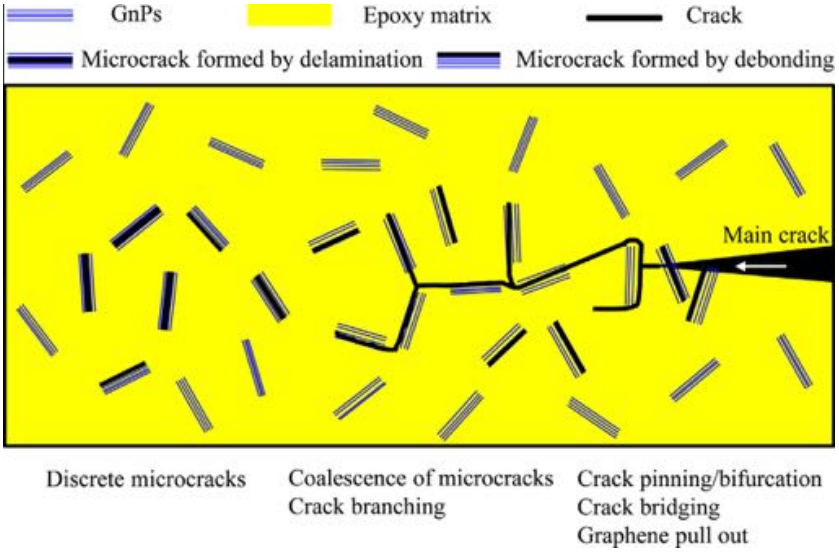

Fig. 9. Schematic of the toughening processes induced by the GnPs.

aligned GnPs. The crack tip in the unmodified epoxy polymer (see Fig. 8a) is well-defined, and there is no evidence of discrete damage processes ahead of the crack, and this observation is typical for brittle-like polymers with relatively low values of fracture toughness. In contrast, the fracture process at, and immediately ahead of the main crack tip was altered by the addition of the GnPs (see Fig. 8b and c). In addition, the crack path has changed from being relatively flat and straight to being very tortuous, which is particularly noticeable for the composites containing aligned GnPs (Fig. 8c). There were no visible differences in the crack path for the nanocomposites containing GnPs aligned parallel or transverse to the crack growth direction.

The fracture and toughening processes induced by the presence of the GnPs are shown schematically in Fig. 9, and the evidence for this schematic is given in Figs. 8, 10 and 11. Discrete microcracks (typically of the size of the GnPs, i.e. ~10–25 μm long) were created immediately ahead of the main crack within the nanocomposites (see Fig. 10b). The microcracks initiated at the epoxy/GnPs interfaces due to the stress concentrations created by the mismatch in the Young's modulus and Poisson's ratio of the graphene and the epoxy polymer. In addition, as evidenced in Fig. 11, microcracks also developed due to delamination between the nanosheets within the GnPs and interfacial debonding of the GnPs from the epoxy polymer matrix. This indicates the relatively weak bonding between the graphene sheets and at the epoxy-graphene interface that occurs when GnPs are used without any functionalization. The formation of microcracks ahead of the main crack is an intrinsic toughening mechanism which increases

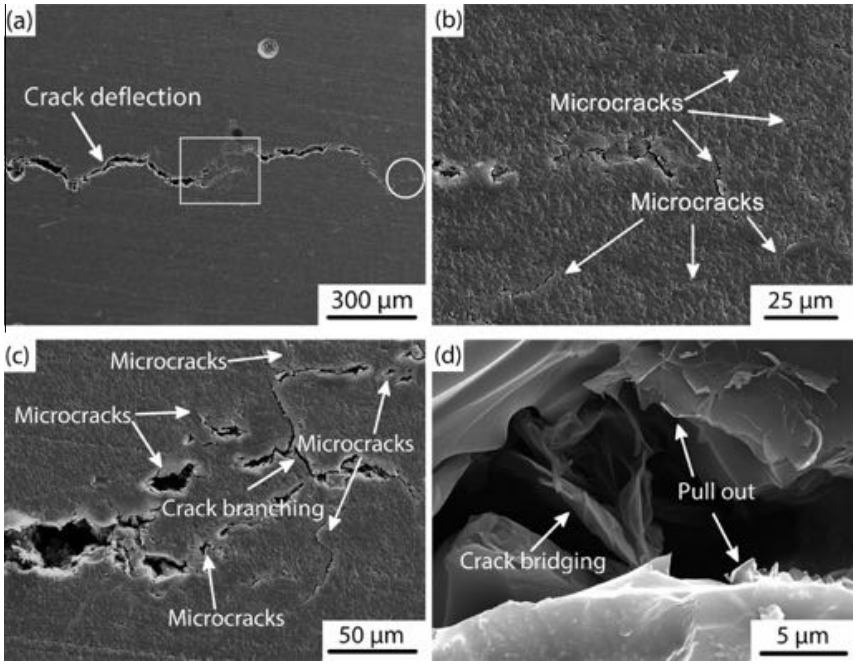

Fig. 10. SEM images of the crack tip region (side-view) of a DCB specimen for an epoxy nanocomposite containing 1.08 vol% of GnPs transversely aligned to the direction of crack growth, showing: (a) tortuous crack path; (b) microcracks at the crack tip; (c) microcracks inducing crack deflection and branching; (d) crack bridging and graphene pull out. (Note: (b) and (c) are magnified SEM images taken from the circular and rectangular regions in (a), respectively.)

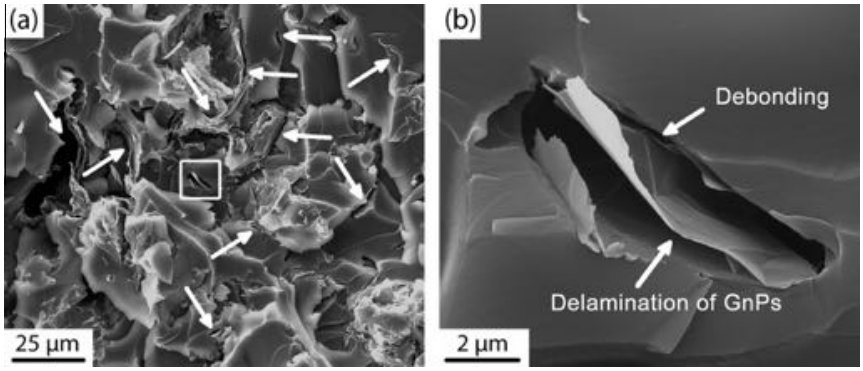

Fig. 11. SEM images of the fracture surfaces of a DCB specimen for an epoxy nanocomposite containing 0.54 vol% of GnPs, transversely aligned to the direction of crack growth, revealing evidence of debonding and delamination of the GnPs. The arrows in (a) indicate microcracks created around the GnPs and (b) is a magnified image from the rectangular area in (a).

the fracture resistance of low toughness materials [48], and this would account, in part, for the higher toughness of the epoxy nanocomposites.

Fig. 10c shows that the discrete microcracks coalesced into a multi-branched network of longer cracks which then connected with the main crack front. This is also an effective intrinsic toughening process which contributes to the increase in the fracture toughness of the nanocomposites. Fig. S6 shows the crack surfaces of the epoxy nanocomposites with increasing content of GnPs, and there is a progressive increase in surface roughness attributed to the increased degree of crack bifurcation and branching. Again these toughening mechanisms will increase the toughness of the epoxy nanocomposites. Furthermore, the orientation of the GnPs at some inclined angle to the crack growth direction will obviously increase the probability of the main crack encountering them and thus induce more crack deflection and branching. Hence, the presence of a relatively high level of inclined GnPs, approximately transverse to the crack growth direction, will provide an enhanced toughening effect in the epoxy nanocomposites. Indeed, examination of the crack tip at high magnification (Fig. 10d) revealed fracture and pull-out of GnPs, and crack bridging by the pulled-out GnPs. The transversely-aligned GnPs tended to initially bridge the crack over a crack-opening distance of up to ~20 μm, which is equivalent to the size of the nanoplatelets. As the crack propagated along the DCB specimen, the GnPs fractured and pulled-out from the epoxy polymer matrix. These very effective extrinsic toughening mechanisms, which are not significant in the epoxy nanocomposites containing randomly-oriented GnPs or GnPs aligned parallel to the crack growth direction, account for the more effective toughening.

4. Conclusions

The application of an AC electric field has been shown to align GnPs, and to drive the GnPs to form a chain-like network

nanostructure, in an epoxy polymer along the electric field direction. Theoretical modeling has indicated that the time required for the GnPs to rotate and form end-to-end 'chain' connections, when the epoxy resin is in its liquid phase, may depend on the aspect ratio of the GnPs, the viscosity of the mixture, and the strength and frequency of the applied electric field. The lower the viscosity and the stronger the applied electric field, then shorter is the time it takes to align the GnPs. The aspect ratio (a/b) of the GnPs and the frequency of the applied electric field have negligible effects on the rotation and chain-formation time.

Compared to the unmodified epoxy polymer, a significantly higher electrical conductivity (of up to about 7–8 orders of magnitude) and thermal conductivity (of up to nearly 60%) have been achieved in the alignment direction of the GnPs. Moreover, aligning the GnPs transverse to the crack growth direction has dramatically improved the fracture toughness (of up to nearly 900%). These properties are far superior to those achieved by randomly-oriented GnPs. Both intrinsic and extrinsic toughening mechanisms have been identified as the major factors responsible for the remarkable increase in fracture toughness. Specifically, the main intrinsic toughening mechanisms for the epoxy nanocomposites containing transversely-aligned GnPs include micro-cracking and debonding of the GnPs, pinning and deflection of the main crack. The extrinsic toughening mechanisms include pull-out of and bridging by the GnPs. The orientation of the aligned GnPs transverse to the crack direction increases the probability of interactions occurring between the advancing crack tip and the GnPs. This greatly enhances the effectiveness of the extrinsic toughening mechanisms and leads to a significant increase in the fracture toughness compared to those containing GnPs aligned parallel to the crack growth direction or randomly-oriented GnPs. The differences in the properties between the epoxy nanocomposites containing randomly-oriented GnPs and aligned GnPs become less marked when the content of the GnPs increases to above about 0.8 vol%. This may be ascribed to the increased agglomeration and reduced degree of alignment of the GnPs at contents above about 0.8 vol%.

The present work has clearly demonstrated that an AC electric field can be applied to control the orientation and alignment of GnPs in an epoxy resin and therefore enables the fabrication of high-performance, multifunctional epoxy/graphene nanocomposites.

Acknowledgements

The authors are thankful for the financial support received from the Australian Research Council's Discovery Grant (DP140100778). The authors acknowledge the Department of Materials Engineering at Monash University for supporting equipment for thermal conductivity measurements.

Appendix A. Supplementary data

Supplementary data associated with this article can be found, in the online version, at http://dx.doi.org/10.1016/j.carbon.2015.07.026.

References

[1] A.K. Geim, K.S. Novoselov, The rise of graphene, Nat. Mater. 6 (2007) 183–191.
[2] S. Stankovich, D.A. Dikin, G.H.B. Dommett, K.M. Kohlhaas, E.J. Zimney, E.A. Stach, et al., Graphene-based composite materials, Nature 442 (2006) 282–286.
[3] M.A. Rafiee, J. Rafiee, Z. Wang, H. Song, Z.-Z. Yu, N. Koratkar, Enhanced mechanical properties of nanocomposites at low graphene content, ACS Nano 3 (2009) 3884–3890.
[4] Q.S. Meng, J. Jin, R.Y. Wang, H.C. Kuan, J. Ma, N. Kawashima, et al., Processable 3-nm thick graphene platelets of high electrical conductivity and their epoxy composites, Nanotechnology 25 (2014) 125707.
[5] J. Ma, Q.S. Meng, I. Zaman, S.M. Zhu, A. Michelmore, N. Kawashima, et al., Development of polymer composites using modified, high-structural integrity graphene platelets, Compos. Sci. Technol. 91 (2014) 82–90.
[6] J.J. Jia, X.Y. Sun, X.Y. Lin, X. Shen, Y.W. Mai, J.K. Kim, Exceptional electrical conductivity and fracture resistance of 3D interconnected graphene foam/epoxy composites, ACS Nano 8 (2014) 5774–5783.
[7] S.H. Song, K.H. Park, B.H. Kim, Y.W. Choi, G.H. Jun, D.J. Lee, et al., Enhanced thermal conductivity of epoxy–graphene composites by using non-oxidized graphene flakes with non-covalent functionalization, Adv. Mater. 25 (2013) 732–737.
[8] X.L. Xie, Y.W. Mai, X.P. Zhou, Dispersion and alignment of carbon nanotubes in polymer matrix: a review, Mater. Sci. Eng., R 49 (2005) 89–112.
[9] Q. Wang, J.F. Dai, W.X. Li, Z.Q. Wei, J.L. Jiang, The effects of CNT alignment on electrical conductivity and mechanical properties of SWNT/epoxy nanocomposites, Compos. Sci. Technol. 68 (2008) 1644–1648.
[10] M. Monti, M. Natali, L. Torre, J.M. Kenny, The alignment of single walled carbon nanotubes in an epoxy resin by applying a DC electric field, Carbon 50 (2012) 2453–2464.
[11] C. Ma, W. Zhang, Y.F. Zhu, L.J. Ji, R.P. Zhang, N. Koratkar, et al., Alignment and dispersion of functionalized carbon nanotubes in polymer composites induced by an electric field, Carbon 46 (2008) 706–710.
[12] T. Prasse, J.Y. Cavaille, W. Bauhofer, Electric anisotropy of carbon nanofibre/epoxy resin composites due to electric field induced alignment, Compos. Sci. Technol. 63 (2003) 1835–1841.
[13] C.S. Lim, A.J. Rodriguez, M.E. Guzman, J.D. Schaefer, B. Minaie, Processing and properties of polymer composites containing aligned functionalized carbon nanofibers, Carbon 49 (2011) 1873–1883.
[14] M.-K. Schwarz, W. Bauhofer, K. Schulte, Alternating electric field induced agglomeration of carbon black filled resins, Polymer 43 (2002) 3079–3082.
[15] R.B. Ladani, S. Wu, A.J. Kinloch, K. Ghorbani, J. Zhang, A.P. Mouritz, et al., Improving the toughness and electrical conductivity of epoxy nanocomposites by using aligned carbon nanofibres, Compos. Sci. Technol. (2015), http://dx.doi.org/10.1016/j.compscitech.2015.06.006.
[16] W.C. Jiao, M. Shioya, R.G. Wang, F. Yang, L.F. Hao, Y. Niu, et al., Improving the gas barrier properties of Fe_3O_4/graphite nanoplatelet reinforced nanocomposites by a low magnetic field induced alignment, Compos. Sci. Technol. 99 (2014) 124–130.
[17] H.Y. Yan, Y.X. Tang, W. Long, Y.F. Li, Enhanced thermal conductivity in polymer composites with aligned graphene nanosheets, J. Mater. Sci. 49 (2014) 5256–5264.
[18] S. Wu, R.B. Ladani, J. Zhang, A.J. Kinloch, Z. Zhao, J. Ma, et al., Epoxy nanocomposites containing magnetite-carbon nanofibers aligned using a weak magnetic field, Polymer 68 (2015) 25–34.
[19] G. Kim, Y.M. Shkel, Polymeric composites tailored by an electric field, J. Mater. Res. 19 (2004) 1164–1174.
[20] G. Kim, Thermo-physical responses of polymeric composites tailored by electric field, Compos. Sci. Technol. 65 (2005) 1728–1735.
[21] H. Wang, H. Zhang, G. Chen, Preparation of unsaturated polyester/graphite nanosheet conducting composite under electric field, Compos. Part A: Appl. Sci. Manuf. 38 (2007) 2116–2120.
[22] G.H. Chen, H.Q. Wang, W.F. Zhao, Fabrication of highly ordered polymer/graphite flake composite with eminent anisotropic electrical property, Polym. Adv. Technol. 19 (2008) 1113–1117.
[23] H. Wang, H. Zhang, W. Zhao, W. Zhang, G. Chen, Preparation of polymer/oriented graphite nanosheet composite by electric field-inducement, Compos. Sci. Technol. 68 (2008) 238–243.
[24] S. Wu, Q. Guo, S. Peng, N. Hameed, M. Kraska, B. Stühn, et al., Toughening epoxy thermosets with block ionomer complexes: a nanostructure–mechanical property correlation, Macromolecules 45 (2012) 3829–3840.
[25] A. Lonjon, P. Demont, E. Dantras, C. Lacabanne, Electrical conductivity improvement of aeronautical carbon fiber reinforced polyepoxy composites by insertion of carbon nanotubes, J. Non-Cryst. Solids 358 (2012) 1859–1862.
[26] B.R.K. Blackman, A.J. Kinloch, Fracture tests on structural adhesive joints, in: D.R. Moore, A. Pavan, J.G. Williams (Eds.), Fracture Mechanics Testing Methods for Polymers, Adhesives and Composites, Elsevier Science, Amsterdam, 2001, pp. 225–267.
[27] V. Tomer, C.A. Randall, G. Polizos, J. Kostelnick, E. Manias, High- and low-field dielectric characteristics of dielectrophoretically aligned ceramic/polymer nanocomposites, J. Appl. Phys. 103 (2008) 034115.
[28] M. Knaapila, J.P. Pinheiro, M. Buchanan, A.T. Skjeltorp, G. Helgesen, Directed assembly of carbon nanocones into wires with an epoxy coating in thin films by a combination of electric field alignment and subsequent pyrolysis, Carbon 49 (2011) 3171–3178.
[29] J. Ma, Q.S. Meng, A. Michelmore, N. Kawashima, Z. Izzuddin, C. Bengtsson, et al., Covalently bonded interfaces for polymer/graphene composites, J. Mater. Chem. A 1 (2013) 4255–4264.
[30] L.-C. Tang, Y.-J. Wan, D. Yan, Y.-B. Pei, L. Zhao, Y.-B. Li, et al., The effect of graphene dispersion on the mechanical properties of graphene/epoxy composites, Carbon 60 (2013) 16–27.
[31] T.B. Jones, Electromechanics of Particles, Cambridge University Press, Cambridge, 1995.
[32] H.C. Berg, Random Walks in Biology, Princeton University Press, Princeton NJ, 1993.

[33] F. Perrin, Mouvement Brownien d'un ellipsoide (II). Rotation libre et dépolarisation des fluorescences. Translation et diffusion de molécules ellipsoidales, J. Phys. Radium. 7 (1936) 1–11.
[34] V.A. Bloomfield, Survey of biomolecular hydrodynamics, in: T.M. Schuster (Ed.), Separations and Hydrodynamics, Biophysical Society, 1980.
[35] http://xgsciences.com/wp-content/uploads/2012/10/10-15-13_xGnP-M_Data-Sheet.pdf.
[36] N. Yousefi, X. Lin, Q. Zheng, X. Shen, J.R. Pothnis, J. Jia, et al., Simultaneous in situ reduction, self-alignment and covalent bonding in graphene oxide/epoxy composites, Carbon 59 (2013) 406–417.
[37] Z.Y. Wang, X. Shen, M.A. Garakani, X.Y. Lin, Y. Wu, X. Liu, et al., Graphene aerogel/epoxy composites with exceptional anisotropic structure and properties, ACS Appl. Mater. Interfaces 7 (2015) 5538–5549.
[38] B. Ahmadi-Moghadam, F. Taheri, Effect of processing parameters on the structure and multi-functional performance of epoxy/GNP-nanocomposites, J. Mater. Sci. 49 (2014) 6180–6190.
[39] Q. Li, Y.F. Guo, W.W. Li, S.Q. Qiu, C. Zhu, X.F. Wei, et al., Ultrahigh thermal conductivity of assembled aligned multi layer graphene/epoxy composite, Chem. Mat. 26 (2014) 4459–4465.
[40] S.U. Khan, J.R. Pothnis, J.-K. Kim, Effects of carbon nanotube alignment on electrical and mechanical properties of epoxy nanocomposites, Compos. Part A: Appl. Sci. Manuf. 49 (2013) 26–34.
[41] Y.T. Park, Y. Qian, C. Chan, T. Suh, M.G. Nejhad, C.W. Macosko, et al., Epoxy toughening with low graphene loading, Adv. Funct. Mater. 25 (2014) 575–585.
[42] M.A. Rafiee, J. Rafiee, I. Srivastava, Z. Wang, H. Song, Z.-Z. Yu, et al., Fracture and fatigue in graphene nanocomposites, Small 6 (2010) 179–183.
[43] S. Chandrasekaran, C. Seidel, K. Schulte, Preparation and characterization of graphite nano-platelet (GNP)/epoxy nano-composite: mechanical, electrical and thermal properties, Eur. Polym. J. 49 (2013) 3878–3888.
[44] S. Chandrasekaran, N. Sato, F. Tolle, R. Mulhaupt, B. Fiedler, K. Schulte, Fracture toughness and failure mechanism of graphene based epoxy composites, Compos. Sci. Technol. 97 (2014) 90–99.
[45] D.R. Bortz, E.G. Heras, I. Martin-Gullon, Impressive fatigue life and fracture toughness improvements in graphene oxide/epoxy composites, Macromolecules 45 (2011) 238–245.
[46] I. Zaman, T.T. Phan, H.-C. Kuan, Q. Meng, L.T. Bao La, L. Luong, et al., Epoxy/graphene platelets nanocomposites with two levels of interface strength, Polymer 52 (2011) 1603–1611.
[47] X. Wang, J. Jin, M. Song, An investigation of the mechanism of graphene toughening epoxy, Carbon 65 (2013) 324–333.
[48] A.C. Garg, Y.W. Mai, Failure mechanisms in toughened epoxy resins—a review, Compos. Sci. Technol. 31 (1988) 179–223.

A. III. Journal Article : Epoxy Nanocomposites Containing Magnetite-Carbon Nanofibers Aligned Using a Weak Magnetic Field

Polymer 68 (2015) 25–34

Contents lists available at ScienceDirect

Polymer

journal homepage: www.elsevier.com/locate/polymer

Epoxy nanocomposites containing magnetite-carbon nanofibers aligned using a weak magnetic field

Shuying Wu [a], Raj B. Ladani [a], Jin Zhang [b], Anthony J. Kinloch [c], Zhiheng Zhao [d], Jun Ma [d], Xuehua Zhang [e], Adrian P. Mouritz [a], Kamran Ghorbani [f], Chun H. Wang [a, *]

[a] Sir Lawrence Wackett Aerospace Research Centre, School of Aerospace, Mechanical & Manufacturing Engineering, RMIT University, GPO Box 2476, Melbourne, VIC 3001, Australia
[b] Australian Future Fibres Research and Innovation Centre, Institute for Frontier Materials, Deakin University, VIC 3220, Australia
[c] Department of Mechanical Engineering, Imperial College London, London SW7 2BX, UK
[d] School of Advanced Manufacturing and Mechanical Engineering, University of South Australia, SA 5095, Adelaide, Australia
[e] School of Civil, Environmental & Chemical Engineering, RMIT University, GPO Box 2476, Melbourne, VIC 3001, Australia
[f] School of Electrical and Computer Engineering, RMIT University, GPO Box 2476, Melbourne, VIC 3001, Australia

ARTICLE INFO

Article history:
Received 21 March 2015
Received in revised form
25 April 2015
Accepted 29 April 2015
Available online 8 May 2015

Keywords:
Carbon nanofibers
Magnetic field alignment
Epoxy nanocomposites

ABSTRACT

Novel magnetite-carbon nanofiber hybrids (denoted by "Fe_3O_4@CNFs") have been developed by coating carbon nanofibers (CNFs) with magnetite nanoparticles in order to align CNFs in epoxy using a relatively weak magnetic field. Experimental results have shown that a weak magnetic field (~50 mT) can align these newly-developed nanofiber hybrids to form a chain-like structure in the epoxy resin. Upon curing, the epoxy nanocomposites containing the aligned Fe_3O_4@CNFs show (i) greatly improved electrical conductivity in the alignment direction and (ii) significantly higher fracture toughness when the Fe_3O_4@CNFs are aligned normal to the crack surface, compared to the nanocomposites containing randomly-oriented Fe_3O_4@CNFs. The mechanisms underpinning the significant improvements in the fracture toughness have been identified, including interfacial debonding, pull-out, crack bridging and rupture of the Fe_3O_4@CNFs, and plastic void growth in the polymer matrix.

1. Introduction

Many applications of polymeric materials in electronic devices, fuel storage and transportation, automotive, and aerospace products demand good mechanical properties for structural integrity and high electrical conductivities to dissipate static electricity [1]. Carbon nanomaterials, such as carbon nanotubes (CNTs), carbon nanofibers (CNFs), and graphene nanosheets (GNSs), have emerged as promising nanofillers for polymer nanocomposites due to their outstanding mechanical and electrical properties [2–4]. The introduction of carbon nanofillers into polymers can greatly improve their electrical and mechanical properties [4–6]. The enhancements in these properties can be achieved at relatively low loadings, which arises from their high aspect ratio, leading to them frequently being superior fillers compared to the conventional micrometer-sized fillers [7]. However, the property improvements achieved to date using carbon nanofillers are still well below the theoretical predictions due to the difficulty in achieving (i) a uniform dispersion of the nanofillers in the polymer matrices, (ii) appropriate interfacial bonding with the polymer matrices [3,5,8], and more importantly, (iii) alignment of the nanofillers. Indeed, aligned carbon nanofillers have been found to produce more significant improvements in the mechanical and electrical properties, in the direction of the alignment, when compared to their randomly-oriented counterparts [9–13].

Different approaches for aligning carbon nanofillers have been reported in the literature, mainly based on mechanical stretching [14,15] or the application of an electric field [16,17] or magnetic field [18–23]. Although using an electric field is recognized as an effective method, this technique is typically restricted to materials with very low electrical conductivity, since the field strength is usually limited to avoid dielectric breakdown of the polymer [23]. Moreover, due to their low magnetic susceptibility [18–21], an extremely strong magnetic field (e.g. of several Teslas) is usually required to align carbon-based nanofillers. For instance, Camponeschi and co-workers [21] employed a magnetic field of up to 25 T

* Corresponding author. Tel.: +61 3 9925 6115.
E-mail address: chun.wang@rmit.edu.au (C.H. Wang).

http://dx.doi.org/10.1016/j.polymer.2015.04.080

to orient and align CNTs in an epoxy resin and found that the properties of the resulting nanocomposites were superior to those prepared in the absence of a magnetic field. Another similar attempt was reported by Mahfuz and co-workers [20] who used magnetic fields of up to 28 T to align CNFs in a two-phase toughened epoxy resin system and achieved 21% and 3% increases in the compressive strength and modulus compared to randomly-oriented CNFs. The necessity to employ such high magnetic fields limits the practical application of this method. Therefore, various methods have been reported to functionalise carbon nanofillers with magnetic nanoparticles, especially iron-based nanoparticles, so as to align the nanofiller in a polymer matrix without needing to employ high magnetic fields [24–27]. For instance, magnetite (Fe_3O_4) decorated single-walled CNTs have been developed using a sonochemical oxidation process and these hybrid nanofillers were successfully aligned in an epoxy using a relatively weak magnetic field [24]. In addition to CNTs, graphene-based magnetic hybrids have also been prepared by attaching Fe_3O_4 nanoparticles onto the graphene nanoplatelets and/or graphene oxide, using a wet-chemical co-precipitation method. The graphene hybrids were aligned in an epoxy under a relatively low magnetic field to achieve high thermal conductivity [26] and good gas barrier properties [27].

CNFs have a relatively high aspect ratio and are an excellent low-cost alternative to CNTs [28]. However, most of the reported research efforts on functionalising CNFs by magnetic iron oxide nanoparticles have been either based on complex chemical methods or a very high temperature treatment [29,30]. Moreover, to the best of our knowledge, there is no report on aligning iron oxide-CNFs in an epoxy resin using a relatively low magnetic field to selectively reinforce the epoxy polymer in a preferred orientation.

The present work aims to explore the functionalisation process to coat carbon nanofibers with magnetic iron oxide nanoparticles by co-precipitation and to align the resultant nanofiber hybrids in an epoxy resin for developing epoxy nanocomposites with anisotropic electrical and mechanical properties. The functionalised carbon nanofibers, denoted by Fe_3O_4@CNFs, are first dispersed into a liquid epoxy resin which is then cured under a relatively weak magnetic field of ~50 mT. The electrical conductivity and fracture toughness of the cured epoxy nanocomposites, containing either randomly-oriented or aligned Fe_3O_4@CNFs are measured and compared. Finally, the toughening mechanisms are identified from fractographic studies.

2. Experimental details

2.1. Materials

Vapour grown carbon nanofibers (VGCNFs) (Pyrograf®-III, grade PR-24-XT-HHT) used in the present work are fully graphitized at 2800 °C and contain a very low content of catalyst (iron <100 ppm). They therefore possess a relatively high electrical conductivity and a low magnetic susceptibility. According to material data supplied by the manufacturer, the CNFs have an average diameter in the range of 70–200 nm and a length of between 50 and 200 μm. The epoxy resin used is a liquid blend of bisphenol A and bisphenol F ('105' from West System) together with a slow-curing hardener ('206' from West System) which is a blend of aliphatic amines and aliphatic amine adducts based on diethylene triamine and triethylenetetramine. Concentrated nitric acid (70%) was obtained from RCI Labscan. Iron (II) sulfate heptahydrate ($FeSO_4 \cdot 7H_2O$), anhydrous iron chloride, and ammonia hydroxide (NH_4OH) were sourced from Sigma–Aldrich, Australia. Carbon fiber composite substrates were manufactured from T700 carbon fiber/epoxy prepreg (VTM 264) supplied by Advanced Composites Group. Twelve plies of this unidirectional prepreg with dimensions of 300 mm × 250 mm × 2.35 mm were used to fabricate the substrates for the fracture toughness tests by curing the prepreg plies in an autoclave at 120 °C and under a pressure of ~650 kPa for 1 h, as recommended by the supplier.

2.2. Preparation of the magnetic Fe_3O_4@CNFs

To functionalise with Fe_3O_4 nanoparticles, the CNFs were first treated with an oxidative mineral acid. Typically, 2 g of as-received CNFs were initially mixed with 200 mL of concentrated nitric acid under vigorous stirring. This mixture was then treated at 100 °C for 6 h under magnetic stirring. After this treatment, the mixture was washed several times by deionized water until reaching a pH value of ~7. The samples were vacuum filtrated and dried in a vacuum oven. After this acid treatment, the CNFs are expected to possess oxygen-containing functional groups, such as carboxylic, lactone and phenolic quinone, on their surfaces and are denoted by CNFs-OX [31].

The Fe_3O_4 nanoparticles were fabricated by a facile co-precipitation method [32,33] from the CNFs-OX materials, prepared as described above. Firstly, 0.225 g of the CNFs-OX were dispersed in 200 mL distilled water by ultraprobe sonication for 15 min, into which 0.225 g of $FeCl_3$ was added whilst stirring. The mixture was vigorously stirred for 15 min whilst being heated to 50 °C under a nitrogen (N_2) atmosphere. Then, 0.18 g of $FeSO_4 \cdot 7H_2O$ was added, with continuous stirring under a N_2 atmosphere for 30 min. Next, 15 mL of 8 M NH_4OH aqueous solution was added drop-wise to precipitate ferric and ferrous salts. The pH value of the mixture was kept at ~10 and the reaction was carried out at 50 °C for 30 min under vigorous magnetic stirring, and N_2 was continuously purged during the reaction to prevent oxidation. The Fe_3O_4@CNFs hybrids were obtained by magnetic separation, washed with distilled water and ethanol, and finally dried under vacuum at 50 °C.

2.3. Preparation of the bulk epoxy nanocomposites with Fe_3O_4@CNFs

The epoxy nanocomposites containing Fe_3O_4@CNFs were prepared as described below. The Fe_3O_4@CNFs were firstly dispersed in a small amount of acetone by bath sonication for 15 min (the typical concentration being 20 mg/mL). Epoxy resin was then added and the sonication process was continued for 1 h. The acetone was then removed under reduced pressure. Subsequently, a stoichiometric amount of hardener was added and the mixture was poured into a rubber mold for curing. To align the Fe_3O_4@CNFs, the mixture was subjected to a weak magnetic field of ~50 mT generated by a pair of permanent magnets whilst it was being cured. Using a gaussmeter, the intensity of the magnetic field was measured to be approximately 50 mT at a distance of 4 cm between a pair of ferrite magnets which were 150 × 50 × 25.4 mm in size. Initial, exploratory, experiments were carried out using different intensities of magnetic field, ranging from 20 mT to 50 mT by changing the gap between the magnets. Since the alignment of the Fe_3O_4@CNFs needs to be completed prior to gelation of the epoxy (the gel time of the epoxy is around 20–30 min at 25 °C), a magnetic field strength of 50 mT was finally selected so that the Fe_3O_4@CNFs could be highly aligned within approximately 10 min from the application of the magnetic field. Epoxy nanocomposites containing various weight contents (i.e. 0.0, 0.2, 0.4, and 0.6 wt%) of the Fe_3O_4@CNFs were prepared.

2.4. Preparation of composite joints

Prior to the application of the liquid epoxy resin mixture as an adhesive to form bonded joints, the surfaces of the carbon-fiber

composite substrates were sandblasted and thoroughly degreased with acetone. The substrates were then cleaned with distilled water and dried using compressed air. A dam made of silicone rubber was used to prevent the liquid epoxy resin mixture from flowing out and spacers (1 mm thick) were placed between the substrates to control the thickness of the adhesive layer. A sharp pre-crack in the mid-plane of the adhesive layer was pre-formed by using Teflon thin film (50 μm thick). The epoxy resin mixtures containing the 0.0, 0.2, 0.4, and 0.6 wt% of Fe_3O_4@CNFs and the hardener were prepared following the procedure described in Section 2.3 and then poured between the substrates which were subsequently placed between two permanent magnets to induce the alignment (Fig. 1a). The magnetic field direction is perpendicular to the bonding surfaces. The joints were cured at room temperature for 48 h. Once cured, the samples were cut into double-cantilever beam (DCB) specimens with the dimensions shown in Fig. 1b.

2.5. Characterization

2.5.1. Characterization of the Fe_3O_4@CNFs

KBr disks were prepared and dried under vacuum at 80 °C, and the measurement of Fourier transform infrared (FTIR) spectra were conducted using a Bruker Vertex 70 FTIR spectrometer. The spectra were recorded by taking the average of sixty four scans in the wave number range of 400–4000 cm^{-1} at a resolution of 4 cm^{-1}. X-ray diffraction (XRD) patterns of the samples were collected using a Bruker D8 Advance diffractometer with Cu-Kα radiation (λ = 1.54 Å). X-ray photoelectron spectroscopy (XPS) was performed using a Thermo K-alpha XPS instrument at a pressure ~1×10^{-9} Torr with the core levels aligned with the C 1s binding energy of 284.8 eV. The morphology of the samples was investigated using a transmission electron microscope (TEM) JEOL JEM 1010 operating at 100 kV and equipped with a Gatan Orius SC600 CCD camera for digital imaging. TEM samples were prepared by dropping ethanol dispersion of Fe_3O_4@CNFs on carbon-coated copper grids (200 mesh). Scanning electron microscopy (SEM) analysis was performed using a FEI Nova NanoSEM, equipped with an Oxford X-MaxN 20 energy dispersive X-ray (EDX) detector, operating at 15 kV and a 5 mm working distance. Samples were drop cast on a piece of silicon wafer which was then attached to an aluminium SEM stub with double-sided carbon tape.

2.5.2. Characterization of the epoxy nanocomposites

The alignment of the Fe_3O_4@CNFs in the epoxy was investigated using optical microscopy, TEM, and SEM. For the optical microscopy observations, a drop of a mixture of the epoxy resin/Fe_3O_4@CNFs was placed onto a glass slide.

For TEM observations, epoxy nanocomposites were microtomed into ultrathin sections of ~70 nm thick with a diamond knife using a Leica EM ultramicrotome, which were collected on 200 mesh copper grids. For SEM observations, the specimens were cryogenically fractured in liquid nitrogen and then surface-coated with a thin layer of gold prior to observation. The electrical resistivity was measured at room temperature using an Agilent 4339B high-resistivity meter equipped with a 16008B resistivity cell. The samples were tightly screw-pressed between two cylindrical electrodes having a diameter of 26 mm, in accordance with ASTM D257-99, and at least three measurements were conducted to obtain the average value. In order to accurately measure the resistivity, the sample surface was coated with a copper paste to ensure good electrical contact. For the nanocomposite samples subjected to alignment by the magnetic field, the resistivity was measured in both the perpendicular and parallel direction of the applied magnetic field.

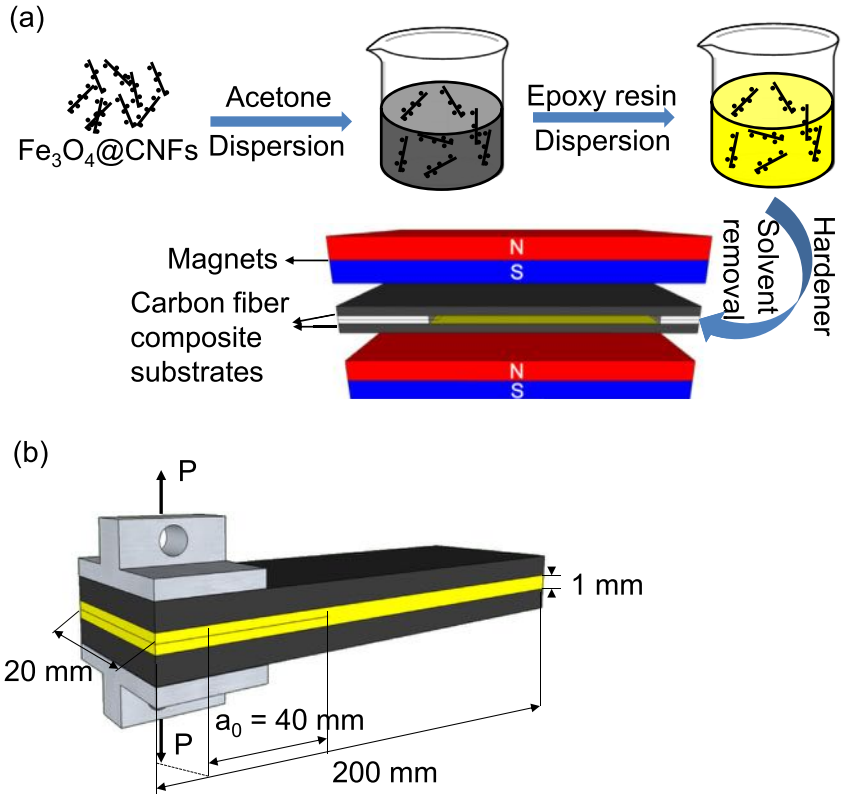

Fig. 1. Schematic of (a) composite joint preparation and (b) the DCB specimen, where a_0 is the initial crack length. The symbols N and S denote the magnetic poles of the permanent magnets.

The mode I fracture energy, G_{Ic}, of the epoxy nanocomposite layer was obtained from tests undertaken using the DCB bonded joints. A sharp crack tip was produced by carefully wedging the crack open from the tip of the inserted Teflon film. Load was applied to the specimens at a crosshead speed of 1 mm/min in accordance with ISO 25217. At least five replicate specimens were tested for each formulation. The crack growth was measured by using a travelling microscope. The mode I fracture energy was calculated based on "corrected beam theory" [34]. The crack was always found to propagate cohesively through the centre of the epoxy polymer layer, and thus the values of G_{Ic} could be readily ascertained.

3. Results and discussion

3.1. Characterization of the magnetic Fe_3O_4@CNFs

Fig. 2a and b shows the representative SEM images of the pristine CNFs and the Fe_3O_4@CNFs. The pristine CNFs show relatively smooth surfaces. By contrast, it can be clearly seen in Fig. 2b that there are some Fe_3O_4 nanoparticles (i.e. the bright domains) attached to the surfaces of the CNFs. It may be noted that the Fe_3O_4 nanoparticles are not covering the entire surface of the nanofibers and randomly distributed on the surface, but tend to form clusters. To further study the attachment of the Fe_3O_4 nanoparticles, TEM images were taken and are shown in Fig. 2c and d. These TEM images show that the clusters consist of small nanoparticles with an average diameter of 5–10 nm. The nanoparticles appear to be firmly anchored to the surface of the carbon nanofibers even after ultrasonication treatment. To verify the composition of the nanofiber hybrids, they were subjected to EDX analysis during the SEM investigation. Fig. 2e shows the EDX spectrum taken at the location indicated by the arrow in the inset image, confirming the presence of Fe and O elements. The magnetic nature of the as-prepared Fe_3O_4@CNFs was demonstrated by placing a magnet next to an ethanol dispersion of the nanofiber hybrids. The photograph on the left hand side in Fig. 2f shows the initial ethanol dispersion of Fe_3O_4@CNFs whilst the one on the right hand side shows its response to an external magnet placed next to it. The Fe_3O_4@CNFs were found to be attracted instantly to the external magnet.

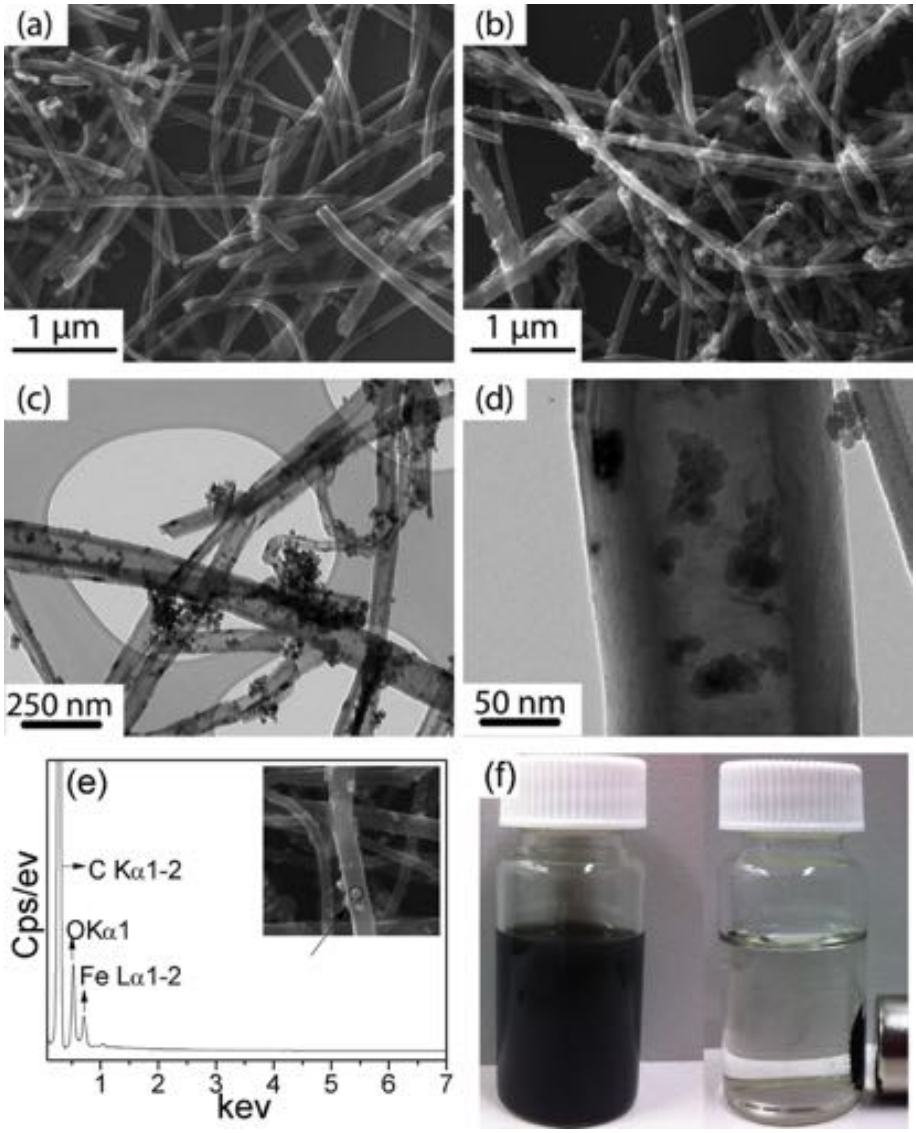

Fig. 2. SEM images of the (a) pristine CNFs and (b) Fe_3O_4@CNFs; (c) and (d) are TEM images of Fe_3O_4@CNFs at low and high magnification, respectively; (e) an EDX spectrum showing the elemental composition of the point indicated by a circle in the inserted SEM image in (e); and (f) shows the ferromagnetic behaviour of the Fe_3O_4@CNFs.

Fig. 3 shows the XRD patterns of the pristine CNFs, CNFs-OX, Fe_3O_4@CNFs, and iron oxide. The iron oxide was prepared following the same procedure as described in Section 2.2 but with the absence of the CNFs-OX for comparison. There is a sharp diffraction peak at 26.6° in the XRD spectrum of the CNFs which can be attributed to the (002) plane of their graphite structure [31]. After acid treatment, this sharp diffraction peak remains unchanged indicating that the crystalline structure of the CNFs has not been affected significantly. The main characteristic XRD peaks of iron oxide are located at 2θ = 30.4°, 35.7°, 43.2°, 53.6°, 57.3°, and 62.8° and they respectively correspond to the (220), (311), (400), (422), (511), and (440) planes of maghemite (γ-Fe_2O_3) and/or magnetite (Fe_3O_4) [35]. Maghemite and magnetite exhibit very similar XRD patterns and it is difficult to distinguish between these two phases [36]. Therefore, XPS (see Fig. 4) was employed to further verify the presence of the phase of the magnetic iron oxide. For the Fe_3O_4@CNFs, the characteristic XRD peaks of both CNFs and iron oxide can be clearly seen in the spectrum. The peak positions agree well with the diffraction peaks of both the iron oxide and the CNFs appearing at 2θ = 30.4°, 35.7°, 43.2°, 53.6°, 57.3°, 62.8°, and 26.6°.

XPS was used to study the surface chemistry of the Fe_3O_4@CNFs and the survey spectrum is given in Fig. 4a. For comparison, the survey spectra of the pristine CNFs and CNFs-OX are also provided. The typical asymmetric peak in the C1s region and symmetric peak in the O1s region can be seen in all the survey spectra of the CNFs, CNFs-OX, and Fe_3O_4@CNFs. The O1s/C1s peak area ratio increases for the CNFs-OX confirming the oxidization of the CNFs. The survey spectrum of the Fe_3O_4@CNFs indicates the presence of the elements Fe, O, and C.

To further characterize the chemical compositions and chemical oxidation states, high resolution XPS scans in the O1s, C1s, and Fe2p regions were recorded. Fig. 4b shows the O1s XPS spectra of the CNFs, CNFs-OX, and Fe_3O_4@CNFs, as well as the Fe2p scans of Fe_3O_4@CNFs. The O1s peaks of the CNFs are deconvoluted into three peaks: peak 1 at 532.0 eV corresponding to oxygen with a double bond to carbon (C═O) [37]; peak 2 at 533.1 eV corresponding to oxygen with a single bond to carbon (C–O) [31]; and peak 3 at 534.8 eV corresponding to oxygen atoms absorbed on the surface of the CNFs. Compared to the O1s spectra of the CNFs, the O1s spectra of the CNFs-OX show similar peaks but peak 1 shifts to 531.4 eV, which is likely due to the presence of more carbonyl groups on the surface after nitric acid oxidation. The relative content of carbonyl groups increases from 27.48% to 31.61%, providing further evidence of oxidation. For the Fe_3O_4@CNFs, an additional peak at 530.1 eV can be seen in the O1s spectrum revealing the presence of lattice oxygen in Fe_3O_4 [38]. From the Fe2p spectrum, the Fe2p1/2 and 2p3/2 peaks are observed at around 710.9 and 724.6 eV indicating the presence of a mixed oxide of Fe(II) and Fe(III), namely, Fe_3O_4 [38,39]. A very small shoulder exists at 719 eV, indicating the presence of a relatively small concentration of γ-Fe_2O_3.

The functionalisation of the CNFs with Fe_3O_4 was further confirmed by using FTIR spectroscopy (see Fig. 5). The pristine CNFs exhibit absorption bands at 1620 and 3440 cm^{-1} which can be assigned to the aromatic C═C [27] and H_2O adsorbed in the KBr disc [40], respectively. Compared to the pristine CNFs, the CNFs-OX were expected to show some new characteristic bands due to polar functional groups that have been introduced, including $\nu_{C=O}$ at ~1700 cm^{-1} and ν_{OH} at ~3400 cm^{-1} [32]. However, these characteristic bands cannot be clearly identified, probably due to the very low concentration of such functional groups. This was confirmed by the above XPS measurements which showed that the concentration of elemental oxygen in the CNFs-OX is 4.2%, which is slightly higher than that of the pristine CNFs (i.e. 3.4%). For the Fe_3O_4@CNFs, the absorption band observed at 597 cm^{-1} is associated with Fe–O–Fe stretching vibrations, which indicates the presence of magnetite nanoparticles [32].

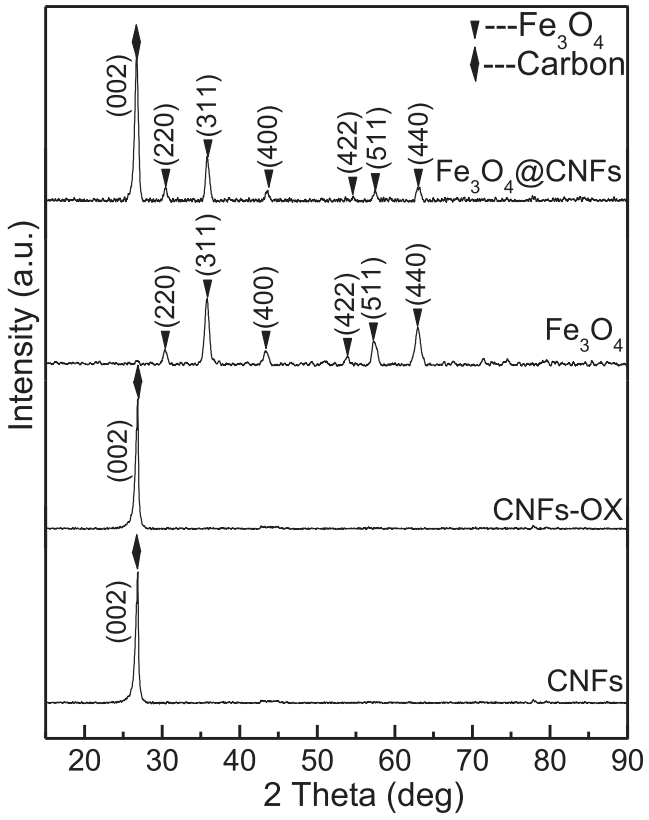

Fig. 3. XRD patterns of pristine CNFs, CNFs-OX, Fe_3O_4, and Fe_3O_4@CNFs.

3.2. Alignment of Fe_3O_4@CNFs in the epoxy nanocomposites

The alignment of the Fe_3O_4@CNFs in the liquid epoxy resin was observed using optical microscopy. Fig. 6a shows a typical optical micrograph of an epoxy resin that was not subjected to the external magnetic field. Clearly, the Fe_3O_4@CNFs are randomly-oriented in the epoxy resin. This micrograph also reveals that the nanofiber hybrids are well dispersed. Fig. 6b shows a typical optical micrograph of the liquid epoxy resin containing Fe_3O_4@CNFs subjected to the applied magnetic field. This micrograph confirms the alignment and chain-like structure of the nanofiber hybrids in the direction of the applied magnetic field, as indicated by the arrow. The alignment and chain-like structure of the Fe_3O_4@CNFs may be ascribed to the anisotropic nature of the dipolar interactions of the iron oxide nanoparticles close to the ends of the Fe_3O_4@CNFs [10,41]. Without an externally applied magnetic field, the magnetic moments of the iron oxide nanoparticles are randomly oriented leading to vanishing net magnetization. However, upon the application of a sufficiently large magnetic field, the magnetic moments of the nanoparticles align along the external field direction and the resultant dipolar interactions orient the Fe_3O_4@CNFs. Attraction of the north and south poles of the magnetic carbon nanofibers resulted in the formation of the chain-like structure.

After the epoxy was cured, the microstructures of the epoxy nanocomposites were examined by SEM and TEM to ascertain whether the aligned structure achieved while the epoxy was liquid remained in place. For comparison, Fig. 6c shows a SEM image of the epoxy nanocomposite without being subjected to any applied

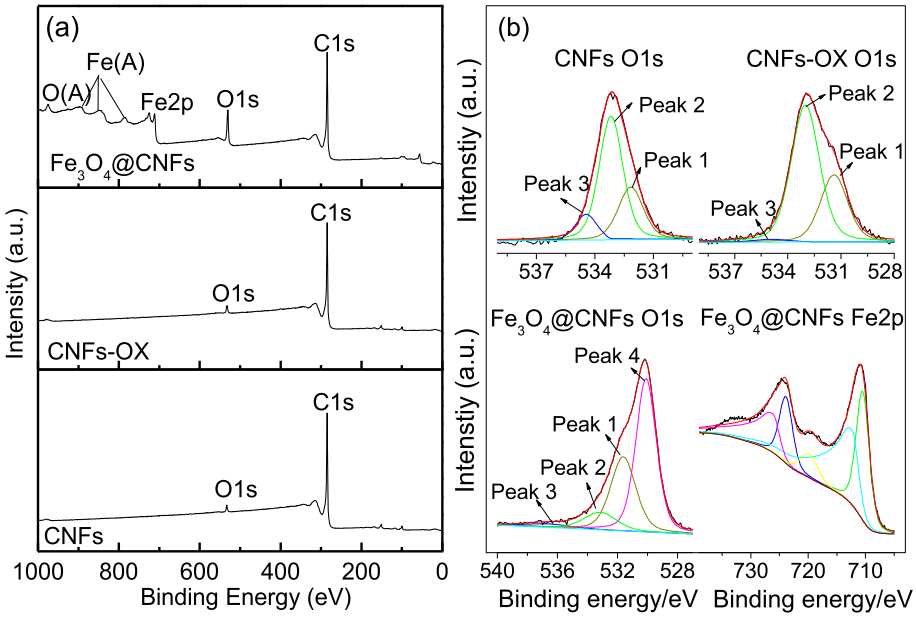

Fig. 4. XPS spectra: (a) survey spectrum of pristine CNFs, CNFs-OX, and Fe_3O_4@CNFs; (b) high resolution O1s and Fe2p scans of CNFs, CNFs-OX, and Fe_3O_4@CNFs.

magnetic field. As expected, the Fe_3O_4@CNFs (i.e. the bright spots) are uniformly dispersed and randomly-oriented in the epoxy polymer (i.e. the grey continuous area). For the epoxy nanocomposites subjected to the magnetic field during curing, Fig. 6d reveals that the Fe_3O_4@CNFs are aligned parallel to the direction of the magnetic field, consistent with the observed alignment in the liquid epoxy resin prior to cure (see Fig. 6b). The TEM images (see Fig. 6e and f) further support the above conclusions on the orientation of the nanofiber hybrids, parallel to the applied magnetic field, in the epoxy nanocomposites.

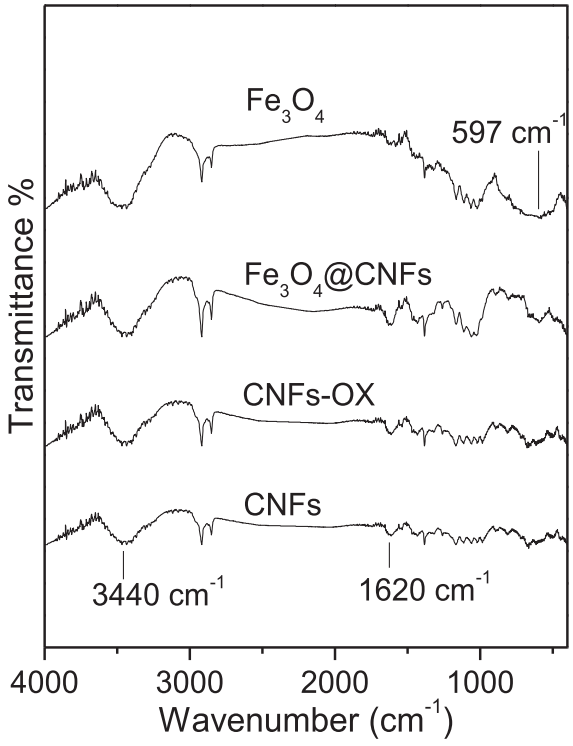

Fig. 5. FTIR spectra of pristine CNFs, CNFs-OX, Fe_3O_4@CNFs, and Fe_3O_4.

3.3. Electrical conductivity studies

Fig. 7 shows the conductivity of the epoxy nanocomposites with different contents of randomly-oriented and aligned Fe_3O_4@CNFs. The electrical conductivities of the Fe_3O_4@CNFs epoxy nanocomposites subjected to the magnetic field were measured in two directions, namely, parallel and perpendicular to the direction of the externally applied magnetic field. The unmodified epoxy exhibits a conductivity of ~10^{-13} S/m which increases to ~10^{-12} S/m and ~10^{-10} S/m for the epoxy nanocomposites containing 0.2 wt% and 0.6 wt% of randomly-oriented Fe_3O_4@CNFs, respectively. For the epoxy nanocomposites cured under the applied magnetic field, a higher electrical conductivity is observed when measured in the direction parallel to the magnetic field. Indeed, the conductivity in the direction parallel to the magnetic field is consistently over one order of magnitude higher than that for the nanocomposites containing randomly-oriented Fe_3O_4@CNFs. This is similar to the reported increase from the use of CNTs aligned by a magnetic field of 25 T [42,43]. By contrast, the electrical conductivity measured normal to the magnetic field shows no significant increase compared to the nanocomposites containing randomly-oriented Fe_3O_4@CNFs. This demonstrates that the application of the magnetic field leads to the resultant epoxy nanocomposites possessing anisotropic electrical properties. However, the improvement of the electrical conductivities was not that remarkable. It has been reported that higher the oxygen concentration present in the CNFs, then higher is the content of CNFs required to reach the percolation threshold [44]. During the preparation of the Fe_3O_4@CNFs, a strong acid was employed to treat the CNFs, which might have introduced some defects and some oxidative surface groups. This partially may account for the relatively low electrical conductivity of the epoxy nanocomposites. Additionally, coating the surface of CNFs with iron oxide nanoparticles, which have a relatively high resistivity, would further reduce the electrical conductivity of the nanocomposite [10,25].

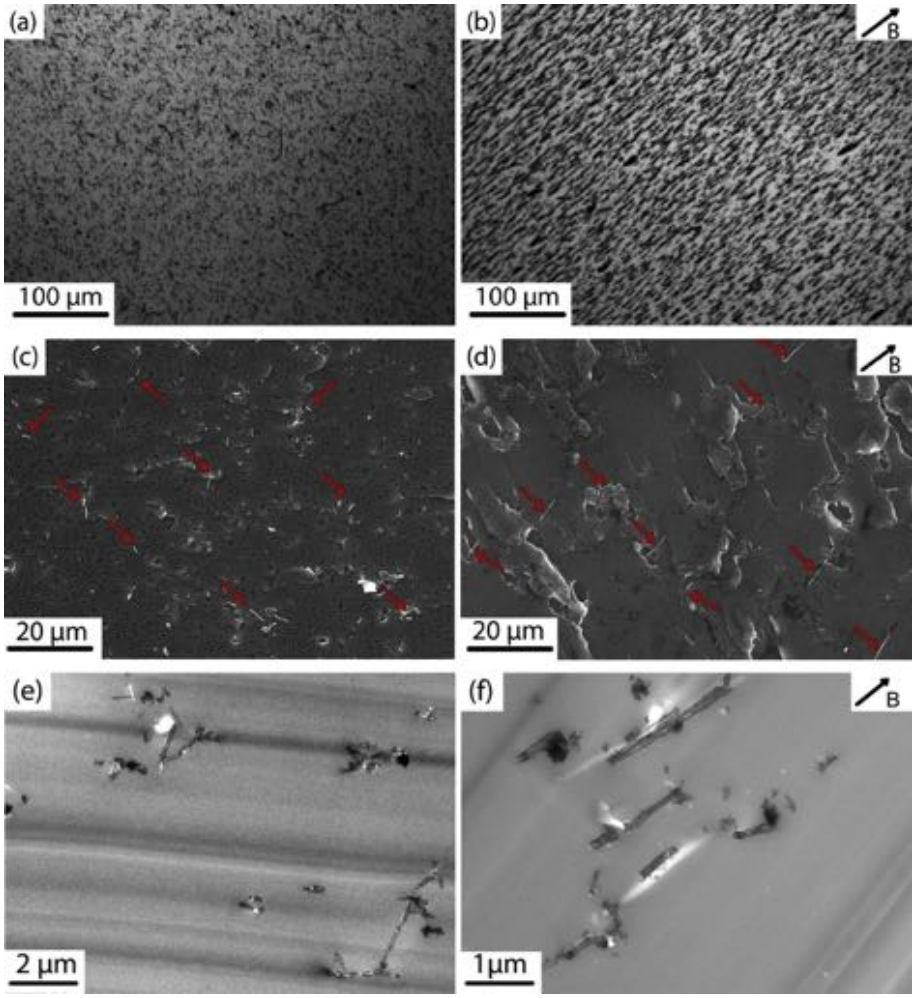

Fig. 6. Representative optical micrographs (a and b), SEM images (c and d), and TEM (e and f) images of epoxy nanocomposites containing 0.6 wt% of randomly-oriented Fe_3O_4@CNFs (i.e. (a), (c), and (e)) and Fe_3O_4@CNFs aligned under the 50 mT magnetic field (i.e. (b), (d), and (f)). The black arrows in (b), (d), and (f) indicate the direction of the applied magnetic field (B). The red arrows in (c) and (d) indicate the nanofiber hybrids. (For interpretation of the references to colour in this figure legend, the reader is referred to the web version of this article.)

3.4. Fracture toughness studies

The effects of the alignment of the nanofiber hybrids on the fracture toughness of the epoxy nanocomposites were studied by investigating the mode I fracture behaviour of the carbon fiber composite joints bonded using the epoxy nanocomposites (or the unmodified epoxy polymer). The unmodified epoxy polymer and all the epoxy nanocomposites exhibited unstable, stick-slip, crack growth behaviour. Such behaviour gives rise to classic 'saw-tooth' shaped load versus displacement curves. Fig. 8a shows the typical load versus displacement curves for an epoxy nanocomposite containing 0.6 wt% of Fe_3O_4@CNFs. The maximum load values are associated with the onset of crack growth, which is followed by very rapid crack growth leading to the crack arresting at the lower load values. Following ISO 25217, the value of the fracture energy, G_{Ic}, for the onset of crack growth was determined using the maximum load values. Fig. 8b presents the values of G_{Ic} of the unmodified epoxy polymer and the epoxy nanocomposites containing either randomly-oriented or aligned nanofiber hybrids. The average fracture energy of the unmodified epoxy polymer is 134 J/m^2. With the addition of 0.4 wt% of randomly-oriented nanofiber hybrids, the fracture energy increased to 242 J/m^2. The application of the external magnetic field, which oriented the Fe_3O_4@CNFs in a direction normal to the crack surface, further improved the fracture energy to 328 J/m^2. It can be seen from Fig. 8b that increasing the content of the Fe_3O_4@CNFs beyond 0.4 wt% did not yield any further significant improvements in G_{Ic} of the epoxy nanocomposites containing either the randomly-oriented or aligned nanofiber hybrids.

3.5. Toughening mechanisms

To identify the toughening mechanisms, the fracture surfaces of the unmodified epoxy polymer and epoxy nanocomposites from the DCB tests were examined, both visually and using the SEM. From a visual inspection, for both the unmodified epoxy polymer and epoxy nanocomposites, there were distinct 'thumbnail lines' on the fracture surfaces where the onset of crack propagation and then crack arrest had occurred. Further, for the epoxy nanocomposites, stress-whitening was observed along the 'thumbnail lines' which indicated the occurrence of more extensive damage at the crack tip prior to crack propagation in the nanocomposites compared to the unmodified epoxy polymer. Such an observation is typically associated with an enhanced toughness.

Fig. 9a shows SEM images of the fracture surfaces of the DCB specimens bonded using the unmodified epoxy polymer. The

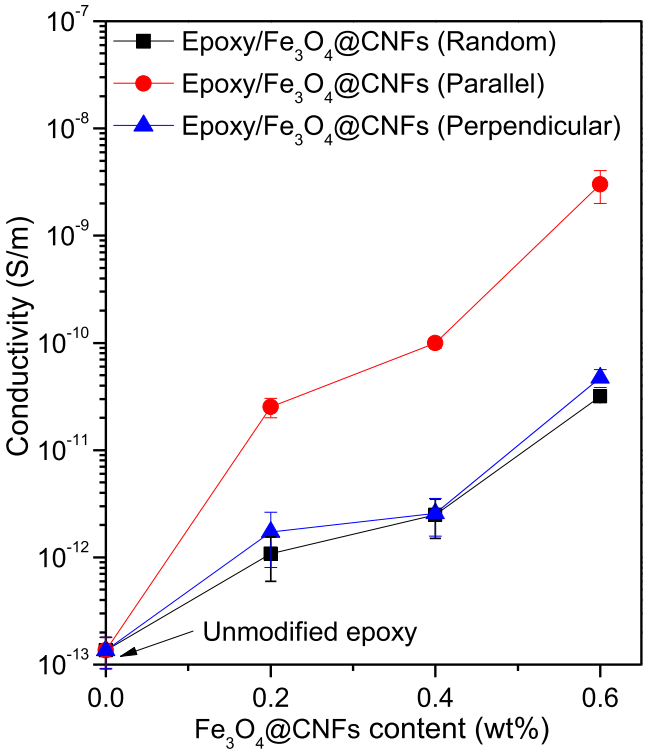

Fig. 7. Electrical conductivity of the epoxy nanocomposites containing 0.0, 0.2, 0.4, and 0.6 wt% of Fe_3O_4@CNFs. (The orientation of the Fe_3O_4@CNFs with respect to the direction of measurement is indicated.)

fracture surface is very smooth and featureless, indicating a very brittle fracture behaviour. On the other hand, the presence of Fe_3O_4@CNFs in the epoxy produced much rougher surfaces and patterns of tear marks, as shown in Fig. 9b–d. These are likely to arise from crack deflection due to the presence of the Fe_3O_4@CNFs and plastic deformation of the epoxy polymer surrounding the Fe_3O_4@CNFs. A closer inspection of the fracture surfaces reveals that the Fe_3O_4@CNFs were pulled out after debonding from the epoxy polymer, with some Fe_3O_4@CNFs being peeled away from the epoxy (see Fig. 9b–d). Cavities and grooves created by the pull-out and debonding of the Fe_3O_4@CNFs, as well as ruptured Fe_3O_4@CNFs, are evident in Fig. 9d and e. A high magnification SEM image (see Fig. 9e) reveals that there are voids surrounding the Fe_3O_4@CNFs. These voids are typically created due to debonding of the Fe_3O_4@CNFs from the epoxy polymer, followed by plastic deformation of the epoxy. This plastic void growth mechanism will also absorb energy and will further enhance the fracture energy of the nanocomposites. Behind the advancing crack tip, Fe_3O_4@CNFs are pulled out from the epoxy polymer and bridge the crack faces, as shown by a cross-section image in Fig. 10. The alignment of the Fe_3O_4@CNFs in the direction normal to the crack surface increases the possibility of such interactions between the advancing crack tip and the Fe_3O_4@CNFs.

Similar toughening mechanisms to those described above have been reported for epoxy nanocomposites containing MWCNTs [45] and all of these toughening mechanisms contribute to the measured increases in the fracture energy, G_{Ic}, for the epoxy nanocomposites. The nanocomposites containing nanofiber hybrids aligned normal to the crack surface are more effective at inducing such toughening mechanisms than those containing only randomly-oriented nanofiber hybrids, leading to a significantly higher G_{Ic}.

4. Conclusions

Fe_3O_4@CNFs hybrids have been fabricated by attaching magnetite nanoparticles to CNFs through a simple and effective co-precipitation method. Using the techniques of optical microscopy, SEM and TEM, it has been conclusively established that the Fe_3O_4@CNFs can be aligned in the liquid epoxy resin by the application of a relatively weak magnetic field (~50 mT), and that this alignment of the nanofiber hybrids is maintained after the epoxy nanocomposites are cured. Compared to the unmodified epoxy polymer, the epoxy nanocomposites exhibit a higher electrical conductivity, especially along the direction of the alignment. In addition, alignment of the Fe_3O_4@CNFs significantly improves the toughening efficiency. For example, the addition of 0.4 wt% of aligned Fe_3O_4@CNFs increases the fracture energy of the epoxy nanocomposites by about 150% above that of the unmodified epoxy polymer. By contrast, randomly-oriented Fe_3O_4@CNFs at the same

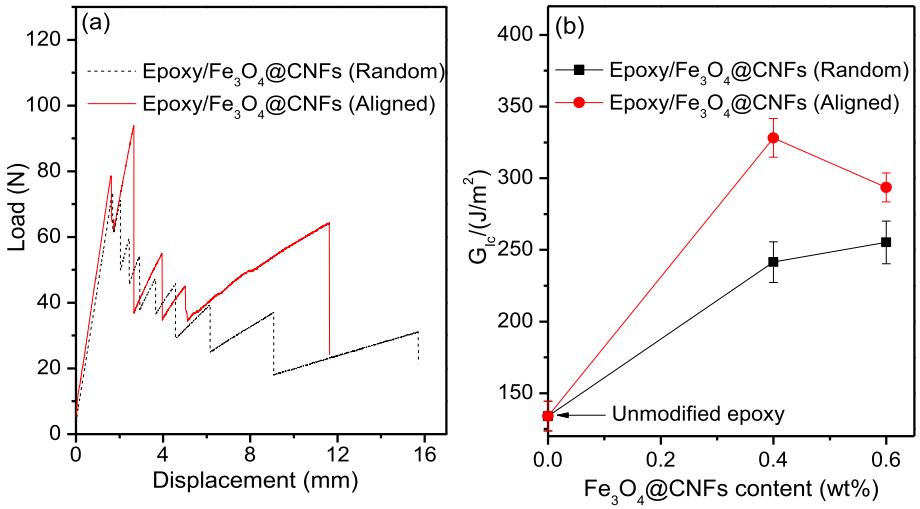

Fig. 8. (a) Representative load versus displacement curves of the epoxy nanocomposites with 0.6 wt% of randomly-oriented or aligned Fe_3O_4@CNFs; (b) the mode I fracture energy, G_{Ic}, of the epoxy nanocomposites as a function of the content of Fe_3O_4@CNFs. (The orientation of the Fe_3O_4@CNFs was either random or aligned normal to the crack surface, as indicated.)

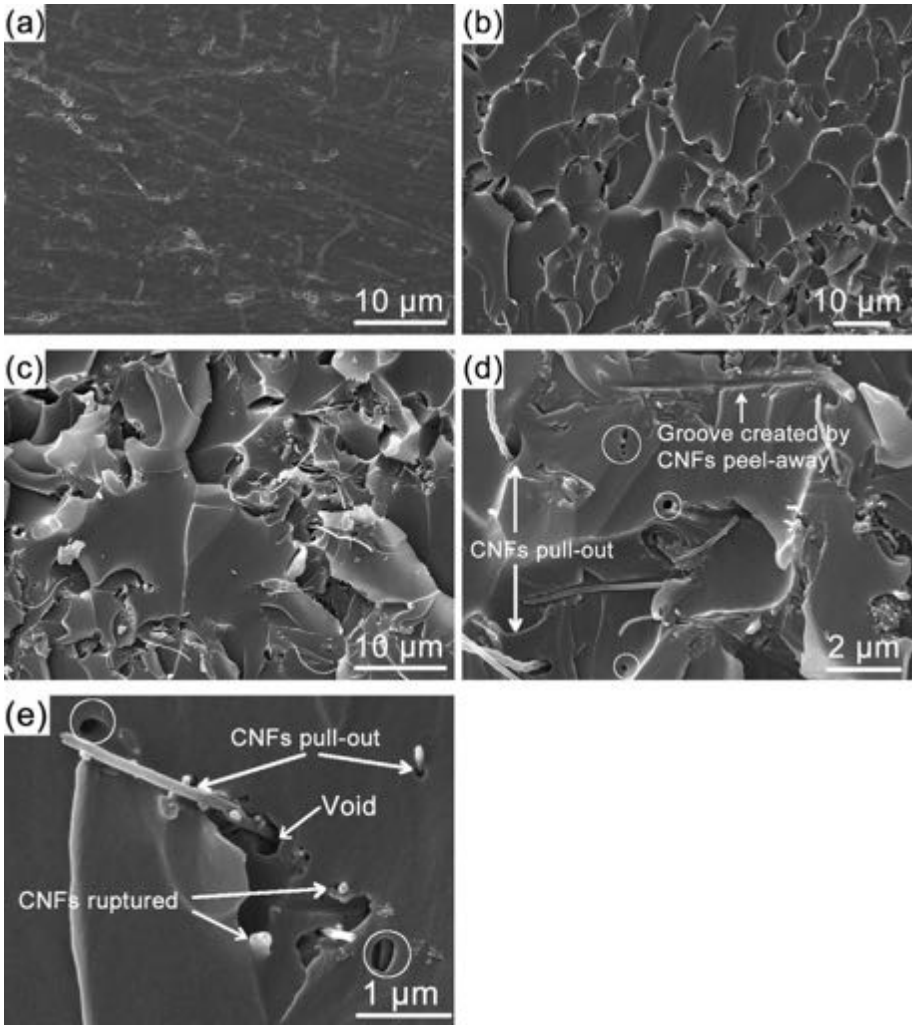

Fig. 9. SEM micrographs of the fracture surfaces of (a) the unmodified epoxy polymer and (b–e) the epoxy nanocomposites containing 0.6 wt% of aligned Fe_3O_4@CNFs. The white circles in (d) and (e) indicate the cavities created by pull-out of the Fe_3O_4@CNFs.

content only give about an 80% improvement. Based on fractographic analyses, the main toughening mechanisms induced by the nanofiber hybrids include interfacial debonding, pull-out, crack bridging and rupture of the Fe_3O_4@CNFs, and plastic void growth in the epoxy polymer. The alignment of the Fe_3O_4@CNFs in the direction normal to the crack surface increases their propensity to interact with the advancing crack tip, leading to more effective toughening. The present work has clearly demonstrated that by attaching magnetite nanoparticles to CNFs the resulting nanofiber hybrids can be aligned in an epoxy polymer using a relatively weak magnetic field. The epoxy nanocomposites so produced exhibit significant improvements in their electrical conductivity and fracture toughness.

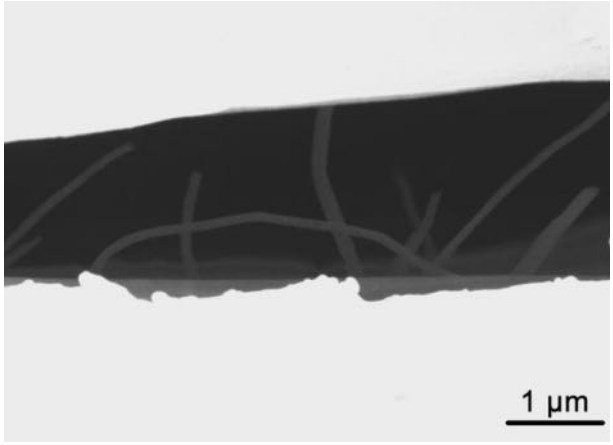

Fig. 10. SEM micrograph of the cross-section (i.e. side view) of the crack tip of a DCB specimen bonded with the epoxy nanocomposites containing 0.6 wt% of aligned Fe_3O_4@CNFs.

Acknowledgements

The authors are thankful for the financial support received from the Australian Research Council's Discovery Grant (DP140100778).

References

[1] Jia JJ, Sun XY, Lin XY, Shen X, Mai YW, Kim JK. ACS Nano 2014;8:5774–83.
[2] Meng QS, Jin J, Wang RY, Kuan HC, Ma J, Kawashima N, et al. Nanotechnology 2014;25:125707.
[3] Roy S, Das T, Zhang L, Li Y, Ming Y, Ting S, et al. Polymer 2015;58:153–61.
[4] Ma HY, Chen XM, Hsiao BS, Chu B. Polymer 2014;55:160–5.
[5] Al-Saleh MH, Sundararaj U. Polymer 2010;51:2740–7.
[6] Liao K-H, Qian Y, Macosko CW. Polymer 2012;53:3756–61.
[7] Park YT, Qian Y, Chan C, Suh T, Nejhad MG, Macosko CW, et al. Adv Funct Mater 2014:575–85.

[8] Vennerberg D, Hall R, Kessler MR. Polymer 2014;55:4156–63.
[9] Ajayan PM, Stephan O, Colliex C, Trauth D. Science 1994;265:1212–4.
[10] Kim IT, Tannenbaum A, Tannenbaum R. Carbon 2011;49:54–61.
[11] Yousefi N, Gudarzi MM, Zheng Q, Lin X, Shen X, Jia J, et al. Compos Part A 2013;49:42–50.
[12] Yousefi N, Sun X, Lin X, Shen X, Jia J, Zhang B, et al. Adv Mater 2014;26:5480–7.
[13] Yousefi N, Lin X, Zheng Q, Shen X, Pothnis JR, Jia J, et al. Carbon 2013;59:406–17.
[14] Wang Q, Dai JF, Li WX, Wei ZQ, Jiang JL. Compos Sci Technol 2008;68:1644–8.
[15] Bradford PD, Wang X, Zhao HB, Maria JP, Jia QX, Zhu YT. Compos Sci Technol 2010;70:1980–5.
[16] Schwarz M-K, Bauhofer W, Schulte K. Polymer 2002;43:3079–82.
[17] Martin CA, Sandler JKW, Windle AH, Schwarz MK, Bauhofer W, Schulte K, et al. Polymer 2005;46:877–86.
[18] Steinert BW, Dean DR. Polymer 2009;50:898–904.
[19] Abdalla M, Dean D, Theodore M, Fielding J, Nyairo E, Price G. Polymer 2010;51:1614–20.
[20] Mahfuz H, Zainuddin S, Parker M, Al-Saadi T, Rangari V, Jeelani S. J Mater Sci 2009;44:1113–20.
[21] Camponeschi E, Vance R, Al-Haik M, Garmestani H, Tannenbaum R. Carbon 2007;45:2037–46.
[22] Shi D, He P, Lian J, Chaud X, Bud'ko SL, Beaugnon E, et al. J Appl Phys 2005;97:064312.
[23] Fragouli D, Das A, Innocenti C, Guttikonda Y, Rahman S, Liu L, et al. ACS Appl Mater Interfaces 2014;6:4535–41.
[24] Malkina O, Mahfuz H, Sorge K, Rondinone A, Chen J, More K, et al. AIP Adv 2013;3:042104.
[25] Prolongo SG, Meliton BG, Del Rosario G, Urena A. Compos Part B 2013;46:166–72.
[26] Yan HY, Tang YX, Long W, Li YF. J Mater Sci 2014;49:5256–64.
[27] Jiao WC, Shioya M, Wang RG, Yang F, Hao LF, Niu Y, et al. Compos Sci Technol 2014;99:124–30.
[28] Al-Saleh MH, Sundararaj U. Carbon 2009;47:2–22.
[29] Ren T, Si Y, Yang JM, Ding B, Yang XX, Hong F, et al. J Mater Chem 2012;22:15919–27.
[30] Si Y, Ren T, Ding B, Yu J, Sun G. J Mater Chem 2012;22:4619–22.
[31] Zhong RS, Qin YH, Niu DF, Zhang XS, Zhou XG, Sun SG, et al. Electrochim Acta 2013;89:157–62.
[32] Cunha C, Panseri S, Iannazzo D, Piperno A, Pistone A, Fazio M, et al. Nanotechnology 2012;23:465102.
[33] Zhang J, Wang JF, Lin T, Wang CH, Ghorbani K, Fang J, et al. Chem Eng J 2014;237:462–8.
[34] Blackman BRK, Kinloch AJ. Fracture tests on structural adhesive joints. In: Moore APDR, Williams JG, editors. European Structural Integrity Society. Elsevier; 2001. p. 225–67.
[35] Kim IT, Nunnery GA, Jacob K, Schwartz J, Liu XT, Tannenbaum R. J Phys Chem C 2010;114:6944–51.
[36] Sun Z, Liu Z, Wang Y, Han B, Du J, Zhang J. J Mater Chem 2005;15:4497–501.
[37] Cuervo MR, Asedegbega-Nieto E, Díaz E, Vega A, Ordóñez S, Castillejos-López E, et al. J Chromatogr A 2008;1188:264–73.
[38] Bhuvaneswari S, Pratheeksha PM, Anandan S, Rangappa D, Gopalan R, Rao TN. Phys Chem Chem Phys 2014;16:5284–94.
[39] Zhu S, Guo J, Dong J, Cui Z, Lu T, Zhu C, et al. Ultrason Sonochem 2013;20:872–80.
[40] Zhou J-H, Sui Z-J, Zhu J, Li P, Chen D, Dai Y-C, et al. Carbon 2007;45:785–96.
[41] Correa-Duarte MA, Grzelczak M, Salgueirino-Maceira V, Giersig M, Liz-Marzan LM, Farle M, et al. J Phys Chem B 2005;109:19060–3.
[42] Choi ES, Brooks JS, Eaton DL, Al-Haik MS, Hussaini MY, Garmestani H, et al. J Appl Phys 2003;94:6034–9.
[43] Kimura T, Ago H, Tobita M, Ohshima S, Kyotani M, Yumura M. Adv Mater 2002;14:1380–3.
[44] Lim CS, Rodriguez AJ, Guzman ME, Schaefer JD, Minaie B. Carbon 2011;49:1873–83.
[45] Hsieh TH, Kinloch AJ, Taylor AC, Kinloch IA. J Mater Sci 2011;46:7525–35.